AFAPL-TR-64-134

LIQUID HYDROGEN PUMP

W. N. Hall
P. Hildebrand
D. S. Ko, et al

AiResearch Manufacturing Company
a Division of The Garrett Corporation

November 1964

TECHNICAL REPORT AFAPL-TR-64-134

Air Force Aero Propulsion Laboratory
Research and Technology Division
Air Force Systems Command
Wright-Patterson Air Force Base, Ohio

NOTICES

When Government drawings, specifications, or other data are used for any purpose than in connection with a definitely related Government procurement operation, the United States Government thereby incurs no responsibility nor any obligation whatsoever; and the fact that the Government may have formulated, furnished, or in any way supplied the said drawings, specifications, or other data, is not to be regarded by implication or otherwise as in any manner licensing the holder or any other person or corporation, or conveying any rights or permission to manufacture, use, or sell any patented invention that may in any way be related thereto.

DDC release to OTS not authorized. (See Foreword.)

Qualified requesters may obtain copies of this report from the Defense Documentation Center (DDC), (formerly ASTIA) - Cameron Station, Bldg. 5, 5010 Duke Street, Alexandria, Virginia, 22314.

Copies of this report should not be returned to the Research and Technology Division, Wright-Patterson Air Force Base, Ohio, unless return is required by security considerations, contractual obligations, or notice on a specific document.

FOREWORD

This report is the culmination of a 16-month Liquid Hydrogen Pump Program conducted by AiResearch Manufacturing Company, a division of The Garrett Corporation, Los Angeles, California, under Research and Technology Division Contract No. AF33(657)-10680. The program was designated Task No. 306603 under Project No. 3066, and covered the period from 1 March 1963 through 30 June 1964.

The project was administered for the Research and Technology Division, Wright-Patterson Air Force Base, Ohio. At AiResearch, the project was under the administrative control of R. L. Schinnerer, chief of environmental control. J. W. Meermans, senior project engineer, prepared the overall research plan, consisting of the schedule of tasks, facility sizing and procurement, obtained and assigned manpower to the various duties, and assisted the project engineer in the performance of his duties J. F. Schwimmer was project engineer, responsible for overall guidance and coordination. Major AiResearch contributors were N. Van Le, chief of aerodynamics, G. Chessmore, systems dynamics chief, and A. D. Meshew, chief of facilities. Acknowledgment is made to L. Nagyszalanczy, W. W. English, D. S. Ko, and Dan Rau for analytical studies, to W. N. Hall, J. L. Sanders, and G. Kasabian for the mechanical design, fabrication, and experimental work, and to P. M. Hildebrand for the analysis of the experimental results.

Special acknowledgment is given to the AiResearch New Products Project, Phoenix, Arizona, for preparing the liquid hydrogen facility for the pump test evaluation.

The AiResearch Document Number for this Program Report is AAC-4788-R.

ABSTRACT

This report describes the design, fabrication, and experimental investigation of a centrifugal liquid hydrogen pump capable of 1700-gpm and 800-psi operation at low net positive suction head (NPSH).

The conceptual design of a liquid hydrogen fuel transfer system using this pump is presented, complete with system dynamic analysis.

CONTENTS

CONTENTS (Continued)

CONTENTS (Continued)

CONTENTS (Continued)

ILLUSTRATIONS

ILLUSTRATIONS (Continued)

ILLUSTRATIONS (Continued)

ILLUSTRATIONS (Continued)

TABLES

SECTION I

PROBLEM STATEMENT

PROGRAM OBJECTIVES

The primary objective of this research effort is to develop the technology necessary to provide a variable capacity fuel transfer system with a high rate of response for a hydrogen-burning turbopropulsion system. Secondary objectives are:

1. Weight and volume reduction of the fuel transfer system
2. Reduction of heat rise and turbulence losses within the pumping system
3. Increase of the high-temperature environmental capabilities of the system
4. Elimination of fuel recirculation by speed control
5. Attainment of a high degree of reliability through design simplicity

The research program calls for the performance of a hydrodynamic design study leading to the design, fabrication and experimental investigation of a liquid hydrogen centrifugal pump capable of a flow range of 20,000 to 60,000 lb per hr. Optimum efficiency is required at maximum flow with a minimum net positive suction head (NPSH) of 10 ft and a pressure rise of 800 psi.

Development of analytical methods to establish off-design performance is also required to provide the characteristic curves of the pump to permit the study of proper turbines to drive the pump.

Preliminary investigation of the conceptual designs of a LH_2 fuel transfer system using the present pump is needed, aimed at bringing out the control requirements and response characteristics of the fuel system.

SECTION 2

SUMMARY

ACCOMPLISHMENTS

This report presents the results of a theoretical and experimental investigation on the problems encountered using a centrifugal pump in a liquid hydrogen fuel transfer system for advanced propulsion engines.

Analytical Studies

The hydrodynamic design studies lead to the selection of a centrifugal pump with 45^0 backward blade angles and a swept-back inducer to handle the cavitation problems associated with low NPSH operation. The pump is designed to deliver a flow rate of 1700 gpm at 800 psi and is capable of operating with a suction specific speed of 300,000. It operates at a tip speed of 1260 ft per second. The impeller is a shrouded wheel designed with sufficient strength to carry the forward leading edges of the swept-back design. Inducer tip speed is 830 ft per second. The centrifugal pump incorporates a series of five separate channels used to improve the overall performance.

The work carried out in this investigation led to the development of a calculation procedure to predict the performance of various pump configurations over a complete range of speeds. The procedure has been computer programmed to expedite calculations.

Investigation has been accomplished to determine the most suitable means of driving the pump serving an airbreathing propulsion engine. An attractive approach is found in a hot turbine driven by a fraction of the delivery flow of the pump which has been heated to a typical temperature level of 2000^0R. A conceptual design of a liquid hydrogen fuel transfer system has been formulated. This, together with the pump characteristics derived from analytical studies, has been used in an investigation of the dynamic response of the fuel transfer system.

Fuel Transfer System Dynamic Analysis

The function of the fuel transfer system is to transfer LH_2 fuel from a remote tank to an operating engine with throttle capabilities. System configuration was determined and components were sized to meet steady state requirements. A dynamic analysis was conducted to determine the open loop dynamic characteristics between throttle area change and fuel flow response.

A mathematical model or set of simultaneous system equations was derived from which an analog computer model was developed. The computer model was used to generate system dynamic response information.

Computer simulation has shown the system to be quite stable and heavily damped throughout its operating range displaying smooth dynamic response characteristics. System gain between throttle area and fuel flow increases by a factor of 25 with increased throttling over the operating range, because of a nonlinear steady state relation between throttle area and fuel flow. System response is consisderably slower in a heavily throttled condition. Fuel flow response to a small-magnitude step change in throttle area at five operating conditions covering an operating range between 14.5 and 1.9 lb per sec fuel flow showed an increased rise time from 1.0 to 7.5 sec with increased throttling. Percent overshoot also increased with increased throttling from 15 to 65 percent, but maintained a high degree of damping. A large magnitude step change would produce a rise time of about 2 to 3 seconds because of the nonlinear relationship between rise time and operating condition. The increase in response time with increased throttling was shown to be primarily a result of the slope of the system operating torque speed curve. System response at the heavily throttled conditions could be significantly improved with proper closed loop control functions.

Pump Design and Performance

A liquid hydrogen pump containing the hubless inducer impeller was designed to meet the specified conditions. One pump, including spares, was fabricated. A total of seven test runs were made; six runs on one configuration (total run time 43 minutes 45 seconds) and one run on an alternate configuration (run time 2 minutes 38 seconds). During these test runs, the liquid hydrogen pump demonstrated the mechanical integrity of the pump design.

Results of these runs are presented in Figure 1.

Test data were obtained in the range of 40 to 85 percent of design speed and showed that pump pressure delivery closely follows calculated performance. At 85 percent design speed, or 33,500 rpm, a pressure rise of 560 psi was demonstrated at a flow rate of 1340 gpm. This data, close to design speed, indicates that full pressure and flow would be within the practical achievement of the pump at the design condition.

Cavitation performance of the backward-swept inducer has been obtained at 62.5 percent of design speed, or approximately 25,000 to 26,000 rpm, with suction specific speeds (SSS) ranging from 90,000 to infinite or negative value. Generalized performance analysis indicate that this inducer design operates smoothly under very small values of the cavitation parameter, and presents a very gradual change in pump head under high SSS values. No pounding phenomenon has been reported. The experimental investigation also demonstrates conclusively the practical strength and integrity of the swept-back inducer operating at high speeds leading to a reduction in weight and size of the turbopump, and improvement in the dynamic response of the fuel transfer system.

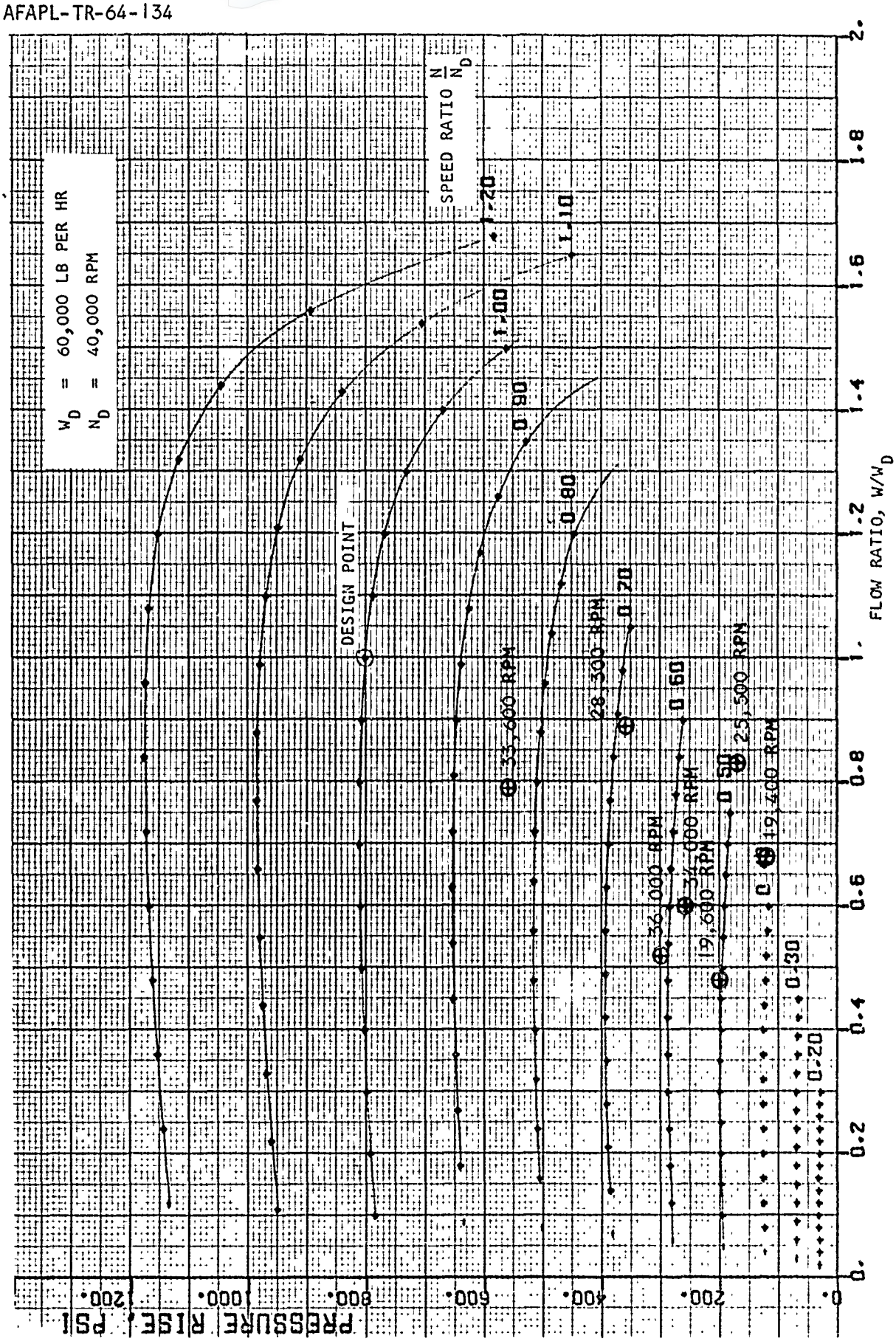

Figure 1. Comparison of Liquid Hydrogen Pump Predicted and Actual Performance

CONCLUSIONS AND RECOMMENDATIONS

Experimental results of the seven pump test runs has produced promising performance which justifies the advanced concept of the pump design introduced into the liquid hydrogen fuel transfer system. Wide range characteristics and cavitation performance with the absence of flow pounding are among the features necessary for such an advanced fuel system. Control simplicity and satisfactory dynamic response of the typical turbopump illustrates the full potential of this design concept as applied to future vehicles.

The experimental investigation to date has produced isolated data which pinpoints the overall performance. Further testing of the pump is recommended to explore its full performance characteristics and establish its complete integrity under operating conditions. Also, integration of the pump into a hot hydrogen driven turbopump is needed to establish a sound approach to the dynamic behavior of the system.

SECTION 3

HYDRODYNAMIC DESIGN STUDIES

SINGLE-STAGE CENTRIFUGAL PUMP

A single-stage centrifugal pump has been found to be the type that provides a most satisfactory solution to the present problem. This design not only offers the desired performance but presents also a wide range of operating characteristics that are required features for simplicity in the control of the fuel transfer system. In introducing high-speed design, the diameter of the rotating group is reduced, and the acceleration characteristics and the response of the fuel system are thereby improved.

Design Speed

Using experimental data presented in Figure 42, the attainable performance of a single-stage centrifugal pump is shown on Figure 2 . The specific speed and suction specific speed achieved are also presented in Figure 3 . The results indicated that design speed can be taken as

$$N = 40{,}800 \text{ rpm}$$

with the pump operating at a relatively good specific speed of 720 and the desired suction specific speed of 300,000.

Cavitation and Swept-Back Inducer

The achievement of an SSS of 300,000 is to be demonstrated in a full-size pump in this program. In a preliminary survey, values of SSS in this range or higher have been reported in small-size experimental inducers of the helical type (References 1 and 2). This possibility of high suction performance of the LH_2 pump has been attributed to its thermodynamic properties (Reference 2), which give an extra depression head as soon as vapor is formed.

Effectively, the head available for cavitation resistance is made up of the NPSH and this extra head, also called thermal suction head. The thermal suction head generated by various amounts of vapor is shown in Figure 4 . Thus, if an amount of vapor as measured by a value of B of 0.8 is found at the pump inlet, the resulting TSH is 110 ft and the effective suction specific speed, S_V, is only 50,000.

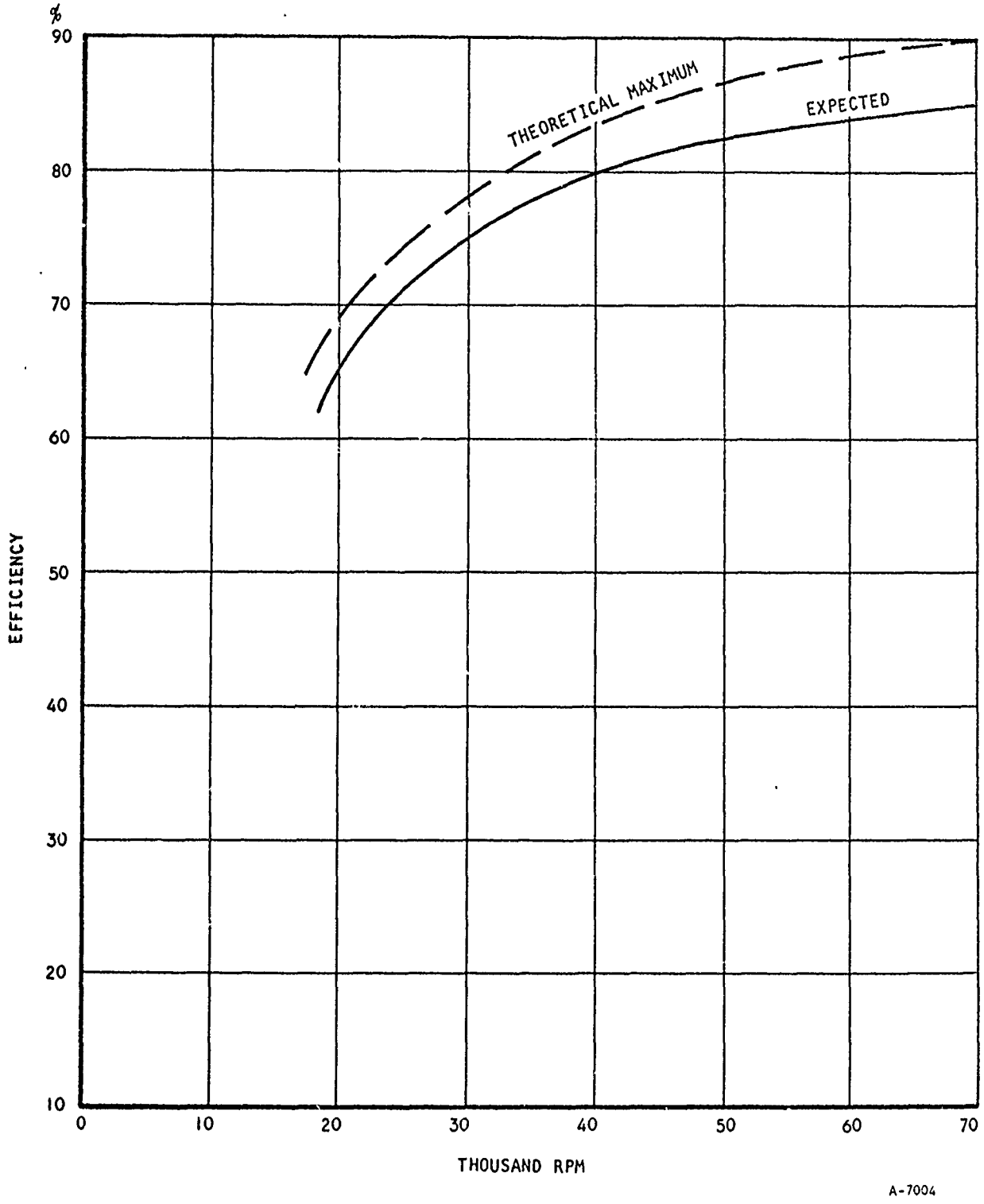

Figure 2. LH_2 Pump Single-Stage Efficiency vs Speed

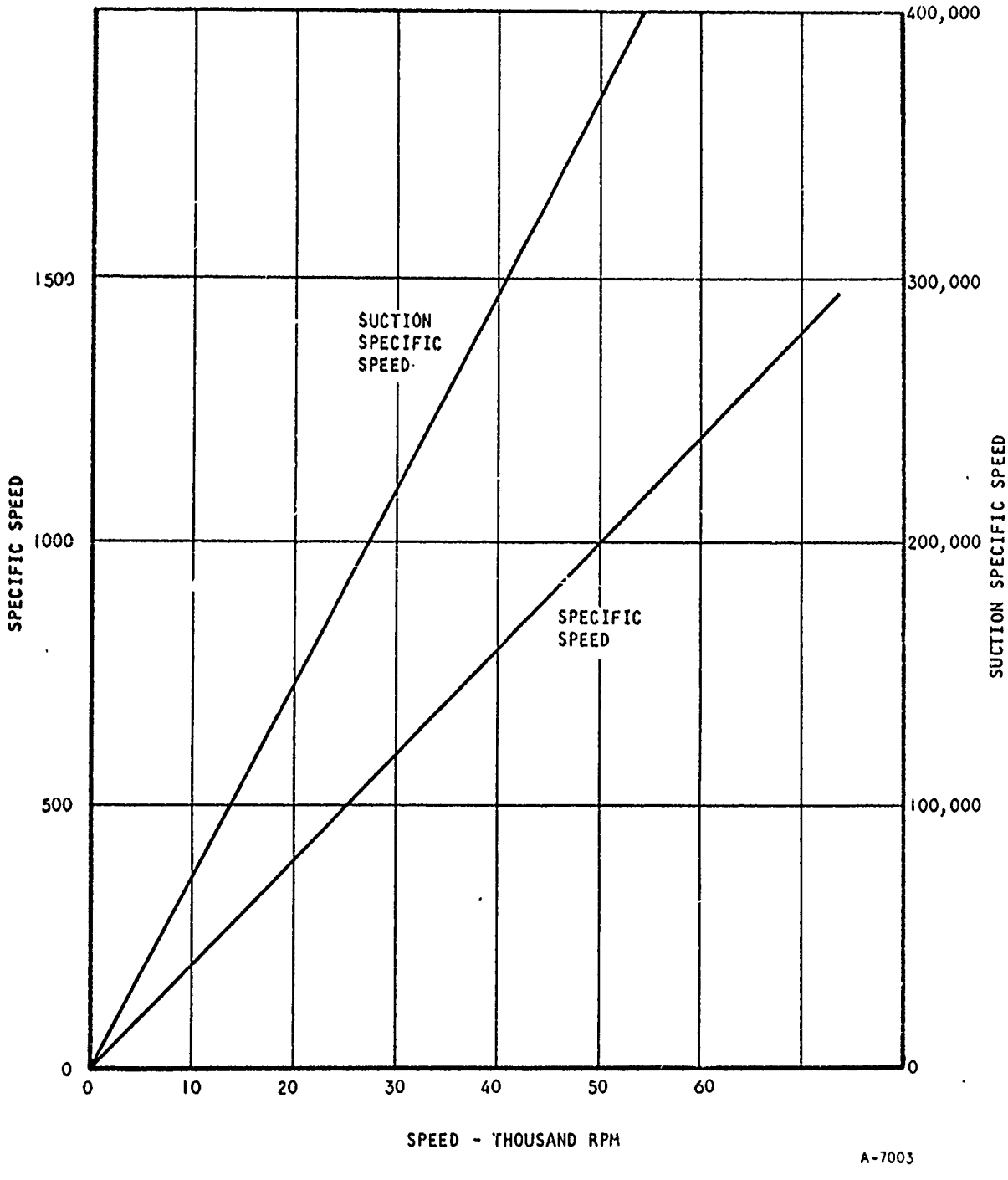

Figure 3. LH_2 Pump Single-Stage Specific Speeds

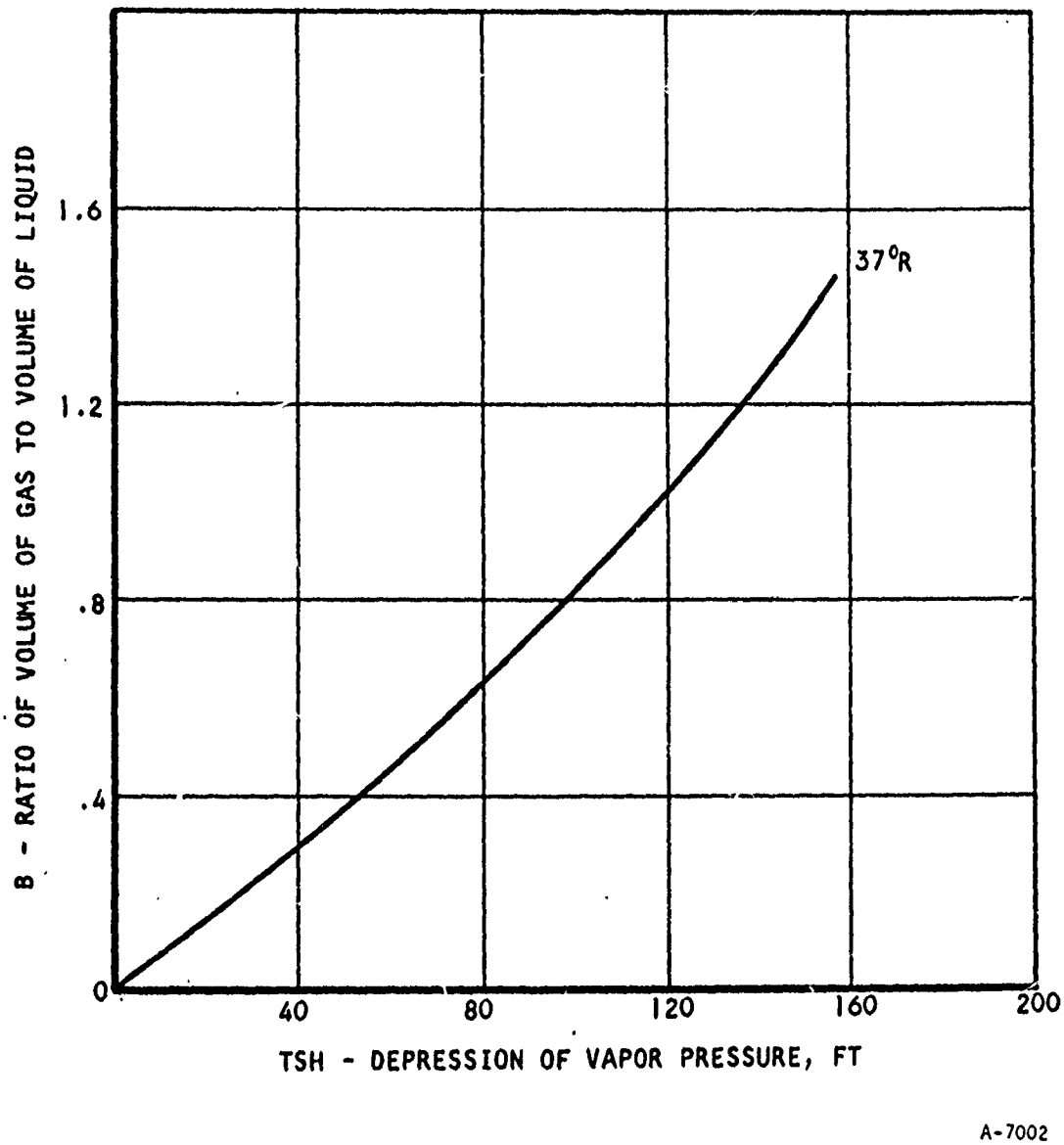

Figure 4. B vs TSH for Fluid with Initial Temperature of 37°R

Two types of inducer can be considered in the present design. The conventional helical inducers have been shown to achieve an S_V value from 40,000 to 50,000, which is close to the desired S_V to realize a 300,000 SSS. Integration of this type of inducer into a centrifugal pump leads to long overhang, which is not a desired feature in high-speed design.

Another approach to inducer design is to achieve the cavitation performance by controlling the shape of the leading edge of the pump inducer, in this case a backward-sweep with the blades protruding forward in the shroud outside diameter, Figure 4, and cut back toward the hub. This design approach handles cavitation performance through various effects.

1. The small-height forward blades induce some swirl in the inlet flow field, tending to centrifuge all cavitation bubbles inward.

2. The two-phase flow in the inlet region, when treated as a homogeneous mixture, has a low speed of sound propagation. Thus, highly supersonic flow is encountered at the inducer inlet (Reference 3). Sweepback has been known to handle this problem effectively.

3. The controlled leading edge approach lends itself to an integral inducer impeller design, tending to improve the overall performance of the pump.

The disadvantage of this design lies in the required strength of the blades needed to hold forwardly located blade elements that rotate at a tip speed on the order of 900 to 1000 fps. A shroud integrally attached to the blades may be considered. Use of the shroud would help to eliminate some of the cavitation due to flow leakage, frequently encountered in helical design. Another disadvantage is that no such design has been tested, particularly at high speed. At the start of this program, a similar design has been under investigation in Reference 4 . It appears at this time that the S_V achieved in water is in the 50,000 to 55,000 range, which compares favorably with the conventional helical design.

After evaluation of these various aspects, the design study and testing predicated on a swept-back approach, which promises great results in advancing the state of the art.

THERMODYNAMIC PROPERTIES OF LIQUID HYDROGEN AND APPROXIMATION OF CAVITATION PARAMETERS

Since the pump must operate at low NPSH and high suction specific speed, the fluid will cavitate in the inlet. Therefore, it is necessary to know the thermodynamic properties of the liquid/vapor mixture to be able to calculate the local pressure and velocities.

Reference 5 gives the properties of parahydrogen at the pressures and temperatures of this investigation. Figure 5 shows a Mollier diagram prepared with these data.

For the basis of the calculation it was assumed that the stagnating liquid has a temperature of $36.5^{0}R$ and a pressure of 14.7 psia and that the inlet flow process is isentropic. The density change along this isentropic expansion is plotted in Figure 6 . It is directly related to the enthalpy drop below the saturated-liquid line which is also the important parameter introduced earlier as the thermal suction head, TSH.

To facilitate hydrodynamic computation, the isentropic density change was approximated with the following function similar to that of the ideal gases:

$$\frac{\rho_o}{\rho} = \left[1 + A(TSH)\right]^{K} = 1 + B$$

where TSH = thermal suction head, ft

ρ_o = density of LH_2

ρ = density of the two-phase mixture, lb/cu ft

A = constant

K = exponent

B = volume of vapor/volume of liquid

The values of the constants A and K for 14.7 psia initial conditions are

A = 0.02814

K = 0.4

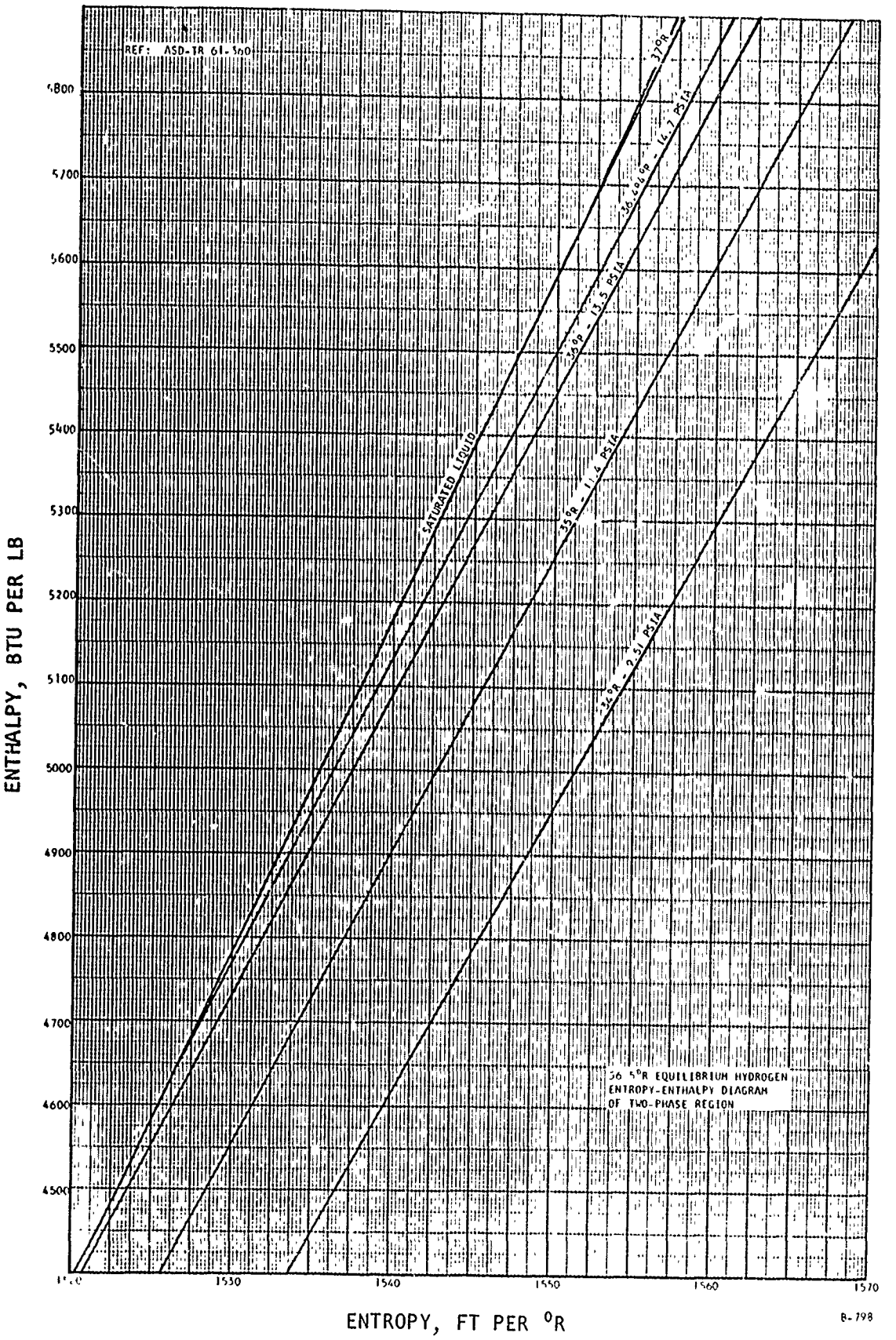

Figure 5. 36.5°R Equilibrium Hydrogen, Entropy-Enthalpy Diagram of Two-Phase Region

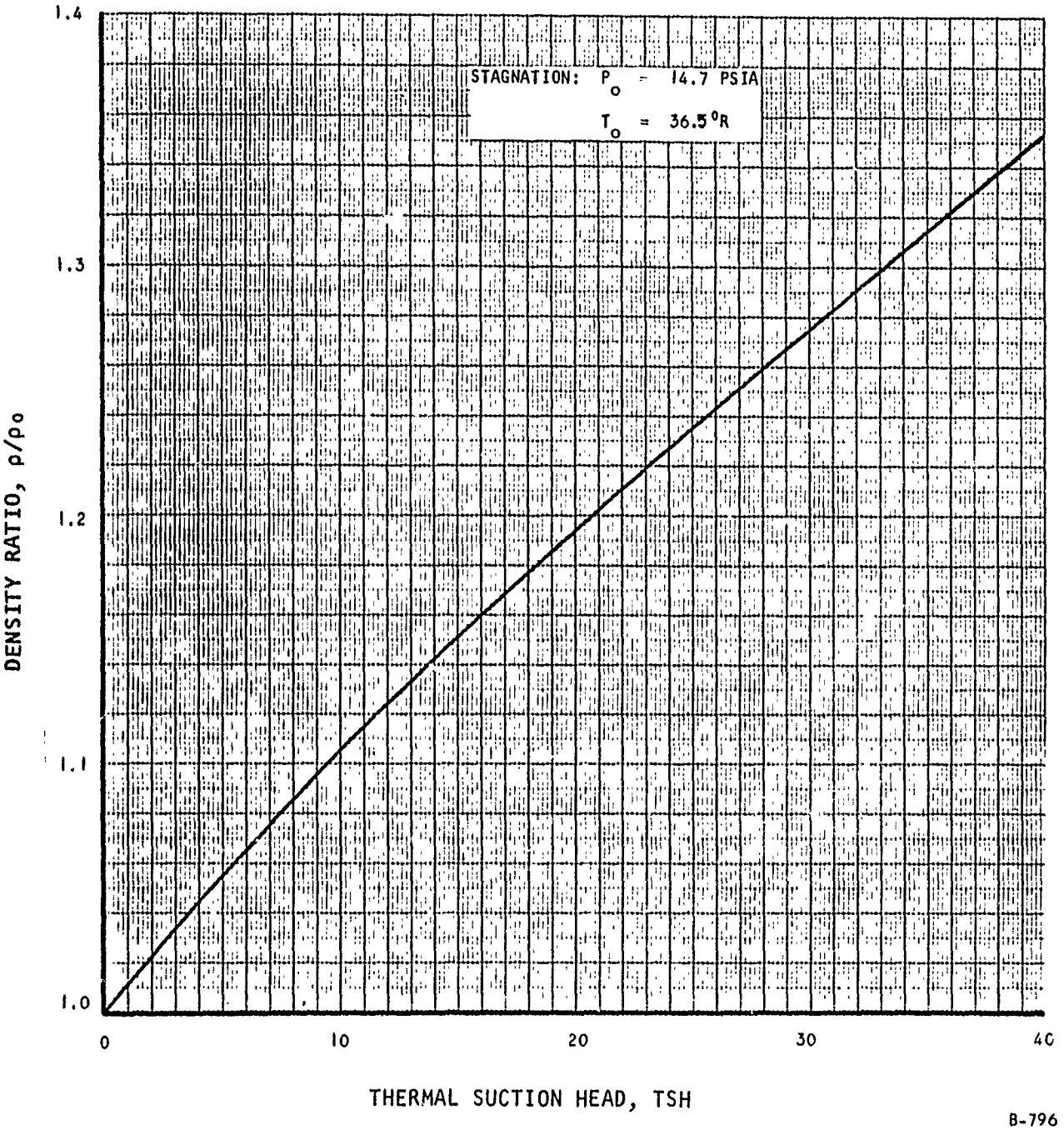

Figure 6. LH_2 Pump Density Ratio vs TSH, Isentropic Expansion

In two-phase flow operation, the suction parameter is often modified to include TSH. Thus, the suction specific speed, based on the effective head, is defined as

$$S_v = \frac{N\sqrt{Q}}{[NPSH + TSH]^{3/4}}$$

The relation between SSS, the conventionally used suction specific speed defined simply with NPSH, and S_v is shown in Figure 7.

The cavitation number commonly defined as $\tau = \frac{2g\ NPSH}{W_i^2}$ can also be modified by the thermal effect, yielding

$$\tau_v = \frac{2g(NPSH + TSH)}{W_i^2}$$

In experimental small size LH_2 inducers (References 1 and 2), the cavitation parameters τ has been shown to range between 0.010 and 0.001; even negative values, i.e., full two-phase flow or negative NPSH are reported.

DESIGN OF THE PUMP INLET

Securing an even pressure, velocity, and fluid quality distribution at the impeller inlet is of major importance. Two-phase fluid must have an even flow pattern, with very low or no secondary flows, and evenly distributed bubbles which are of minimum size, when entering the inducer.

To achieve these goals, the constant fluid stress principle, given by the following expression, is utilized:

$$\frac{\partial F}{\partial Z} = \text{constant}$$

where F = the force acting on the fluid

Z = axial distance

For two-phase steady flow, the following continuity equations are to be satisfied:

$$C = \frac{4W}{\eta D^2 \rho_o}\ (\rho_o/\rho)$$

and $(\rho_o/\rho) = [1 + A(\frac{C^2}{2g} - NPSH)]^K$

where C = local velocity

W = weight flow rate

D = local diameter

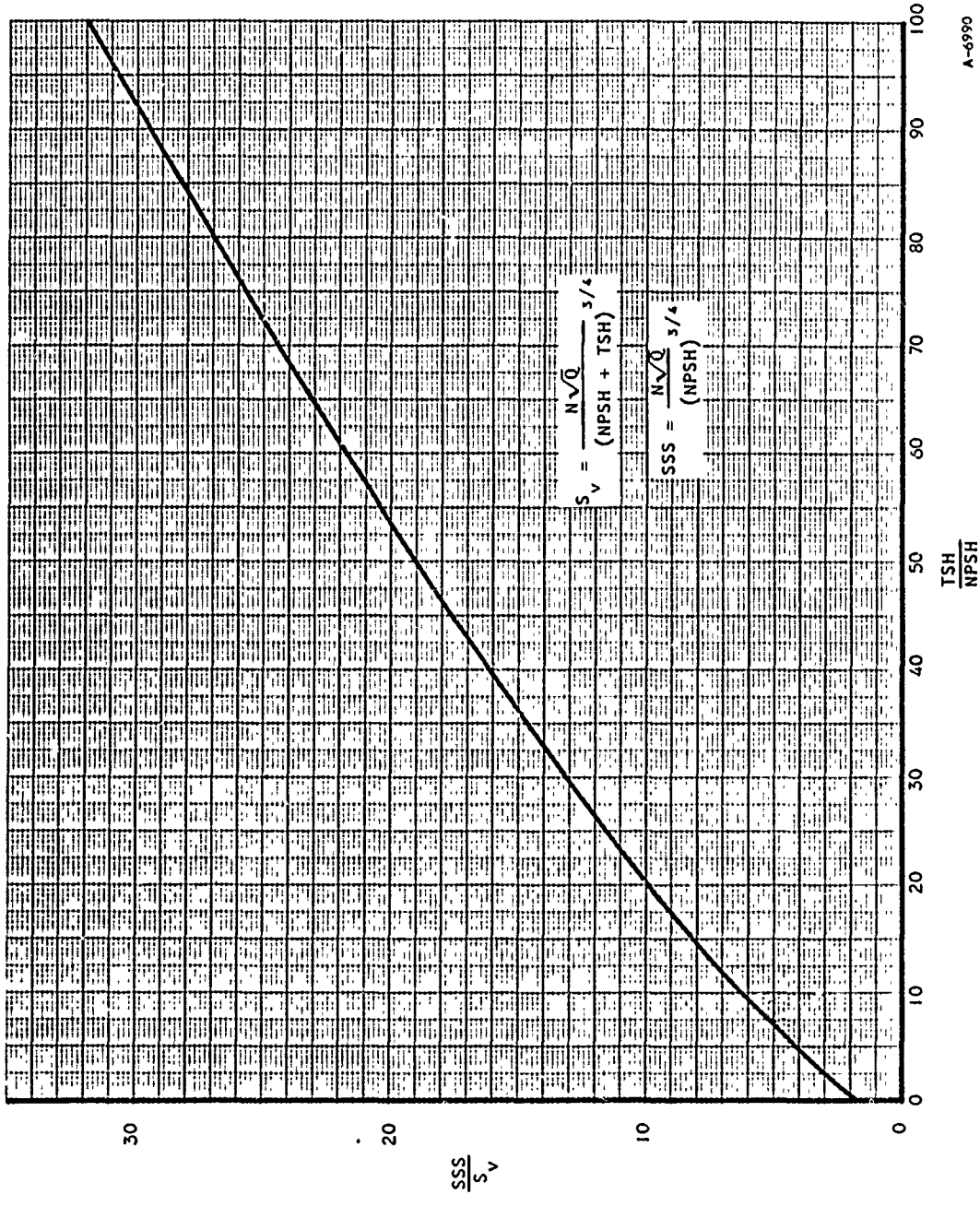

Figure 7. Relation Between SSS and S_V

ρ_o = density at stagnation

ρ = local density

g = 32.175 ft/sec^2

A and K are constants

From these equations, the coordinates of the inlet contour can be established as a parameter of the local velocity:

$$\frac{Z}{Z_o} = \frac{\left(1 + \frac{C^2}{C_o^2}\right)^{3/2} - 1}{\sqrt{8} - 1}$$

$$\frac{D}{D_o} = \sqrt{\frac{C_o}{C}\left[1 + A\left(\frac{C^2}{2g} - NPSH\right)\right]^K}$$

C_o, Z_o and D_o represent an initial noncavitating boundary condition. The inlet nozzle profile is shown in Figure 8.

Inducer Diameter

A parametric investigation was made to determine the optimum inlet diameter and flow angle, which are the basis of good cavitating performance.

The results of a one-dimensional flow calculation at the inlet, presented in Figure 9, show the change of the inlet diameter, inlet flow angle, and cavitation number as a function of the suction thermal depression head.

The diagram illustrates the conflicting conditions of the problem: to reach relatively better inlet flow angle and cavitation number, the fluid should be expanded further, which results in larger inducer areas, more vapor, and more loss from necessary recompression. Smaller diameters and smaller areas, on the other hand, increase the danger of choking.

To obtain a better judgment of the loading, a computer program was established to calculate the two-dimensional velocity distribution between the inlet edge and the throat of the inlet channel. Assuming a parabolic turn of the flow, the computer calculates the local velocity distribution, the corresponding densities, and the geometric blockage of the vanes and integrates the mass flow across the throat area. Full two-phase flow with isentropic expansion as defined previously is assumed.

The input variables are the inlet meridional velocity (which is a direct function of the inlet diameter and basic flow angle) and the angular turning of the flow between the inlet and the throat. The flow and the speed were

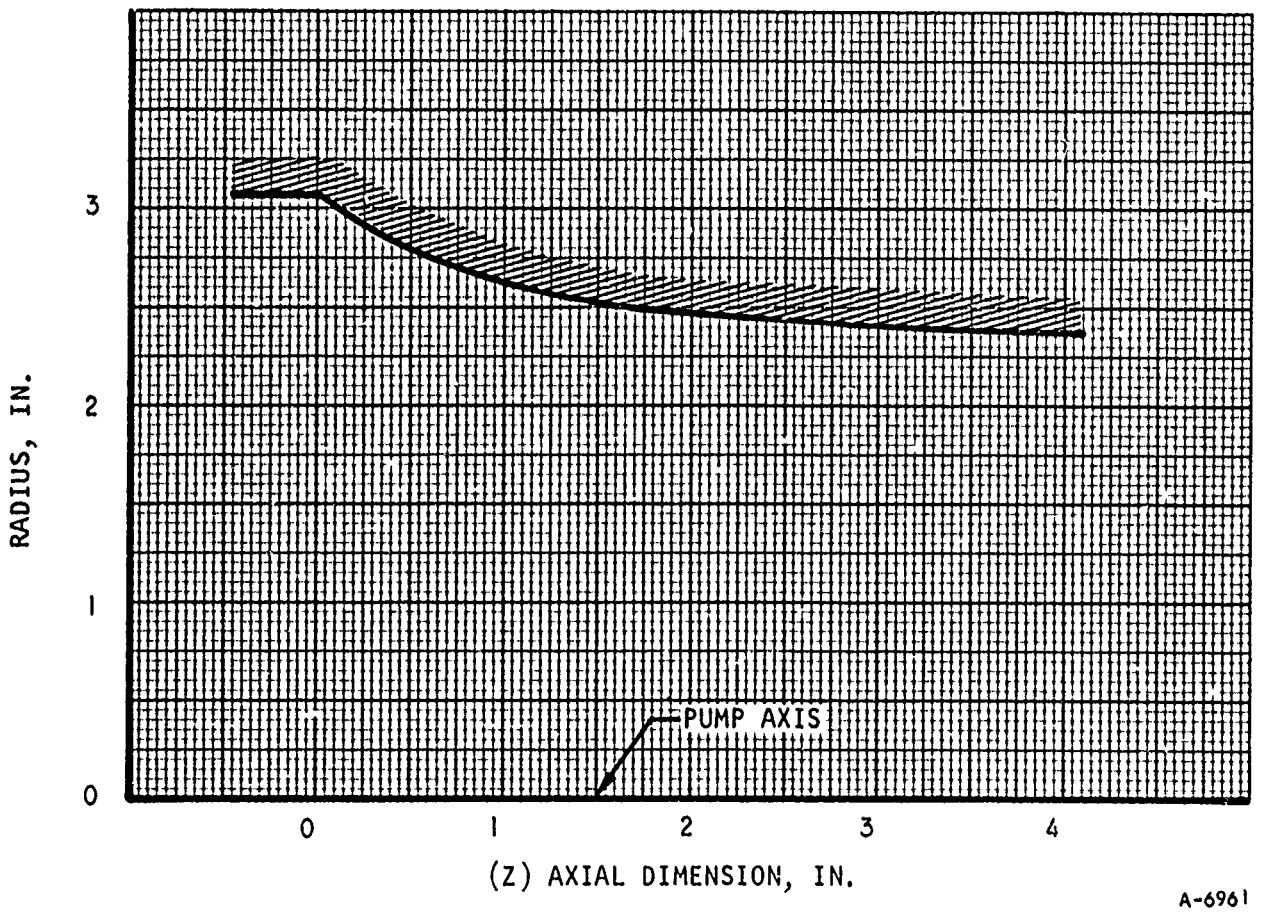

Figure 8. Inlet Nozzle Profile for Inducer Impeller

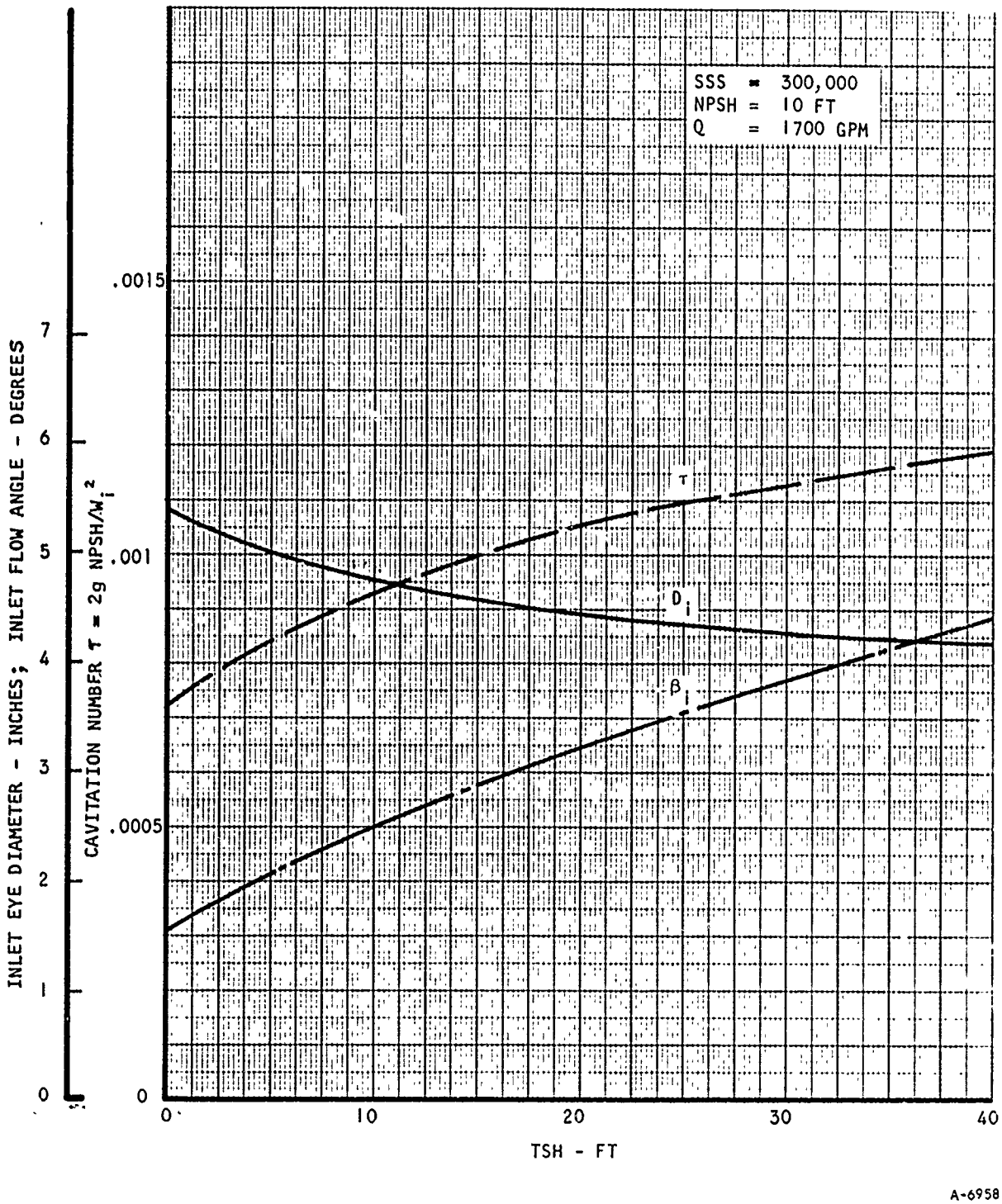

Figure 9. LH_2 Pump Inlet Characteristics vs TSH

kept constant during computation. The minimum possible vane thickness was set at 0.020 in. at the inlet edge and 0.050 in. at the throat. The blockage due to boundary-layer buildup was not taken in account.

Figures 10 through 13 present the relative velocities in the throat as a function of inlet diameter for various turning angles.

Although these diagrams show lower velocities and loading at smaller inlet diameters, no solution seems to exist for small turning angles. This shows sensitivity of the expanded flow, which needs more turning to recompress the flow into liquid. Since the boundary-layer buildup reduces the turning of the flow, these solutions based on smaller diameters were not considered practical.

As a result of these calculations, an inlet diameter of 4.750 in. was made slightly larger to accommodate boundary-layer and other nonuniformities of the velocity flow profile. These conditions are as follows:

NPSH, 10 ft

Flow angle at eye, β_{VANE}, 4.55 degrees

Number of vanes, Z, 4

Vane thickness in throat, T_o, 0.100 in.

Establishing the Inlet Edge Profile For a Swept-Back Design

To prevent extensive crossflow in the inlet region of the pump impeller, the shape of the inlet edge must be designed with an equalized pressure potential.

At any station Z, Figure 14, the leading edge radius r_o is then determined by the condition:

$$\frac{\Delta P_S}{\rho} \int_{Z_o}^{Z_1} = \Delta h_{ST} \int_{r_o}^{r_1} \qquad (a)$$

When the inlet flow has no radial velocity, pressure equilibrium in the radial direction is governed by the relation

$$\frac{\partial p}{\rho \partial r} = \frac{C_u^2}{r}$$

From the energy equation the static pressure can be expressed as

$$dh_{ST} = \frac{\partial p}{\rho} = \frac{C_u^2}{r} \partial r$$

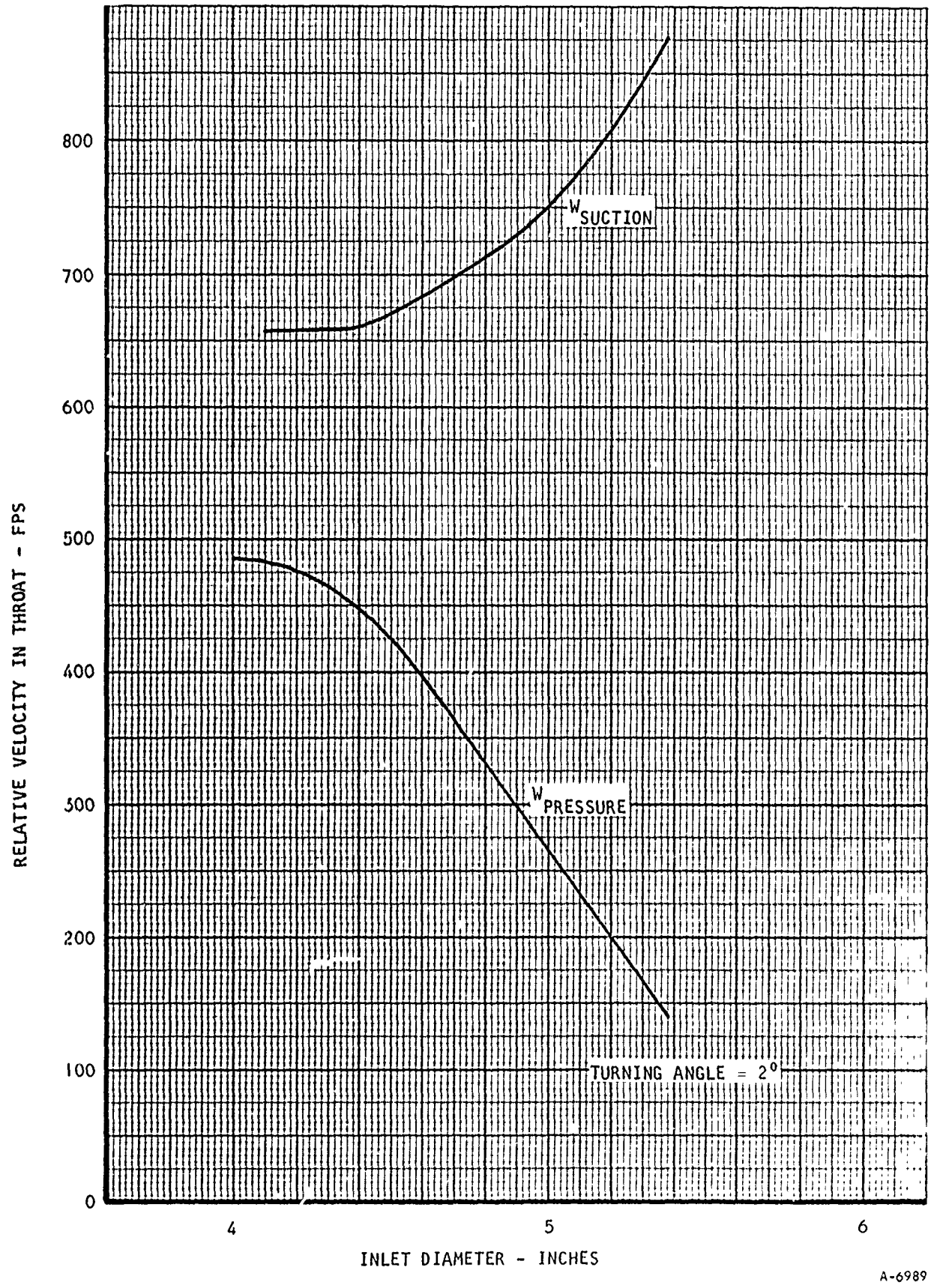

Figure 10. LH_2 Test Pump Inlet Edge Loading, 2-Degree Turning Angle

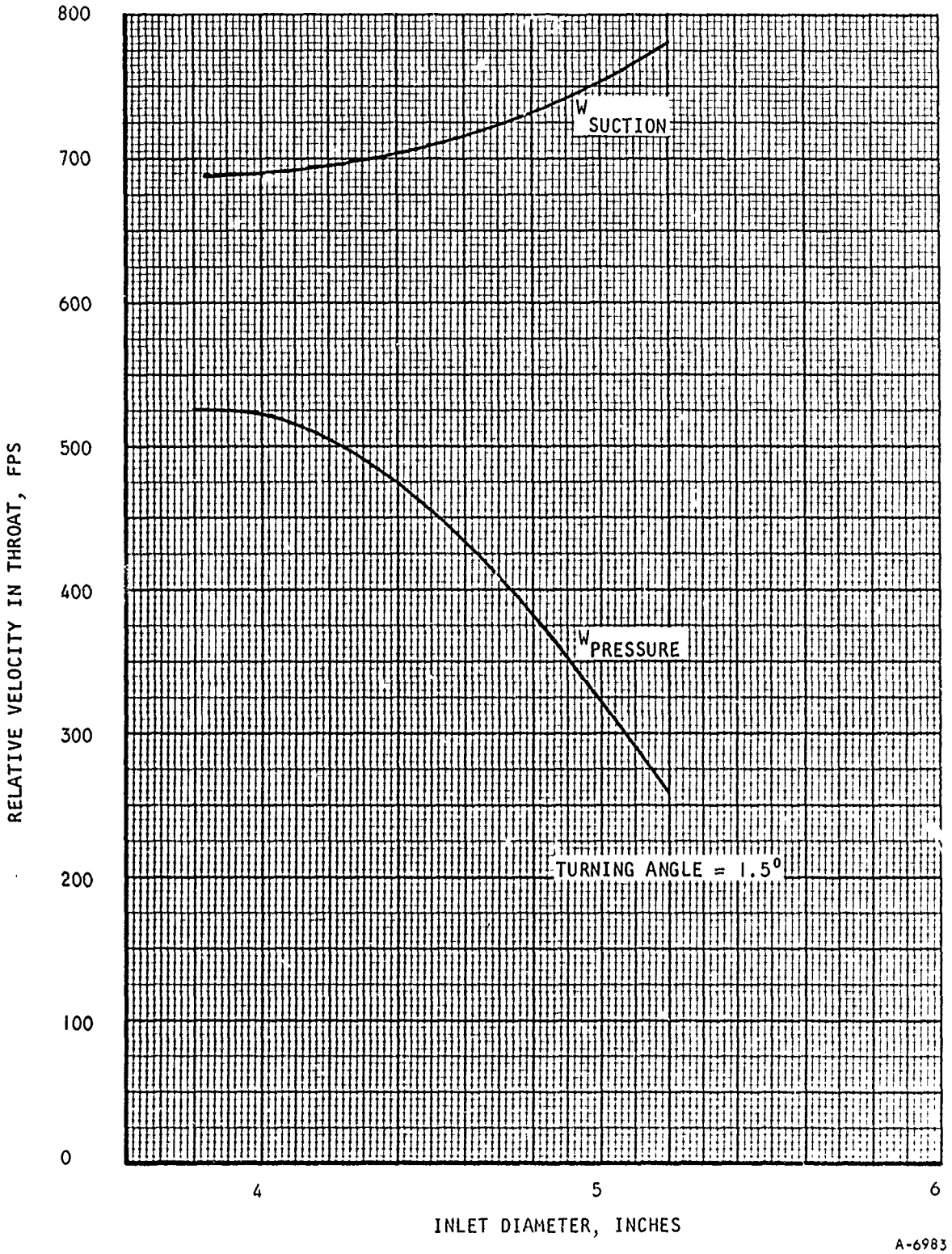

Figure 11. LH_2 Test Pump Inlet Edge Loading, 1.5-Degree Turning Angle

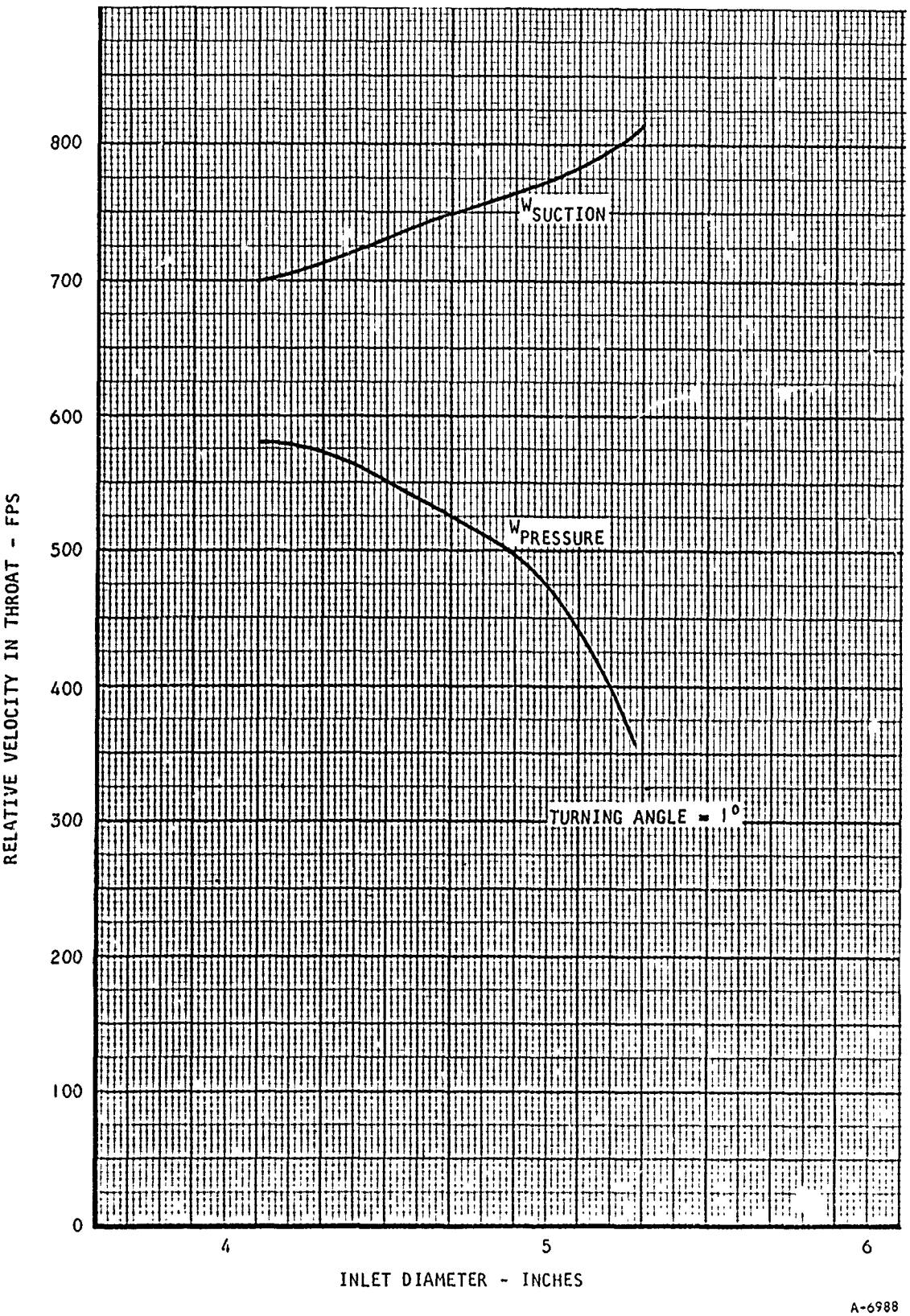

Figure 12. LH_2 Test Pump Inlet Edge Loading, 1-Degree Turning Angle

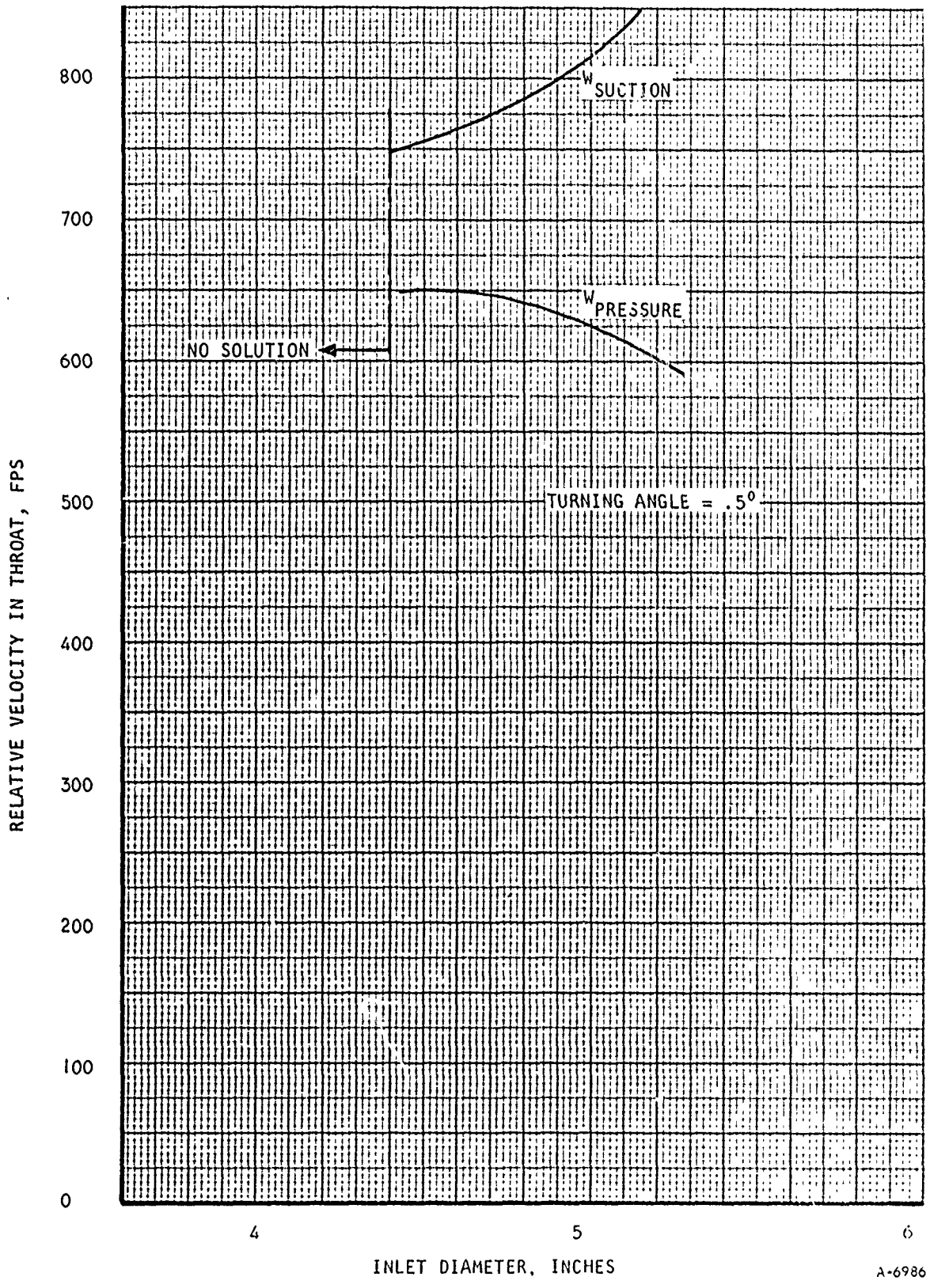

Figure 13. LH_2 Test Pump Inlet Edge Loading, 5-Degree Turning Angle

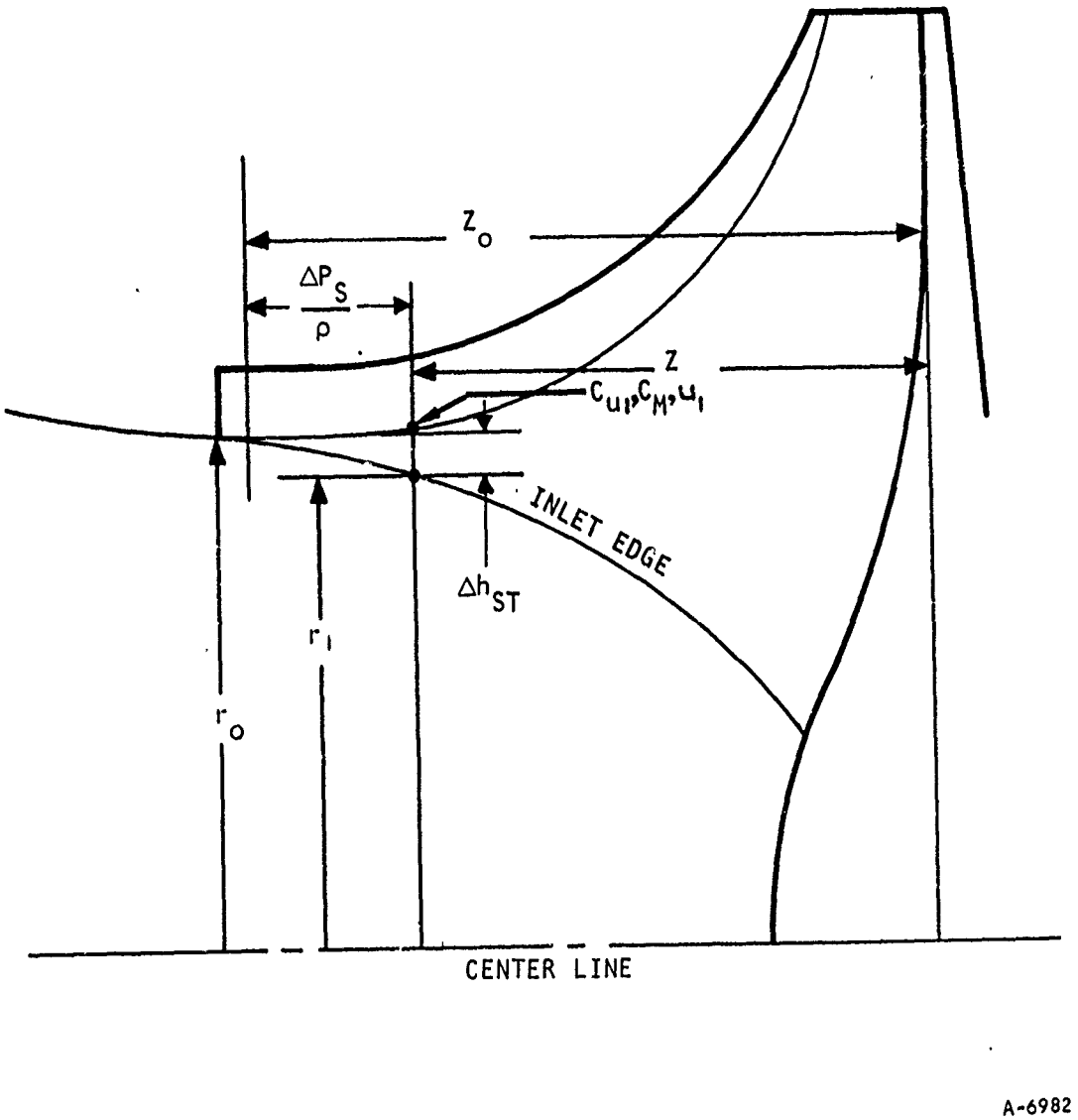

Figure 14. Inlet Edge Profile

With the assumption of a linear change in C_u along the streamlines, i.e.,

$$Cu = Cu_1 \frac{r - r_o}{r_1 - r_o}$$

The change in static pressure $\Delta h_{ST} \int_{r_o}^{r_1}$ can be obtained from the integration of the previous equation.

Now along the shroud streamline, the static pressure change $\frac{\Delta P_S}{\rho} \int_{Z_o}^{Z_1}$ is given by the work input as:

$$\frac{\Delta P_S}{\rho} = \frac{U_1 Cu_1}{g} - \frac{Cu_1^2}{2g} - \frac{2 C_M^2}{2g}$$

With the assumption that

$$C_M = C_1$$

The basic requirement for equilibrium (a) then yields the relation

$$u_1/C_{u_1} - 0.5 - \left(C_{M/C_{u_1}}\right)^2 = g \left[\frac{r_1^2 + r_o^2}{2(r_1 - r_o)} - \frac{2r_o}{(r_1 - r_o)} + \frac{r_o^2}{(r_1 - r_o)^2} \log \frac{r_1}{r_o} \right]$$

Once the C_u values along the shroud streamline are known, the equation can be solved for r_o, which represents the local inner radius of the inlet edge.

To obtain a three-dimensional picture of the flow at the inlet, much detailed calculation will be needed. An approximate method using the actuator disk concept is presented in later paragraphs.

IMPELLER DESIGN

To evaluate a large number of design configurations, a generalized pump performance program was established. The program calculates the impeller, inducer, and diffuser dimensions, velocities, losses, and efficiencies. The calculation, programmed for the IBM 7074 computer, is presented in Section 4 .

This program has been used to determine the best design point for the impeller.

Here, the inlet conditions and the geometry of the pump are maintained constant for each of the designs investigated, as determined by the inlet calculations. In addition to the fixed geometry, the variables fed into the IBM program were

Vane angle at impeller tip, β_2	0, 30, 45, 60^0
Slip factor, $C_{u_2}/C_{u_{2\infty}}$	0.7 to 0.9
Impeller tip flow factor, C_{M_2}/U_2	0.05 to 0.30

The output provides the following design parameters:

1. Impeller and diffuser dimensions and velocities
2. Reynolds numbers and friction factors
3. Boundary-layer buildup in the channels (based on one-dimensional velocities)
4. Friction, diffusion, and leakage losses
5. Hydraulic efficiency
6. Overall efficiency

Figure 15 gives the optimum calculated efficiencies at different tip vane angles of the impeller. The number of vanes and the impeller channel diffusion ratio are also shown in the diagram. There is very little difference in the efficiencies for considerable change of the diffusion ratio and the number of vanes. An ideal combination would be the highly backward-curved blading, but this design has high stresses in the shroud and also in the blades. A 45-degree backward-curved impeller blading is selected to offer a good compromise.

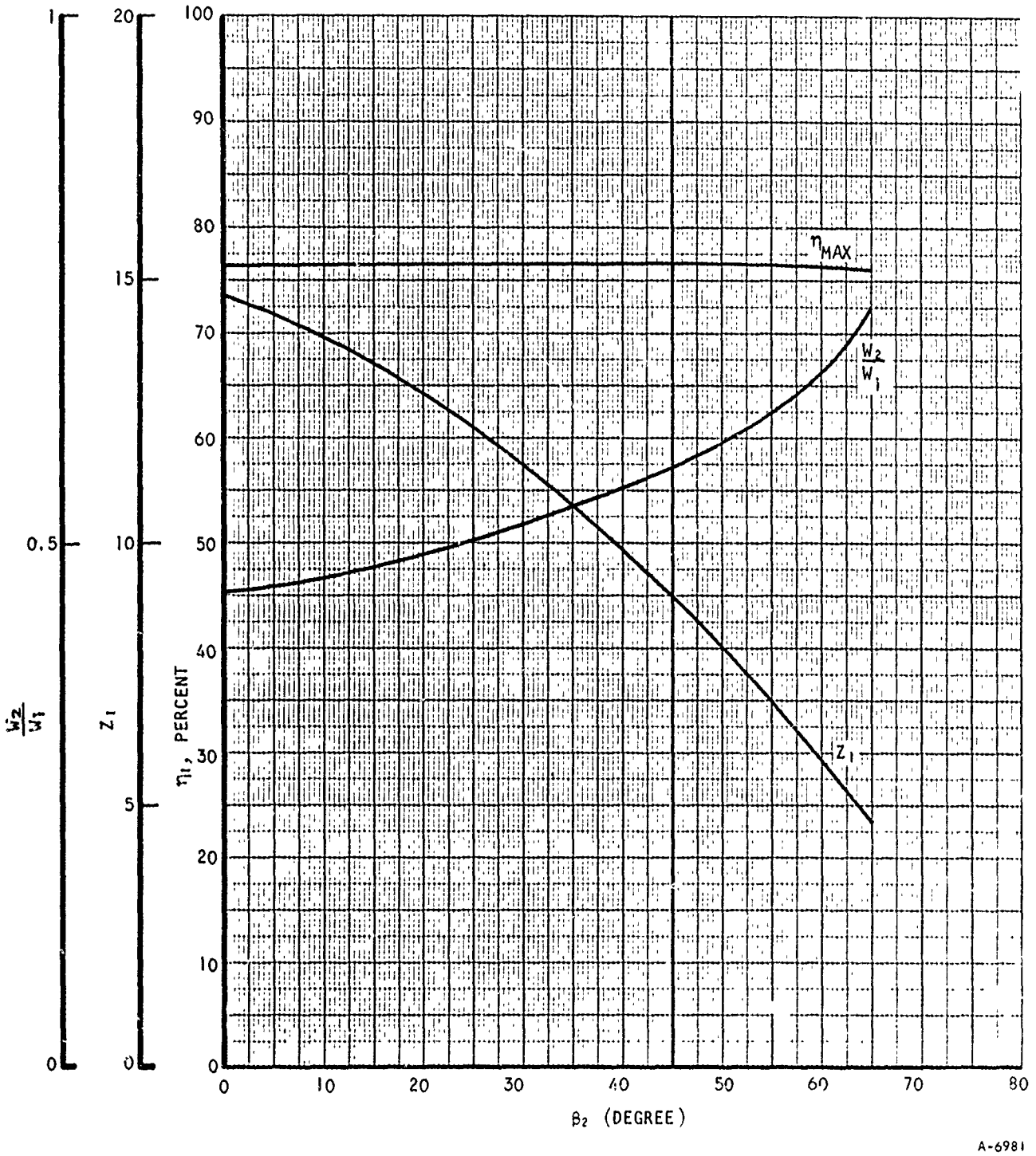

Figure 15. Efficiency, Diffusion Ratio, and Number of Blades vs Blade Angle

In Figures 16 through 20, the characteristic values of the 45-degree blade angle pump are presented. The decrease of the slip factor associated with a reduced number of vanes shows somewhat improved efficiencies. An improvement in the diffusion ratio (W_2/W_1) is noted. Since the number of vanes chosen for the inducer was four, for good cavitation performance, an eight-blade impeller is selected. This design presents one intermediate vane per channel, thereby avoiding the incidence problem encountered in multi-splitter vane design.

On the basis of this evaluation, the configuration chosen as the design point is identified by the following data:

Impeller tip diameter, D_2 = 7.225 in.

Impeller tip width, b_2 = 0.150 in.

Impeller vane number, Z_1 = 8

Impeller vane angle, β_2 = 45 degrees

Impeller diffusion ratio, W_2/W_1 = 0.555

Calculated overall efficiency, η = 76.5 percent

Geometric Design of the Impeller

Based on the design data obtained from the general performance calculations, the geometry of the impeller was established as follows:

1. The shroud streamline was calculated between the inducer inlet eye diameter and the impeller tip, using a natural hyperbolic function. This assures a smooth change in the curvature and angle and provides large radius of curvature at the eye. Using mathematical functions also increases the accuracy of the computation of velocities.

The curve is expressed by the following equation:

$$r = \frac{a}{Z^{2n}} + \frac{b}{Z^{n}} + c$$

where r = radius, in.

Z = axial distance, in.

a,b,c,n = constants

Figure 21 shows the resulting shroud profile with the following constants:

a = .44978 b = .51936 c = 2.52493 n = .5

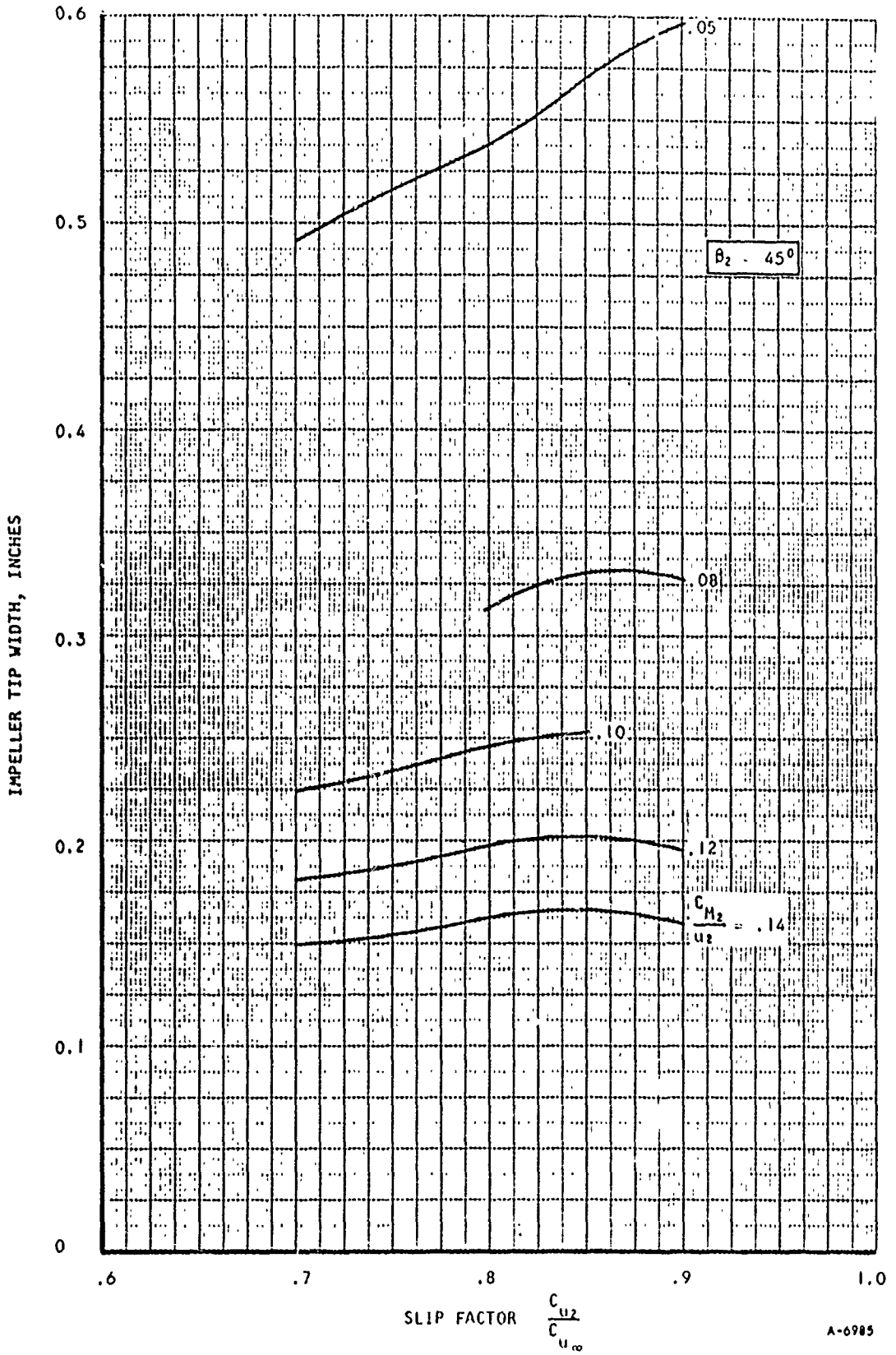

Figure 16. Impeller Tip Width vs Slip Factor, 45-Degree Blade Angle

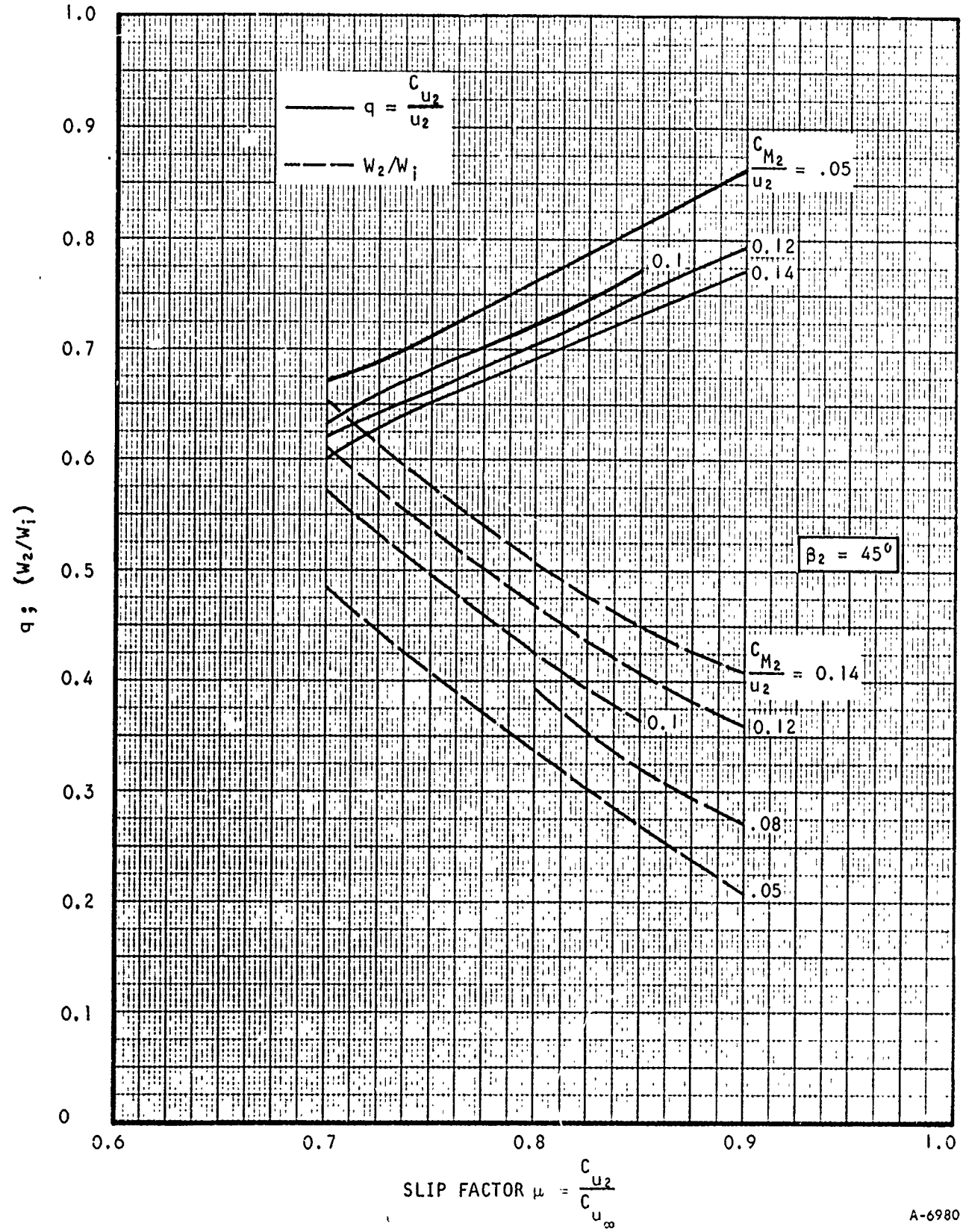

Figure 17. Head and Flow Factor vs Slip Factor, 45-Degree Blade Angle

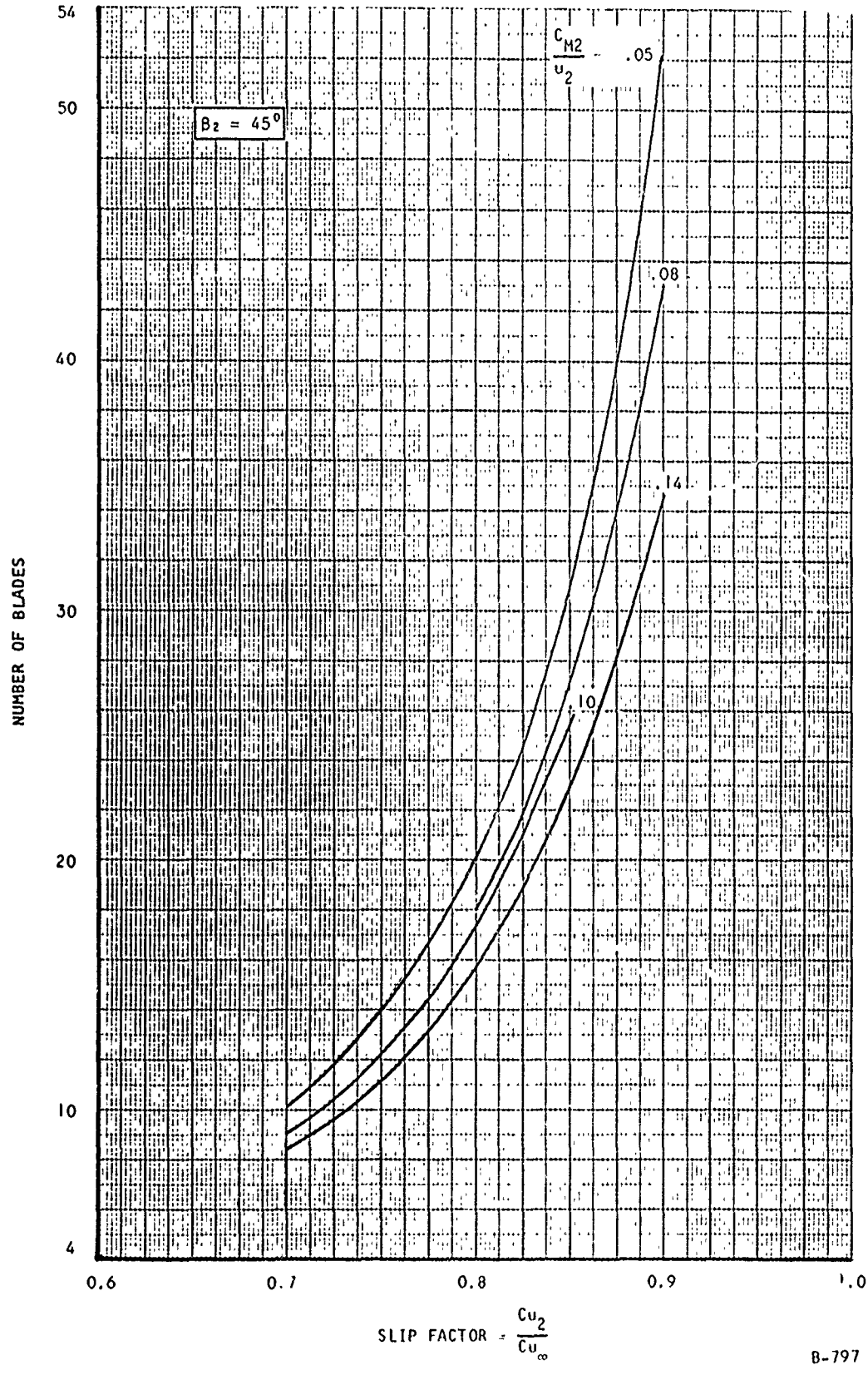

Figure 18. Number of Blades vs Slip Factor, 45-Degree Blade Angle

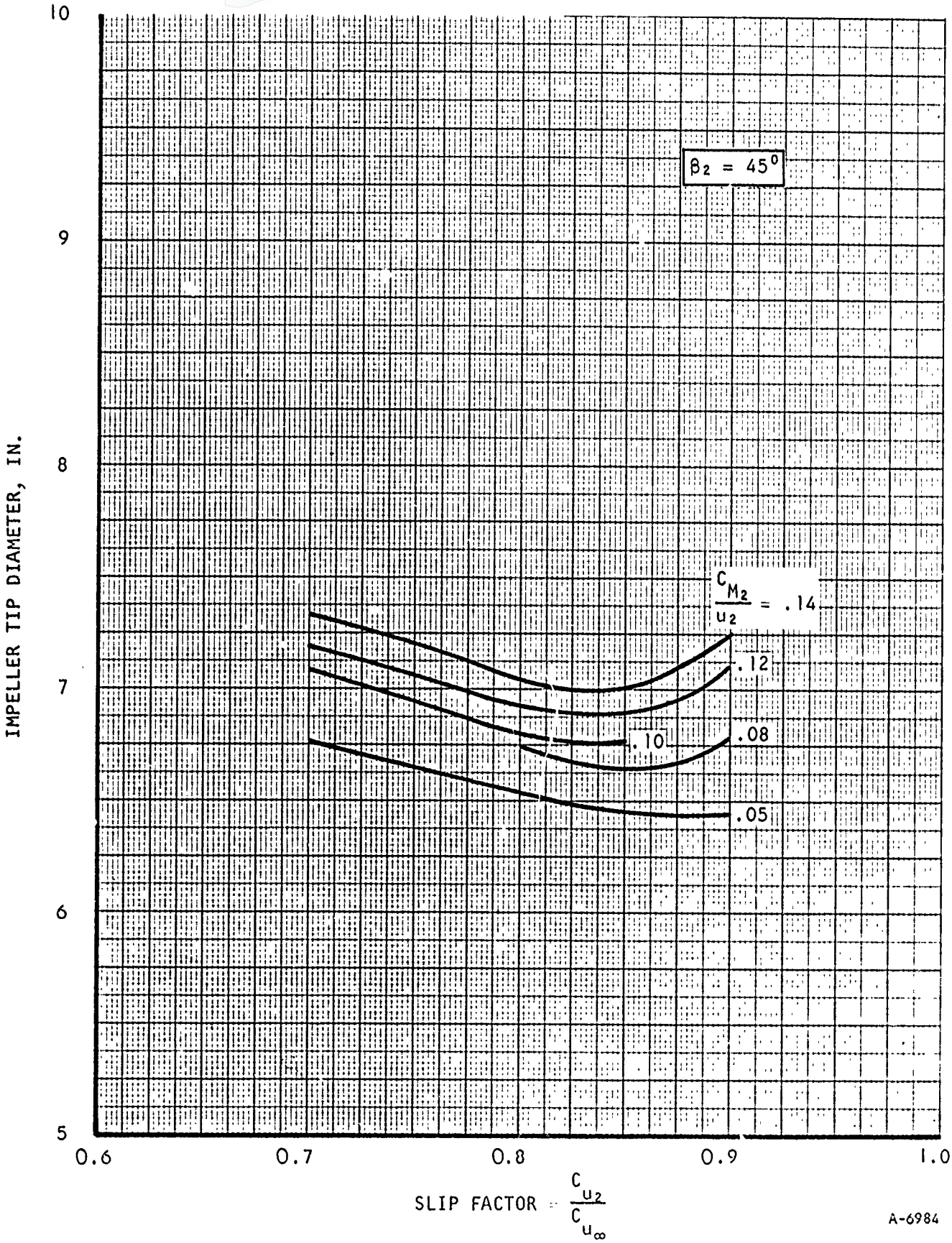

Figure 19. Impeller Tip Diameter vs Slip Factor, 45-Degree Blade Angle

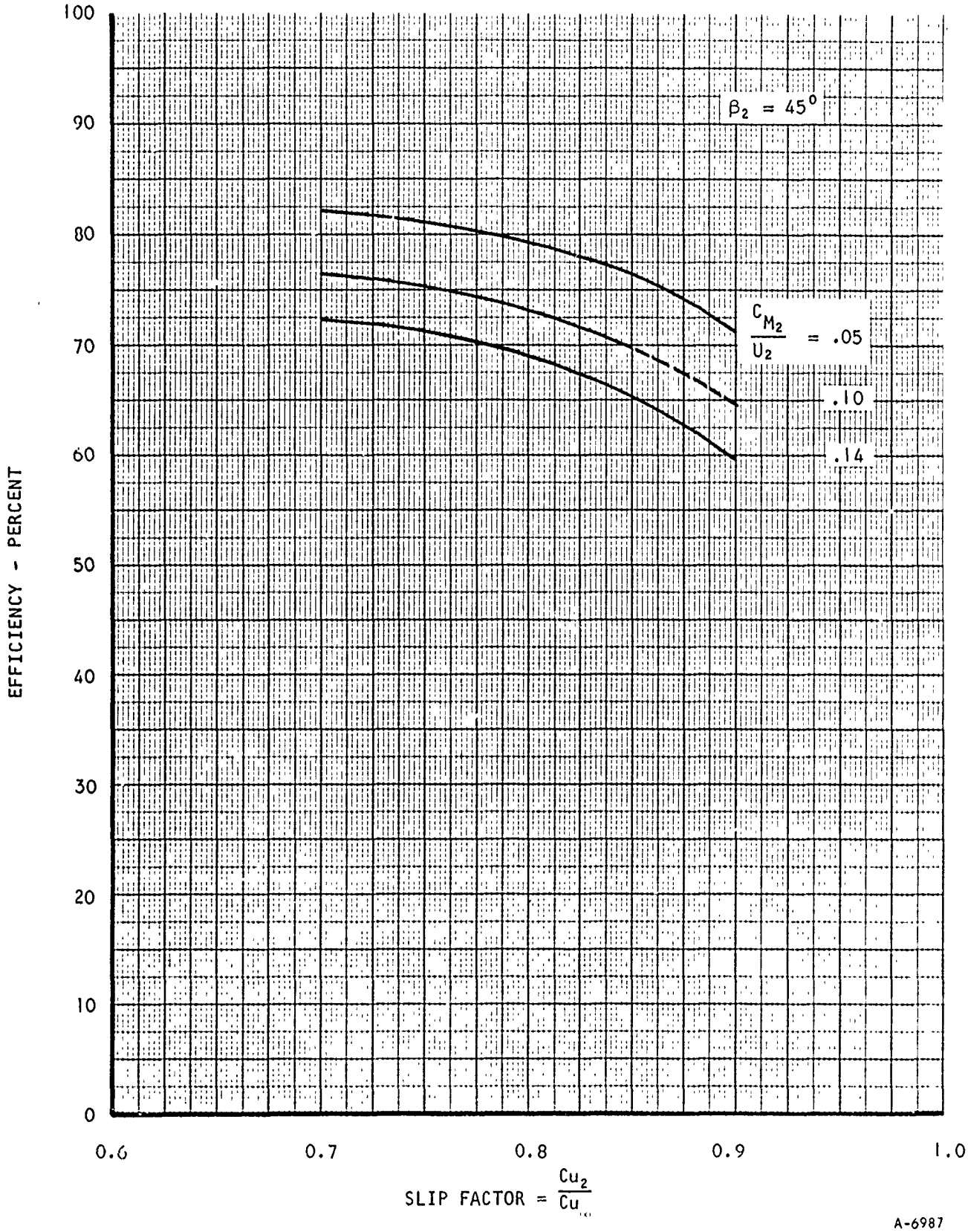

Figure 20 Efficiency vs Slip Factor, 45-Degree Blade Angle

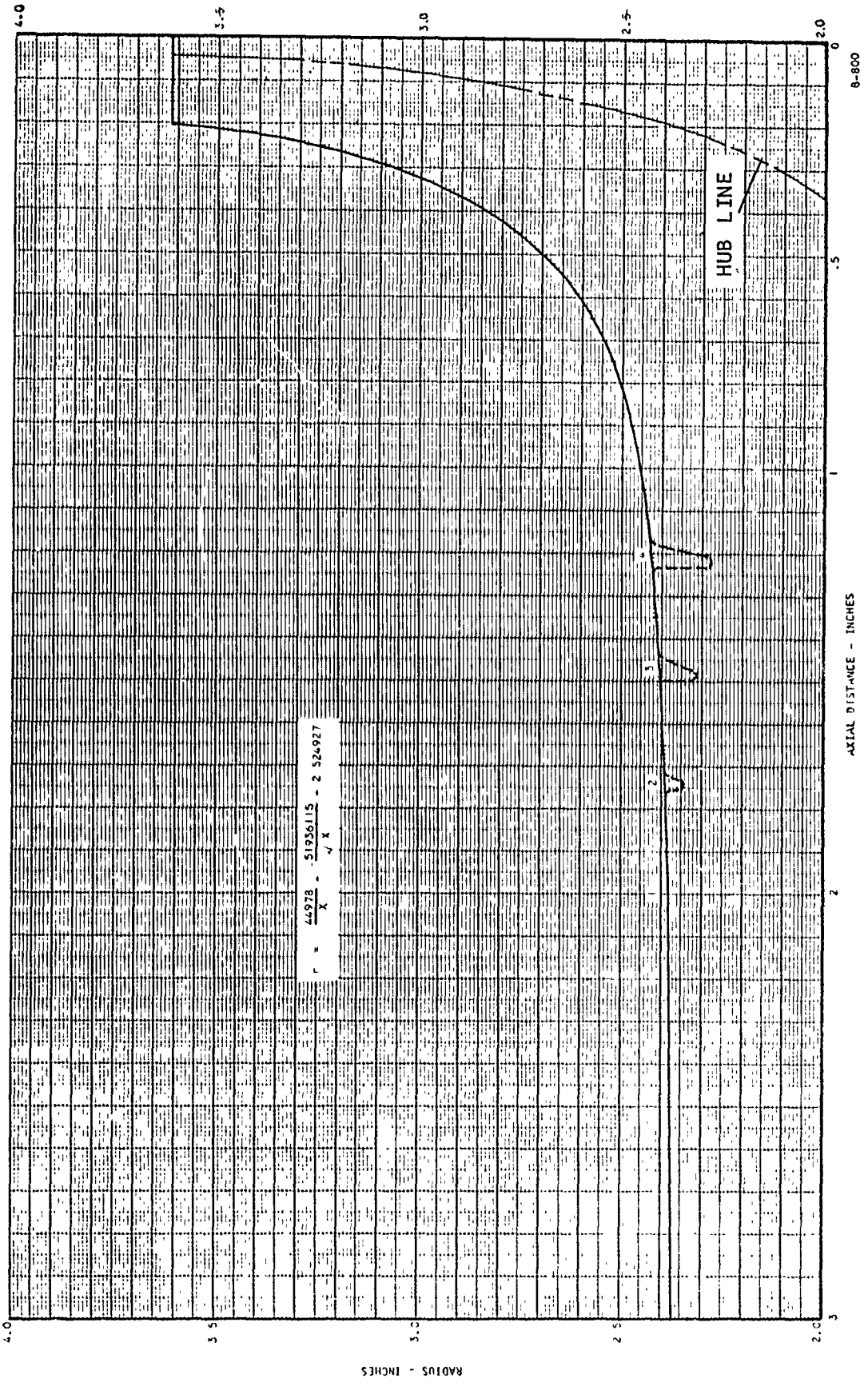

Figure 21. 1700-gpm LH_2 Pump Shroud Line

2. The vane angle variation along the shroud was established by the conformal transformation method. The vane is described by two adjoining parabolic arcs in the transformed coordinate system, both expressed by similar functions:

$$\tan \beta = \frac{d\xi}{d\eta} = A\xi + B$$

the transformation is given by

$$dm = r d\xi$$

$$d\eta = d\varphi$$

with dm as obtained from the shroud streamline equation

$$dm = \sqrt{1 + \left(\frac{dr}{dZ}\right)^2}\, dZ$$

and

$$r = \frac{a}{Z} + \frac{b}{\sqrt{Z}} + c$$

where β = vane angle

ξ and η = transformed coordinates

m = arc length along shroud line

φ = angular position

r = radius

A and B = constants

Z = axial distance

a, b, c = constants

3. The desirable average velocity distribution was assumed along the shroud streamline. Average flow areas, vane thicknesses, and impeller channel widths were then computed to establish the hubline.

4. The vane surface development was generated, with straight radial projection elements used along the pressure side of the vanes between the shroud and the hub (see Figure 22). The necessary cone angle (θ) of the projection line was chosen so as to give a favorable vane angle distribution along the hub and along the mean streamline. The trailing sides of the vanes were developed according to the calculated necessary blade thicknesses and also from consideration of straight projection elements.

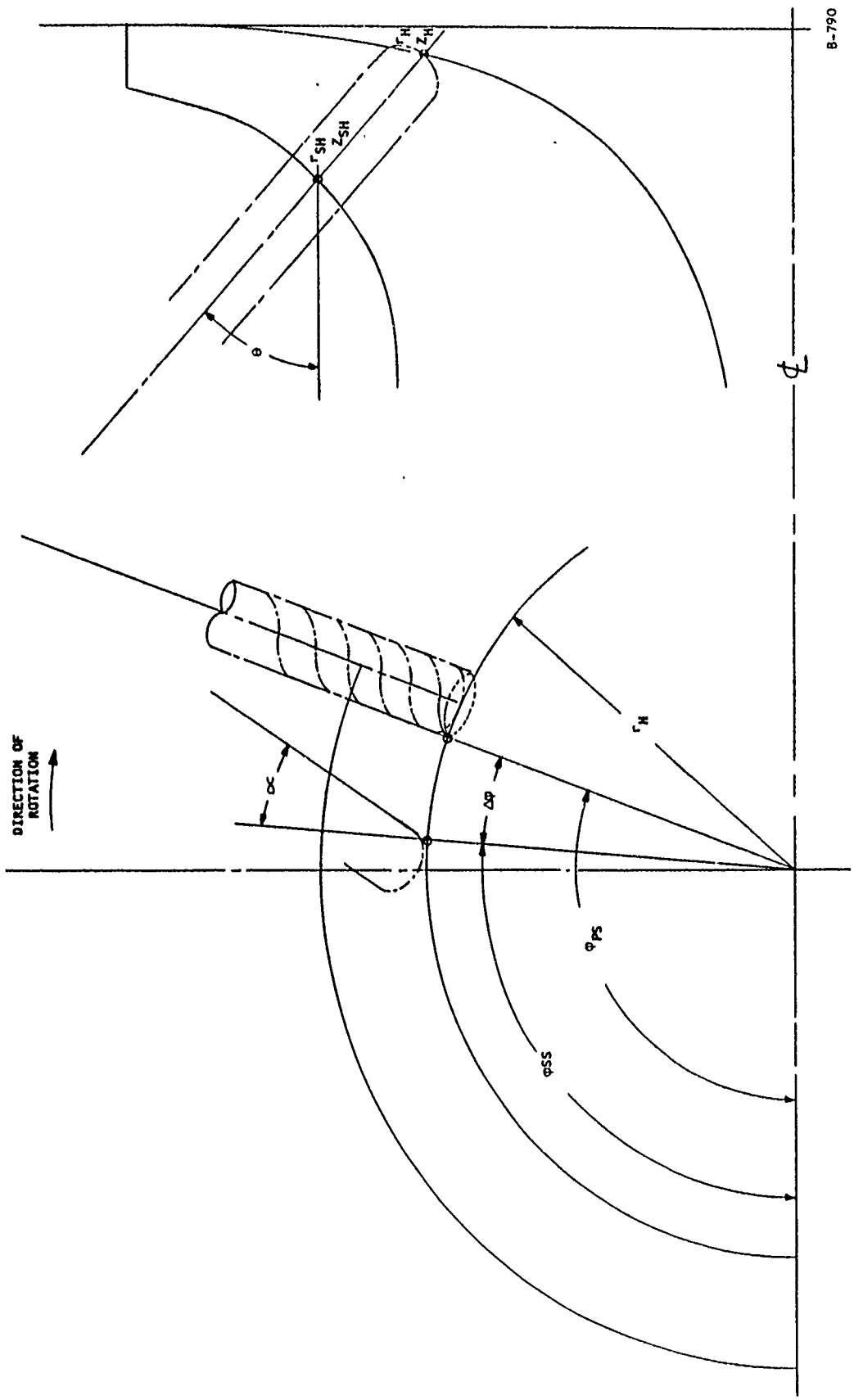

Figure 22. Generation of Vane Surfaces

This type of design has been adopted with due consideration for the fabrication technique, which calls for generation of the blade using machines similar to the "Keller".

Loading of the Impeller-Velocity Distribution

After the geometric design of the impeller, based on one-dimensional calculations, was established, the velocity distribution along the various streamlines of the impeller channel was calculated by means of the approximate method developed by AiResearch for three-dimensional flow analysis of a centrifugal impeller (Reference 6). Essentially, it analyzes the flow in the impeller as follows:

1. An electric analog field plot is made to obtain two-dimensional, rotationless potential lines between the hub and shroud lines of the impeller.

2. IBM program then carries out the following computations pertinent to design of a pump impeller for cavitating and incompressible flow.

   a. It reads input data, such as flow, inlet conditions, speed, fluid properties (including two-phase properties) geometrical parameters, and field plot data (shroud and hub meridional streamline coordinates and potential lines).

   b. From the input, the geometry of the entire impeller blade is calculated.

   c. Velocity distributions along each potential line are then obtained.

   d. The points giving the intersection of a general streamline (defined by a selected mass flow between this streamline and the shroud) with each potential line are calculated. From these points, the meridional distance in the axial direction Z, and the radial distance r coordinates of each streamline are obtained.

   e. The pressure and suction surface velocity distributions (loading) along the streamlines are computed. Density change is also calculated where the pressure is lower than the saturated liquid pressure.

   f. The output gives the blade loading velocity-pressure data along each streamline and the streamline geometry.

The velocity triangles at the inlet are shown in Figure 23 and at the discharge in Figure 24.

The average meridional velocities are given in Figure 25 for the mean and shroud streamlines.

The relative velocity distributions of the suction side, pressure side, and average streamline are shown in Figures 26 and 27.

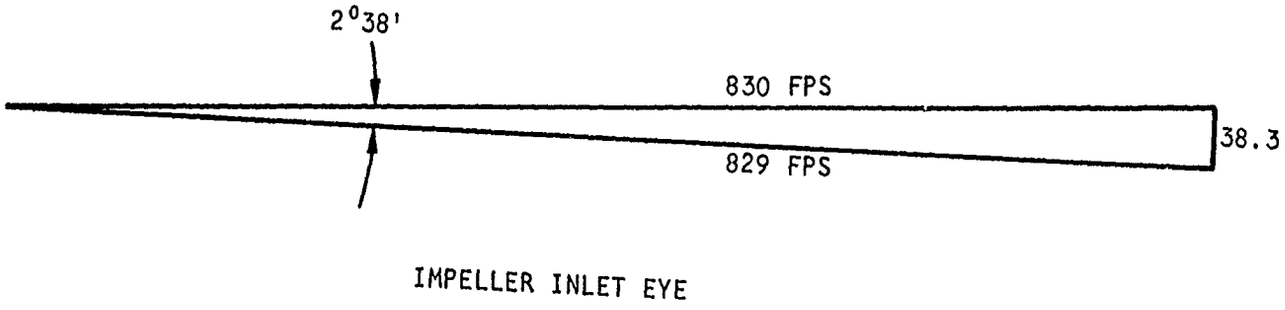

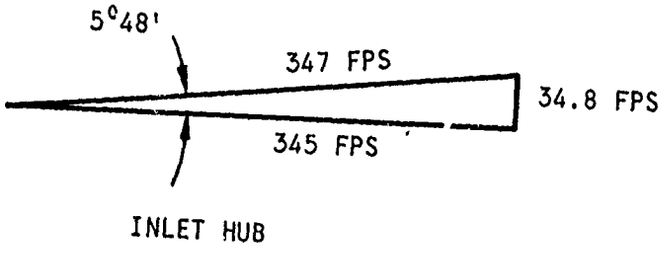

A-7009

Figure 23. LH_2 Test Pump Inlet Velocity Triangles

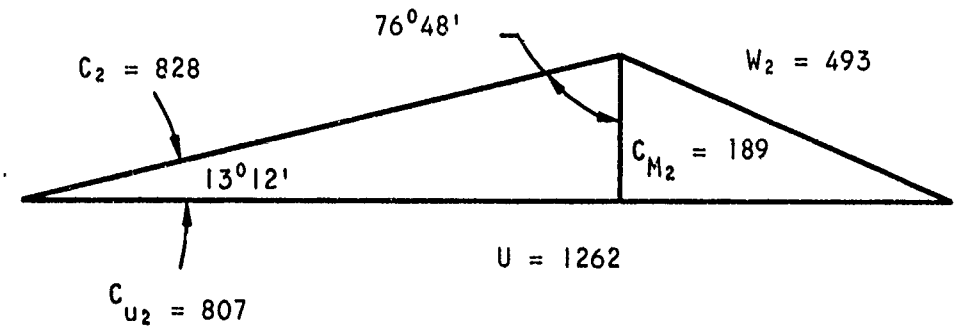

IMPELLER TIP

A-7010

Figure 24. LH_2 Test Pump Impeller Tip Velocity Triangle

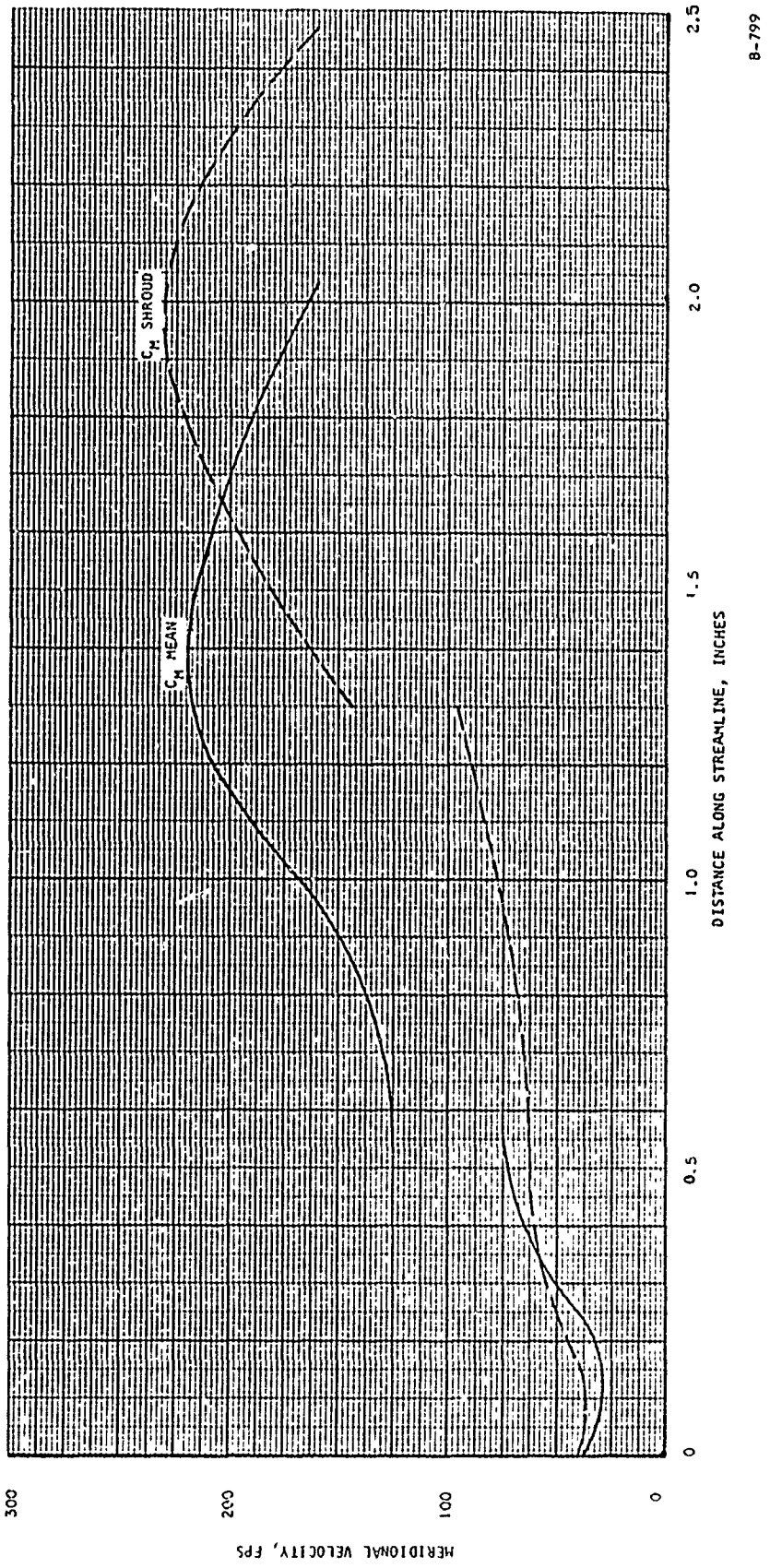

Figure 25. LH_2 Test Pump Average Meridional Velocity

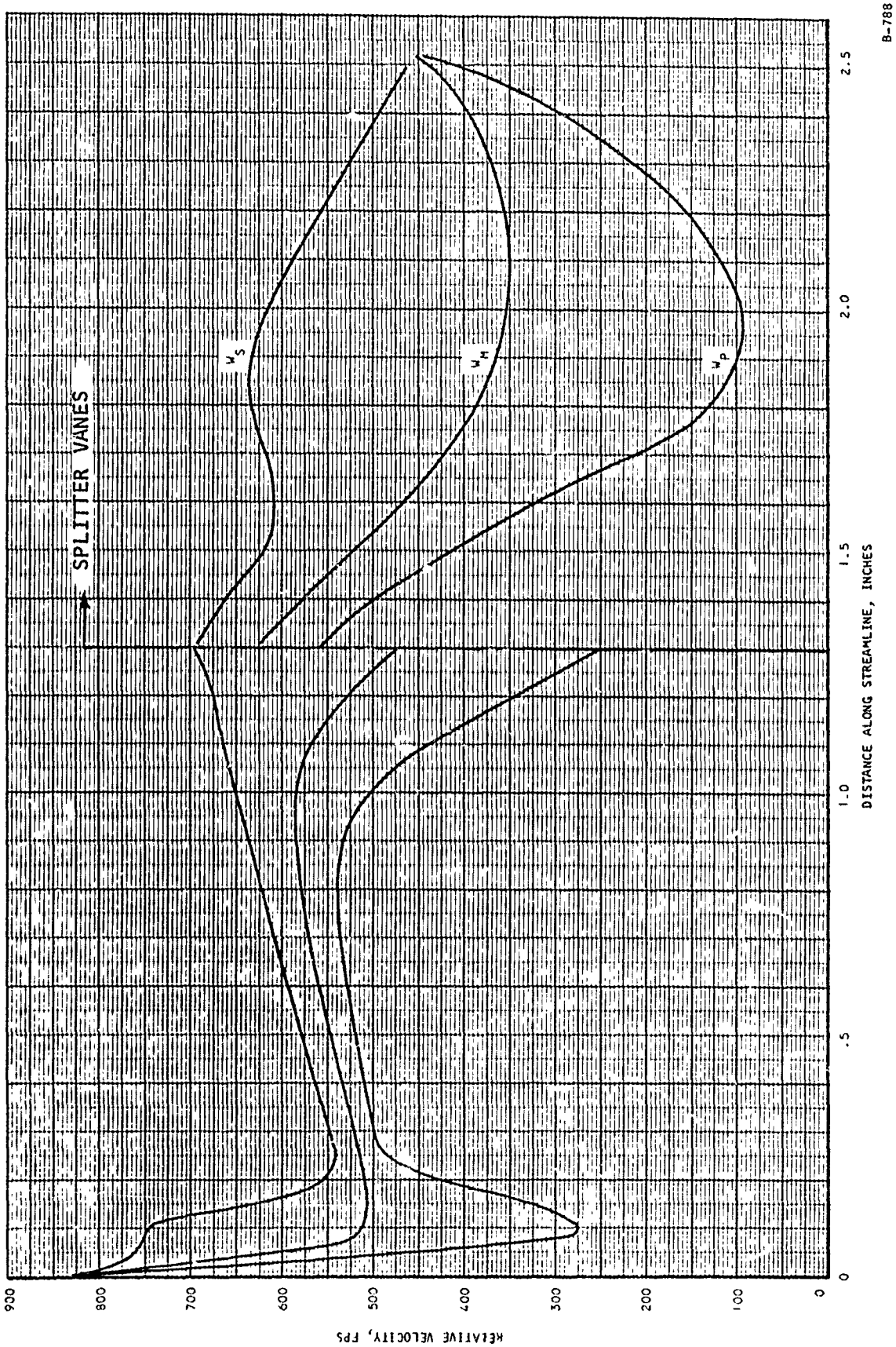

Figure 26. LH_2 Test Pump Velocity Distribution Along Shroud

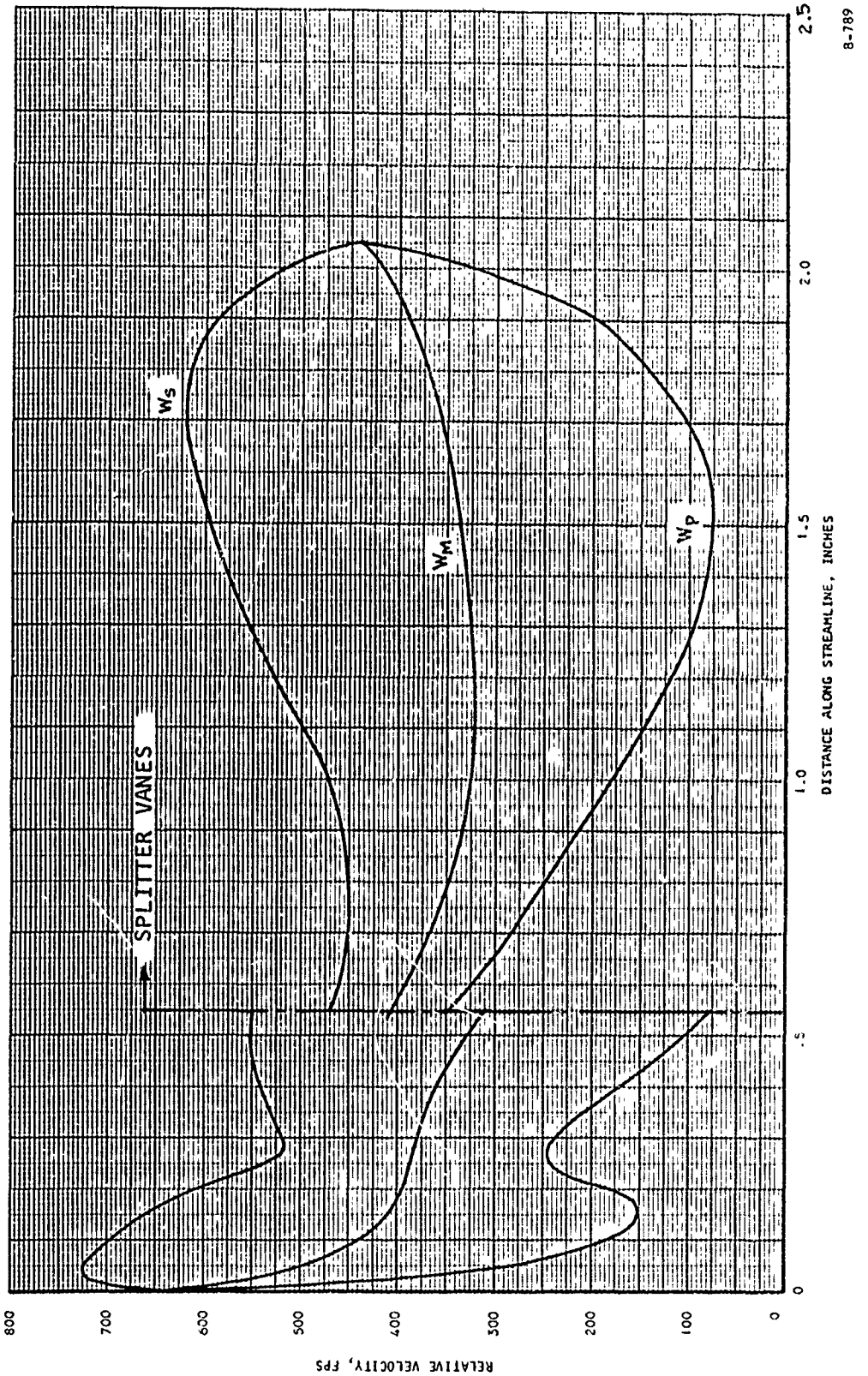

Figure 27. LH_2 Test Pump Velocity Distribution, Mean Streamline

In order to avoid stagnation on the pressure side of the blades, intermediate blades were used. Thus, the inducer region has four blades and the impeller outlet region has eight blades.

The velocity distributions as presented do not take into account the restriction of the channel due to the boundary-layer buildup, which would produce an increase in the mean relative velocities, thereby decreasing the loading on the blades. This is the reason for the low relative velocities in the exit part of the impeller. Here, a relatively large blade thickness has been used to provide enough strength for the backward-curved blading, which also helpsin controlling the low velocities.

The velocity distribution curves show a high loading at the inlet to the blades, which is caused by the sudden turning of the flow. This turning is necessary to recompress the vapor bubbles into liquid. This loading is larger at the lower streamlines because of the shroud-to-hub sweepback of the blading. There the throat was opened up more to compensate for the possible self-induced prerotation of the flow. This effect was not included in the calculation of the loading. Experience shows also that the forward extension of the blades along the shroud tend to force the lighter bubbles toward the hub (centrifuge effect), thus increasing the relative volume. It is then necessary to open the throat up to make it possible to pass the flow through.

Behind the throat, the loading is reduced and the velocity is kept nearly constant to give the remaining bubbles a chance to disappear because of condensation.

DIFFUSER DESIGN

The design of the diffuser matching the integral hubless inducer-impeller was completed. To eliminate the radial load on the impeller, a multicontour vane design was selected.

Peak diffuser performance is vital in this application to regain some of the performance lost because of inlet cavitation in the impeller. To assure maximum diffuser performance, the following conditions must be fulfilled:

1. Minimum friction (short length and rapid deceleration)
2. Minimum boundary-layer growth (short length and slow deceleration)
3. Retarded separation (short length and slow deceleration)
4. Maximum diffusion - maximum recovery (long length and rapid deceleration)

Since these factors are contradictory, determination of the optimum combination is necessary. The design chosen is composed of three major portions (Figure 28):

1. A vaneless annulus around the impeller
2. A hyperbolic scroll design upstream of the throat
3. Straight diffusing throat channels

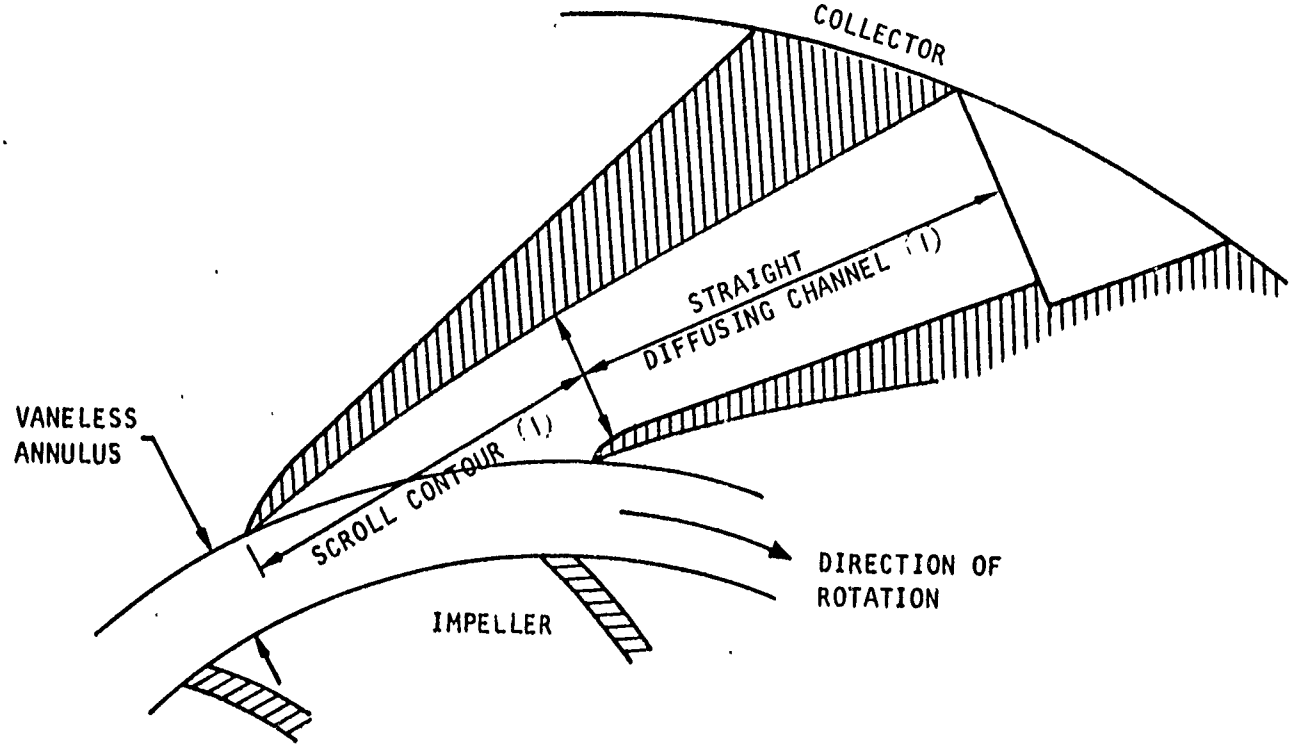

(1) CONTAINS CIRCULAR CROSS-SECTIONS

A-6959

Figure 28. Multicontour Diffuser Configuration

The vaneless annulus should be small but should be sufficient to equalize the flow distribution between the diffuser vanes without influencing the impeller flow.

The inlet scroll portion should guide the high-velocity fluid to the throat of the straight diffuser portion with low friction and minimum boundary-layer buildup. This can be assured by the use of circular cross-sections. Selection of a conical straight diffuser design was made since this configuration produces the best pressure recovery.

The vaneless annulus was calculated according to the well-established incompressible flow procedure.

The circular cross-sectional scroll calculation was established to provide a natural deceleration of the flow induced by the radius increase and the momentum reduction by the friction on the walls. This theory is assumed to produce an effective deceleration rate and low friction without the danger of separation due to a pressure gradient that is too large.

The basic momentum equation that follows is in accordance with the above theoretical concept and illustrated in Figure 29.

$$-\frac{\partial M}{\partial m} = \frac{\partial (C_u r)}{\partial X} \quad C = \frac{f\, C^2 \cos\alpha\, (d\pi - b)\, 2r}{2^2\, \pi}$$

The continuity equation resolves into the following form:

$$\partial X = r\partial\varphi = \frac{C_u r \pi d}{2\, b\, C_{Mo} r_o}\, \partial d$$

where M = momentum

m = mass

C_u = tangential velocity component

r = radius

X = distance in velocity direction

C = velocity

d = local diameter of circular channel

b = vaneless space channel width

C_M = radial velocity component

φ = angular position

f = friction factor

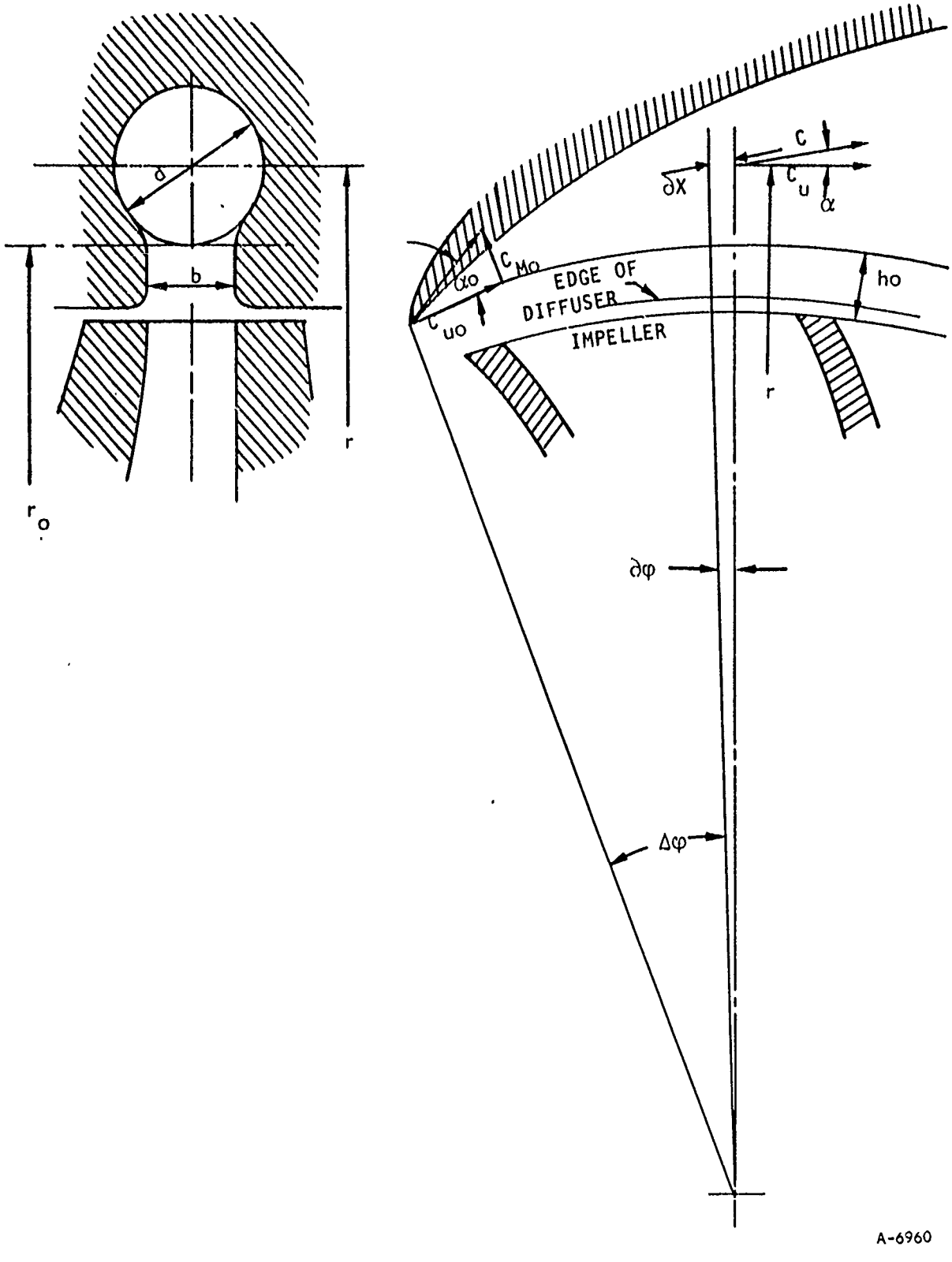

Figure 29 Diffuser Geometry and Velocities

The above differential equations were integrated. The resulting equations were programmed on the IBM computer. The output of the computer determined the channel geometry up to the throat, the pressure and velocity distributions, and the friction losses up to any desired point.

The boundary-layer buildup was calculated based on these results. The efficiency of the straight diffuser is a function of the relative boundary-layer thickness in the inlet throat. This effect was investigated in Reference 7. Figure 30 shows the measured influence of the boundary-layer thickness in the throat on pressure recovery of the diffuser channel. This curve was chosen to calculate the overall efficiency of the straight diffuser portion. Geometry of the diffuser is presented in Section 4.

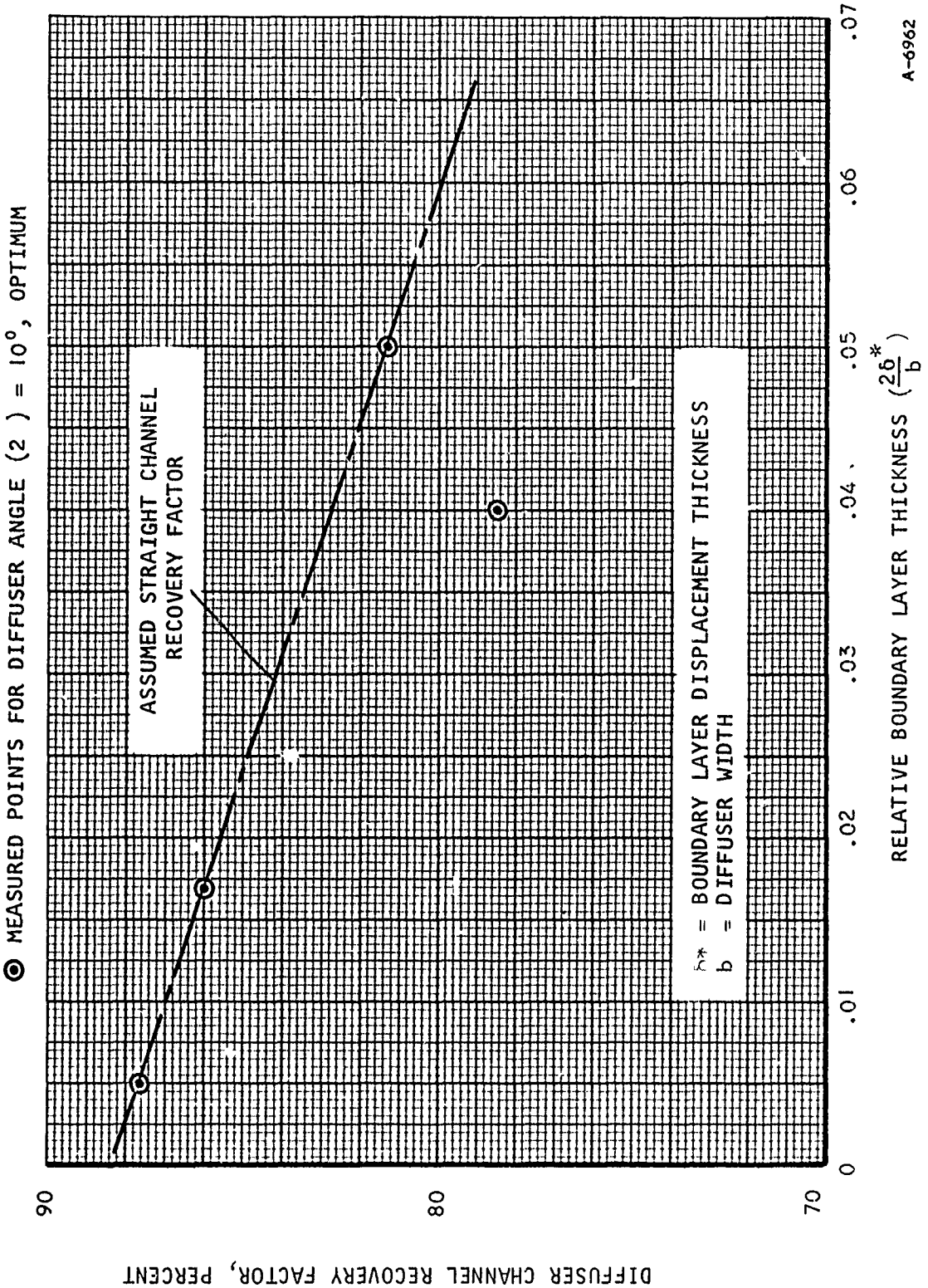

Figure 30. Influence of Boundary Layer Thickness on Diffuser Channel Pressure Recovery

EFFECT OF INDUCER SWEEPBACK ON AXIAL VELOCITY DISTRIBUTION

With the increased use of sweepback or shaping of the inducer leading edge to handle cavitation problems, determination of the radial variation of the axial velocity of the inlet flow is needed for a better calculation of the inducer blading. It is recognized that tangential swirls induced by blade rotation, as well as axial velocity, contribute to controlling the angle of attack on these blades. The present study deals only with the axial velocity component to clarify some of these effects.

The inducer blades are now replaced by an actuator disk which is tilted in accordance with the sweepback, Figure 31.

Following Reference 8, the general equation for incompressible, axially symmetric flow on either side of an actuator disk is established as

$$\frac{dH}{d\psi} = \frac{1}{r^2}\left[\theta \frac{d\theta}{d\psi} + \eta r\right] \qquad (1)$$

where H = stagnation enthalpy

ψ = stream function defined by

$$rC_r = \partial\psi/\partial x \quad ; \quad rCx = -(\partial\psi/\partial r)$$

η = $(\partial Cr/\partial x) - (\partial Cx/\partial r)$, tangential vorticity

θ = rCu, tangential momentum

It is assumed that, as the ring vortices pass downstream along cylindrical surfaces, the value of the tangential vorticity, η, at any radius is constant and equal to its value at infinity. In accordance with the actuator disk approach, the axial velocity at the disk will be almost exactly the arithmetic mean of the two infinity values at the same radius, i.e.,

$$Cx_{o_1} = Cx_{o_2} = \frac{Cx_{1\infty} + Cx_{2\infty}}{2} \qquad (2)$$

where subscript o_1 = conditions immediately upstream

o_2 = conditions immediately downstream

1∞ = conditions far upstream

2∞ = conditions far downstream

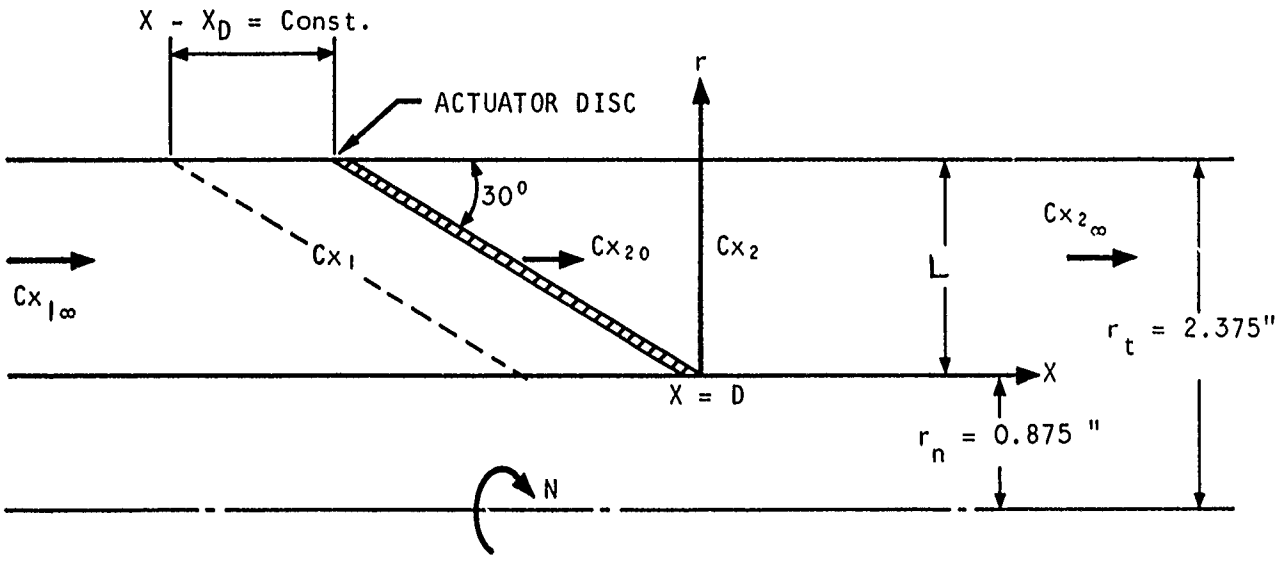

N = 40,000 rpm

Cx_{1_∞} = 36.63 fps

A-6957

Tan β_{02} = 72.2568 r

i.e. (β_{02}) tip = 86° $\quad (\beta_{02})_{hub}$ = 79.25°

ACTUATOR DISC (X_D)

X_D = 20.7852 r + 1.5156 inches

Figure 31. Illustrative Problem Statements

With these assumptions, a solution of Equation (1) is given as

$$\frac{dCx_{2\infty}}{dr} - \frac{\tan\beta_{o_2}}{r} \frac{d}{dr} \left[r \left\{ u - \left(\frac{Cx_{1\infty} + Cx_{2\infty}}{2} \right) \tan\beta_{o_2} \right\} \right]$$

$$= \frac{dCx_{1\infty}}{dr} - \frac{2(u - Cx_{1\infty}\tan\alpha_1)}{r\,(Cx_{1\infty}+Cx_{2\infty})} \frac{d}{dr} \left(rCx_{1\infty}\tan\alpha_1 \right) \qquad (3)$$

where β_{o_2} = exit rotor air angle measured relative to the moving blade

u = blade speed = $\frac{2\pi rN}{60}$

α_1 = absolute air angle far upstream of the rotor

Equation (3) may generally be written as an equation of the form

$$Cx_{2\infty}^2 + A(r)\, Cx_{2\infty} \frac{dCx_{2\infty}}{dr} + B(r)\, Cx_{2\infty} + C(r) \frac{dCx_{2\infty}}{dr} + D(r) = u \qquad (4)$$

A(r), B(r), C(r), and D(r) are all known functions of radius only. These are usually nonlinear differential equations and may be solved by numerical or graphical methods with the additional continuity condition to be satisfied. For illustrative purposes, the present problem has been solved with some reasonable assumption in order to simplify the governing equation. The problem statement and coordinates are shown in Figure 31. With a uniform upstream infinity axial velocity and zero absolute air angle (i.e., C_{x_1} = constant, and $\alpha_1 = 0$), Equation (3) becomes

$$\frac{dCx_{2\infty}}{dr} - \frac{\tan\beta_{o_2}}{r} \frac{d}{dr} \left[r \left\{ u - \frac{Cx_{1\infty} + Cx_{2\infty}}{2} \tan\beta_{o_2} \right\} \right] = 0 \qquad (5)$$

where u may be expressed as

$$u = \frac{N\, 2\pi r}{60} = cr$$

C is constant for a given problem. The further assumption is made, concerning exit blade angle β_{2_o}, that

$$\tan\beta_{o_2} = a\, r$$

Then, Equation (4) can be arranged as

$$\frac{dCx_{2\infty}}{dr} + \frac{\partial a^2 r}{a^2 r^2 + 2} Cx_{2\infty} + \frac{[2a^2 rCx_{1\infty} - 4Car]}{a^2 r^2 + 2} = 0 \qquad (6)$$

Solving this equation yields

$$Cx_{2\infty} = \frac{K + (2c - a(x_1)ar^2}{a^2r^2 + 2} \qquad (7)$$

where K is a constant determined from continuity relation

$$\int_{r_h}^{r_t} Cx_{1\infty} r dr = \int_{r_h}^{r_t} Cx_{2\infty} r dr$$

and

$$K = \frac{\partial a(aCx_1 - C)(r_t^2 - r_h^2}{\log \frac{a^2 r_t^2 + 2}{a^2 r_h^2 + 2}} + \frac{2(2C - aCx_1)}{a}$$

With the numerical values given in Figure 31, C_{x_2} is solved and plotted as functions of radius r in Figure 32. The axial velocity on the actuator disk given by Equation (2) is also shown. Note the reverse flow near the hub; this might result from the high rotational speed and undesired blade angle distribution.

The axial velocity over the entire flow field may be obtained with known infinity values. The results given in References 8 and 9 were based on an actuator disk plane placed normal to the axial direction. A slight modification will yield the following results to include the effect of the shape of the actuator disk. A tilted actuator disk is now expressed by

$$X_D = f(r)$$

The axial velocity distribution can be expressed as

$$Cx_1 = Cx_{1\infty} + \sum_i \frac{1}{k_i} \left[f_i(r) + \frac{1}{r} f_i(r) \right] e^{k_i (x - x_D)/\ell}$$

for $X < X_D$ and

$$Cx_2 = Cx_{2\infty} - \sum_i \frac{1}{k_i} \left[f_i'(r) + \frac{1}{r} f_i(r) \right] e^{-k_i (x - x_D)/\ell}$$

for $X > X_D$

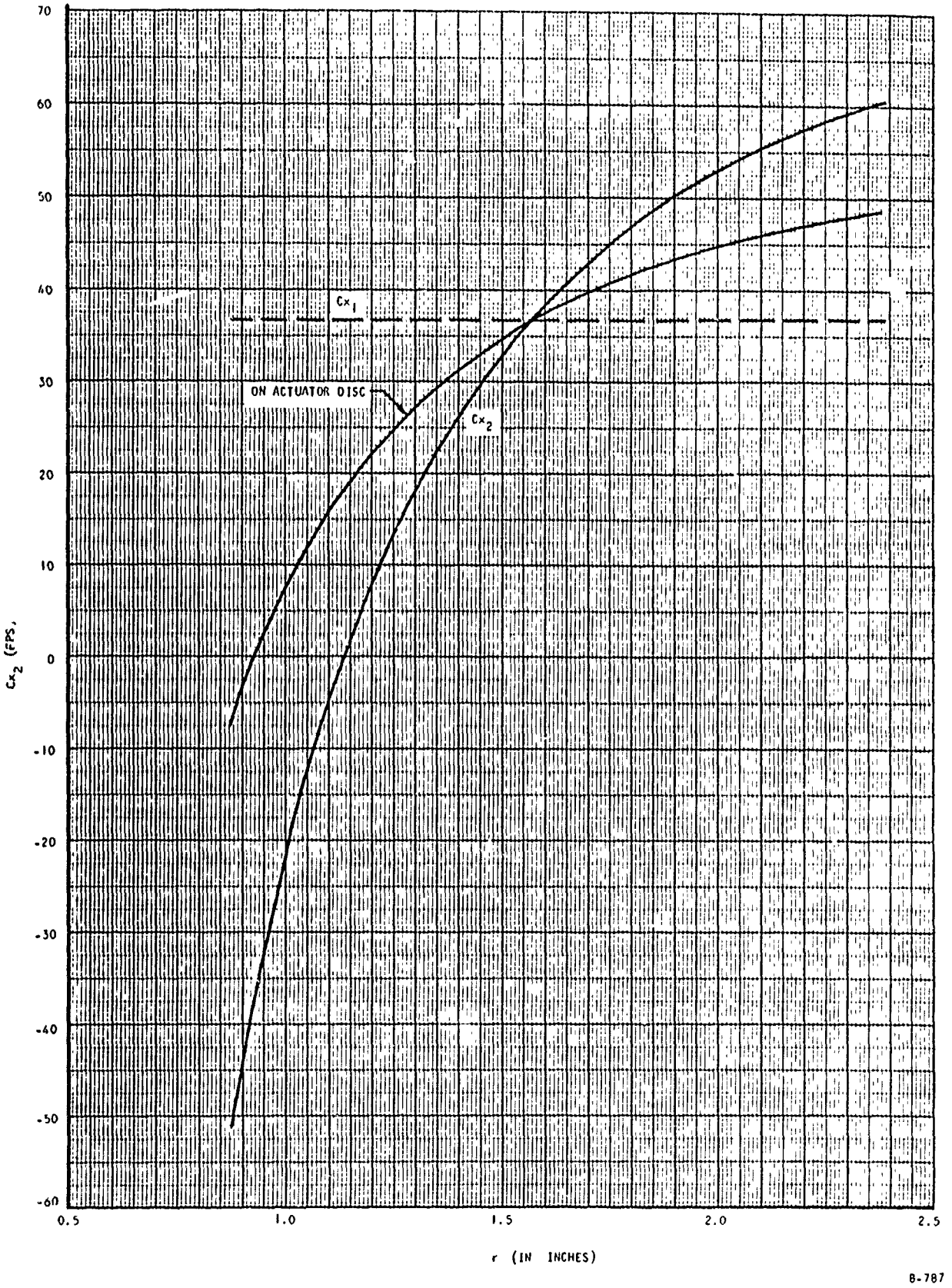

Figure 32. Axial Velocity Distribution at Infinity and on the Disk

where $f_i(r) = A_i J_1(k_i r) + B_i Y_1(k_i Y)$

J_1, Y_1 are the first order Bessel function of the first and second kind, respectively

$l = r_t - r_n$, the blade length

and k_i is only dependent on the values of r_t and r_h, given by

$$J_1(k_i r_n)\, Y_1(k_i r_t) - J_1(k_i r_t)\, Y_1(k_i r_h) = 0$$

The first six roots of this equation are tabulated by Janke and Emde (Reference 10).

For the present, $r_t/r_n = 2.714$

$k_1 = 3.249$

$k_2 = 6.3445$

$k_3 = 9.467$

$k_4 = 12.5988$

$k_5 = 15.7377$

$k_6 = 18.8774$

Since $Cx_{10} = Cx_{20} = \dfrac{Cx_{2\infty} + Cx_{1\infty}}{2}$ at $X = X_D$

$$\sum_i \frac{1}{k_i}\left[f_i'(r) + \frac{1}{r} f_i(r)\right] = \frac{Cx_{2\infty} - Cx_{1\infty}}{2}$$

Taking only the first root, the axial velocity distribution may be approximated as

$$Cx_1 = Cx_{1\infty} + \left(\frac{Cx_{2\infty} - Cx_{1\infty}}{2}\right) e^{k_1 (X - X_D)/\ell}$$

for $X < X_D$

$$Cx_2 = Cx_{2\infty} - \left(\frac{(Cx_{2\infty} - Cx_{1\infty})}{2}\right) e^{k_1 (X - X_D)/\ell}$$

for $X > X_D$

The axial velocity distribution at different sections upstream of the actuator disk for the illustrative case is calculated and shown in Figure 33.

These results indicate that the assumption, usually made, of uniform flow at the rotor inlet, is not a suitable approach. An estimate with the present method will yield a more reasonable velocity profile at the inlet. Allowance must be made for viscosity effects that tend to smooth out this gradient.

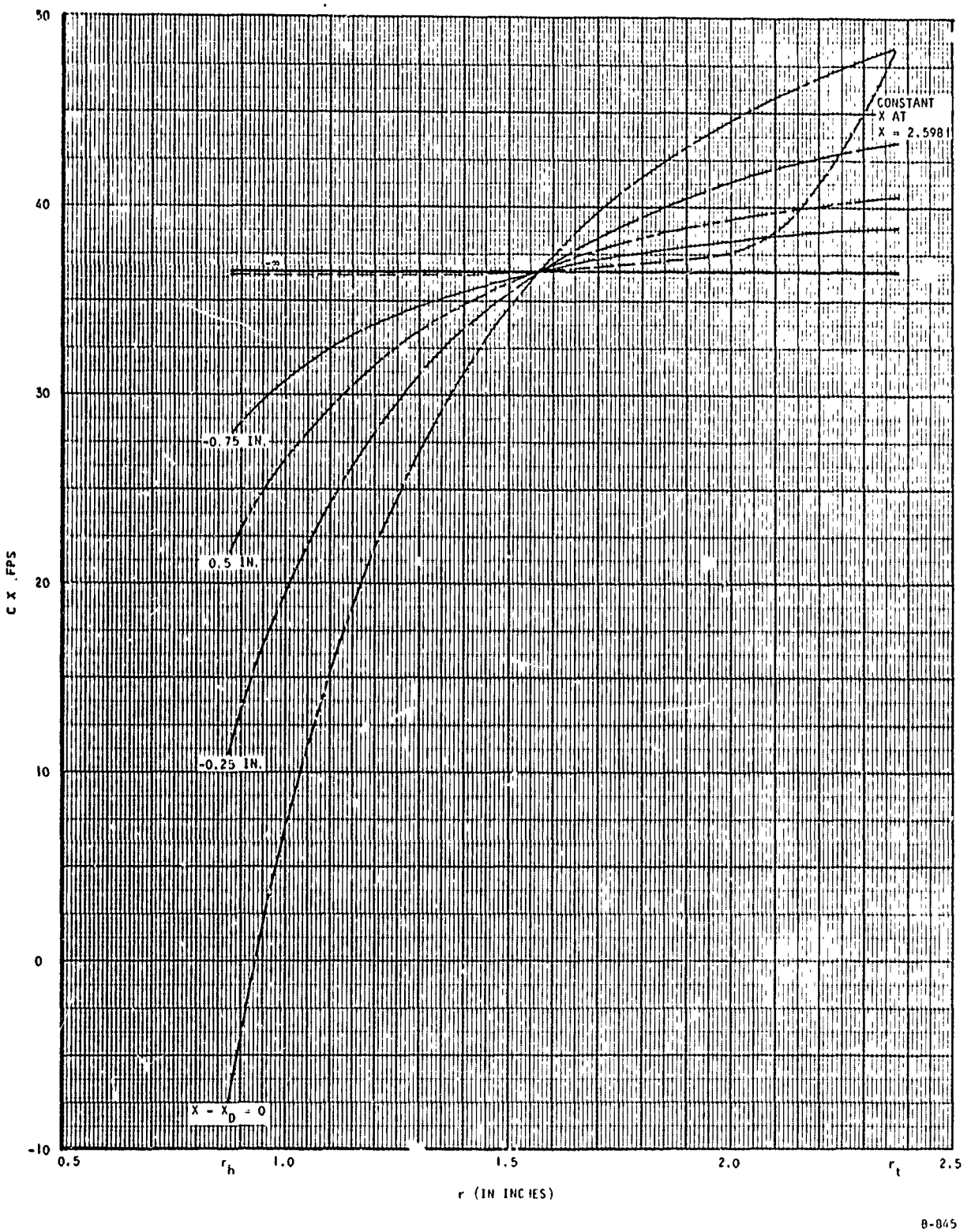

Figure 33. Axial Velocity Distribution Upstream of the Disk

SECTION 4

PERFORMANCE CALCULATION FOR CENTRIFUGAL PUMPS

This section presents the basis for calculating the performance of centrifugal pumps. The calculation is carried out with a computer program that handles the problem of performance at design point as well as that of off-design operation.

DESIGN POINT PERFORMANCE

Calculation of Design Geometry and Performance at Design Point

The first part of the calculation investigated the performance of different design combinations capable of meeting a given problem statement as expressed by the flow and pressure rise required by the fluid. The geometric dimensions, as well as the losses and efficiencies of these combinations, are presented to the designer, who can then choose the one most suitable for his purposes.

The program is based on one-dimensional calculation of the flow along the mean streamline, including friction, diffusion, loading, and boundary-layer-buildup factors. The equations contain experimental factors, which can be adjusted whenever the state of the art requires it.

The basic geometric design form of the pump is that of the Francis type, consisting of a centrifugal impeller having an integral mixed flow inducer portion and a radially arranged diffuser followed by a collector torus or scroll. This design arrangement, the most efficient combination, is shown in Figure 34 .

Within this general layout, there are many possible detail designs. The present program calculates four different inducer variations and four different diffuser designs.

1. Input Constants

The general design point performance program requires the following input values, which will be kept invariant during the calculations:

Flow, V_o - ft^3/sec

Pressure rise, ΔP_o - psi

Density, γ_o - lb/cu ft

Kinematic viscosity, ν_* - ft^2/sec

Inducer design case (Case 1 to 4)

Diffuser design case (Case 1 to 4)

Impeller loss factors (ξ_1, ξ_2, ξ_3, ξ_8, ξ_9)

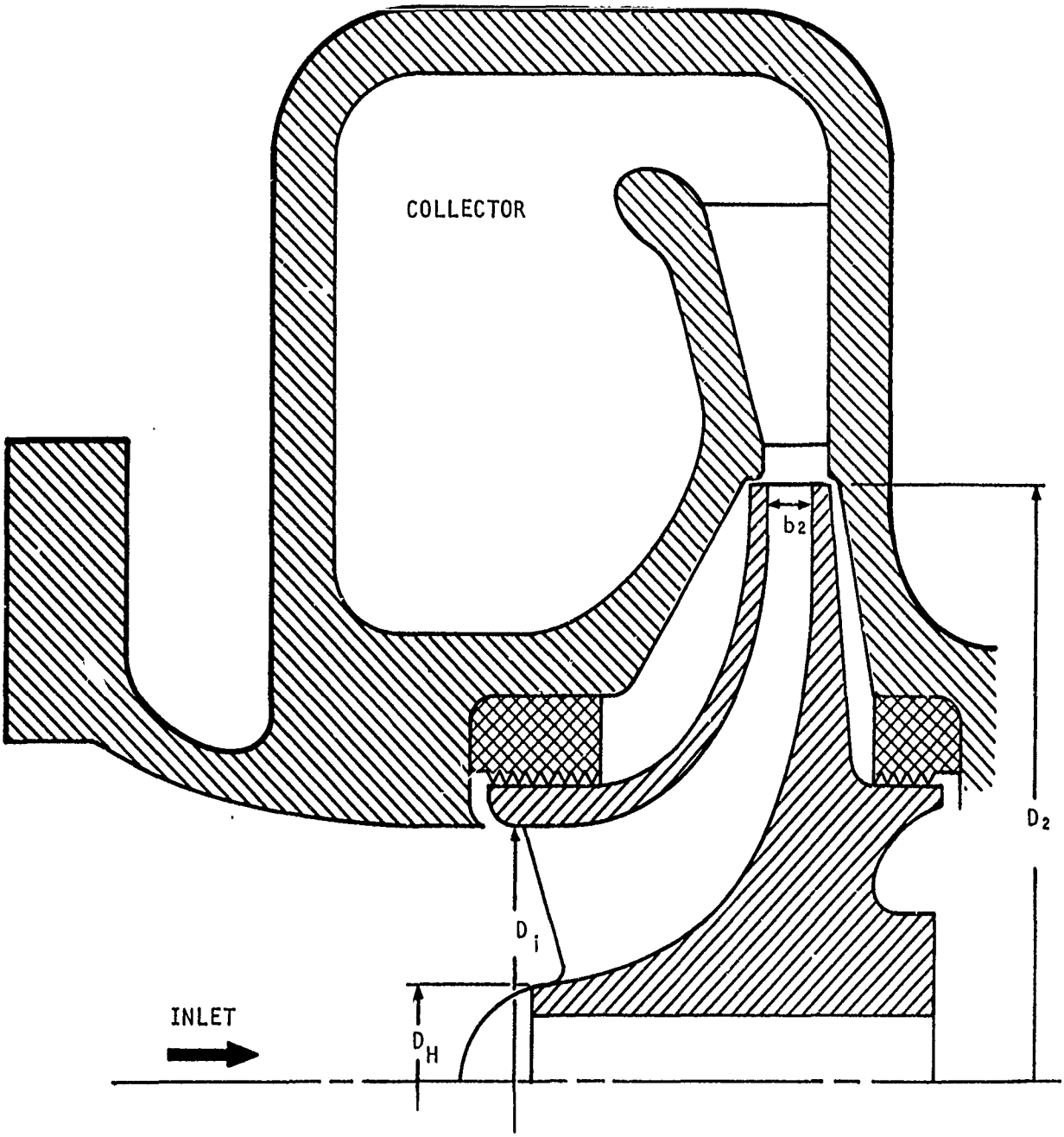

Figure 34. Typical Centrifugal Pump

The necessary inputs for the inducer and diffuser design cases are different, depending on the case.

2. Input Variables

The performance of a pump impeller depends on (1) its geometric configuration, (2) the discharge vane angle, (3) the slip, which is primarily a function of the number of vanes, and (4) the discharge flow angle or flow factor. After these factors have been varied, the combination that performs best can be selected. In many cases, the optimum running speed is still to be established, so that the speed is also variable.

The variable inputs are then

Impeller tip vane angle, β_2, deg

Impeller slip factor, $\mu = \dfrac{C_{2_u}}{C_{2_{u\infty}}}$

Impeller flow factor, $\lambda = \dfrac{C_{2_M}}{u_2}$

Speed, N - rpm

3. Basic Relations

The basic relations used to establish the performance and geometrical characteristics of the pumps are derived in the following.

Pump Inducer

The size of the pump inducer is governed essentially by the availability of the suction head. A high suction head permits the flow to accelerate through the inducer without danger of cavitation. The inducer size is then reduced due to high-speed flow. With the condition of low NPSH (net positive suction head) the danger of cavitation is immediate, the flow speed must be kept low, and the inducer must be much larger. Thus, the following four alternates are considered for the sizing of the inducer:

1. The NPSH is given, and no cavitation at all is allowed.
2. Inlet vane angle is given, and no cavitation is allowed.
3. Inlet vane angle is given as 60 degrees; this case calculates low-pressure compressors, where compressibility effect is negligible.
4. There is cavitation at the inducer and inducer dimensions are precalculated.

Case 1 - NPSH Given and No Cavitation

The program calculates the inlet dimensions on the basis of the assumption that half of the NPSH can be used to produce the inlet velocity head, the other half of the head assuring a cavitation-free impact on the blades. This assumption, together with continuity requirements, yields the inlet diameter as:

$$D_i^2 = \frac{576\ V_o}{\pi \sqrt{32.175\ NPSH}} + D_H^2 \quad \text{(inches)}$$

Inlet flow angle is

$$\cot \beta_i = \frac{720 \sqrt{32.175\ NPSH}}{\pi\ N\ D_i}$$

The velocities become

$$C_i = \sqrt{32.175\ NPSH} \quad \text{(fps)}$$

$$W_i = \sqrt{32.175\ NPSH + \frac{N^2 \pi^2 D_i^2}{518{,}400}} \quad \text{(fps)}$$

Case 2 - Inlet Vane Angle is Chosen - No Cavitation

The conventional pump inlet can be designed with this case, selecting 67.5^0 for blade angle; other values can be used just as well.

The inlet diameter is

$$D_i = \sqrt[3]{\frac{44{,}355\ V_o}{N\ K_i \cot \beta_i}} \quad \text{(inches)}$$

where K_i represents the restriction due to the hub

$$K_i = 1 - \left(\frac{D_H}{D_i}\right)^2$$

The velocities are given as:

$$U_i = \frac{\pi N D_i}{720} \quad \text{(fps)}$$

$$C_i = U_i \cot \beta_i$$

$$W_i = \frac{U_i}{\sin \beta_i}$$

The velocity-head necessary to accelerate the fluid into the inlet is

$$NPSH_o = \frac{C_i^2}{64.35} \quad (ft)$$

The actual NPSH must be higher than this value.

Case 3 - 60-Degree Vane Angle Inducer

This case is the same as Case 2, except that the vane angle is fixed at 60 degrees, because this value gives the minimum inlet relative velocity for incompressible flow. It must be noted that the cavitation performance of such an inlet is not too good.

Case 4 - Cavitating Inducer

In a cavitating inducer, two-phase flow is encountered at the inlet. If the flow is assumed to be homogeneous, the density of the mixture can be approximated as

$$\frac{\gamma_o}{\gamma} = \left[1 + A\,\Delta h_o\right]^k$$

where γ_o = density of the saturated liquid

γ = density of the mixture

Δh_o = depression head, inlet, below the saturated state (TSH)

A and k are constant characteristics of the pumping fluid

For LH_2, the constants are

$$A = 0.02814 \qquad k = 0.4$$

This flow function, together with the diameters of the hub and tip of the inducer, is used to calculate the velocity and angle of the flow.

$$C_i\left(\frac{D_i^2\pi}{4} - \frac{D_H^2\pi}{4}\right) = \frac{144\,V_o}{\epsilon_i}\left[1 + A\left(\frac{C_i^2}{64.35} - NPSH\right)\right]^K$$

$$U_i = \frac{D_i N\pi}{720} \quad (fps)$$

$$W_i = \frac{U_i}{\sin\beta_i} \quad (fps)$$

The flow angle is

$$\cot \beta_i = \frac{C_i}{U_i}$$

The flow factor ϵ_i represents the resistance of the inlet. A value of 0.95 can be chosen if the inlet is an undisturbed coaxial design.

Losses at the Inlet

In the case of a shockless inlet, which is usual in normal pump design, the program does not separate the inlet loss from the general impeller losses. The cavitating inducer represents another case, because its incidence is designed to overcome, even at normal operating conditions, the effect of the very low angle and cavitation in the inducer throat. This operation results in additional losses, which will be calculated later in the part-load performance section.

Losses and Design Characteristics of the Impeller

The performance of a pump as measured by the pressure rise is often expressed in terms of energy in foot-pounds per pound of fluid flow or in head of fluid in feet. They are related together as

$$H_o = 144 \frac{\Delta P_o}{\gamma_o} \text{ (ft)}$$

To deliver this energy, the pump impeller must develop a head, H_{th}, through a change in momentum imparted to the flow stream. The hydraulic efficiency of the pump, as related to the impeller and pump head, is

$$\eta_{HYD} = \frac{H_o}{H_{th}} \tag{8}$$

To start the calculation in the program, a first approximate value of η_{HYD} of 0.9 is assumed. Iteration is then carried out using the proper value for η_{HYD}.

1. Diameter

For convenience in performance calculation, dimensionless parameters are introduced by normalizing all values of head and losses with respect to $\frac{u_2^2}{g}$. Thus, the impeller head is associated with the head coefficient defined by

$$q = H_{th} \Big/ \frac{u_2^2}{g} \tag{9}$$

The Euler momentum equation, then, relates q to other characteristic parameters of the impeller

$$q = \frac{C_{u_2}}{u_2} = \mu (1 - \lambda \tan \beta_2) \qquad (10)$$

The diameter and tip speed of the wheel are derived from Equations 8, 9, and 10.

$$D_2 = \frac{720}{\pi N} \sqrt{\frac{32.175\ H_{TOT}}{q}} \quad \text{(inches)}$$

$$U_2 = \sqrt{\frac{32.175\ H_{TOT}}{q}} \quad \text{(fps)}$$

This gives the relative velocity at the impeller tip:

$$W_2 = U_2 \sqrt{\lambda^2 + (1 - q)^2} \quad \text{(fps)}$$

2. Number of Blades

The other parameter of importance in the impeller design is the number of blades. The proper number depends upon the amount of flow "slip" at the impeller exit, upon the limit allowable for the blade loading, and upon other considerations such as the physical geometry and velocity triangles of the blades (Figure 35).

Following the investigation of Reference 11 which takes into account these various factors, the number of blades can be determined as

$$Z_1 = \xi_1 \frac{\pi \mu \cos \beta_2}{2 (1 - \nu_2) (1 - \mu)} \left(1 + \frac{.08}{\zeta_1}\right)$$

where ξ_1 is an experimental factor which is normally close to 1.

$\nu_2 = \frac{D_i}{D_2}$, the impeller diameter ratio

$\zeta_1 = \frac{W_2}{W_i}$, the ratio of velocity diffusion in the impeller

The average length of the streamline in the flow passage is

$$\Delta \ell = \frac{0.8 (D_2 - D_H)}{\cos \beta_i + \cos \beta_2} \quad \text{(inches)}$$

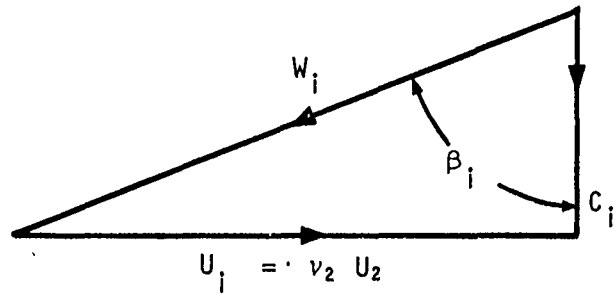

INLET - WITHOUT PREROTATION

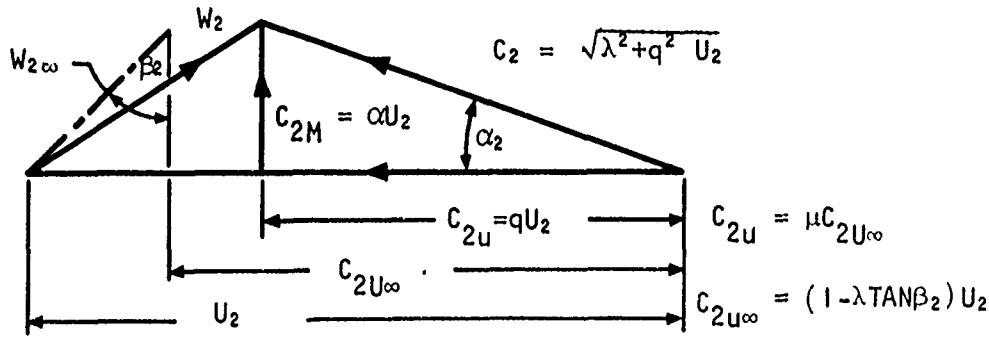

IMPELLER TIP

A-6979

Figure 35. Velocity Triangles at Mean Streamline

The average diameter of the impeller passage is calculated as

$$d_{HYD_1} = D_2 \left[\frac{1}{\frac{Z_1}{\pi \cos \beta_2} + \frac{1}{B_2}} + \frac{\nu_2}{\frac{2}{1 - \nu^2} + \frac{2Z_1}{\pi(1 + V_2)} \sqrt{1 + \tan^2 \beta_i \left(\frac{1 + \nu_2^2}{2} \right)}} \right] \text{(inches)}$$

B_2, the dimensionless tip width of the wheel, is given by

$$B_2 = \frac{b_2}{D_2} = \frac{144\ V_o}{\epsilon_2 \lambda u_2 \left(D_2^2 \pi - D_2 \frac{0.030\ Z_1}{\cos \beta_2} \right)}$$

ϵ_2 is the restriction factor, generally assumed equal to 0.92.

The average relative velocity through the impeller is then needed

$$W_{AV} = \sqrt{\frac{W_i^2 + W_2^2}{2}} \text{ (fps)}$$

The Reynolds number of the impeller passage is calculated with the values

$$Re_i = \frac{d_{HYD_1} W_{AV}}{12\ \nu_{ft}}$$

$$f_1 = \frac{0.0462}{Re^{0.2}}$$

The skin friction loss coefficient through the impeller passage is

$$\Delta q_{SF} = \frac{\Delta H_{SF}}{q \frac{u_2^2}{g}} = \xi_2 \frac{f_1 \Delta \ell_1}{d_{HYD_1}} \frac{W_{AV}^2}{u_2^2 q}$$

The experimental factor, ξ_2, is close to 1.

Another source of loss in the impeller arises from the diffusion of the flow in the blade passage. This is expressed by a blade loading factor, Δ, similar to the concept of the diffusion factor used in axial flow compressors. From Reference 11, Δ is given as

$$\Delta = 1 - \xi_1 + \frac{q (\cos B_i + \cos \beta_2)}{2 \frac{W_i}{u_2} \left[\frac{Z_1}{\pi} (1 - \nu_2) + 2 \nu_2 \right]}$$

The loss coefficient associated with this diffusion is then

$$\Delta q_{DIFF} = \frac{\Delta H_{DIFF}}{q \frac{u_2^2}{g}} = \xi_3 \Delta^2 \left(\frac{W_i^2}{q u_2^2} \right)$$

ξ_3 is an experimental factor; for average calculations, 0.1 can be assumed.

In the experimental investigation of the interaction between the impeller and diffuser, it has been found that some of the flow that has passed the impeller does not enter the diffuser, but returns into the impeller, giving rise to a considerable energy loss. This phenomenon has not been fully investigated (References 11 and 15). At present, a recirculation loss parameter is used to account for this source of energy dissipation.

$$\Delta q_{RC} = \frac{\Delta H_{RC}}{q \frac{u_2^2}{g}} = \xi_4 \Delta \frac{q}{2}$$

The best value of ξ_4 factor has not yet been determined for all cases, but the calculations of shrouded impeller pumps show that it is close to zero. In the case of an unshrouded impeller, we arbitrarily assume the value 0.05. The foregoing are all of the internal losses of the impeller.

The internal static efficiency of the impeller is calculated as

$$\eta_{imp} = \frac{H_{TH} - \frac{C_2^2}{2g} - \Delta H_{DL}}{H_{TH} - \frac{C_2^2}{2g} + \Delta H_{SF} + \Delta H_{RC}}$$

or

$$\eta_{imp} = \frac{1 - \frac{\lambda^2 + q^2}{2q} - \Delta q_{DL}}{1 - \frac{\lambda^2 + q^2}{2q} + \Delta q_{SF} + \Delta q_{RC}}$$

Diffuser

An infinite variety of diffuser designs is possible. This program incorporates four different solutions, such as

1. Conical or parallel-sided straight-vaned diffuser

2. Multiscroll circular cross-section diffuser

3. Collector scroll (or torus)

4. Vaneless diffuser

The program calculates the transition portion from the impeller into the diffuser with an increased friction value. This increase of loss is due to the mixing of the uneven discharge from the impeller. The boundary-layer buildup is also estimated along this transition and the recovery of the following diffuser portion is estimated as a function of the calculated displacement thickness of the boundary layer (Reference 16).

Case I - Straight Wall Diffuser (Figure 36)

The straight-wall diffuser of the geometry shown in Figure 36 is a design concept that lends itself readily to hardware fabrication.

For calculation purposes, it can be considered to be made up of a scroll element followed by a straight diffusing section. The boundaries between these elements appear as a throat. For high performance, diffusers are generally designed with a square throat section so that

$$\zeta_D = \frac{h_{THROAT}}{b_{THROAT}} = 1.5$$

The average velocity ratio in the scroll is

$$\left(\frac{C_{M2}}{Cu}\right) = \left(\frac{r}{r_2}\right) \frac{F(h)}{q} \sqrt{\lambda^2 + q^2}$$

where $$\frac{r}{r_2} = 1.04 + 0.69333\ \zeta_D\ B_2 \left(\frac{3 + 2\ \zeta_D \tan \gamma}{2 + \zeta_D \tan \gamma}\right)$$

and F(h) is a function characteristic of the geometry given by

$$F(h) = \frac{\lambda}{\sqrt{\lambda^2 + q^2}} + f_2 \left\{ \zeta_D (2 + \tan \gamma) + \frac{1}{2} \log_e \left(\frac{\zeta_D B_2 + 0.02}{0.02}\right) - \left(\frac{2}{\tan \gamma} + \frac{1}{2}\right) \log_e \left[\frac{B_2(\zeta_D \tan \gamma + 2) + 0.02 \tan \gamma}{2B_2 + 0.02 \tan \gamma}\right] \right\}$$

Another parameter characterizing the flow in the diffuser is the Reynolds number

$$Re_{b_2} = 2B_2 \sqrt{\lambda^2 + q^2}\ Re_2$$

$$Re_2 = \frac{D_2 U_2}{12\ \nu^*}$$

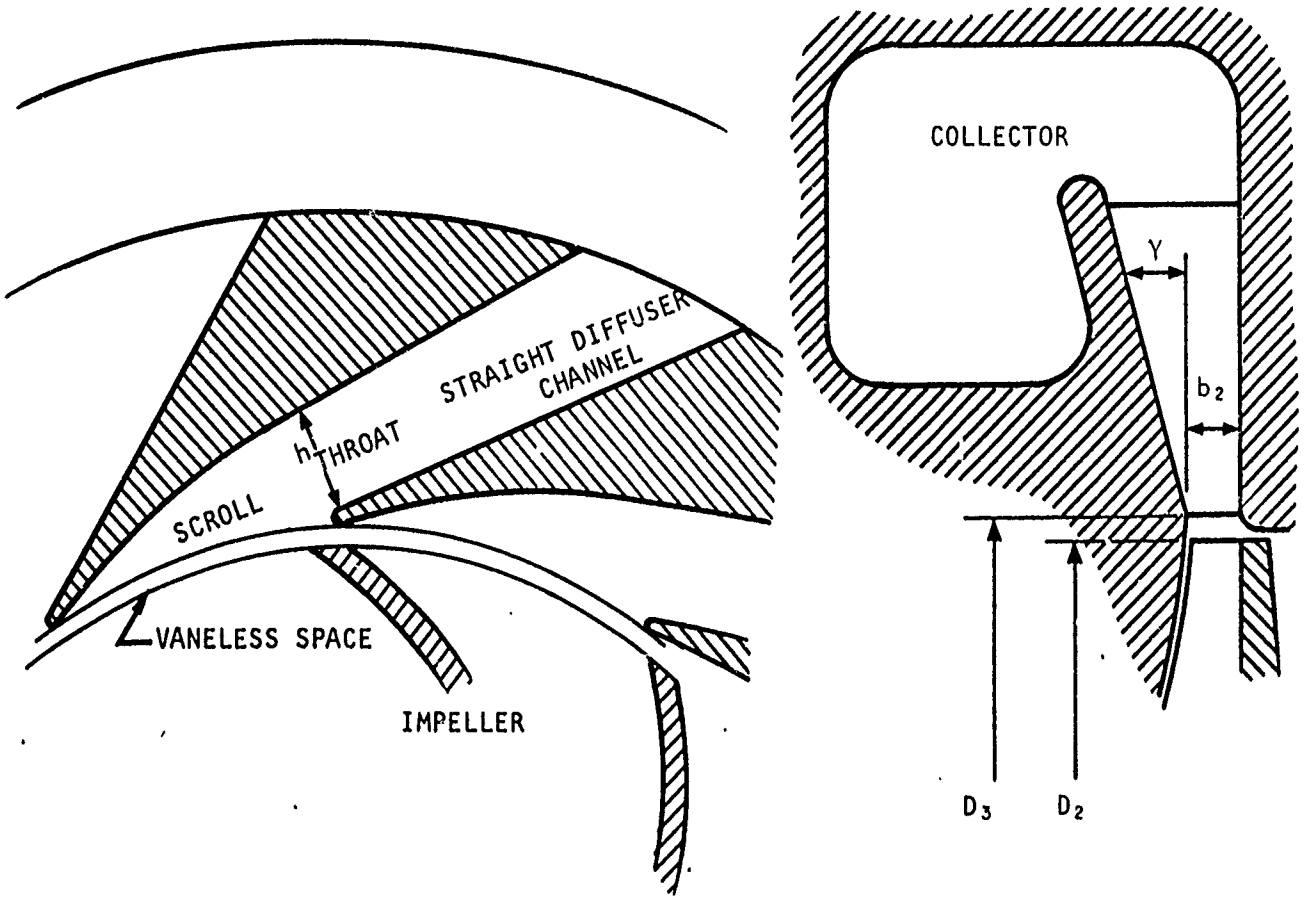

Figure 36. Straight-Wall Diffuser

With D for turbulent flow, the local friction factor is

$$f_2 = \frac{0.0462}{Re_{b_2}^{0.2}} \qquad (11)$$

This local friction factor can be used to a Reynolds number lower limit of 10^4.

For Re_{b_2} lower than 10^4, an adjustment has to be made, since the computer will extrapolate (11) for calculation purposes.

The actual vane number of the diffuser as given later is

$$Z_2 = \frac{2\pi}{\zeta_D B_2 (2 + \zeta_D \tan \gamma)} \left(\frac{C_{M_2}}{Cu} \right)$$

Practical reasons set the number of diffuser vanes between 6 and 16. Therefore, the program checks the value and, if it is different, adjusts the ξ_D value and recalculates.

This geometry represents the natural deceleration in the scroll. It gives the loss

$$\Delta q_{SC} = \frac{\lambda^2 + q^2}{2q} \frac{2 f_2 \Delta \ell_2}{d_{H_2}} \left[1 + \left(\frac{Cu}{C_{M_2}} \right)^2 \frac{\lambda^2}{q^2} \right]$$

where length of the flow path $\Delta \ell_2$ is

$$\Delta \ell_2 = D_2 \left[\frac{0.02 \sqrt{\lambda^2 + q^2}}{\lambda} + \sqrt{1.04 \frac{\pi^2}{Z_2^2} + \frac{B_2^2}{4}} \right] \text{ (inches)}$$

and the hydraulic diameter

$$d_{H_2} = D_2 \frac{4 B_2 \zeta_D (2 + \zeta_D \tan\gamma)}{2 + 2 \zeta_D + \zeta_D \tan \gamma} \text{ (inches)}$$

The loss in the following straight diffuser is then expressed as

$$\Delta q_{D_2} = \frac{\lambda^2 + q^2}{2q} \left(\frac{Cu}{C_{M_2}} \right)^2 \frac{\lambda^2}{q^2} \left[\zeta_5 + \zeta_6 f_2 \frac{\Delta \ell_2}{dH_2} \right]$$

The loss factors were chosen according to the test results presented in Figure 30. $\zeta_5 = 0.2$ and $\xi_6 = 1.5$ give good approximations.

The overall diffuser loss is then

$$\Delta q_D = \frac{\Delta H_{DIFF}}{q\ u_2^2/g} = \Delta q_{SC} + \Delta q_{D2}$$

Case 2 - Multiscroll Diffuser with Circular Diffusers (Figure 37)

As the figure shows, the diffuser design consists of three portions - a vaneless space, a scroll and a straight circular diffuser.

As presented in Reference 15, the loss in the vaneless space is equal to

$$\Delta q_{2\text{-}3} = \frac{\delta}{2\cos\left(\frac{\alpha_2 + \alpha_3}{2}\right)} \left(1 + \frac{\cos^2\alpha_2}{1.0816\cos^2\alpha_3}\right) \frac{\lambda^2 + q^2}{2q}$$

where

$$\delta = \frac{0.32\ f_2}{B_2}$$

$$\cos\alpha_3 = \frac{(1+\cos\alpha_2)^2\, e^{\delta} - \sin^2\alpha_2}{(1+\cos\alpha_2)^2\, e^{\delta} + \sin^2\alpha_2}$$

$$\cot\alpha_2 = \frac{\lambda}{q}$$

The vaneless space is assumed to have a diameter

$$D_3 = 1.04\ D_2$$

The width ratio is given as

$$B_3 = \frac{b_2}{D_3}$$

In the scroll portion of the diffuser, the diameter ratio is given by

$$\frac{Z_2}{4\ B_3\cot\alpha_3}\ \frac{D_3}{D_4}\left(\frac{D_4}{D_3} - 1\right)^2 = 1 + \frac{f_2\pi}{B_3\cot\alpha_3}\left(\frac{D_4}{D_3} - 1\right)$$

The $\frac{D_3}{D_4}$ ratio is calculated from this equation.

The number of scrolls is an important design parameter. The single-volute collector design corresponds to $Z_2 = 1$. A higher number for Z_2 is considered. In the present program, Z_2 is set $Z_2 = 4$ for a typical calculation.

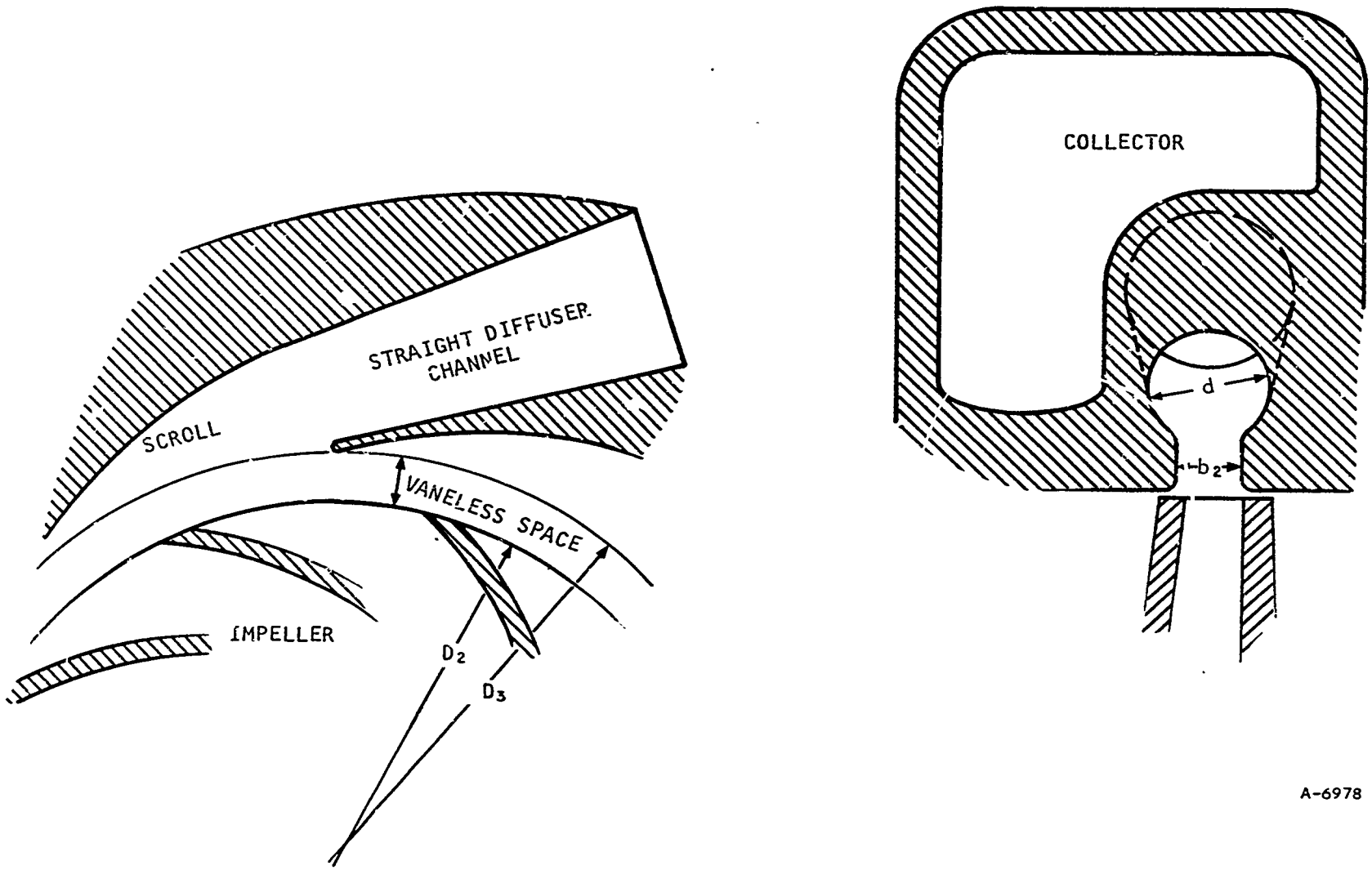

Figure 37. Multiscroll Circular Cross-Section Diffuser

The loss coefficient in the scroll is then

$$\Delta q_{3-4} = \frac{\pi f_2}{2}\left(\frac{\lambda^2 + q^2}{2q}\right)\left(\frac{D_2 \cos \alpha_2}{D_3 \cos \alpha_3}\right)^2 \left(\frac{1 + D_4/D_3}{D_4/D_3 + 2B_3 - 1}\right)\left[1 + \frac{B_3^2 \cos^2 \alpha_3}{(D_4/D_3 - 1)^4}\right]$$

For the straight circular diffusing element, the minimum possible loss achieved with the best recovery yields a loss coefficient of

$$\Delta q_{4-5} = \left(\frac{\lambda^2 + q^2}{2q}\right)\left(\frac{D_2 \cos \alpha_2}{D_3 \cos \alpha_3}\right)^2 \frac{B_3^2 \cos^2 \alpha^3}{\left(\frac{D_4}{D_3} - 1\right)^4}\left[\zeta_6 + \frac{\zeta_7 (D_4/D_3 + 1)}{Re_{b_2}{}^{0.2}(D_4/D_3 - 1)}\right]$$

The boundary layer buildup factors are

$$\zeta_6 = 0.2 \text{ and } \zeta_7 = 0.0314$$

The total diffuser loss in the multiscore design is then

$$\Delta_{q_D} = \Delta q_{2-3} + \Delta q_{3-4} + \Delta q_{4-5}$$

Case 3 - Single Scroll and Diffuser

This case is similar to Case 2, except that $Z_2 = 1$.

Case 4 - Vaneless Diffuser

$$\Delta q_{2-3} = \frac{\delta}{2 \cos\left(\frac{\alpha_2 + \alpha_3}{2}\right)}\left(1 + \frac{\cos^2 \alpha_2 D_2{}^2}{\cos^2 \alpha_3 D_3{}^2}\right)\frac{\lambda^2 + q^2}{2q}$$

where $\delta = \dfrac{3f_2 (D_3/D_2 - 1)}{B_2}$

$$\cos \alpha_3 = \frac{(1 + \cos \alpha_2)^2 e^{\delta} - \sin^2 \alpha_2}{(1 + \cos \alpha_2)^2 e^{\delta} + \sin^2 \alpha_2}$$

$$\cot \alpha_2 = \frac{\lambda}{q}$$

After the long vaneless space, a quite inefficient additional recovery is possible in the collector.

Here a fraction of the kinetic energy of the velocity leaving the impeller is assumed to be lost.

$$\Delta q_{3-4} = 0.66 \left(1 - \frac{\cos \alpha_2 \; D_2}{\cos \alpha_3 \; D_3}\right)^2 \quad \frac{\lambda^2 + q^2}{2q}$$

The total diffuser loss in the vaneless diffuser is then

$$\Delta q_D = \Delta q_{2-3} + \Delta q_{3-4} + \Delta q_{4-5}$$

Hydraulic Performance of the Pump

The hydraulic performance measures directly the work which produces the pump pressure. This means that the head output of the pump must be equal to the required value after all the internal losses are deducted.

The hydraulic efficiency of the pump is then

$$\eta_{HYD} = \frac{H_o}{H_{TH}} \quad \frac{1 - \Delta q_{DL} - \Delta q_D}{1 + \Delta q_{SF} + \Delta q_{RC}} \qquad (12)$$

The hydraulic efficiency is now calculated from Equation (12) with various loss parameters which are obtained by starting the computation with an assumed value for η_{hyd}. The value from Equation (12) must be within 2 percent of the assumed value, or otherwise the computer will proceed to iterate.

Overall Efficiency and Power Input of the Pump

Besides the loss in energy in the impeller area diffuser passages, external losses must be considered. These are due to friction from the hub disc which supports the impeller blades and the leakage through the seal clearance.

The disk friction loss is often given as

$$\Delta q_{FR} = \frac{\xi_8}{10^3 \lambda q \; B_2} \left(\frac{10^6}{Re_2}\right)^2$$

The experimental factor $\xi_3 = 0.285$ is to be assumed for the case of a shrouded wheel and $\xi_8 = 0.366$ for an unshrouded wheel.

$$\Delta q_L = \frac{\xi_9 \; .006 \; \nu_1^2}{B_2} \sqrt{\frac{2q - \lambda^2 - q^2}{2q}}$$

The factors are $\xi_9 = 1.0$ for a shrouded impeller and $\xi_9 = 0.5$ or 0 for an unshrouded one.

The overall efficiency of the pump, from which the hydrodynamic power input is obtained, is then

$$\eta = \frac{H_{out}}{H_{in}} = \frac{\eta_{hyd}}{1 + \Delta q_{FR} + \Delta q_L}$$

With the change in flow rate and speed, the flow factor at the impeller changes so that the head coefficient is now calculated

$$q = \mu \left(1 - \lambda_o M_o \tan \beta\right)$$

$$\mu = \frac{1}{1 + \zeta_1 \frac{\pi \cos \beta_2}{2 Z_1 (1 - \nu_2)} \left(1 + \frac{0.08}{\zeta_1}\right)}$$

with

$$\zeta_1 = \sqrt{\frac{M_o^2 \lambda_o^2 + (1 - q)^2}{\nu_2^2 + M_o^2 \phi_o^2}}$$

where $$\phi_o = \frac{C_o}{U_{2o}} = \nu_2 \cot \beta_{io}$$

At off-design, an incidence is encountered at the inducer inlet so that the incidence loss is given as

$$\Delta q_{inc} = \psi_2 \left(\frac{W_i}{U_2}\right)^2 \frac{1}{2q}$$

where ψ_2 is an experimental constant. According to the test values on axial compressors, ψ_2 is a parabolic function of the incidence angle:

$$\psi_2 = a_1 + a_2 \Delta \beta_i + a_3 \Delta \beta_i^2$$

$$\Delta \beta_i = \left| \beta_i - \beta_{io} \right| \quad \text{(absolute value)}$$

$$\cot \beta_i = M \cot \beta_{io}$$

The average relative velocity in the impeller passages is

$$W_{AV} = \frac{U_2}{\sqrt{2}} \sqrt{(1 + \zeta_1)^2 \left(M^2 \cot^2 \beta_{io} + \nu_2^2\right)}$$

The Reynolds number calculated with this velocity inside the impeller passages is

$$Re_i = \frac{d_{HYD_i} W_{AV}}{12 \nu^*}$$

$$U_2 = \frac{D_2 \pi N_o}{720} \left(\frac{N}{N_o}\right)$$

d_{HYD_i} is given by the design point calculation. The new friction factor becomes

$$f_1 = \frac{0.0462}{Re_i^{0.4}}$$

With the change in flow rate and speed, the flow factor at the impeller changes so that the head coefficient is now calculated

$$q = \mu \left(1 - \lambda_o M_o \tan \beta\right)$$

$$\mu = \frac{1}{1 + \zeta_1 \frac{\pi \cos \beta_2}{2 Z_1 (1 - \nu_2)} \left(1 + \frac{0.08}{\zeta_1}\right)}$$

with

$$\zeta_1 = \sqrt{\frac{M_o^2 \lambda_o^2 + (1 - q)^2}{\nu_2^2 + M_o^2 \phi_o^2}}$$

where $$\phi_o = \frac{C_o}{U_{2o}} = \nu_2 \cot \beta_{io}$$

At off-design, an incidence is encountered at the inducer inlet so that the incidence loss is given as

$$\Delta q_{inc} = \psi_2 \left(\frac{W_i}{U_2}\right)^2 \frac{1}{2q}$$

where ψ_2 is an experimental constant. According to the test values on axial compressors, ψ_2 is a parabolic function of the incidence angle:

$$\psi_2 = a_1 + a_2 \Delta \beta_i + a_3 \Delta \beta_i^2$$

$$\Delta \beta_i = \left| \beta_i - \beta_{io} \right| \quad \text{(absolute value)}$$

$$\cot \beta_i = M \cot \beta_{io}$$

The average relative velocity in the impeller passages is

$$W_{AV} = \frac{U_2}{\sqrt{2}} \sqrt{(1 + \zeta_1)^2 \left(M^2 \cot^2 \beta_{io} + \nu_2^2\right)}$$

The Reynolds number calculated with this velocity inside the impeller passages is

$$Re_i = \frac{d_{HYD_i} W_{AV}}{12 \nu^*}$$

$$U_2 = \frac{D_2 \pi N_o}{720} \left(\frac{N}{N_o}\right)$$

d_{HYD_i} is given by the design point calculation. The new friction factor becomes

$$f_1 = \frac{0.0462}{Re_i^{0.4}}$$

With this factor, the friction is to be calculated

$$\Delta q_{SF} = \xi_2 \frac{f_1 \Delta \ell_i}{d_{HYD1}} \frac{W_{AV}^2}{U_2^2 q}$$

$\Delta \ell_1$ is to be taken from the design point calculation.

The diffusion factor through the impeller is

$$\Delta = 1 - \frac{W_i}{W_2} + \frac{q (\cos \beta_1 + \cos \beta_2)}{2 \frac{W_i}{U_2} \left[\frac{Z_1}{\pi} (1 - \nu_2) + 2\nu_2\right]}$$

where $$\frac{W_i}{U_2} = \sqrt{\nu_2^2 + \nu_2^2 \cot^2 \beta_{io} M^2}$$

The diffusion loss is then

$$\Delta q_{DL} = \xi_3 \Delta^2 \left(\frac{W_i^2}{U_2^2 q}\right)$$

And the recirculation loss becomes

$$\Delta q_{RC} = \xi_4 \Delta \frac{q}{M_o \lambda_o}$$

The constants ξ_2, ξ_3, and ξ_4 are the same as in the design point program.

2. Cavitating Performance

The calculation of the cavitating impeller performance is similar to that for the previously described one, but since the density is not constant in the inlet, the inlet velocities are a function of the flow.

The head factor is

$$q = \mu (1 - \lambda_o M \tan \beta_2)$$

$$M = \frac{1}{1 + \xi_1 \frac{\pi \cos \beta_2}{2Z_1 (1 - \nu_2)} \left(1 + \frac{0.08}{\zeta_1}\right)}$$

$$\zeta_1 = \sqrt{\frac{M^2 \lambda_o^2 + (1 - q)^2}{\nu_2^2 + S_1^2 M^2 \phi_o^2}}$$

$$\phi_o = \frac{C_{1o}}{U_2}$$

$$U_2 = \frac{D_2 \pi N_o}{720} \left(\frac{N}{N_o}\right)$$

$$C_{1o} = C_i \left(\frac{N}{N_o}\right)$$

The inducer entering velocity C_i results from the design point calculation. Following the correlation of the mixture density given previously, the density change at the inlet to the cavitating inducer changes with speed and flow rate as

$$\frac{\gamma\left(\text{at } M_o, \frac{N}{N_o}\right)}{\gamma(\text{at design})} = S_1 = \left[\frac{1 + A\left(M_o^2 \frac{C_{1o}^2}{2g} - \text{NPSH}\right)}{1 + A\left(\frac{C_i^2}{2g} - \text{NPSH}\right)}\right]^K$$

where the design point corresponds to the value of 1 for the parameters M_o and $\frac{N}{N_o}$. When the inlet velocity head $\left(M_o^2 \frac{C_{1o}^2}{2g}\right)$ is smaller than the NPSH, no density changes take place. Then $S_1 = 1$.

The inducer incidence loss is similar to the previous case:

$$\Delta q_{inc} = \psi_2 \frac{\left(\frac{W_i}{U_2}\right)^2}{2q}$$

where $\psi_2 = a_1 + a_2 \Delta\beta_i + a_3 \Delta\beta_i^2$

$\Delta\beta_i = |\beta_i - \beta_{io}|$ (absolute value)

$$\cot \beta_i = \frac{S_1 M \phi_o}{\nu_2}$$

$$\left(\frac{W_i}{U_2}\right)^2 = \nu_2^2 + S_1^2 M^2 \phi_o^2$$

The loss constants can be assumed to be

$a_1 = 0$

$a_2 = 0$

$a_3 = 0.025$

There is, however, an additional loss with cavitating operation--the cavitation loss:

$$\Delta q_{CAV} = \psi_C \left[\left[1 + A \left(M_o^2 \frac{C_{o1}^2}{2g} - NPSH \right) \right]^K - 1 \right] (\nu_2^2 + S_1^2 M^2 \phi_o^2)$$

The value of ψ_c can be assumed to be between 0.5 and 1.0.

The impeller skin friction is

$$\Delta q_{SF} = \xi_2 \frac{f_1 \Delta \ell_1}{d_{HYD_1}} \frac{W_{AV}^2}{U_2^2 q}$$

where $$f_1 = \frac{0.0462}{Re_1^{0.2}}$$

$$Re_1 = \frac{d_{HYD_1} W_{AV}}{12 \nu^*}$$

$$W_{AV} = U_2 \sqrt{\frac{(1 + \zeta_1^2)(S_1^2 M^2 \phi_o^2 + \nu_2^2)}{2}}$$

The diffusion factor is

$$\Delta = 1 - \zeta_1 + \frac{q (\cos \beta_1 + \cos \beta_2)}{2 \frac{W_1}{U_2} \left[\frac{Z_1}{\pi} (1 - \nu_2) + 2\nu_2 \right]}$$

$$\frac{W_i}{U_2} = \sqrt{\nu_2^2 + S_1^2 M^2 \phi_o^2}$$

With these values, the diffusion loss is

$$\Delta q_{DL} = \xi_3 \Delta^2 \left(\frac{W_i^2}{U_2^2 q} \right)$$

and the recirculation loss will be

$$\Delta q_{RC} = \xi_4 \Delta \frac{q}{\lambda_o M_o}$$

ξ_1, ξ_2, ξ_3, and ξ_4 factors are the same as in the design point program.

Diffuser Performance at Part Load

At off-design operation, the diffuser vanes or scrolls suffer incidence loss on their tip:

$$\Delta q_{DIN} = \psi_3 \frac{(q - q_o)^2 + (\lambda_o - M_o\lambda_o)^2}{2q}$$

ψ_3 factor is also a function of the incidence angle. As the angle of attack is normally very small with the low flow angles encountered in pump design practice, this value can be assumed constant and equal to unity.

The diffusion loss can be calculated by assuming the same relative loss percentage of the available energy as was assumed at the design point.

$$\Delta q_D = \Delta q_{Do} \frac{M_o q_o}{q} \sqrt{\frac{(\lambda_o^2 M_o^2 + q^2)\, q_o}{(\lambda_o^2 + q_o^2)\, q}}$$

where Δq_{Do} is the diffuser loss at design point.

Pressure Ratio

The head and pressure can be calculated from the hydraulic losses.

The total head output is

$$H_{TH} = \frac{q\, U_2^2}{32.175} \quad (ft)$$

The hydraulic efficiency is

$$\eta_H = \frac{1 - \Delta q_{INC} - \Delta q_{CAV} - \Delta q_{DL} - \Delta q_{RC} - \Delta q_{DIN} - \Delta q_D}{1 + \Delta q_{SF}}$$

The head of the pump becomes

$$H_o = \eta_H H_{TH} \quad (ft)$$

and the pressure rise is

$$\Delta P_o = \frac{\gamma_o H_c}{144} \quad (psi)$$

Outside Losses and Overall Efficiency

The wheel friction changes with the flow and the Reynolds number:

$$\Delta q_{FR} = \frac{\xi_8}{1000\ \lambda_o M_o q B_2} \left(\frac{10^6}{Re_2}\right)^{0.2}$$

$$Re_2 = \frac{U_2\ D_2}{12\ \nu^*}$$

The leakage changes also

$$\Delta q_L = \frac{\xi_9 0.006\ \nu_2{}^2}{B_2} \sqrt{\frac{2q - \lambda_o{}^2 M_o{}^2 + q^2}{2q}}$$

ξ_8 and ξ_9 factors are similar to those of the design point.

The overall efficiency is calculated with these losses.

$$\eta = \frac{\eta_H}{1 + \Delta q_{FR} + \Delta q_L}$$

The power consumption of the wheel is then

$$HP = \frac{H_o\ M_o\ V_o\ \gamma_o}{\eta\ 550} \left(\frac{N}{N_o}\right)$$

The program prints out the losses, the efficiencies, the head, the pressure and the horsepower values. In addition, it prints out a diagram of the pressure rise and the efficiency versus relative flow with relative speed as a parameter.

COMPUTER PROGRAMS FOR PERFORMANCE CALCULATION (PROGRAMS A-0545 AND A-0546)

The following paragraphs present the computer program written for the method of performance calculation developed previously.

Program A-0545 calculates pump designs for all combinations of input values for N, β_2, μ, and λ. If desired, it will then calculate off-design points for different values of M_o and N/N_o. Automatic plotting of ΔP and η curves for pump off-design is also possible. Programs A-0546 and D-0100 are chained to A-0545 for this purpose.

Input for A-0545

If only the pump design point program is used, 11 cards of input are needed for each case. If the pump off-design program is used, 14 cards of input are needed for each case. Input for pump design point program:

1. Card No. 1 — FORMAT 72H

   Alphanumeric heading card
   "1" in column 1

2. Card No. 2 — FORMAT 5F10.5

   γ_o, lb/cu ft, Density

   V_o, cu ft/sec, Flow

   ΔP_o, psi, Pressure rise

   ν_{kt}, ft^2/sec, Kinematic viscosity

   Test = 0 if pump design point program

   = 1 if pump off-design point program

3. Card No. 3, Inlet — FORMAT I10, 7F10.5

   Case No. 1 = NPSH Given - noncavitating

   2 = β_i given

   3 = Best performance

   4 = Diameters and NPSH given - cavitating operation

   D_H, in. Hub diameter

   NPSH, ft Net positive suction head

   β_i, deg Inlet flow angle

	K_i	Hub-blockage	$K_i = 1 - \left(\frac{D_H}{D_i}\right)^2$
	D_i, in.	Inlet tip diameter	
	A, 1/ft K	Density function constants	

4. Card No. 4 — FORMAT F10.5

   E_i — Blockage factor

5. Card No. 5, N values — FORMAT I10, 7F10.5/ 8F10.5

   No. of N values (max 10 values)

   N_1 RPM

   N_2

   N_3

   etc.

6. Card No. 6, Impeller — FORMAT 4F10.5

   ξ_1

   ξ_2

   ξ_3 — Loss constants

   ξ_4

7. Card No. 7, β_2 values — FORMAT I10, 7F10.5/ 8F10.5

   No. of β_2 values

   $\beta_2(1)$

   $\beta_2(2)$ — Impeller tip vane angle

   $\beta_2(3)$

   etc.

8. Card No. 8, μ values — FORMAT I10, 7F10.5/ 8F10.5

No. of μ values

μ_1

μ_2

μ_3

etc.

Slip factor $= \frac{C_{u_2}}{C_{u_{2\infty}}}$

9. Card No. 9, λ values — FORMAT I10, 7F10.5/ 8F10.5

No. of λ values

λ_1

λ_2

λ_3

etc.

Flow factor $= \frac{C_{m_2}}{U_2}$

10. Card No. 10, Diffuser — FORMAT I10, 6F10.5

Case No.	1 = Vaned diffuser
	2 = Scroll diffuser
	3 = Collector ring
	4 = Vaneless diffuser
ξ_D	Throat side-to-width ratio
γ, deg	Wall angle
ξ_5	Boundary layer factor
ξ_6	Boundary layer factor
ξ_7	Loss coefficient
$\frac{D_3}{D_2}$	Vaneless space diameter ratio

11. Card No. 11, Outside Losses — FORMAT 2F10.5

	Wheel friction loss factor
	Leakage loss factor

Input for Pump off-design program:

Cards 1 thru 11 of previous section are needed in addition to the following

12. Card No. 12 — FORMAT 8F10.5

ξ_1	
a_1	
a_2, 1/Deg	Incidence loss coefficients
a_3, $1/Deg^2$	
ψ_c	Cavitation loss coefficient
ξ_2	
ξ_3	
ξ_4	

13. Card No. 13 — FORMAT 5F10.5

ψ_3	Diffuser incidence loss coefficient
ξ_8	
ξ_9	
ν_{pt} - ft^2/sec	Kinematic viscosity for part load
γ - lb/cu ft	Density for part load
NPSH, ft	Net positive suction head for part load

14. Card No. 14 FORMAT 6F10.5

M_o	Mass flow ratio
M_o	
$(M_o)_N$	
$(N/N_o)_o$	Speed ratio
$\Delta(N/N_o)$	
$(N/N_o)_n$	

Input for A-0546

If plotting of pump off-design points is desired, two blank cards plus the following cards should be inserted behind the data deck.

1. Card No. 1 FORMAT 3I10

   No. of problems to plot

   No. of N/N_o values for 1st problem

   No. of M_o values for 1st problem

2. Card No. 2 FORMAT 2I10

   No. of N/N_o values for 2nd problem

   No. of M_o values for 2nd problem

3. Repeat Card No. 2 for as many problems as are to be plotted.

Output

The output consists of three parts (a copy of a sample output is attached).

1. The input is printed out
2. For a particular N, β_2, μ and λ the following quantities are printed out:

   a. Inlet Case

N, RPM	Speed
D_i, inches	Inlet diameter
β_i, deg	Inlet flow angle
NPSH, ft	Net positive suction head

	W_i, FPS	Inlet relative velocity inducer
	ζ_o/ζ	Suction density ratio

b. Impeller Input

	β_2, Deg	Impeller tip vane angle
		Slip factor (= $Cu_2/Cu_{2\infty}$)
		Flow factor (= C_{m2}/u_2)

c. Impeller Answers

1	q	Head factor
	D_2, inch	Impeller tip diameter
	U_2, FPS	Impeller tip velocity
	ξ_1	Impeller relative velocity ratio
	Z_1	Number of vanes
2	B_2	Impeller width ratio (= b_2/D_2)
	R_{ei}	Impeller channel ave. Reynolds No.
	Δq_{SF}	Impeller friction loss
	Δq_{DL}	Diffusion loss
	Δq_{RC}	Recirculation loss
	η_{imp}	Impeller efficiency (Internal)

d. Diffuser Answers

If Case No. 1 - the following line is printed:

1.	Case No.	
	Re_{b_2}	Diffuser inlet Reynolds No.
	Re_2	Impeller tip Reynolds No.
	Z_2	Number of diffuser vanes
	Δq_{sc}	Scroll friction
	$\Delta q_{diff\ 2}$	Straight diffuser loss
	Δq_D	Total diffuser loss

If Case No. 2 - the following line is printed:

1. Case No.

$\Delta q_{2\text{-}3}$	first	diffuser loss
$\Delta q_{3\text{-}4}$	second	
$\Delta q_{4\text{-}5}$	third	
Δq_d	Total diffuser loss	

For both Cases 1 and 2, the following 2nd line is printed:

2. η_{hyd} Hydraulic efficiency

H_{TOT}, ft Total head

Δq_{FR} Wheel friction

Δq_L Leakage

η Overall efficiency

3. If pump off-design program is calculated for a constant N/No, the following is printed for each value of Mo:

a. Mo Mass flow ratio

q Head factor

$\Delta\beta_1$, deg Incidence angle

η_H Hydraulic efficiency

ΔP, psi Pressure rise

η Overall efficiency

b. N/No is then varied and line A is repeated for all values of Mo. This is continued until N/No equals final value of N/No.

4. Items 2 and 3 are repeated for all values of N, β_2, μ and λ.

Application of the IBM Programs to Performance Calculation

1. Generalized Performance of Centrifugal Pumps

In order to compare the calculation results with statistical average and predicted optimum performances, a number of data were gathered on high-Reynolds-number pump performances and plotted in Figure 42. For comparative purpose, three points were calculated by the present computer program using water as fluid, assuming no cavitation and a Reynolds number close to 10^7. The specific speeds of the calculated samples were 500 to 1000 and 2000. The results of the calculations were also plotted in the diagram. The points fit the top efficiency curve quite well; the program therefore might be used to predict the performance of advanced pump designs with confidence.

2. Performance Characteristics of the LH_2 Pump

The performance calculation procedure developed previously has been applied to establish the characteristic curves of the pump designed and built in this program. Figures 38 and 39 present the characteristics over a wide range of speed and flow.

Execution Instructions

Program A-0545 consists of three chains. Chains 2 and 3 are Programs A-0546 and D-0100 and are used only for plotting.

Tape 22 is always required by Program A-0545. If plotting is called for, tape 22 will be the plotter tape. When plotting is done, tapes 21 and 11 are used as work tapes.

Each of the programs just mentioned takes approximately 1-1/2 min per case with 150 solutions.

Following this page are given:

1. Flow chart of program
2. Fortran listing of program
3. Sample input data listing
4. Sample output listing
5. Sample plots

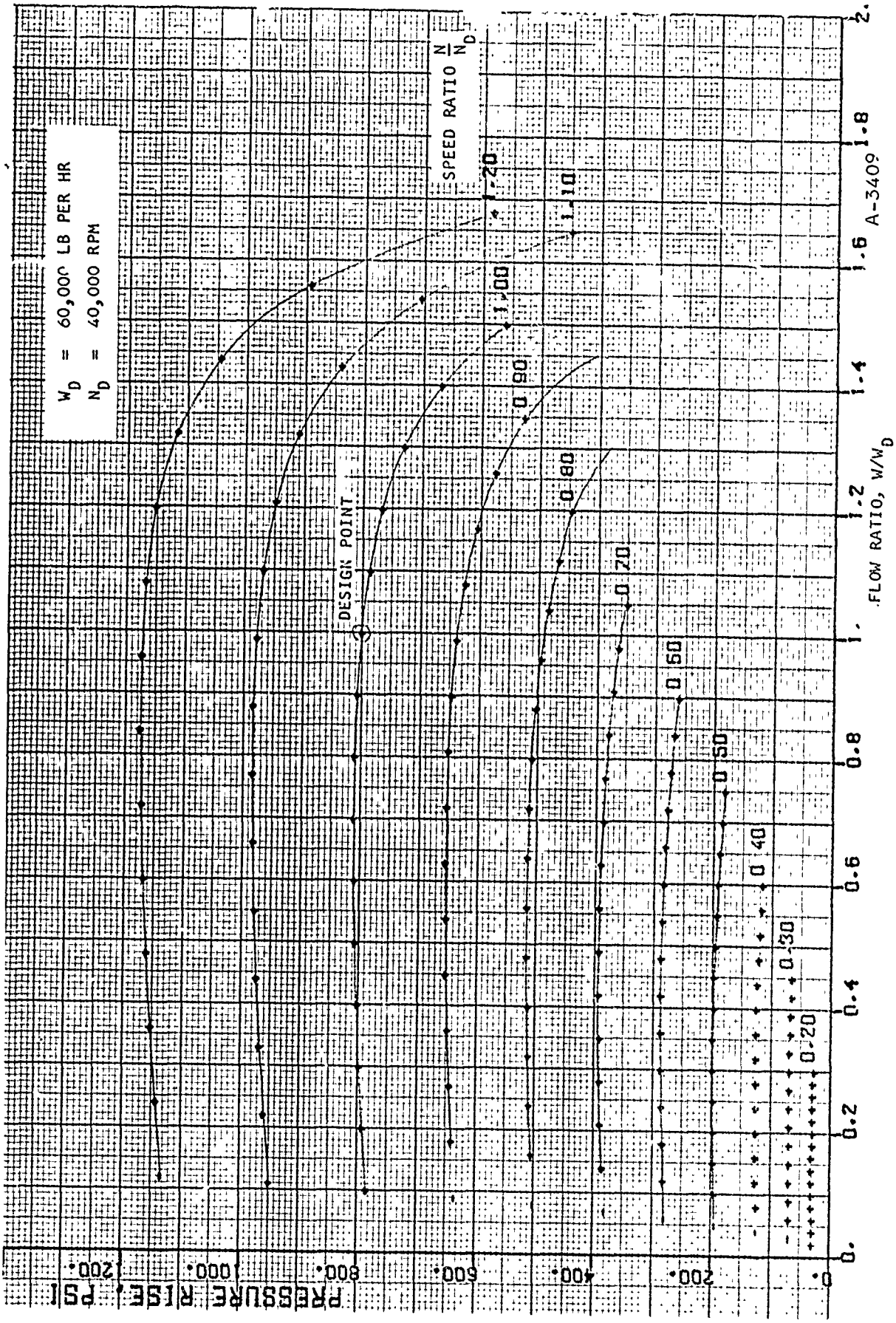

Figure 38. Pressure Rise vs Mass Flow Ratio, Single-Stage LH_2 Pump (60,000 lb/hr)

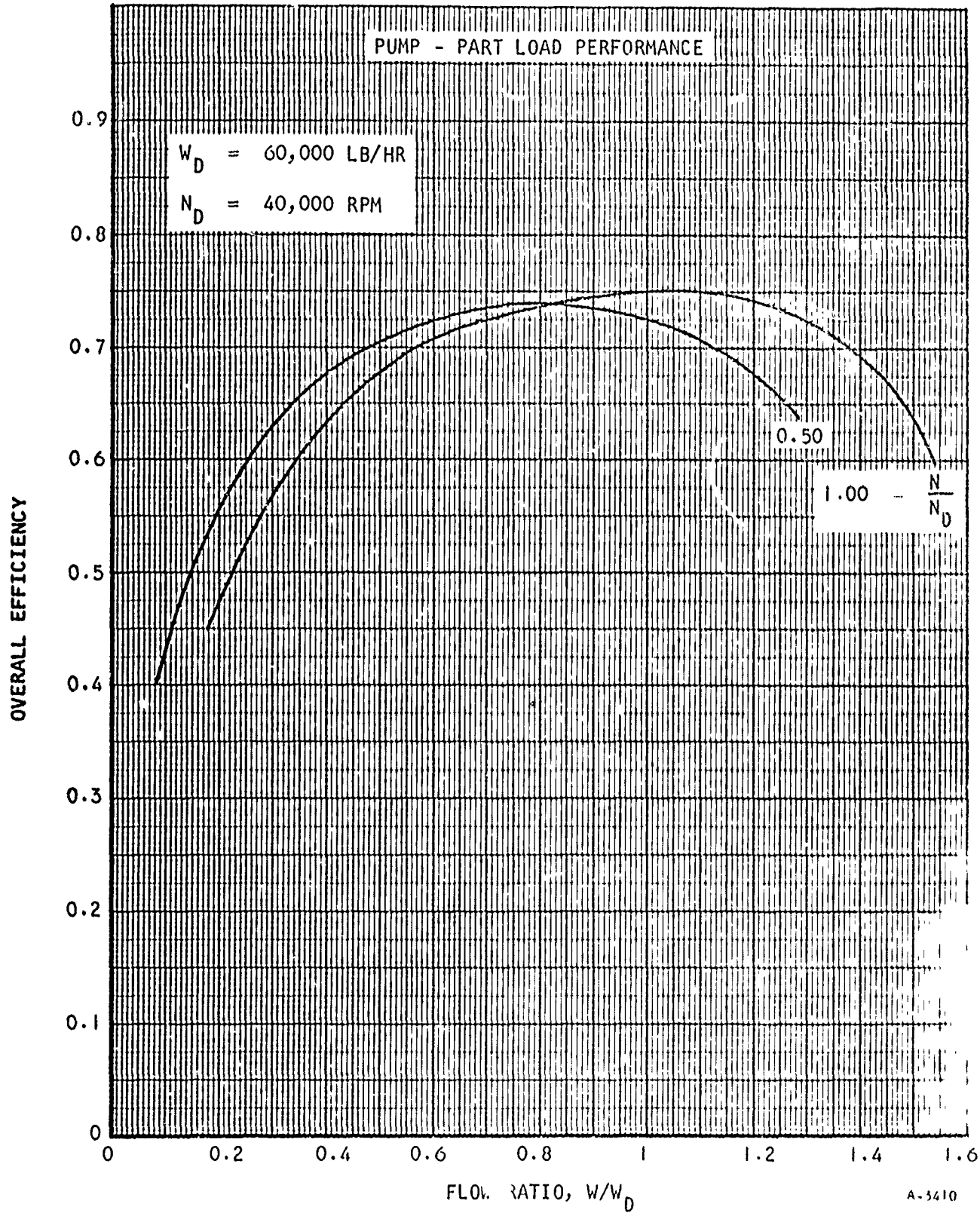

Figure 39. Overall Efficiency vs Mass Flow Ratio, Single-Stage LH_2 Pump (60,000 lb/hr)

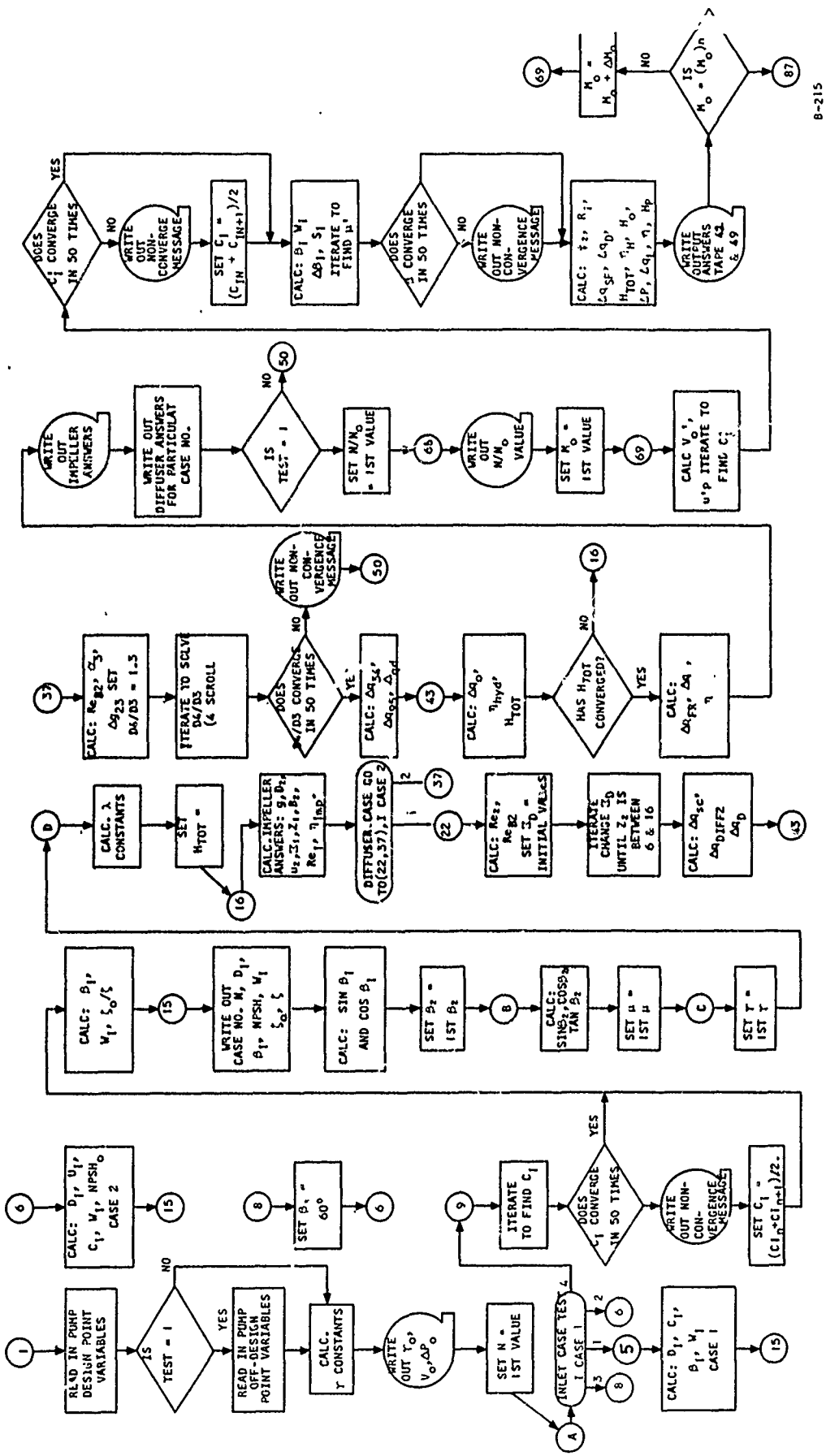

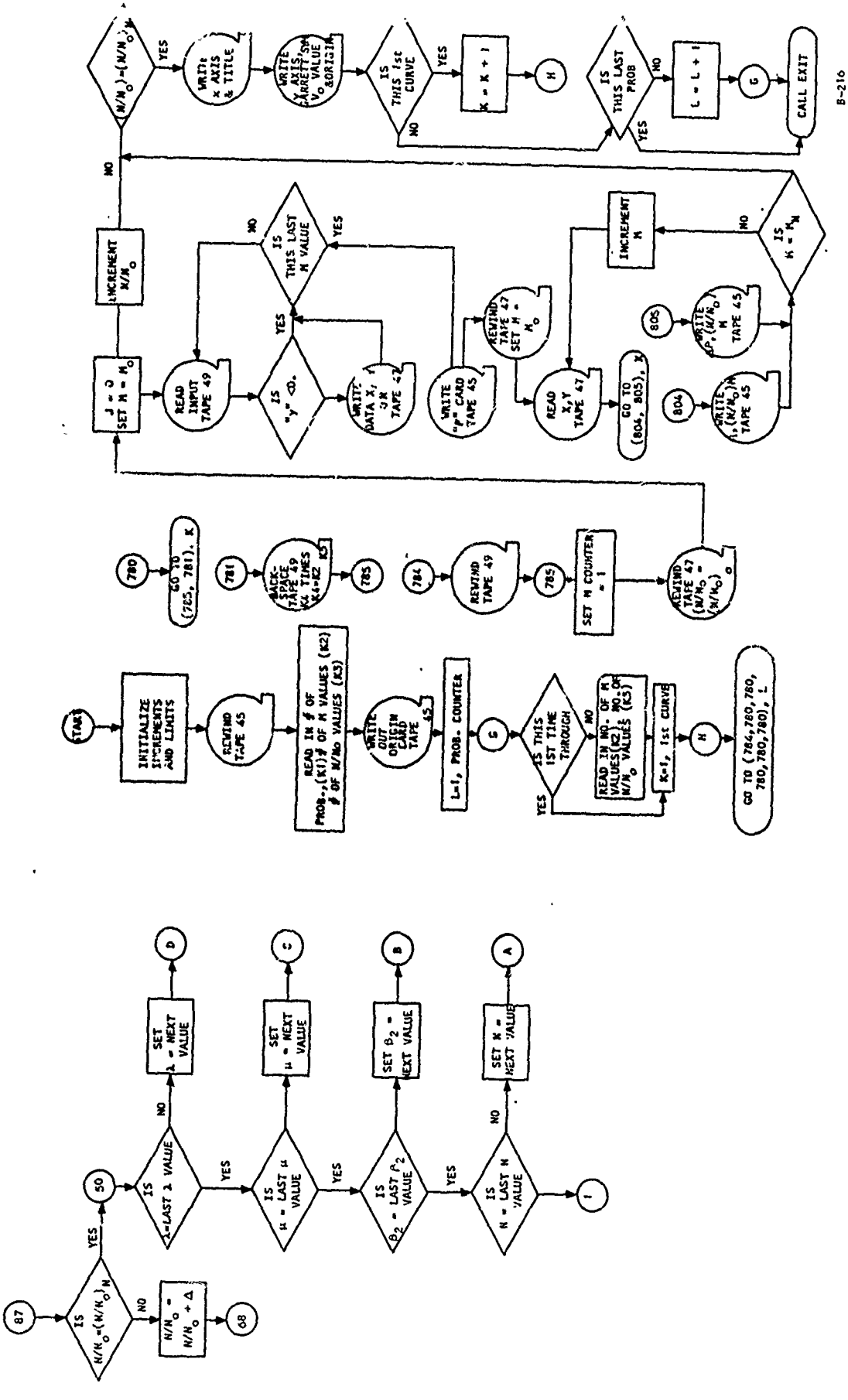

```
*     JOB      A0546      PUMP DESIGN PLOT PROGRAM WITH GARLIC CHAIN
  125 FORMAT(5F14.7)
  126 FORMAT(18HP210.0     10.0     ,I2,1H+,4X,1H1,4X,F4.2,6X,4F10.1)
  127 FORMAT(10X,2F10.7)
  128 FORMAT(2H0 ,2F7.1)
  129 FORMAT(13HX 0.0       .0,20X,18H           MO(N/NO))
  130 FORMAT(5CHAC5.        9.0    .12  PUMP - PART LOAD PERFORMANCE/)
  131 FORMAT(13HY 0.0      0.0,20X,18HOVERALL EFFICIENCY)
  132 FORMAT(13HY 0.0      0.0,20X,18HPRESSURE RISE, PSI)
  133 FORMAT(12HG 2.0     9.5)
  134 FORMAT(39HA01.5       8.6    .12  FLOW, CUFT/SEC = F7.3/)
  136 FORMAT(1HE)
  137 FORMAT(10X,F10.7,F10.4)
  138 FORMAT(3I10)
      DIMENSION ANS1(2),YOR(2),DELTY(2)
      XOR=0.0
      DELTX=2.0
      YOR(1)=0.0
      YOR(2)=0.0
      DELTY(1)=1.0
      DELTY(2)=4000.
      XORIGN=0.0
      YORIGN=0.0
      REWIND 45
      READ INPUT TAPE 41,138,K1,K2,K3
      WRITE OUTPUT TAPE 45,128,XORIGN,YORIGN
      DO 816 L=1,K1
      IF(L-1)779,779,778
  778 READ INPUT TAPE 41,138,K2,K3
  779 DO 815 K=1,2
      GO TO (784,780,780,780,780,780),L
  780 GO TO (785,781),K
  781 K4=K2*K3
      DO 782 I=1,K4
  782 BACKSPACE 49
      GO TO 785
  784 REWIND 49
  785 DO 806 I=1,K2
      REWIND 47
      J=0
      DO 803 I=1,K3
      READ INPUT TAPE 48,125,VO,ANS1(2),ANS1(1),ANS,ANNO
      IF(ANS1(K))803,802,802
  802 J=J+1
      WRITE OUTPUT TAPE 47,125,ANS,ANS1(K)
  803 CONTINUE
      WRITE OUTPUT TAPE 45,126,J,ANNO,XOR,DELTX,YOR(K),DELTY(K)
      REWIND 47
      DO 806 I=1,J
      READ INPUT TAPE 47,125,ANS,ANS1(K)
      GO TO (804,805),K
  804 WRITE OUTPUT TAPE 45,127,ANS,ANS1(K)
      GO TO 806
  805 WRITE OUTPUT TAPE 45,137,ANS,ANS1(K)
  806 CONTINUE
      WRITE OUTPUT TAPE 45,129
      WRITE OUTPUT TAPE 45,130
      GO TO (808,809),K
```

```
808 WRITE OUTPUT TAPE 45,131
    GO TO 810
809 WRITE OUTPUT TAPE 45,132,
810 WRITE OUTPUT TAPE 45,133,
    WRITE OUTPUT TAPE 45,134,V0
    XORIGN=18.
815 WRITE OUTPUT TAPE 45,128,XORIGN,YORIGN
816 CONTINUE
    WRITE OUTPUT TAPE 45,136
    ENDFILE 45                                                    A0546
    REWIND 45                                                     A0546
    REWIND 48
    CALL CHAIN(03,46)                                             A0546
    END
```

```
*      JOB       A0545      KEMPF/MX 032564 PUMP PART LOAD PERFORMANCE
*E     COMP      A0545
C      GENERAL PUMP EFFICIENCY
       DIMENSION ALAMDA(10),AMUI(10),BETA2I(10),ANI(10)
  100  FORMAT (I10,7F10.5/(8F10.5))
  101  FORMAT (8F10.5)
  102  FORMAT(I8,6F10.3,10X,35HINLET CASE NO.,N,DI,BI,NPSH,WI,ZETA)
  103  FORMAT (57H0  4 SCROLL OERLIKON, D4/D3, DOES NOT CONVERGE, D4/D3-1
     1 =F8.1,11H, D4/D3-2 =F8.1,12H, ALPHA-3 = F8.5)
  104  FORMAT (36H0   CASE 4 CI DOES NOT CONVERGE CI1=F10.5,6H, CI2=F10.5
     1)
  105  FORMAT (22H0   INPUT-   DENSITY =F7.3,8H, FLOW =F7.3,15H, PRESS. R
     1ISE =F6.1,15H, KINEM.VISC. =F9.6)
  107  FORMAT(40H0  IMPELLER Z1 IS GREATER THAN 100, Z1 =F10.5,6H, Q = F1
     10.5,7H, D2 = F10.5,9H, ZETA1 =F10.5)
  108  FORMAT (F8.1,2F10.3,40X,27HIMPELLER- BETA-2, MU, LAMDA/F8.2,F10.2,
     1F10.1,F10.4,F10.1,20X,20HQ, D2, U2, ZETA1, Z1/F8.5,F10.1,4F10.5,10
     2X34HB2, REI, DQSF, DQDL, DQRC, ETA-IMP)
  109  FORMAT (47H0  DIFFUSER Z2 NOT BETWEEN 6 AND 16, ZETA D1 = F8.3,12H
     1, ZETA D2 = F8.3,7H, Z2 = F8.2)
  110  FORMAT(2F10.5,13H  D4D3, D4D3N)
  114  FORMAT(34H0  HTOT DOES NOT CONVERGE, HTOT = F10.3, 11H,  HTOT2 = F
     110.5)
  115  FORMAT(I8,2F10.0,F10.2,3F10.5, 7X45HDIFFUSER CASE NO.,REB2,RE2,Z2,
     1DQSC,DQDIF2,DQD)
  116  FORMAT(I8,4F10.5,30X,40HDIFFUSER CASE NO., DQ23, DQ34, DQ45, DQD)
  117  FORMAT (8X,F10.5,F10.3,3F10.5,20X,29HETA-HYD, HTOT, DQRE, DQL, ETA
     1)
  118  FORMAT (72H
     !                  )
  119  FORMAT(29H0  Q DOES NOT CONVERGE, Q1 = F10.5,7H, Q2 = F10.5,7H, MU
     1 = F10.5)
  120  FORMAT(5F14.7)
  121  FORMAT(F8.2,2F10.4,F10.5,F10.2,10X26H  MO, Q, DELTA-P, ETAH, HO/8X
     1,F10.3,F10.5,F10.1,30X,16HDELTA-P, ETA, HP)
  122  FORMAT (6X,7HN/NO = F8.3)
  123  FORMAT(24H1  PART LOAD PERFORMANCE/)
  124  FORMAT (36HOPART LOAD CIP DOES NOT CONVERG CI1=F10.5,6H, CI2=F10.5
     1)
C      INLET
       REWIND 48
     1 READ INPUT TAPE 41,118
       WRITE OUTPUT TAPE 42,118
C      TEST = 0 IF PUMP DESIGN POINT PERF,  = 1 . IF PUMP OFF DESIGN PERF
       READ INPUT TAPE 41,101,      GAMO,VO,DPO,VSTAR,TEST
       IF(GAMO+VO+DPO)201,200,201                                    A0545
  200  ENDFILE 48
       REWIND 48
       CALL CHAIN(02,46)                                             A0545
  201  READ INPUT TAPE 41,100,ICASE,DH,   ANPSH,BI,AKI,DI,A,AK,EI
       READ INPUT TAPE 41,100,N1,(ANI(I),I=1,N1)
       READ INPUT TAPE 41,101,          X1,X2,X3,X4
       READ INPUT TAPE 41,100,N2,(BETA2I(I),I=1,N2)
       READ INPUT TAPE 41,100,N3,(AMUI(I),I=1,N3)
       READ INPUT TAPE 41,100,N,(ALAMDA(I),I=1,N)
       READ INPUT TAPE 41,100,ICASE2,ZETAD,GAMMA,X5,X6,X7,D3D2
       READ INPUT TAPE 41,101,X8,X9
       IF (TEST)3,3,2
```

```
    2 READ INPUT TAPE 41,101,X1PL,A1,A2,A3,PSIC,X2PL,X3PL,X4PL,PSI3,X8PL
     1,X9PL,VSTAPL,GAMP,ANPSP                                          A0549
      READ INPUT TAPE 41,101,AM00,DELTM,AMN,ANN00,DELTAN,ANNON
    3 GAMR=GAMMA*.01745329
      TGAM=SINF(GAMR)/COSF(GAMR)
      CONS4=2./TGAM+.5
    4 WRITE OUTPUT TAPE 42,105,GAM0,V0,DP0,VSTAR
      DO 50 K1=1,N1
      AN=ANI(K1)
      GO TO (5,6,8,9),ICASE
    5 CONS1=(32.175*ANPSH)**.5
      DI=(576.*V0/(3.1415927*CONS1)+DH*DH)**.5
      BI=ATANF(3.1415927*DI*AN/(720.*CONS1))
      WI=(32.175*ANPSH+(AN*3.1415927*DI/720.)**2)**.5
      BI =BI*57.29578
      GO TO 15
    6 BIR=BI*.01745329
      CBI=COSF(BIR)
      CTBI=CBI/SINF(BIR)
    7 DI=(44354.36*V0/(CTBI*AN*AKI))**.33333
      UI=3.1415927*AN*DI/720.
      CI=UI*CTBI
      WI=UI/SINF(BIR)
      ANPSH =CI*CI/64.35
      GO TO 15
    8 BI=60.
      GO TO 6
    9 AKI=1.-(DH/DI)*DH/DI
      UI=DI*AN*3.1415927/720.
      CONS1=144.*V0/(EI*DI*DI*AKI*.7853982)
      J=1
      CI1 = CONS1
      IF(CONS1*CONS1/64.35-ANPSH)14,14,10
   10 CI2=CONS1*(1.+A*(CI1*CI1/64.35-ANPSH))**AK
      IF(ABSF(CI1/CI2-1.)-.0001)14,14,11
   11 J=J+1
      IF(J-50)12,12,13
   12 CI1=CI2
      GO TO 10
   13 WRITE OUTPUT TAPE 42,104,CI1,CI2
      CI1=(CI1+CI2)/2.
   14 BI=ATANF(UI/CI1)
      WI=UI/SINF(BI)
      ZETA=(1.+A*(CI1*CI1/64.35-ANPSH))**AK
      BI =BI*57.29578
   15 WRITE OUTPUT TAPE 42,102,ICASE,AN,DI,BI,ANPSH,WI,ZETA
C     IMPELLER CALCULATIONS
      BIR=BI*.01745329
      CBI=COSF(BIR)
      TBI=SINF(BIR)/CBI
      DO 50 K2=1,N2
      BETA2=BETA2I(K2)
      BT2=BETA2*.01745329
      SB2=SINF(BT2)
      CB2=COSF(BT2)
      TB2=SB2/CB2
      DO 50 K3=1,N3
```

```
      AMU=AMUI(K3)
      CONS16=X1*1.5707963*AMU*CB2/(1.-AMU)
      DO 50 I=1,N
      CONS8=ALAMDA(I)*ALAMDA(I)
      Q=AMU*(1.-ALAMDA(I)*TB2)
      CONS3=(CONS8+Q*Q)/(2.*Q)
      CONS5=(CONS8+Q*Q)**.5
      CONS6=ALAMDA(I)/CONS5
      CONS17=(CONS8+(1.-Q)**2)**.5
      CONS18=1.-CONS3
      J2=1
      HO=144.*DPO/GAMO
      ETAHYD=.9
      HTOT=HO/ETAHYD
   16 U2=(32.175*HTOT/Q)**.5
      D2=720.*U2/(3.1415927*AN)
      W2=U2*CONS17
      V2=DI/D2
      ZETA1=W2/WI
      Z1=CONS16*(1.+.08/ZETA1)/(1.-V2)
      IF(Z1-100.)21,21,20
   20 WRITE OUTPUT TAPE 42,107,Z1,Q,D2    ,ZETA1
      GO TO 50
   21 DEL1=.8*(D2-DH)/(CBI+CB2)
      B2 =144.*VO/(.9*ALAMDA(I)*U2*(D2*D2*3.14159-D2*.03*Z1/CB2))
      DHYD1=D2*(1./(Z1/(3.1415927*B2)+1./CB2)+V2/(2./(1.-V2)+(2.*Z1/(3.1
     1415927*(1.+V2)))*(1.+TBI*TBI*(1.+V2*V2)/2.)**.5))
      WAVE=((WI*WI+W2*W2)*.5)**.5
      REI=DHYD1*WAVE/(12.*VSTAR)
      F1=.0462/REI**.2
      DQSF=X2*DEL1*WAVE*WAVE*F1/(DHYD1*U2*U2*Q)
      DELTA=1.-ZETA1+Q*(CBI+CB2)/(2.*WI*(Z1*(1.-V2)/3.1415927 +2.*V2)/U2
     1)
      DQDL=X3*(DELTA*WI/U2)**2/Q
      DQRC=X4*DELTA*Q/ALAMDA(I)
      ETAIMP=(CONS18-DQDL)/(CONS18+DQSF+DQRC)
C     DIFFUSER
      GO TO(22,37),ICASE2
C     VANED DIFFUSER W/CONICAL SIDEWALLS
   22 RE2=D2*U2/(12.*VSTAR)
      REB2=2.*B2*RE2*CONS5
      F2=.0462/REB2**.2
      DEL=.1
      J1=0
      J=1
      ZETAD1=ZETAD
   23 CONS7=ZETAD1*TGAM
      RRO=1.04+.69333*ZETAD1*B2*(3.+2.*CONS7)/(2.+CONS7)
      FH=CONS6              +F2*(ZETAD1*(2.+TGAM)+.5*LOGF((ZETAD1*CB2+.02)/
     1.02)-CONS4*LOGF((B2*(ZETAD1*TGAM+2.)+.02*TGAM)/(2.* B2+.02*TGAM)))
      CM2CU=RRO*FH*CONS5/Q
      Z2=6.2831853*CM2CU/(ZETAD1* B2*(2.+CONS7))
      J1=J1+1
      IF(J1-50)24,24,34
   24 IF(Z2-6.0)26,36,25
   25 IF(Z2-16.0)36,36,29
   26 GO TO (28,28,27),J
```

```
 27 DEL = DEL*0.1
 28 J = 2
    ZETAD1 = ZETAD1 - DEL
    GO TO 23
 29 GO TO (31,30,31),J
 30 DEL = DEL*0.1
 31 J = 3
    ZETAD1 = ZETAD1 + DEL
    GO TO 23
 34 WRITE OUTPUT TAPE 42,109,ZETAD,ZETAD1,Z2
    GO TO 50
 36 DEL2=D2*(.02/CONS6           +(1.04*(3.1415927/Z2)**2+ B2* B2/4.)**
   1.5)
    DH2=D2* 4.* B2*ZETAD1*(2.+CONS7)       /(2.+2.*ZETAD1+CONS7)
    DQSC=CONS3*F2*DEL2*(1.+(ALAMDA(I)/(Q*CM2CU))**2)/(.5*DH2)
    DQDIF2=CONS3*(ALAMDA(I)/(Q*CM2CU))**2*(X5+X6*F2*DEL2/DH2)
    DQD=DQSC+DQDIF2
    GO TO 43
 37 DELTAC=F2*.32/ B2
    REB2=2.*B2*CONS5*RE2
    RE2=D2*U2/(12.*VSTAR)
    ALPHA2=ATANF(ALAMDA(I)/Q)
    CALP2=COSF(ALPHA2)
    SALP2=SINF(ALPHA2)
    CONS9=(1.+CALP2)**2*EXPF(DELTAC)
    CALP3=(CONS9-SALP2*SALP2)/(CONS9+SALP2*SALP2)
    ALPHA3=ASINF((1.-CALP3*CALP3)**.5)
    DQ23=DELTAC*(1.+CALP2*CALP2/(1.0816*CALP3*CALP3))*CONS3/(2.*COSF((
   1ALPHA2+ALPHA3)/2.))
    F2=.0462/REB2**.2
    D3=1.04*D2
    SB2= B2*D2
    CONS11=-1.+2.*SB2/D3
    CONS12=(SB2*CALP3/D3)**2
    CONS13=3.1415927*F2/8.
    CONS14=SINF(ALPHA3)*SINF(ALPHA3)
    D4D3=1.3
    J3=1
 38 CONS15=CONS13*(1.+D4D3)/(D4D3+CONS11)
    D4D3N=(CONS12/((CONS14/(D4D3*D4D3)-CONS15)/(1.+CONS15)))**.25+1.
    IF (ABSF(D4D3/D4D3N-1.)-.001)42,42,39
 39 J3=J3+1
    IF(J3-50)40,40,41
 40 D4D3=D4D3N
401 IF(D4D3-1.)400,38,38
400 D4D3=D4D3+.1
    GO TO 401
 41 WRITE OUTPUT TAPE 42,103,D4D3,D4D3N,ALPHA3
    GO TO 50
 42 DQ34=1.5707963*CONS3*F2*(D2*CALP2/(D3*CALP3))**2*((1.+D4D3)/(D4D3+
   1CONS11))*(1.+(B2*CALP3/(D3*(D4D3-1.)*(D4D3-1.)))**2)
    DQ45=CONS3*(D2*CALP2*SB2*CALP3/(D3*CALP3*D3*(D4D3-1.)*(D4D3-1.)))*
   1*2*(X6+X7*(D4D3+1.)/(RE2**.2*(D4D3-1.)))
    DQD=DQ23+DQ34+DQ45
    GO TO 43
 43 ETHYD2=(1.-DQOL-DOD)/(1.+DQSF+DQRC)
    HTOT2=HO/ETHYD2
```

```
      IF(ABSF(HTOT2/HTOT-1.)-.02)47,47,44
   44 J2=J2+1
      IF(J2-50)45,45,46
   45 HTOT=HTOT2
      GO TO 16
   46 WRITE OUTPUT TAPE 42,114,HTOT,HTOT2
      GO TO 50
   47 DQFR=X8*(1.0E6/RE2)**.2/(1.E3*ALAMDA(I)*Q* B2)
      DQL=X9*.006*V2*V2*(1.-CONS3)**.5/ .2
      ETA=ETHYD2/(1.+DQFR+DQL)
      WRITE OUTPUT TAPE 42,108,BETA2,AMU,ALAMDA(I),
     1                                    Q,D2,U2,ZETA1,Z1,B2,REI,DQSF,DQ
     1DL,DQRC,ETAIMP
      GO TO (48,49),ICASE2
   48 WRITE OUTPUT TAPE 42,115,ICASE2,REB2,RE2,Z2,DQSC,DQDIF2,DQD
      GO TO 491
   49 WRITE OUTPUT TAPE 42,116,ICASE2,DQ23,DQ34,DQ45,DQD
  491 WRITE OUTPUT TAPE 42,117,ETHYD2,HTOT2,DQFR,DQL,ETA
      IF(TEST)50,50,492
  492 WRITE OUTPUT TAPE 42,123
      ANNO=ANNOO
   68 WRITE OUTPUT TAPE 42,122,ANNO
      AMO=AMOO
   69 ANPL=ANNO*AN
      AM=AMO+DQL
      VOP=VO*AMO*ANNO
      UIP=UI*ANNO
      CONS1=144.*VOP/(EI*DI*DI*AKI*.7853982)
      J=1
      CI1P = CONS1
      IF(CONS1*CONS1/64.35-ANPSP)710,710,700                              A0545
  700 CI2P=CONS1*(1.+A*(CI1P*CI1P/64.35-ANPSP))**AK                       A0545
      IF(ABSF(CI1P/CI2P-1.)-.0001)710,710,701
  701 J=J+1
      IF(J-50)702,702,703
  702 CI1P=CI2P
      GO TO 700
  703 WRITE OUTPUT TAPE 42,124,CI1P,CI2P
      CI1P=(CI1P+CI2P)/2.
  710 BIPL=ATANF(UIP/CI1P)
      DELTBI = ABSF(BIPL*57.29578-BI)
      WIP=UIP/SINF(BIPL)
      CONS1=CI1*CI1/64.35-ANPSP                                           A0545
      CONS2=CI1P*CI1P/64.35-ANPSP                                         A0545
      IF(CONS1)704,704,705
  704 RI=1.0
      GO TO 706
  705 RI=(1.+A*CONS1)**AK
  706 IF(CONS2)707,707,708
  707 RIP=1.0
      GO TO 709
  708 RIP=(1.+A*CONS2)**AK
  709 U2P=U2*ANNO
   73 CONS1=(WIP/U2P)**2
      CONS2=AMO*AMO*ALAMDA*ALAMDA
      CONS3=X1PL*3.1415927*CB2/(2.*Z1*(1.-V2))
      CONS4=1.-ALAMDA*AMO*TB2
```

```
      AMUPL=AMU
      J=1
      QPL1=AMUPL*CONS4
   74 ZETA1=((CONS2+(1.-QPL1)**2)/CONS1)**.5
      AMU2=1./(1.+CONS3*(1.+.08/ZETA1))
      QPL2=AMU2*CONS4
      IF(ABSF(QPL1/QPL2-1.)-.05)78,78,75
   75 J=J+1
      IF(J-50)76,76,77
   76 QPL1=QPL2
      GO TO 74
   77 WRITE OUTPUT TAPE 42,119,QPL1,QPL2,AMU2
   78 PSI2=A1+A2*DELTBI+A3*DELTBI*DELTBI
      DQINC=PSI2*CONS1/(2.*QPL2)
      WAVEU2=.5*(CONS1+CONS2+(1.-QPL2)**2)
      IF(ICASE-4)80,81,80
   80 PSIC=0.0
      DQCAV=0.0
      GO TO 84
   81 DQCAV = PSIC*(RIP-1.)*CONS1/QPL2
   84 WAVE=WAVEU2**.5*U2P
      REI=DHYD1*WAVE/(12.*VSTAPL)
      F1=.0462/REI**.2
      DQSF=X2PL*F1*DEL1*WAVEU2    /(DHYD1*QPL2)
      WIU2=CONS1**.5
      CL=COSF(BIPL)
      DELT=1.-ZETA1+QPL2*(CL+CB2)/(2.*WIU2*(Z1*(1.-V2)/3.1415927+2.*V2))
      DQDL=X3PL*DELT*DELT*CONS1/QPL2
      AM=AMO
      DQRC=X4PL*DELT      /(ALAMDA*AM)
      DQDIN=PSI3*((QPL2-Q)**2+(ALAMDA-AM*ALAMDA)**2)/(2.*QPL2)
      DQDPL=DQD*AM*Q*((CONS2+QPL2*QPL2)*Q/((ALAMDA*ALAMDA+Q*Q)*QPL2))**.
     15/QPL2
      HTOT=QPL2*U2P*U2P/32.175
      ETAH=(1.-DQINC-DQCAV-DQDL      -DQDIN-DQDPL)/(1.+DQSF +DQRC)
      HO=ETAH*HTOT
      DELTP=GAMP*HO/144.
      RE2=U2P*D2/(12.*VSTAPL)
      DQFR=X8PL*(1.E6/RE2)**.2/(1.E3*ALAMDA*AMO*QPL2*B2)
      DQLPL=X9PL*.006*V2*V2*((2.*QPL2-CONS2+QPL2*QPL2)/(2.*QPL2))**.5/B2
      ETA=ETAH/(1.+DQFR+DQLPL)
      HP=HO*AMO*VO*GAMP*ANNO/(ETA*550.)
      ANS=AMO*ANNO
      WRITE OUTPUT TAPE 48,120,VO,DELTP,ETA,ANS,ANNO
      WRITE OUTPUT TAPE 42,121,AMO ,QPL2,DELTBI,ETAH,HO,DELTP,ETA,HP
      IF(AMO-AMN )86,87,87
   86 AMO=AMO+DELTM
      GO TO 69
   87 IF(ANNO-ANNON)88,89,89
   88 ANNO=ANNO+DELTAN
      GO TO 68
   89 CONTINUE
   50 CONTINUE
      GO TO 1
      END
```

SAMPLE INPUT LISTING

AM-275-MR
A-0545

```
1       G E   80,000 LB PER HR PUMP ART LOAD              8/5/63
4.421     5.03        1800.       .00002     1.
          40.0        10.         0.0        0.0        5.458      .02814     .4
.92
          140000.
1.0       1.0         .1          0.0
          10.0
          1.7
          1.1
          12.0        15.         .18        1.5
.285      1.0
1.0       0.0         0.0         .05        .5         1.0        .1         0.0
1.0       .285        1.0         .00002
.1        .1          1.5         .2         .1         1.2
1       G E  300,000 LB PER HR PUMP ART LOAD              8/5/63
4.421     18.85       1500.       .00002     1.
          40.0        10.         0.0        0.0        10.580     .02814     .4
.92
          120000.
1.0       1.0         .1          0.0
          10.0
          1.7
          1.1
          12.0        15.         .18        1.5
.285      1.0
1.0       0.0         0.0         .05        .5         1.0        .1         0.0
1.0       .285        1.0         .00002
.1        .1          1.5         .2         .1         1.2
1       150,000 LB/HR   LH2 PUMP - G.E.      8/1/63
4.421     9.425       1500.       .00002     1.0
          40.0        10.         0.0        0.0        7.480      .02814     .4
.92
          130000.
1.0       1.0         .1          0.0
          10.0
          1.7
          1.1
          12.0        15.         .18        1.5        0.0        0.0
.285      1.0
1.0       0.0         0.0         .05        .5         1.0        .1         0.0
1.0       .285        1.0         .00002
.1        .1          1.5         .2         .1         1.3
```

/A-0545

```
G E   80,000 LB PER HR PUMP ART LOAD                    8/5/63

                                                SAMPLE LISTING OF OUTPUT

 INPUT-   DENSITY =  4.421, FLOW =   5.030, PRESS. RISE =1800.0, KINEM.VISC. = 0.000020
     4 40000.000      5.458     87.721     10.000    953.355      1.127
                                                    INLET CASE NO.,N,DI,BI,NPSH,WI,ZETA
     0.0      0.700     0.100                        IMPELLER- BETA-2, MU, LAMDA
    0.70      10.25    1788.4     0.5932      8.9                Q, D2, U2, ZETA1, Z1
 0.01376   387913.9    0.06417   0.01947   0.00000   0.88171     B2, REI, DQSF, DQDL, DQRC, ETA-IMP
       1  1485482. 76357191.      15.15     0.02738   0.05499   0.08237
                                                    DIFFUSER CASE NO.,REB2,RE2,Z2,DQSC,DQDIF2,DQD
          0.84401 69465.444     0.01971   0.09922   0.75430
                                                        ETA-HYD, HTOT, DQRE, DQL, ETA
```

N/NO = 0.200					
0.10	0.6987	2.1013	0.84718	2353.63	MO, Q, DELTA-B, ETAH, HO
	72.260	0.29593	6.4		DELTA-P, ETA, HP
0.20	0.6987	1.9239	0.84742	2354.45	MO, Q, DELTA-B, ETAH, HO
	72.285	0.42304	9.0		DELTA-P, ETA, HP
0.30	0.6988	1.7463	0.84694	2353.36	MO, Q, DELTA-B, ETAH, HO
	72.251	0.49338	11.6		DELTA-P, ETA, HP
0.40	0.6989	1.5684	0.84574	2350.36	MO, Q, DELTA-B, ETAH, HO
	72.159	0.53756	14.1		DELTA-P, ETA, HP
0.50	0.6990	1.3902	0.84382	2345.43	MO, Q, DELTA-B, ETAH, HO
	72.008	0.56735	16.7		DELTA-P, ETA, HP
0.60	0.6992	1.2116	0.84116	2338.55	MO, Q, DELTA-B, ETAH, HO
	71.797	0.58825	19.3		DELTA-P, ETA, HP
0.70	0.6994	1.0324	0.83776	2329.68	MO, Q, DELTA-B, ETAH, HO
	71.524	0.60318	21.9		DELTA-P, ETA, HP
0.80	0.6996	0.8526	0.83361	2318.80	MO, Q, DELTA-B, ETAH, HO
	71.190	0.61379	24.4		DELTA-P, ETA, HP
0.90	0.6998	0.6722	0.82871	2305.88	MO, Q, DELTA-B, ETAH, HO
	70.794	0.62114	27.0		DELTA-P, ETA, HP
1.00	0.7000	0.4908	0.82304	2290.88	MO, Q, DELTA-B, ETAH, HO
	70.333	0.62589	29.6		DELTA-P, ETA, HP
1.10	0.7003	0.3086	0.81658	2273.74	MO, Q, DELTA-B, ETAH, HO
	69.807	0.62850	32.2		DELTA-P, ETA, HP
1.20	0.7005	0.1254	0.80934	2254.44	MO, Q, DELTA-B, ETAH, HO
	69.214	0.62928	34.8		DELTA-P, ETA, HP
1.30	0.7008	-0.0589	0.80128	2232.91	MO, Q, DELTA-B, ETAH, HO
	68.553	0.62846	37.4		DELTA-P, ETA, HP
1.40	0.7011	-0.2444	0.79241	2209.11	MO, Q, DELTA-B, ETAH, HO
	67.823	0.62620	39.9		DELTA-P, ETA, HP
1.50	0.7014	-0.4311	0.78269	2182.99	MO, Q, DELTA-B, ETAH, HO
	67.021	0.62261	42.5		DELTA-P, ETA, HP
N/NO = 0.300					
0.10	0.6987	2.1013	0.85248	5328.80	MO, Q, DELTA-B, ETAH, HO
	163.602	0.31239	20.7		DELTA-P, ETA, HP
0.20	0.6987	1.9237	0.85273	5330.69	MO, Q, DELTA-B, ETAH, HO
	163.660	0.44040	29.4		DELTA-P, ETA, HP
0.30	0.6988	1.7458	0.85226	5328.33	MO, Q, DELTA-B, ETAH, HO
	163.587	0.50973	38.0		DELTA-P, ETA, HP
0.40	0.6989	1.5672	0.85108	5321.70	MO, Q, DELTA-B, ETAH, HO
	163.384	0.55270	46.7		DELTA-P, ETA, HP
0.50	0.6990	1.3879	0.84918	5310.75	MO, Q, DELTA-B, ETAH, HO
	163.047	0.58142	55.4		DELTA-P, ETA, HP
0.60	0.6992	1.2075	0.84655	5295.42	MO, Q, DELTA-B, ETAH, HO
	162.577	0.60140	64.1		DELTA-P, ETA, HP
0.70	0.6994	1.0258	0.84317	5275.65	MO, Q, DELTA-B, ETAH, HO
	161.970	0.61554	72.8		DELTA-P, ETA, HP
0.80	0.6996	0.8428	0.83904	5251.29	MO, Q, DELTA-B, ETAH, HO
	161.222	0.62549	81.5		DELTA-P, ETA, HP
0.90	0.6998	0.6580	0.83414	5222.25	MO, Q, DELTA-B, ETAH, HO
	160.330	0.63225	90.2		DELTA-P, ETA, HP
1.00	0.7000	0.4714	0.82845	5188.37	MO, Q, DELTA-B, ETAH, HO
	159.290	0.63648	98.9		DELTA-P, ETA, HP
1.10	0.7003	0.2826	0.82194	5149.50	MO, Q, DELTA-B, ETAH, HO
	158.097	0.63860	107.6		DELTA-P, ETA, HP
1.20	0.7005	0.0915	0.81459	5105.44	MO, Q, DELTA-B, ETAH, HO
	156.744	0.63890	116.3		DELTA-P, ETA, HP
1.30	0.7008	-0.1026	0.80638	5055.98	MO, Q, DELTA-B, ETAH, HO

	155.226	0.63759	125.0		DELTA-P, ETA, HP
1.40	0.7011	-0.2994	0.79725	5000.88	MO, Q, DELTA-B, ETAH, HO
	153.534	0.63481	133.8		DELTA-P, ETA, HP
1.50	0.7014	-0.4995	0.78718	4939.88	MO, Q, DELTA-B, ETAH, HO
	151.661	0.63064	142.5		DELTA-P, ETA, HP
N/NO =	0.400				
0.10	0.6987	2.1013	0.85602	9512.82	MO, Q, DELTA-B, ETAH, HO
	292.057	0.32422	47.5		DELTA-P, ETA, HP
0.20	0.6987	1.9235	0.85628	9516.28	MO, Q, DELTA-B, ETAH, HO
	292.163	0.45260	68.0		DELTA-P, ETA, HP
0.30	0.6988	1.7451	0.85584	9512.28	MO, Q, DELTA-B, ETAH, HO
	292.040	0.52107	88.6		DELTA-P, ETA, HP
0.40	0.6989	1.5656	0.85468	9500.78	MO, Q, DELTA-B, ETAH, HO
	291.687	0.56314	109.1		DELTA-P, ETA, HP
0.50	0.6990	1.3845	0.85281	9481.73	MO, Q, DELTA-B, ETAH, HO
	291.102	0.59108	129.7		DELTA-P, ETA, HP
0.60	0.6992	1.2016	0.85022	9454.94	MO, Q, DELTA-B, ETAH, HO
	290.280	0.61041	150.3		DELTA-P, ETA, HP
0.70	0.6994	1.0165	0.84689	9420.23	MO, Q, DELTA-B, ETAH, HO
	289.214	0.62401	170.9		DELTA-P, ETA, HP
0.80	0.6996	0.8288	0.84279	9377.31	MO, Q, DELTA-B, ETAH, HO
	287.896	0.63351	191.5		DELTA-P, ETA, HP
0.90	0.6998	0.6379	0.83790	9325.84	MO, Q, DELTA-B, ETAH, HO
	286.316	0.63987	212.1		DELTA-P, ETA, HP
1.00	0.7000	0.4433	0.83219	9265.43	MO, Q, DELTA-B, ETAH, HO
	284.462	0.64373	232.8		DELTA-P, ETA, HP
1.10	0.7003	0.2447	0.82561	9195.55	MO, Q, DELTA-B, ETAH, HO
	282.316	0.64548	253.4		DELTA-P, ETA, HP
1.20	0.7005	0.0414	0.81812	9115.60	MO, Q, DELTA-B, ETAH, HO
	279.862	0.64540	274.1		DELTA-P, ETA, HP
1.30	0.7008	-0.1670	0.80965	9024.91	MO, Q, DELTA-B, ETAH, HO
	277.077	0.64364	294.8		DELTA-P, ETA, HP
1.40	0.7011	-0.3816	0.80014	8922.61	MO, Q, DELTA-B, ETAH, HO
	273.937	0.64032	315.5		DELTA-P, ETA, HP
1.50	0.7014	-0.6026	0.78949	8807.77	MO, Q, DELTA-B, ETAH, HO
	270.411	0.63549	336.2		DELTA-P, ETA, HP
N/NO =	0.500				
0.10	0.6987	2.1013	0.85866	14909.47	MO, Q, DELTA-B, ETAH, HO
	457.741	0.33347	90.4		DELTA-P, ETA, HP
0.20	0.6987	1.9233	0.85893	14915.07	MO, Q, DELTA-B, ETAH, HO
	457.913	0.46197	130.5		DELTA-P, ETA, HP
0.30	0.6988	1.7442	0.85850	14909.19	MO, Q, DELTA-B, ETAH, HO
	457.733	0.52971	170.7		DELTA-P, ETA, HP
0.40	0.6989	1.5633	0.85738	14891.86	MO, Q, DELTA-B, ETAH, HO
	457.201	0.57106	210.9		DELTA-P, ETA, HP
0.50	0.6990	1.3802	0.85556	14862.88	MO, Q, DELTA-B, ETAH, HO
	456.311	0.59839	251.1		DELTA-P, ETA, HP
0.60	0.6992	1.1941	0.85302	14821.99	MO, Q, DELTA-B, ETAH, HO
	455.056	0.61724	291.3		DELTA-P, ETA, HP
0.70	0.6994	1.0044	0.84974	14768.72	MO, Q, DELTA-B, ETAH, HO
	453.420	0.63045	331.5		DELTA-P, ETA, HP
0.80	0.6996	0.8102	0.84569	14702.51	MO, Q, DELTA-B, ETAH, HO
	451.388	0.63961	371.8		DELTA-P, ETA, HP
0.90	0.6998	0.6109	0.84083	14622.48	MO, Q, DELTA-B, ETAH, HO
	448.930	0.64568	412.0		DELTA-P, ETA, HP
1.00	0.7000	0.4057	0.83509	14527.61	MO, Q, DELTA-B, ETAH, HO
	446.018	0.64924	452.4		DELTA-P, ETA, HP
1.10	0.7003	0.1933	0.82841	14416.61	MO, Q, DELTA-B, ETAH, HO
	442.610	0.65068	492.7		DELTA-P, ETA, HP

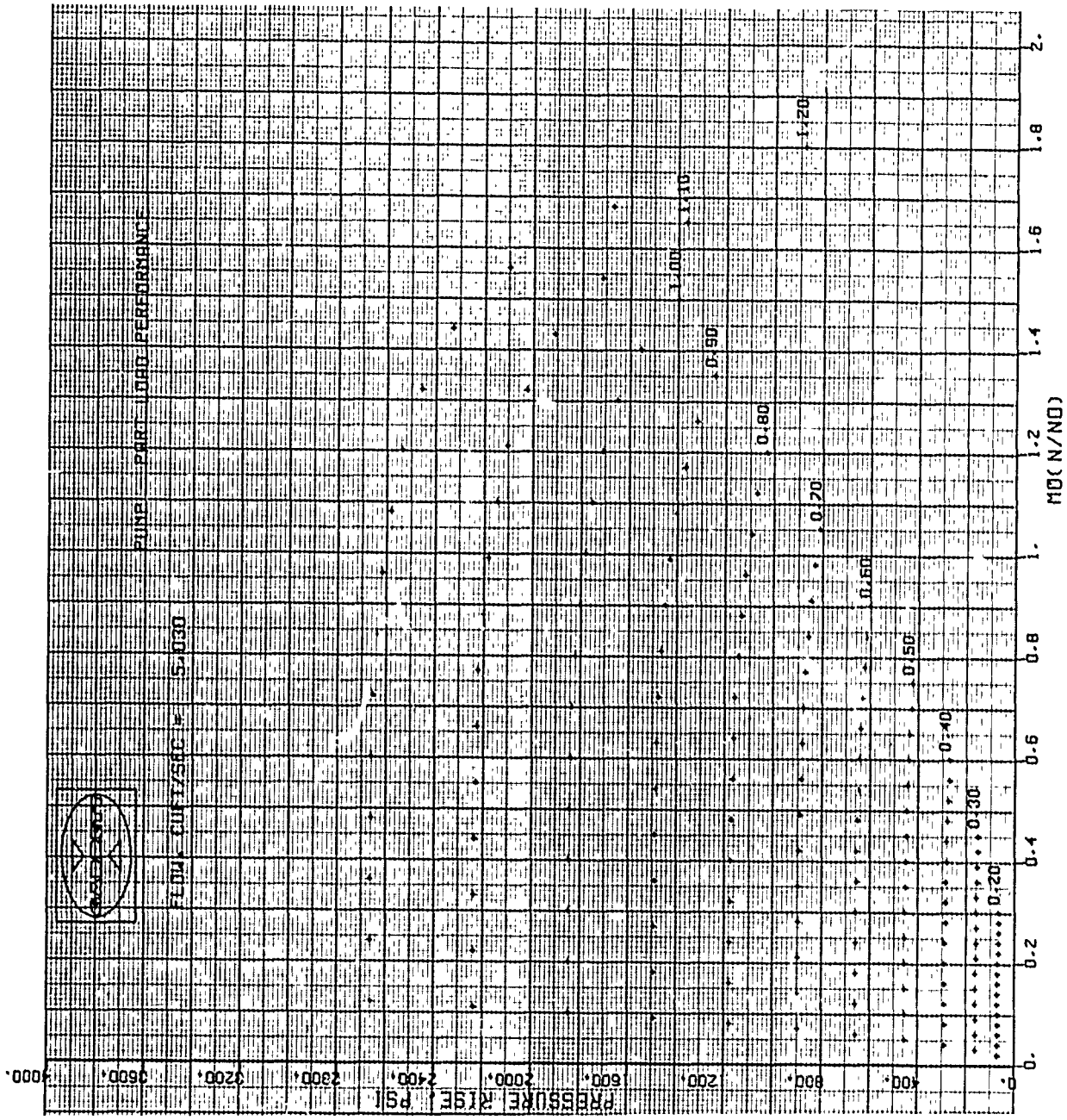

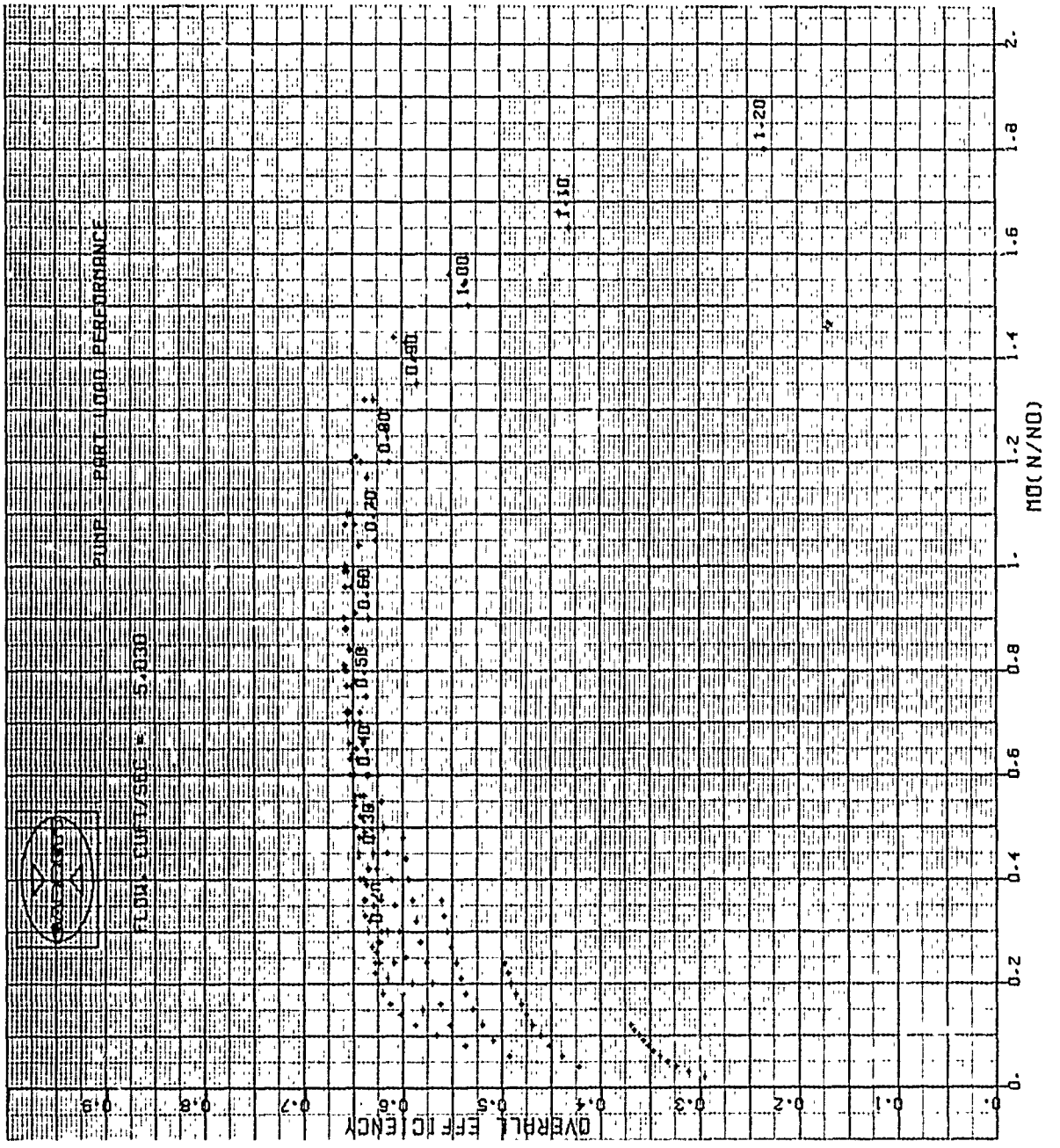

GEOMETRY AND PARAMETER CALCULATIONS, COMPARISON WITH TEST RESULTS, AND NOMENCLATURE

Calculation of the Inlet Scroll of a Vaned Diffuser with Conical Sideplate

Figure 36 shows the general arrangement of the inlet scroll of a vaned diffuser with conical sideplate. The numerical calculation of the inlet scroll profile is based on the natural deceleration principle. This means that the momentum of the fluid is decreased only by the friction on the walls.

The geometry of the diffuser scroll is shown in Figure 40.

The decelerating momentum is expressed by the friction on the walls:

$$dM = frc^2 (2h - 2h_o + b) \frac{\rho}{2} \cos\alpha \, dx$$

The mass element of the fluid is

$$dm = \rho(h - h_o) \frac{b_o + b}{2} dx$$

The width of the channel is a function of the sideplate angle:

$$b = b_o + (h - h_o) \tan \gamma$$

Combining these equations results in

$$\frac{dM}{dm} = \frac{f c^2 \cos\alpha \, r (2h - 2h_o + b)}{(h - h_o)(b_o + b)}$$

The momentum equation is given as

$$-\frac{dM}{dm} = \frac{d(c_u r)}{dt} = c \frac{d(c_u r)}{dx}$$

Finally, the first form of the differential equation is

$$\frac{d(c_u r)}{dx} = \frac{f c_u r (2h - 2h_o + b)}{(h - h_o)(b_o + b)} \qquad (13)$$

The relation between x and h is given by the continuity. The volume changes along a $d\varphi$ angle when the flow is incompressible:

$$dV = C_{Mo} b_o r_o d\varphi = \frac{C_u}{2} \left[(h - h_o) \tan \gamma + b + b_o \right] dh$$

The dx is expressed as a function of $d\varphi$

$$dx = r d\varphi = \frac{C_u r}{2 b_o C_{Mo} r_o} \left[(h - h_o) \tan \gamma + b + b_o \right] dh$$

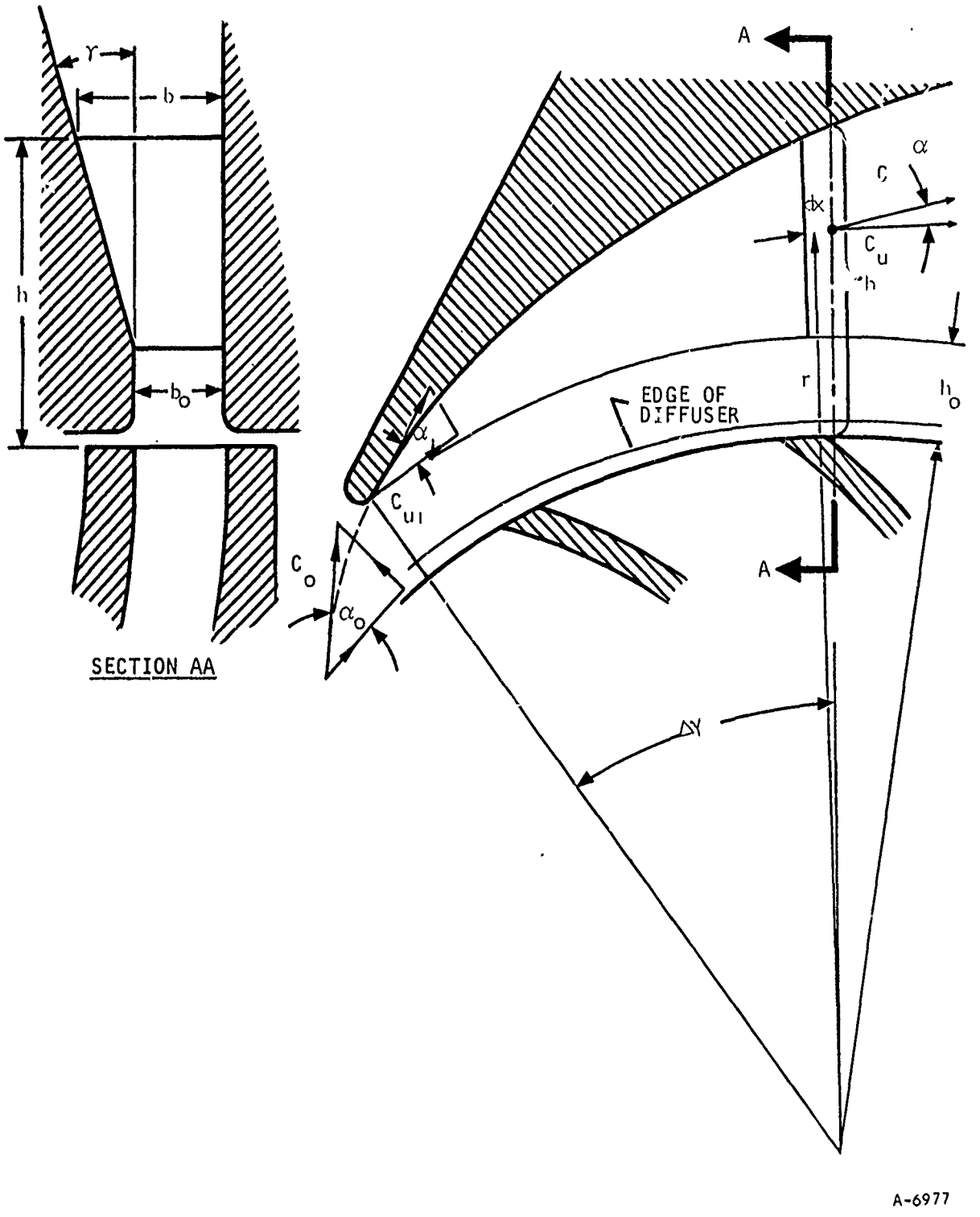

Figure 40. Diffuser Geometry and Velocities

Since $dM = frc^2 (d\pi - b_o) \frac{\delta}{2} \cos\alpha dx$ and $dm = \rho \frac{d^2\pi}{4} dx$, combining these with Equations (14) and (15) results in

$$\frac{d(C_u r)}{(C_u r)^2} = - \frac{f \pi}{C_{Mo} b_o r_o} \left(1 - \frac{b_o}{\pi d}\right) d(d)$$

The integral is then

$$- \frac{1}{C_u r} = -A \left(d - \frac{b_o}{\pi} \log d\right) + \text{constant}$$

In this expression the logarithmic term represents the so called "tongue" effect--the increased friction due to the theoretically high losses connected with the very small diameter in the beginning of the scroll. This is only theoretically so; in practice, the channel always has a minimum width--the width of the vaneless diffuser portion where the flow can adjust itself and reduce the relative friction. Therefore, this logarithmic term of the equation can be replaced by a constant and an increased friction factor given by experimental comparison with existing diffuser results.

$$\frac{C_{uo} r_o}{C_u r} = 1 + \frac{f 2\pi (r - r_o)}{b_o \tan \alpha_o}$$

$$\frac{C_{uo}}{C_u} = \frac{r}{r_o} \left[1 + \frac{\pi f}{B_o \tan \alpha_o} \left(\frac{r}{r_o} - 1\right)\right]$$

$$\frac{C_{uo}}{C_u} = \left(1 + \frac{d}{D_o}\right) \left(1 + \frac{f\pi}{B_o \tan \alpha_o} \frac{d}{D_o}\right)$$

The angular position of the cross section given in degrees of angle is

$$\Delta\varphi = \frac{90}{B_o \tan \alpha_o} \left(\frac{Cu}{C_{uo}}\right)\left(\frac{d}{D_o}\right)^2$$

This equation also can be expressed as the number of diffuser vanes

$$Z_2 = \frac{B_o \tan \alpha_o \left(\frac{C_{uo}}{Cu}\right)}{4\left(\frac{d}{D_o}\right)^2}$$

Estimating Straight Diffuser Recovery from Boundary Layer Thickness in the Throat

Reference 16 describes some tests conducted with straight and curved channels, measuring the maximum pressure recovery of different diffuser configurations having variable boundary-layer thicknesses in the diffuser inlet throat. In the report, the actual displacement thickness of the boundary layer is given.

The recovery factor of a diffuser is defined as the ratio of the pressure rise across the diffuser and the total inlet velocity energy entering the diffuser:

$$R_C = \frac{2g\Delta p}{\rho c_i^2}$$

The relative displacement thickness of the boundary layer at the inlet throat of the diffuser is given as the ratio of the integral average displacement thickness and the width of the throat, $\frac{2\delta^*}{b}$.

The measured test results were plotted in Figure 41 for straight channels and for curved-elliptic channels. The result shows the well known fact that the straight channel has better recovery than a curved one.

The measured performance points of the straight diffusion channels can be connected by a linear function. The general form of the loss vs relative boundary layer thickness will take the following form:

$$C_\ell = a_1 + a_2 \frac{2\delta^*}{b_2}$$

For general calculations, it seems to be better to replace the diffuser width by the hydraulic diameter of the diffuser throat.

$$C_\ell = a_1 + a_3 \frac{\delta^*}{d_{HYD}} \qquad (16)$$

The a_1 and a_3 constants are functions of the form of the throat The circular cross section gives lower losses and higher recovery than a flat rectangular one.

With the help of this approximate equation of the pressure loss factor, it is possible to estimate the loss of the straight portion of the diffuser The displacement thickness can be calculated from the average length of a streamline and the Reynolds number, while the hydraulic diameter is given by the geometry of the diffuser.

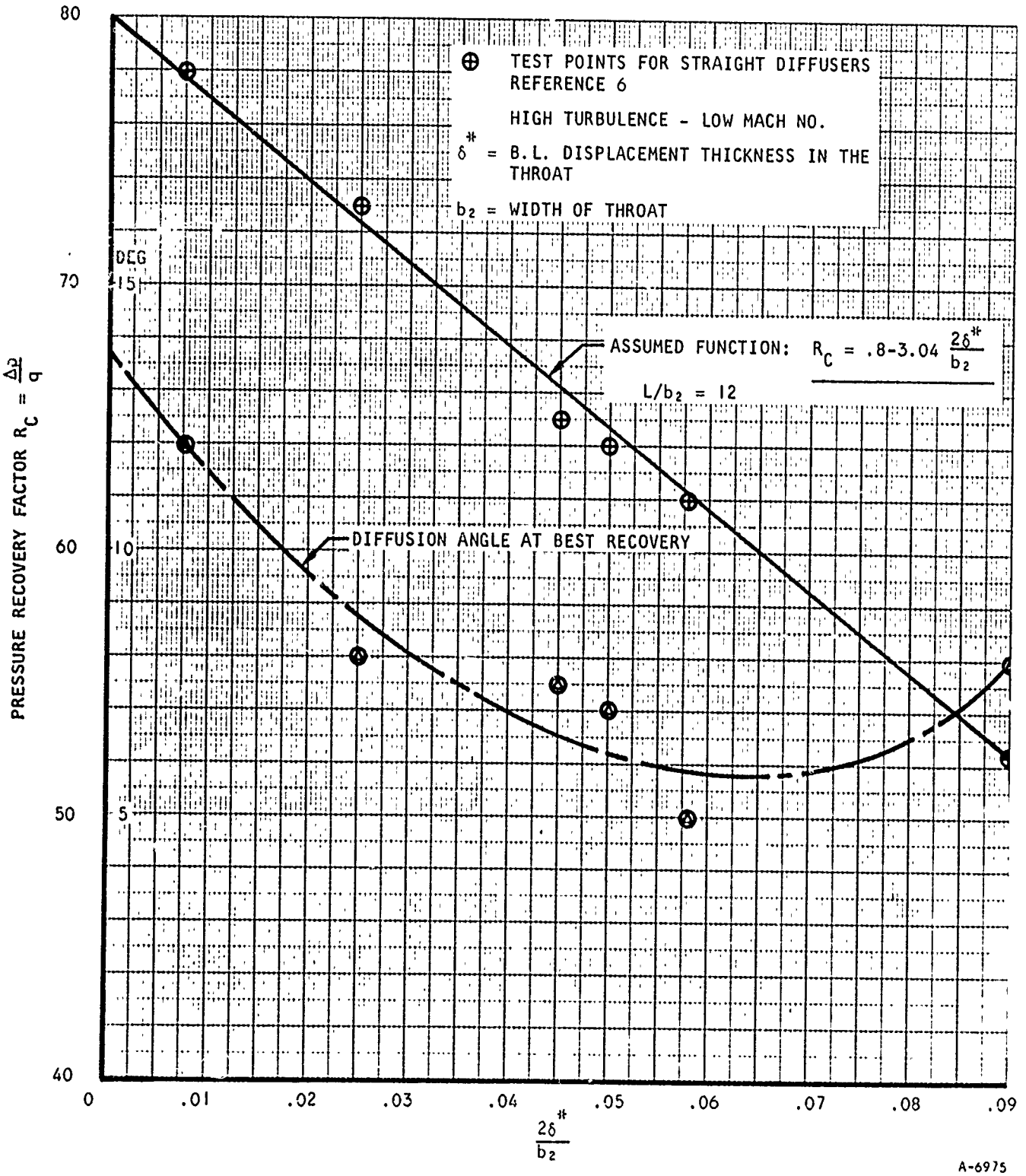

Figure 41. Diffusers - Maximum Recovery vs Throat-Boundary-Layer Thickness

In the case of conical sidewalled vaned diffusers, the length of the streamline is $\Delta\ell_2$, the hydraulic diameter is d_{H2}. The displacement thickness with turbulent flow is a function of Reynolds number and length of the streamline:

$$\delta^* = \frac{a_4}{Re^{0.2}} \Delta\ell_2 \qquad (17)$$

The friction factor in the diffuser function is similarly a function of the Reynolds number, so the displacement thickness also can be expressed in the following form:

$$\delta^* = a_5 f_2 \Delta\ell_2$$

Combining (16) and (17) gives

$$C_\ell = a_1 + a_3 a_5 f_2 \frac{\Delta\ell_2}{d_{H2}}$$

The total loss of diffusion after the throat is the product of the loss factor given above and the available velocity energy in the diffuser throat. The velocity ratio between the impeller tip and the diffuser throat can be calculated as shown in preceding paragraphs. The velocity energy ratio becomes

$$\frac{C_T^2}{2g\,H_{TH}} = \frac{q^2 + \lambda^2}{2q} \left(\frac{C_u}{C_{M_2}}\right)^2 \frac{\lambda^2}{q^2}$$

and the relative loss in the straight diffuser is

$$\Delta q_{DIFF\ 2} = \frac{\lambda^2 + q^2}{2q} \left(\frac{C_u}{C_{M_2}}\right)^2 \left(a_1 + a_3\, a_5\, f_2 \frac{\Delta\ell_2}{d_{H^2}}\right)$$

or, with combined loss factors

$$\Delta q_{DIFF\ 2} = \frac{\lambda^2 + q^2}{2q} \left(\frac{C_u}{C_{u_2}}\right)^2 \left(\xi_5 + \xi_6\, f_2 \frac{\Delta\ell_2}{d_{H_2}}\right)$$

Comparison with Test Results

As was emphasized earlier, this program calculates the performance of an assumed ideal pump configuration and does not compute efficiency of existing pump geometries. This fact must be kept in mind when calculations are compared with test results for existing machinery.

In order to compare the calculation results with statistical average and predicted optimum performances, a number of data were gathered on high-Reynolds-number pump performances and plotted in Figure 42. For comparative purposes, three points were calculated by the present computer program using water as fluid, assuming no cavitation and a Reynolds number close to 10^7. The specific speeds of the calculated samples were 500 to 1000 and 2000. The results of the calculations were also plotted in the diagram. The points fit the top efficiency curve quite well; the program therefore might be used to predict the performance of advanced pump designs with confidence.

Nomenclature

- γ density (lb/cu ft)
  - γ_o average liquid density
- P pressure (psia)
  - ΔP_o pressure rise (psi)
- H head (ft/lb/lb)
  - H_o actual head (ft)
  - H_{TOT} total head developed by impeller (ft)
- η efficiency
  - η_o actual efficiency
  - η_{HYD} hydraulic efficiency
- β relative angle (degrees)
  - β_i inlet flow angle
  - β_1 inlet vane angle
  - β_2 discharge flow angle
  - β_{2o} discharge vane angle
- NPSH net positive suction head (ft)
- D diameter (inches)
  - D_i inlet eye diameter
  - D_H inlet hub diameter at D_i
  - D_2 impeller tip diameter
- V flow (cfs)
  - V_o liquid flow
- N speed (rpm)

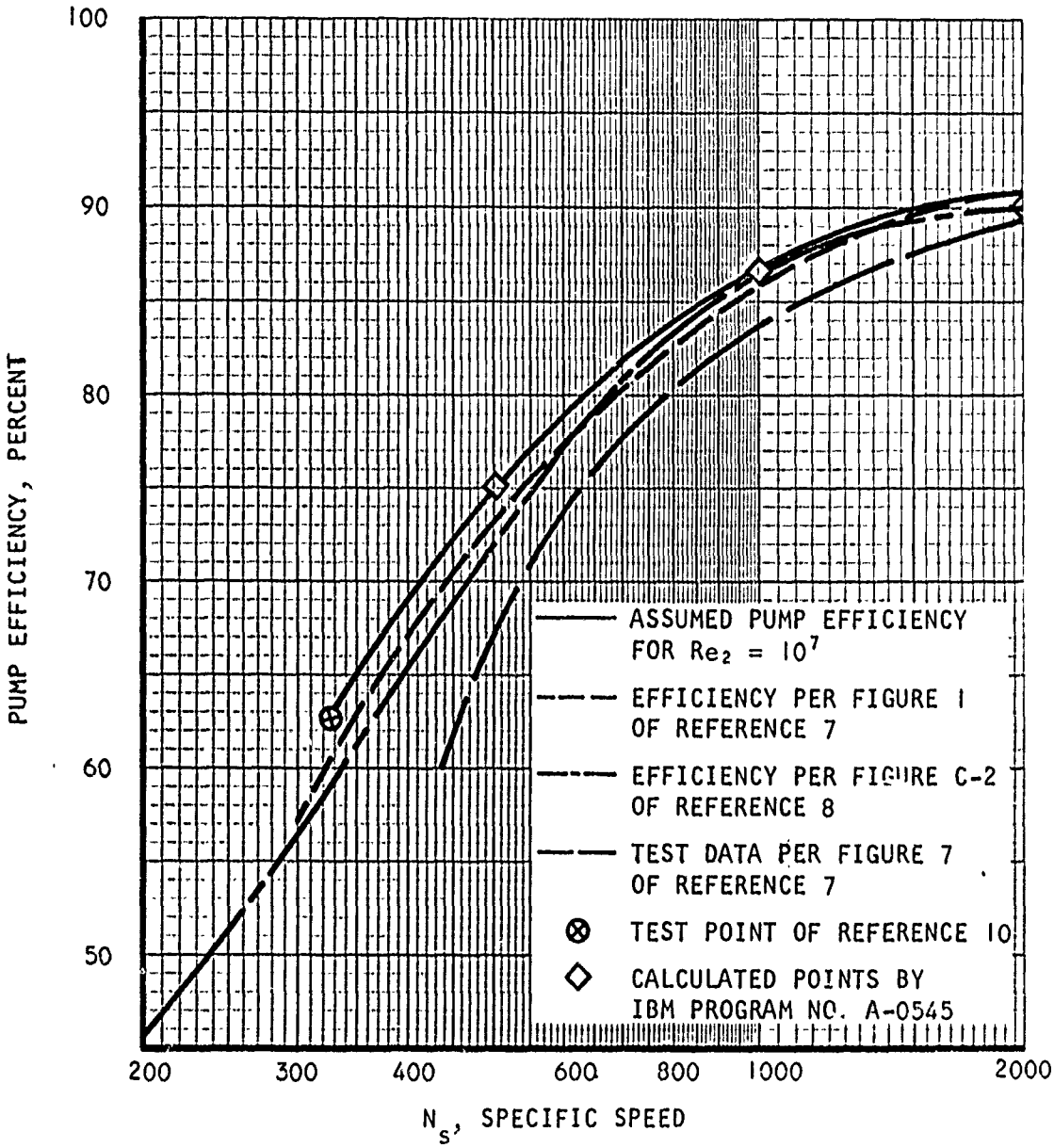

Figure 42. Efficiency Comparison with Published Data

C absolute velocity (fps)

C_i inlet velocity

C_2 discharge velocity at impeller tip

C_{1_M} inlet meridional velocity

C_{2_M} discharge meridional velocity

C_{2_u} discharge tangential velocity

W relative velocity (fps)

W_i inlet relative velocity at impeller eye

W_{2_0} discharge relative velocity at impeller tip - theoretical

W_2 discharge relative velocity at impeller tip - actual

U rotational velocity (fps)

U_i inlet rotational velocity at impeller eye

U_2 discharge rotational velocity at impeller tip

K blockage factor

K_i inlet hub blockage factor

ε flow contraction factor

K inlet density function exponent

A inlet density function constant (1/ft)

q total head factor (C_{2_u}/u_2)

μ slip factor $(C_{2_u}/C_{2_{uoo}})$

λ flow factor (C_{2_M}/u_2)

ν_2 impeller diameter ratio (D_i/D_2)

ζ_I impeller diffusion ratio (W_2/W_i)

ζ_D diffuser throat width ratio

Z number of vanes

Z_1 of impeller

Z_2 of diffuser

ξ loss constants

- ξ_1 heat
- ξ_2 impeller friction
- ξ_3 diffusion
- ξ_4 recirculation
- ξ_5, ξ_6, ξ_7 diffuser boundary layer
- ξ_8 wheel friction
- ξ_9 leakage

$\Delta\ell_1$ mean streamline length (inches)

$\Delta\ell_2$ diffuser scroll streamline length (inches)

B_2 impeller width factor (b_2/D_2)

b_2 impeller tip width (inches)

d flow channel diameter (inches)

d_{HYD} hydraulic diameter (inches)

d_{H2} diffuser scroll hydraulic diameter (inches)

Re Reynolds number

f friction factor

Δq loss (dimensionless)

- Δq_{SF} impeller skin friction loss
- Δq_{DL} impeller diffusion loss
- Δq_{RC} impeller recirculation loss
- Δq_{SC} diffuser scroll friction loss
- Δq_{D2} straight diffuser loss
- Δq_L leakage loss
- Δq_{FR} disk friction loss
- Δq_D total diffuser loss
- Δq_{inc} inducer inlet incidence loss

ν_* kinematic viscosity (ft^2/sec)

Δ diffusion factor-impeller

γ diffuser wall angle (deg)

α absolute flow angle (deg)

- α_1 inlet flow angle (prerotation)
- α_2 impeller discharge flow angle
- α_3 flow angle end of vaneless space

SECTION 5

FUEL TRANSFER SYSTEM

An important application of the pump studied in this contract can be found in the fuel transfer system for advanced airbreathing propulsion engines. Here, the pump is used to transfer the LH_2 from the storage tank to the engine. The pump is usually driven by a turbine which can be operated either from the heated hydrogen bled from the pump or from high-temperature air tapped off from the main engine.

With the size of the engine and the type of mission considered in the following investigation, it has been found that hydrogen-driven turbopumps offer definite advantages over the air-driven type because of the improvement in size, weight, and acceleration characteristics, accompanied by simplicity in mechanical design, where the problem of sealing the air-side shaft from the hydrogen side can be avoided. Investigation leading to the hydrogen-driven turbopump is presented below.

DEFINITION OF THE FUEL TRANSFER SYSTEM

The basic elements of the system are shown in Figure 43. LH_2 from the tank is pumped to a high pressure by the turbopump. At the pump exit, most of the flow is sent to the engine, providing on the way a cooling capacity for use in cooling the vehicle structure or exhaust nozzle. This is represented functionally by a heat exchanger in Figure 43. At the exit of the heat exchanger, the hydrogen is then injected to the combustor.

The fractional capacity bled off at the pump exit is further heated in a separate heat exchanger, flows past a control valve, and then expands in the driver turbine of the turbopump. For system simplicity, the turbine is allowed to exhaust into an auxiliary nozzle that provides a small amount of thrust to the vehicle.

PUMP DISCHARGE PRESSURE IN A TYPICAL MISSION

To study the problems encountered in the application of the pump with an estimated performance map shown in Figure 44, the fuel flow requirements of a turbojet engine flying a typical mission are considered. Table I presents these flight conditions and fuel flows.

The pump delivery pressures for the various fuel flows are now established with the following assumptions.

1. The combustor static pressure is calculated from the combustor flow Mach number of 0.2 and given total pressure delivered by the compressor.

2. Temperature of hydrogen at injector is $2000^{\circ}R$.

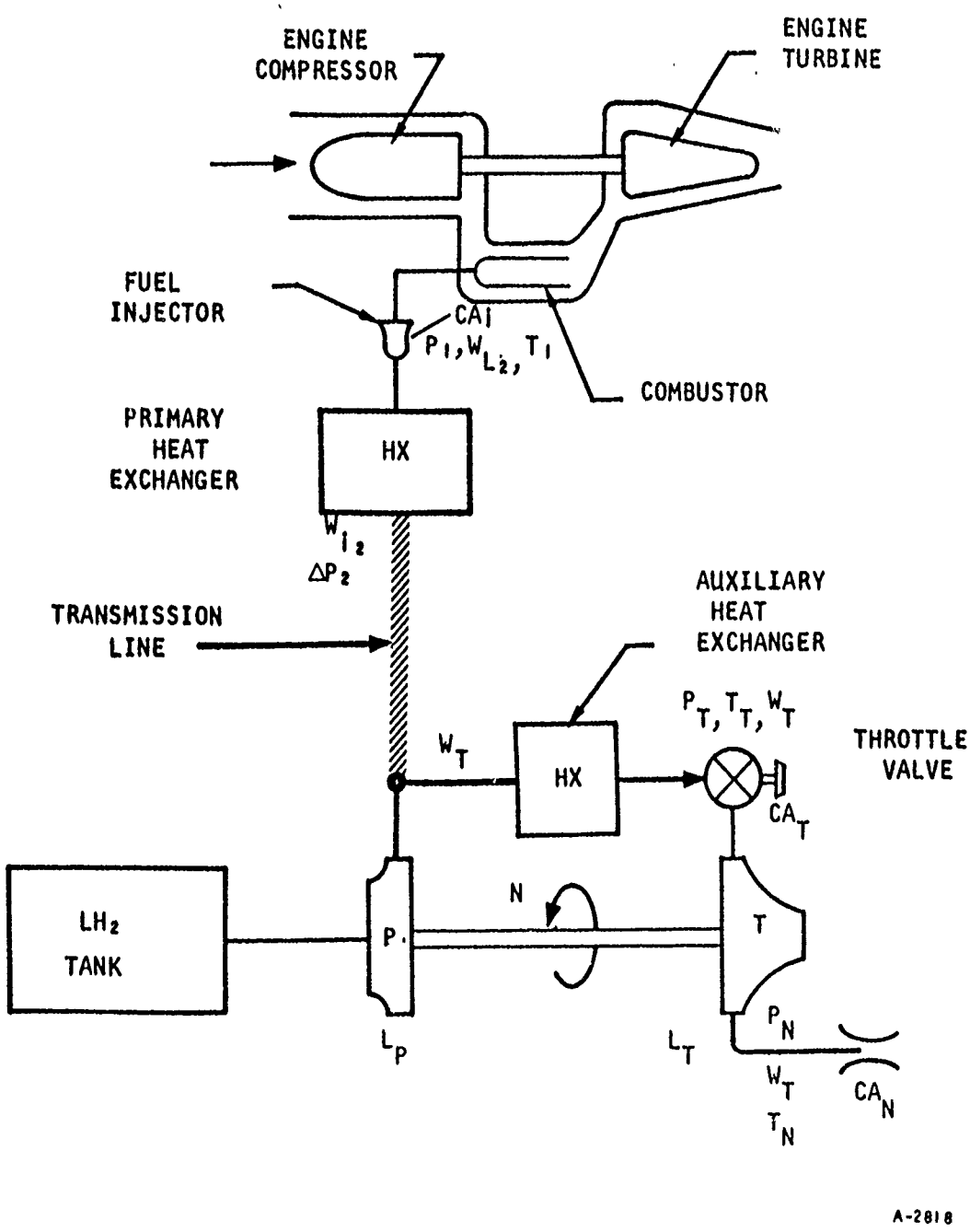

Figure 43. Fuel Transfer System Model H-1 Schematic Diagram

TABLE I

PERFORMANCE CHARACTERISTICS OF LIQUID HYDROGEN PUMP*

Flight Condition		Pump Discharge	Fuel Injector	$\frac{W_i}{W_j}$*	Fuel Flow, Hydrogen Flow Rate, W_j lb/sec	Enthalpy Rise, Pump Btu/lb	Total Heat Input, Heat Exchanger, Btu/sec	Rotation Speed, rpm
1	Pressure, psia	962	862	1.0	14.5	50.1	103,000	43,000
	Enthalpy, Btu/lb	-57.9	6950					
2	Pressure, psia	770	703	0.82	11.9	40.6	82,800	38,000
	Enthalpy, Btu/lb	-67.4	6950					
3	Pressure, psia	545	510	0.593	8.61	29.2	60,400	31,500
	Enthaply, Btu/lb	-77.8	6950					
4	Pressure, psia	236	229	0.265	3.83	14.6	27,100	20,300
	Enthalpy, Btu/lb	-93.4	6950					
5	Pressure, psia	117	112	0.130	1.80	8.88	13,300	14,100
	Enthalpy, Btu/lb	-99.1	6950					

* An engine with a maximum fuel flow of 52,000 lb/hr is considered

3. The fuel injector operates "choked" under all conditions to minimize upstream propagation of combustor instabilities. The injector nozzle is fixed and sized for an injection velocity of M = 1.2. This may not be an optimum from the combustor design viewpoint.

4. At maximum flow, the pressure drop in the heat exchanger and other elements of the system is on the order of 10 psi. At other flow rates, the pressure drop will vary as the square of the fuel flow.

Figure 45 shows, on a pressure-enthalpy chart, the state points from pump inlet to pump discharge for the five operating conditions located in Figure 44. Figures 45 and 46 show the state points of the hydrogen during its passage through the heat exchanger. Table I lists the state points of the hydrogen at various locations in the system for the five operating conditions described above.

Referring to Figure 45, it can be seen that heating of the liquid hydrogen at pump discharge pressures below 190 psi results in two-phase flow in the heat exchanger. However, the change in specific volume under these conditions should offer no problem, since this condition only occurs at very low flow rates, and the heat exchanger is sized to handle the maximum flow rate of the system.

PRELIMINARY DESIGN OF THE HYDROGEN TURBINE

In the preliminary sizing of the hydrogen turbine that drives the pump, a main objective is to simplify the control schemes. Inlet temperature of the hydrogen working fluid is assumed constant at 2000°R for all operating points.

It is desired to find a compromise in the turbine design which yields a good fuel consumption, a low moment of inertia needed for acceleration characteristics, and also to avoid the use of variable components in the exhaust nozzle or in the turbine stators. The requirement for a small size, lightweight unit compatible with airborne components impose further restrictions on the design study. The inlet pressure to the turbine will then be modulated through a throttle valve to permit the control of the turbopump that delivers the proper fuel flow.

A satisfactory solution to this problem is a two-stage axial flow turbine, illustrated in Figure 47. Impulse design is used in all stages with 20-percent partial admission in the first and 75-percent admission in the last stage. The largest diameter of the turbine rotor is 8.50 in., resulting in a maximum tip speed of 1600 fps at 43,000 rpm.

Over the flight conditions, the turbine operates at a pressure ratio of 20:1, resulting in a low velocity ratio and a low performance as shown in Table 2. This, however, has yielded a reasonable fuel flow ratio W_T/W_i ranging from 0.033 to 0.013.

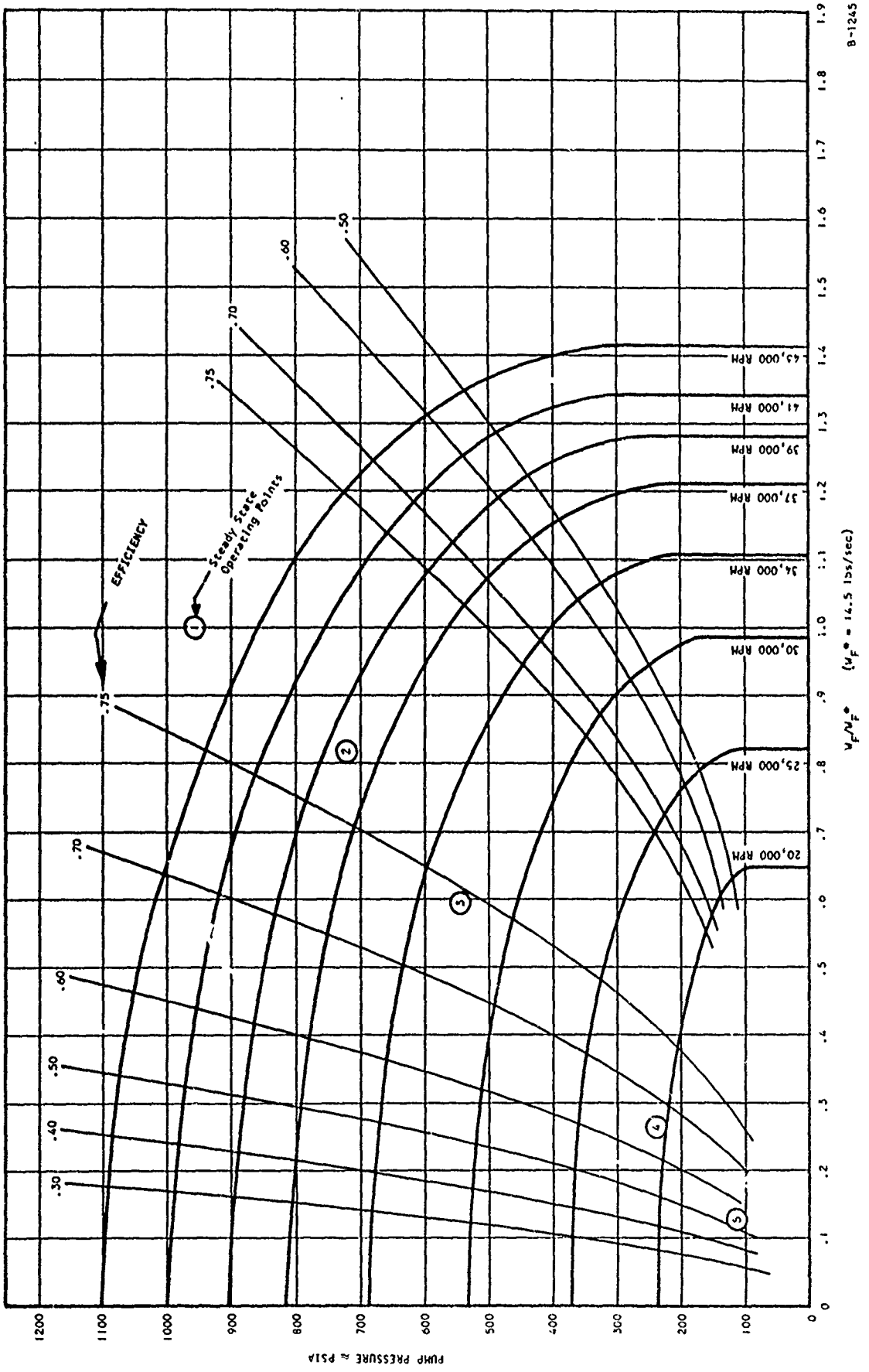

Figure 44. LH_2 Pump Performance Characteristics, First-Order Estimate

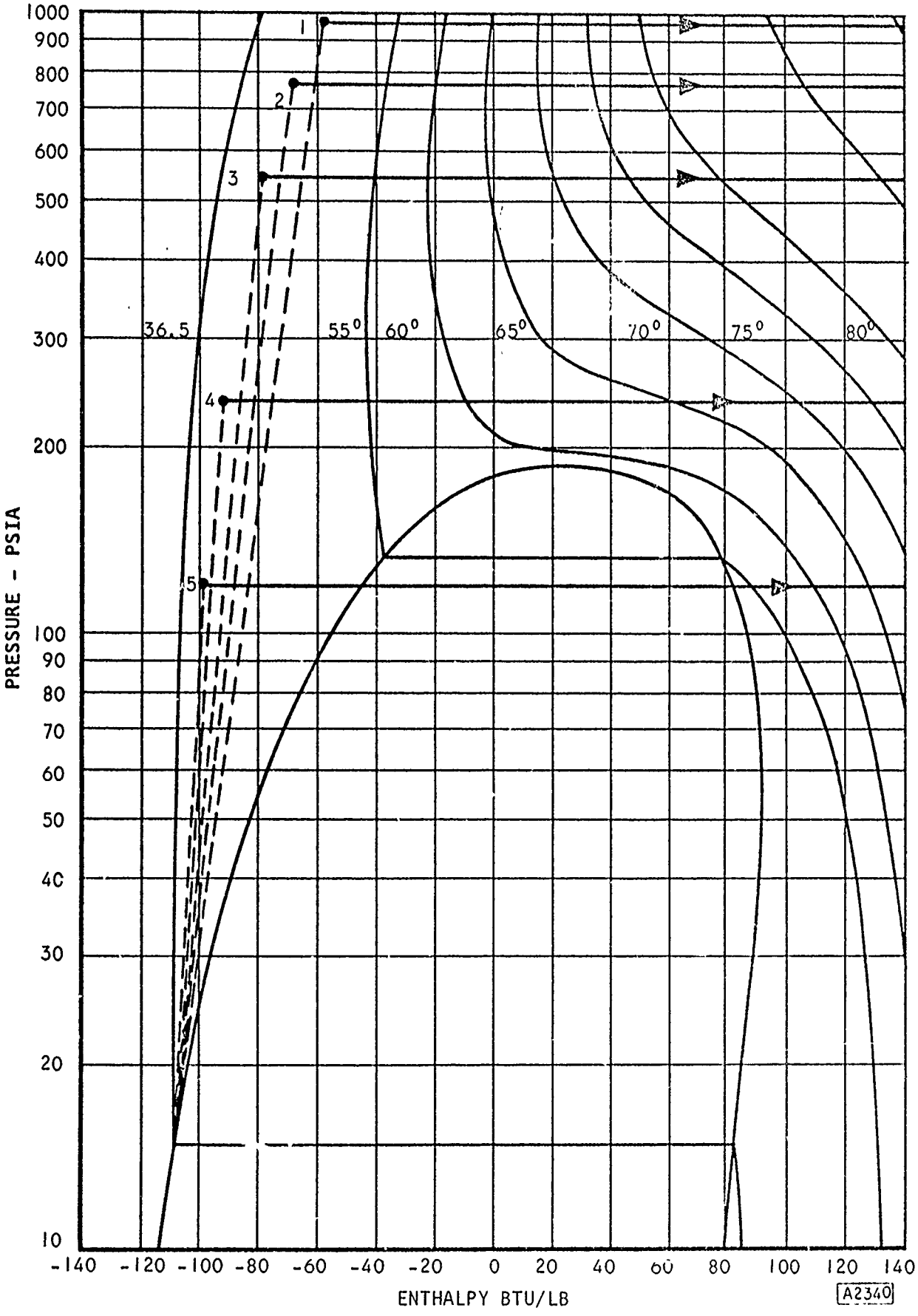

Figure 45. State Points at Discharge of Liquid Hydrogen Pump

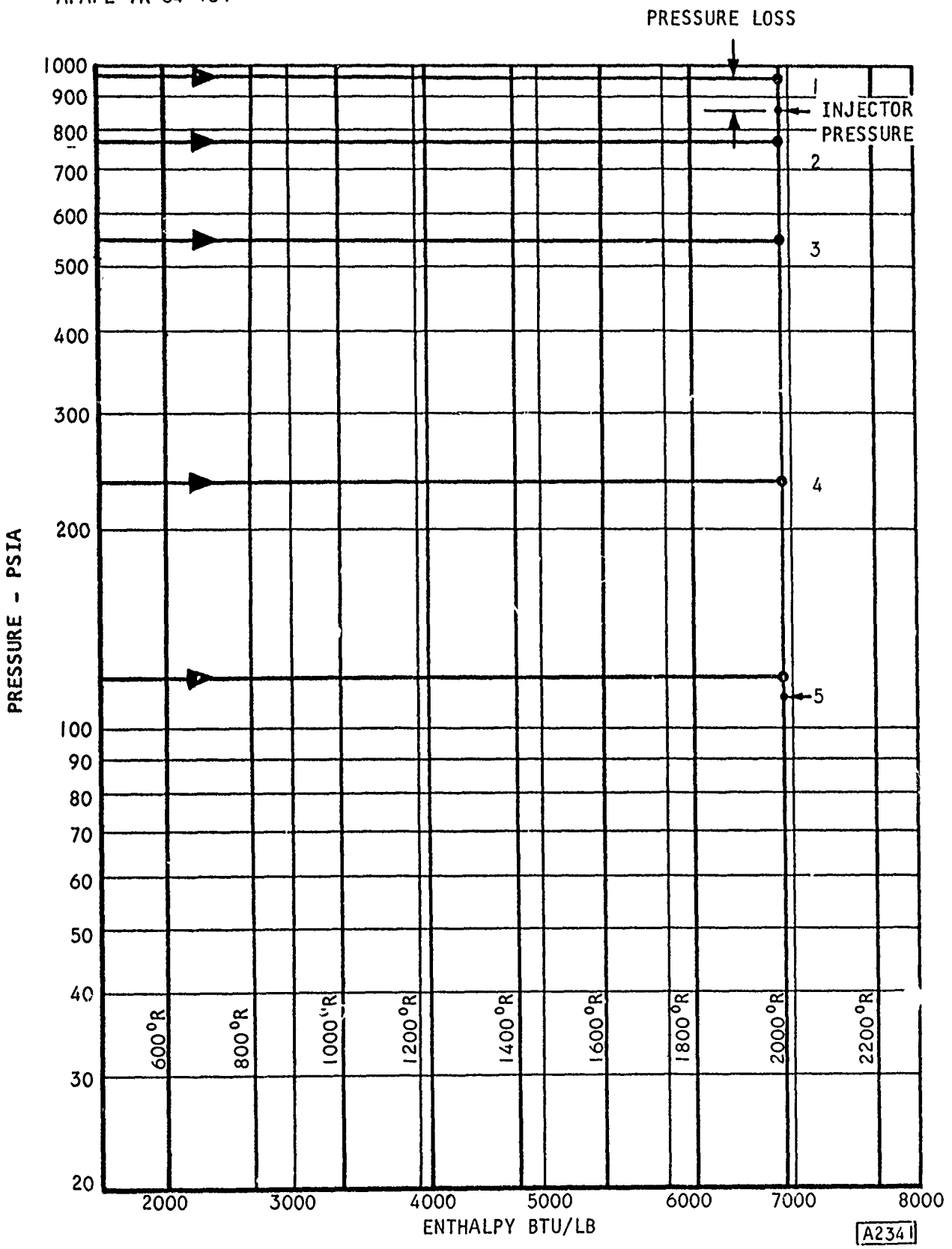

Figure 46. State Points of Hydrogen Gas at Exit of Heat Exchanger

TABLE 2

FUEL TRANSFER SYSTEM OPERATING CONDITIONS

Parameter Description	Symbol	Units	Flight Conditions 1	2	3	4	5
Fuel Flow Ratio	W_i/W_i^*	--	1.0	.820	.593	.265	.130
Fuel Flow (Pump)	W_i	lb/hr	52,200	42,800	31,000	13,800	6780
Fuel Flow (Pump)	W_i	lb/sec	14.5	11.9	8.61	3.83	1.88
LH_2 Sump Pressure	P_R	psia	14.7	14.7	14.7	14.7	14.7
LH_2 Sump Temperature	T_R	°R	36.5	36.5	36.5	36.5	36.5
Pump Pressure	P_I	psia	962	770	545	236	117
Required Injector Pressure	P_i	psia	862	703	510	229	112
Pump Discharge Temperature	T_{ci}	°R	46.2	44.6	42.8	40.0	38.8
Pump Power		HP	1105	735	389	88	27.2
Pump Torque (S.S.)	LT	in-lb	1620	1203	760	258	110.9
Pump-Turbine Speed	N	rpm	43,000	38,500	32,250	21,500	15,500
Pressure Upstream Throttle Valve		psia	914	731	518	224	111.0
Upstream Turbine Pressure	P_T	psia	866	583	339	109.3	45.5
Downstream Turbine Pressure	P_N	psia	43.3	29.1	17.2	5.75	2.445
Turbine Pressure Ratio	P_T/P_N		20	20	19.7	19	18.6
Upstream Turbine Temperature	T_T	°R	2000	2000	2000	2000	2000
Downstream Turbine	T_N	°R	1540	1540	1580	1705	1781
Turbine H_2 Flow	W_T	lb/sec	.475	.32	.186	.06	.025
W_T/W_I			.0329	.0269	.0216	.0156	.0133
Turbine Tip Speed	U_t	fps	1600	1430	1200	800	576
Turbine Velocity Ratio	U/C_o		.112	.1007	.0844	.0563	.04
Turbine Efficiency			.415	.41	.375	.265	.195
Turbine Power		HP	1128	750	397	89.8	27.8
Turbine Nozzle Area	CA_{TN}	in^2	.1755	.1755	.1755	.1755	.1755
Turbine Exhaust Area	CA_N	in^2	3.08	3.08	3.08	3.08	3.08
Throttle Flow Area	CA_T	in^2	.367	.17	.1191	.0857	.0722
Heat Exchanger ΔP (Primary)	ΔP_{xp}	psi	100	67	35	7	2
Heat Exchanger (Auxiliary)	$\Delta P/P$	--	.05	.05	.05	.05	.05

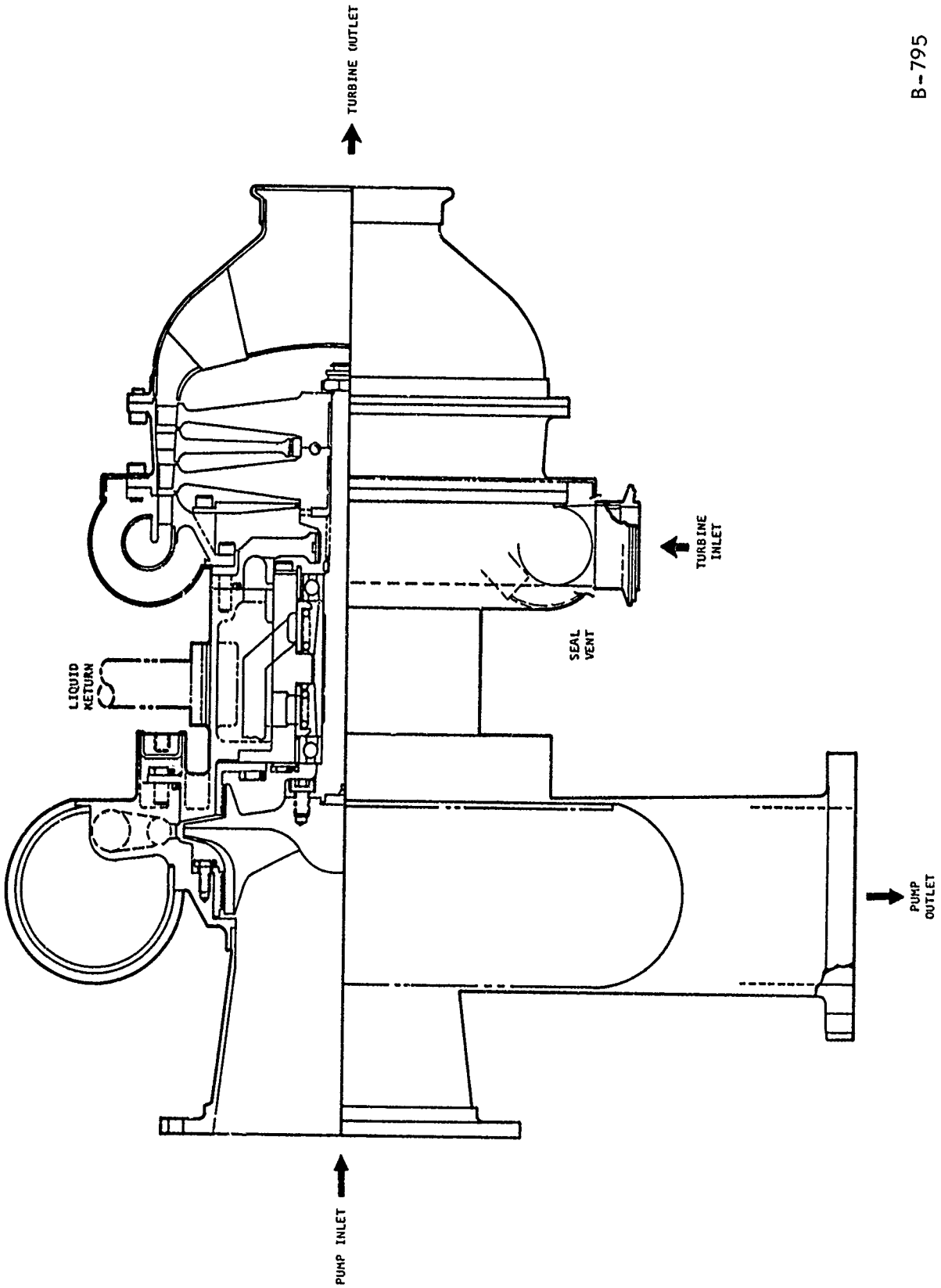

Figure 47. Two-Stage Axial-Flow Turbine

SYSTEM DYNAMIC ANALYSIS

The function of the fuel transfer system is to transfer LH_2 fuel from a remote tank to an operating engine with throttle capabilities. System configuration was determined and components were sized to meet steady-state requirements. The purpose of this analysis is to determine the open-loop dynamic characteristics between throttle area change and fuel flow response.

A mathematical model or set of simultaneous system equations was derived from which an analog computer model was developed. The computer model was used to generate system dynamic response information. The computer model results, derivation of the system equations, and development of the computer model are discussed and presented in the following paragraphs.

Summary of Results

Computer simulation has shown the system to be quite stable and heavily damped throughout its operating range, displaying smooth dynamic response characteristics. System gain between throttle area and fuel flow increases by a factor of 25 with increased throttling over the operating range, because of a nonlinear steady-state relation between throttle area and fuel flow. System response is considerably slower in a heavily throttled condition. Fuel flow response to a small-magnitude step change in throttle area at five operating conditions covering an operating range between 14.5 and 1 9 lb/sec fuel flow showed an increased rise-time from 1.0 to 7.5 sec with increased throttling. Percent overshoot also increased with increased throttling, from 15 to 65 percent, but maintained a high degree of dampling. A large-magnitude step change would produce a rise-time of about 2 to 3 sec, because of the nonlinear relation between rise-time and operating condition. The increase in response time with increased throttling was shown to be primarily a result of the slope of the system operating torque-speed curve. System response at the heavily throttled conditions could be significantly improved with proper closed-loop control functions.

Discussion of Results

1. Fuel Transfer System Description

The fuel transfer system consists of a remote liquid hydrogen tank and pump, transporting the hydrogen through a liquid transmission line to the engine combustion chamber jacket, which serves as a heat exchanger. The hydrogen flows through the chamber jacket, absorbing heat from the combustion process, and is injected into the engine as a gas. A small portion of the liquid hydrogen is bled off to another section of the chamber jacket that serves as the auxiliary heat exchanger. This hydrogen is heated to a high temperature in the auxiliary heat exchanger and is transported through a gas transmission line to a remote turbine which drives the liquid hydrogen pump Upstream of the hydrogen turbine is a throttle valve which regulates the flow of hydrogen to the turbine thereby controlling the flow of fuel to the engine Figure 48 is a schematic of the fuel transfer system.

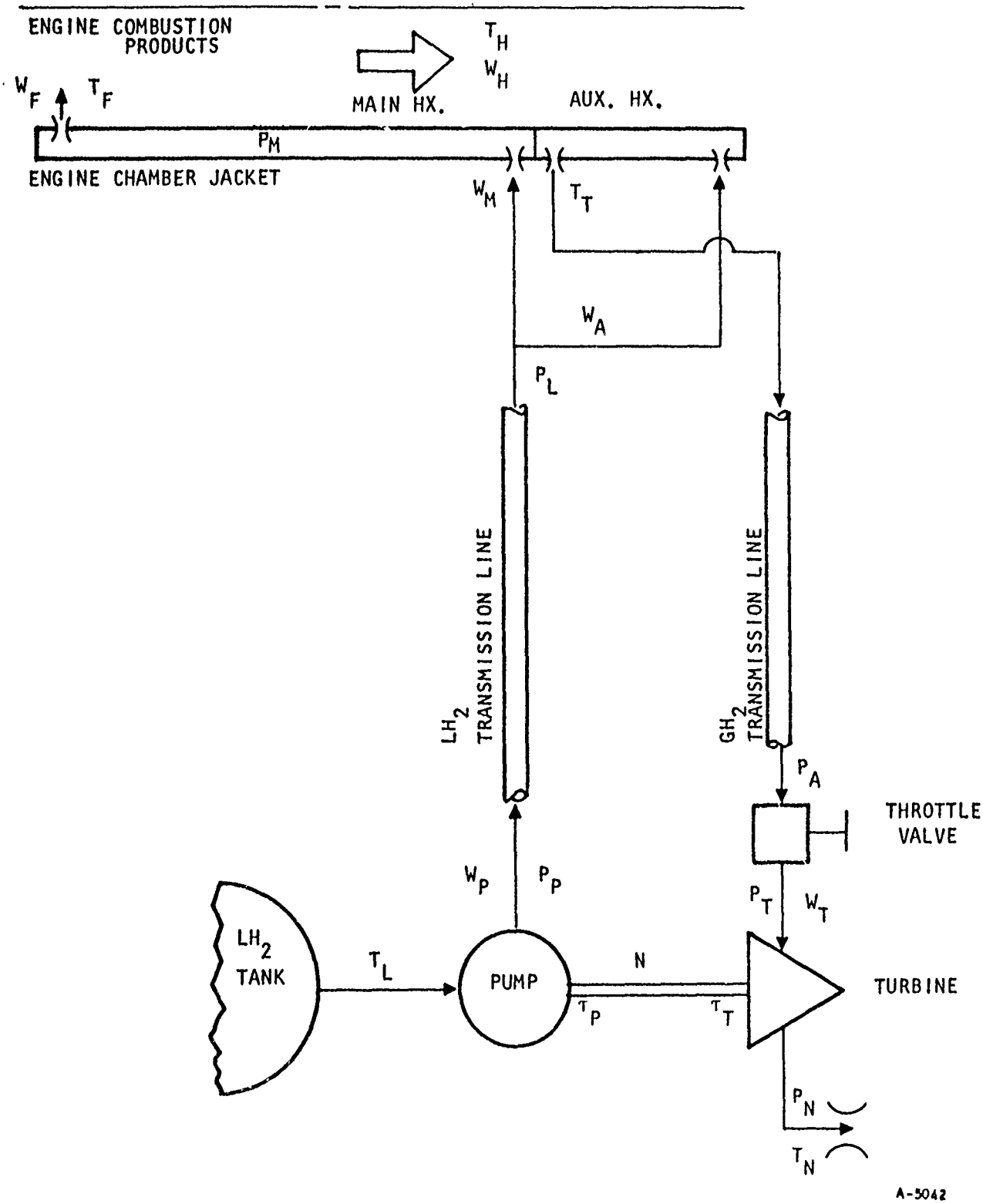

Figure 48. LH_2 Fuel Transfer System Schematic

2. Study Procedure

A linearized analog computer model of the fuel transfer system was constructed and used to study system dynamic response characteristics at five system operating conditions. The linear model simulates system dynamic characteristics around an operating point of the system, and these characteristics vary with the operating condition due to actual nonlinearities in the system. Magnitudes of change due to dynamic disturbance are meaningful only in terms of gain (ratio of change between two parameters). Both gain and time response functions vary with system operating condition. The model was also normalized, so that all parameters are represented as percent changes from their nominal value at the particular steady-state operating condition being studied.

In each of the five conditions being studied, a step change in throttle valve area was introduced, and the time responses of fuel flow and several other parameters were recorded for analysis.

3. Computer Results

Response to a step change in throttle area was quite stable at all five operating conditions. No significant effects were observed as a result of transmission line or gas storage (compressibility) dynamics when represented as lumped parameters. Distributed parameter representation was not investigated. Effects of distributed parameters would be in a frequency range much higher than the range which dominates system performance. Response time became significantly longer as throttling was increased.

Figures 49 through 53 show parameter response traces for conditions 1 through 5, respectively. Percent change magnitude scales were held consistent for each condition to provide qualitative comparison between parameters. Time scales are identical for the first four conditions, but the scale compressed for condition No. 5.

Table 1 shows the nominal parameter values for each of the five steady-state conditions being studied. This table represents steady-state solutions of the nonlinear system equations for each of the five operating conditions which determine the coefficients of the normalized linear dynamic model. It also serves as a reference for percent parameter changes.

Figure 54 compares fuel flow response traces for the five operating conditions. All five conditions are shown with the same time base for qualitative comparison. The increase in response time with increased throttling is noticeably apparent. The time response for each condition is independent of the magnitude of the step input. The trace for condition No 5 was repeated on a compressed time based to show its dynamic characteristics more clearly.

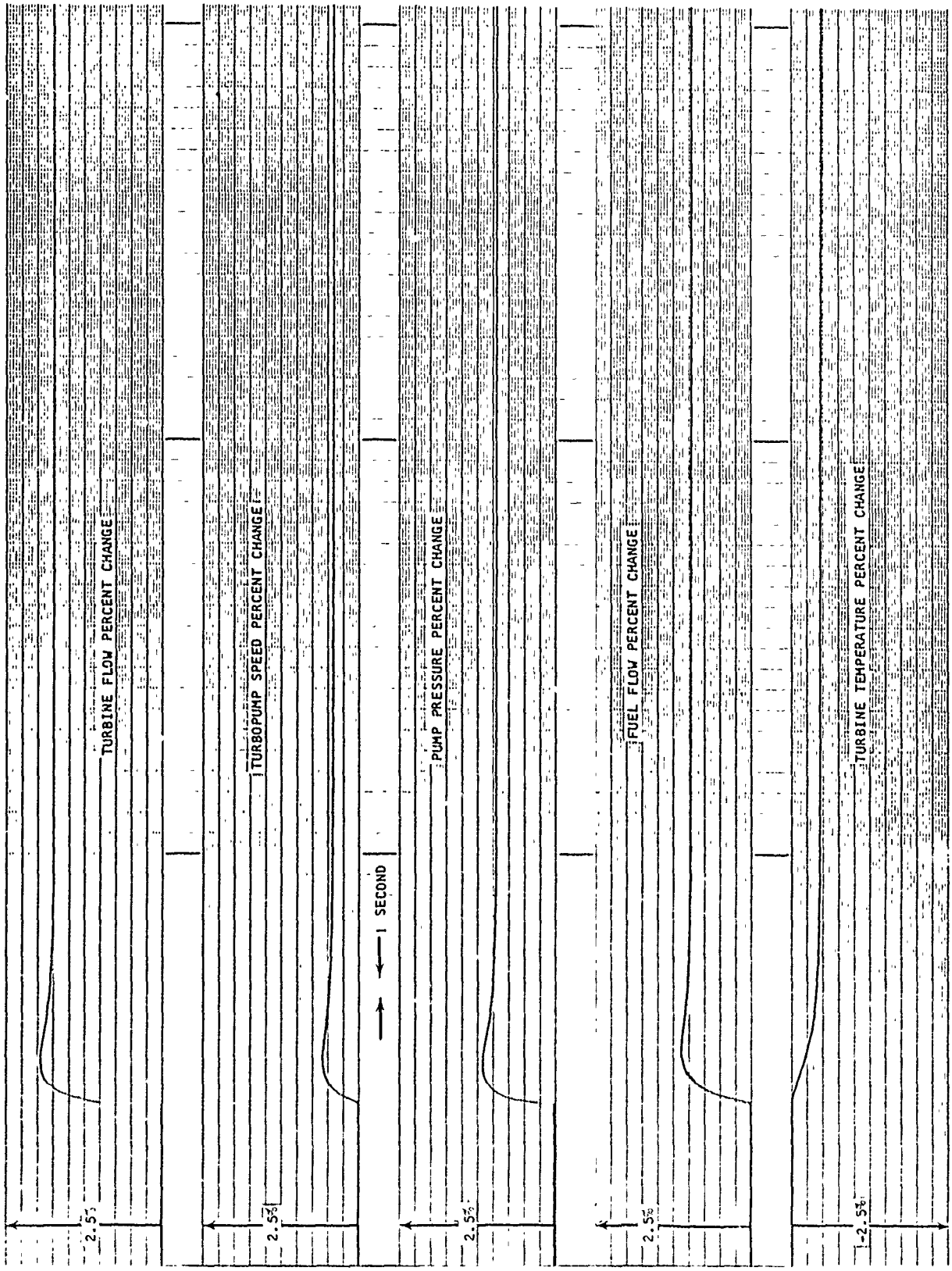

S-1274

Figure 49. System Response to a 10-Percent Step Change in Throttle Area for Condition 1

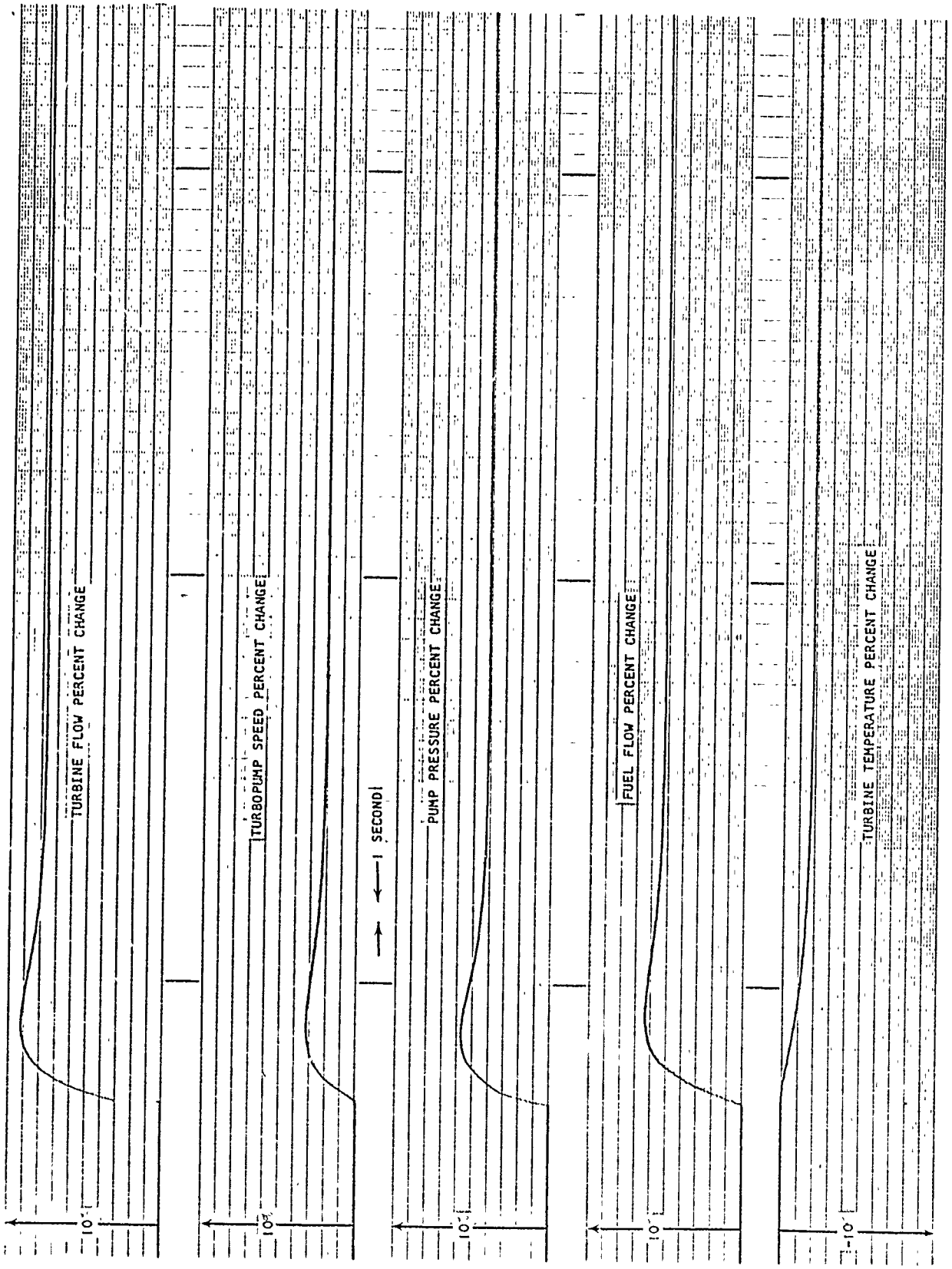

Figure 50. System Response to a 10-Percent Step Change in Throttle Area for Condition 2

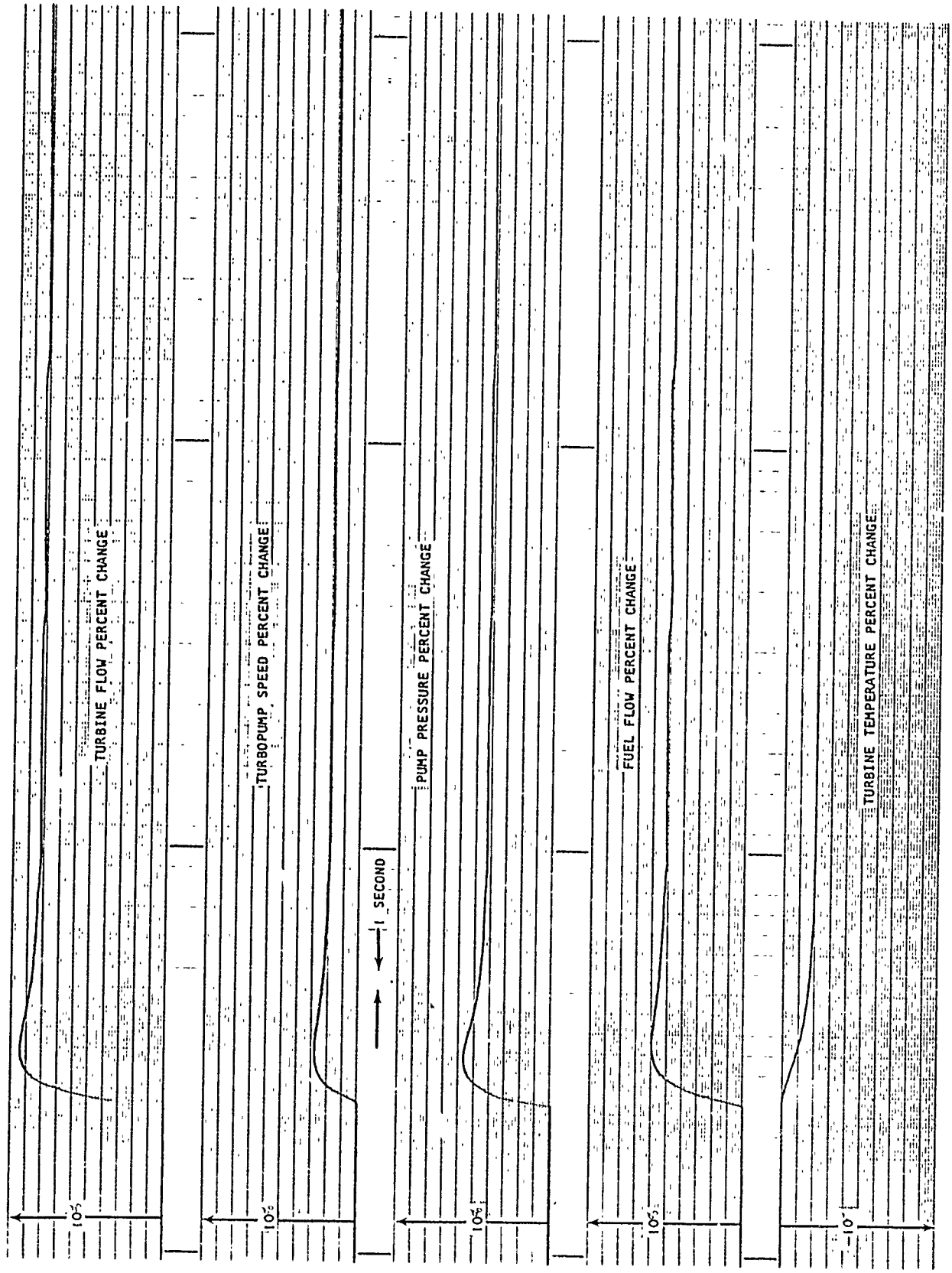

3-1275

Figure 51. System Response to a 5-Percent Step Change in Throttle Area for Condition 3

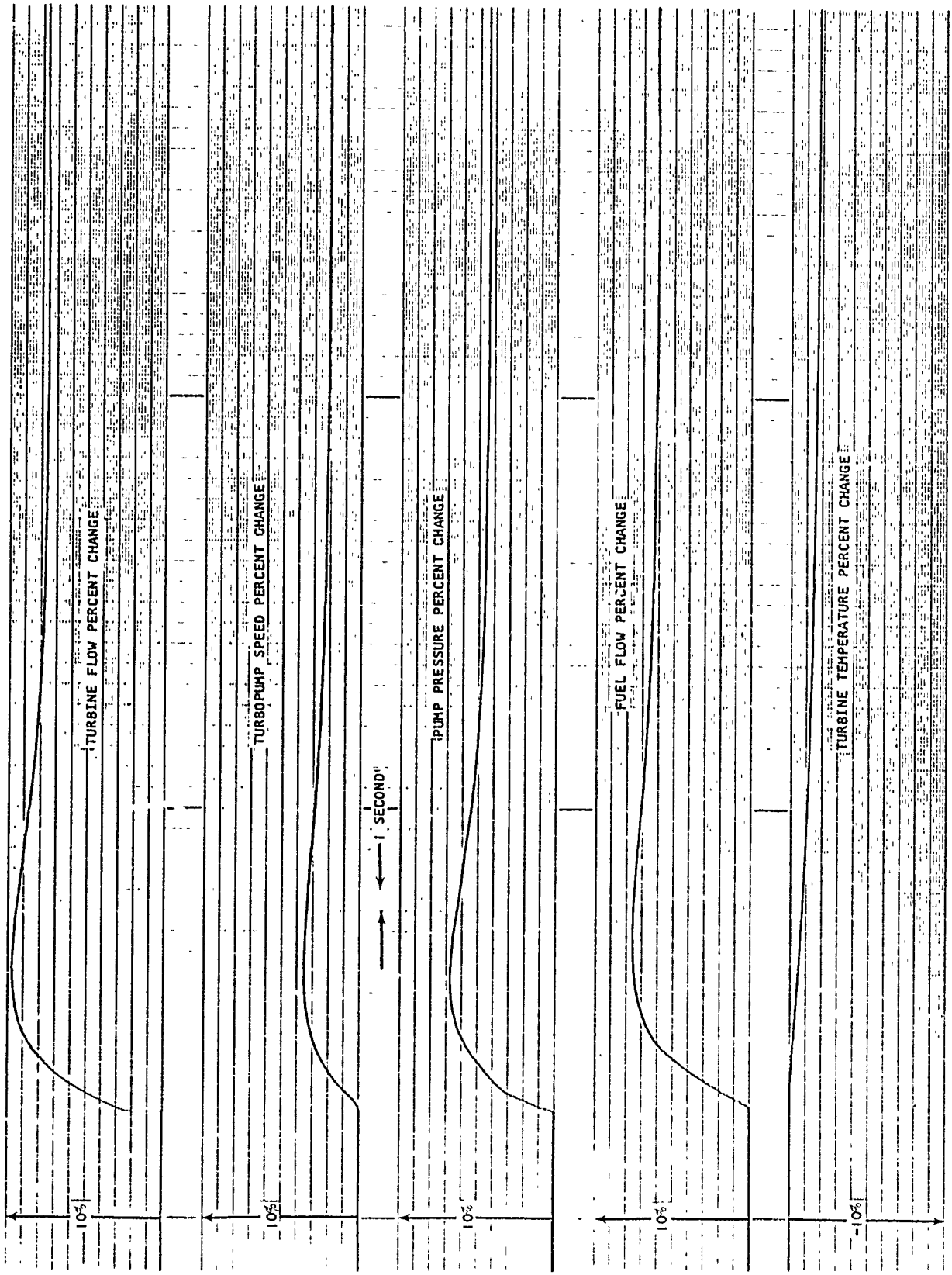

B-1277

Figure 52. System Response to a 3-Percent Step Change in Throttle Area for Condition 4

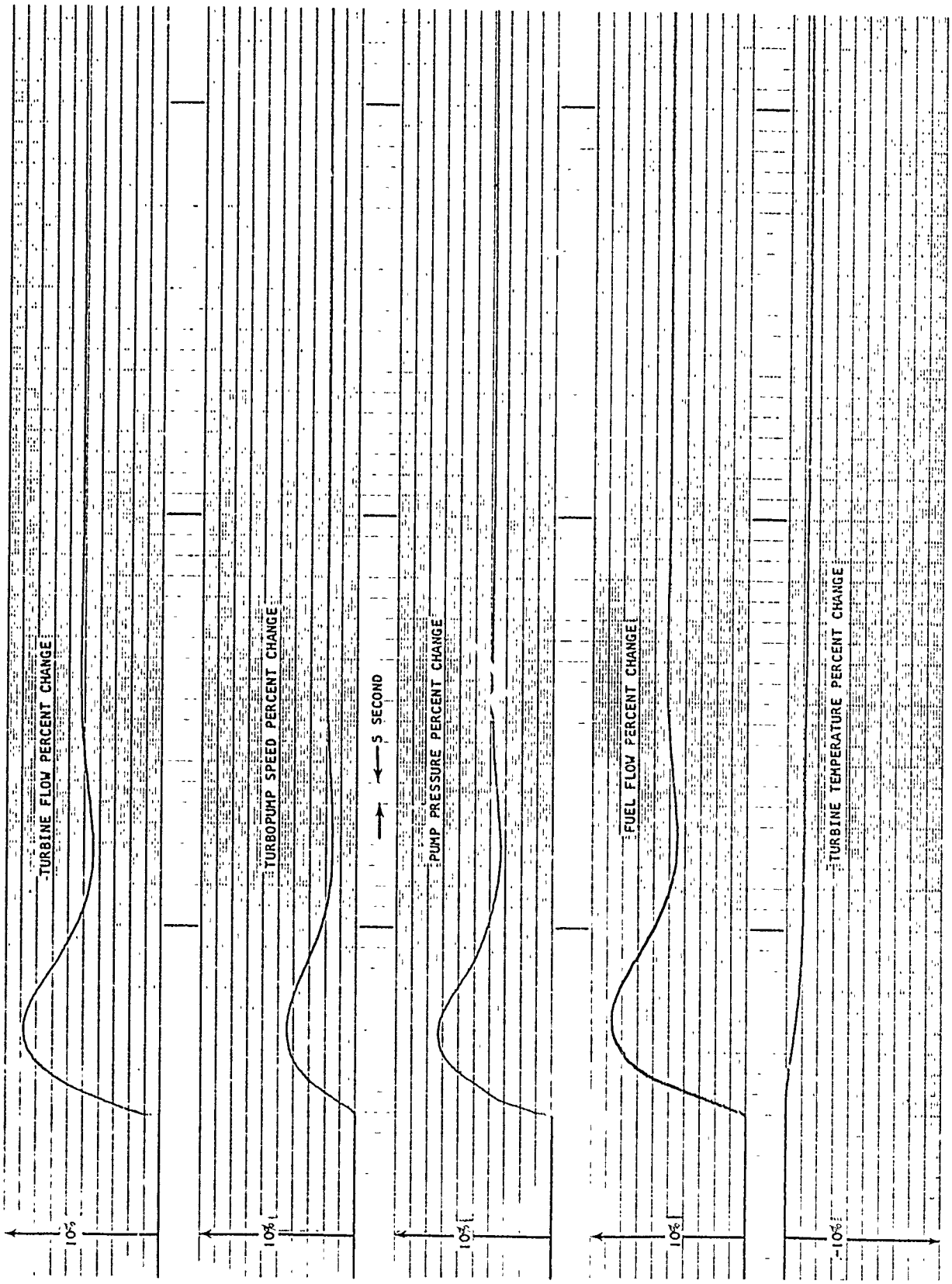

B-1278

Figure 53. System Response to a 1.5-Percent Step Change in Throttle Area for Condition 5

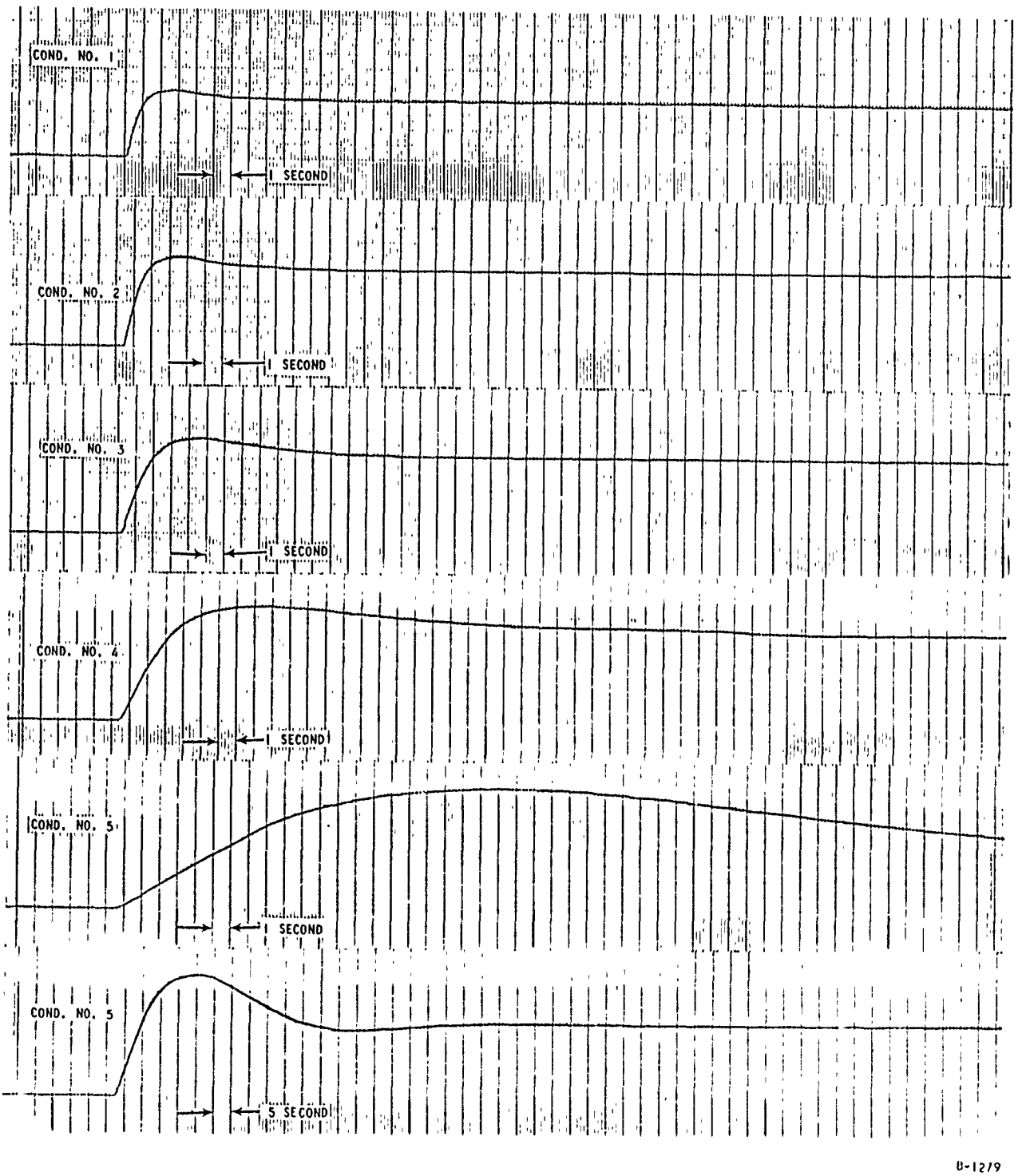

Figure 54. Fuel Flow Response to a Step Change in Throttle Area

4. Analysis of Results

A summary of the open-loop system performance characteristics has been plotted for each condition and is presented in Figure 55. Included are fuel flow and system gain vs throttle area and rise time and percent overshoot vs nominal fuel flow. Open-loop performance refers to the response of fuel flow to arbitrary changes in throttle area. System gain is the ratio of steady-state fuel flow change to a change in throttle area having the units of $\frac{lb}{sec}$ /in.^{2}. Rise-time and percent overshoot are defined in the sketch below.

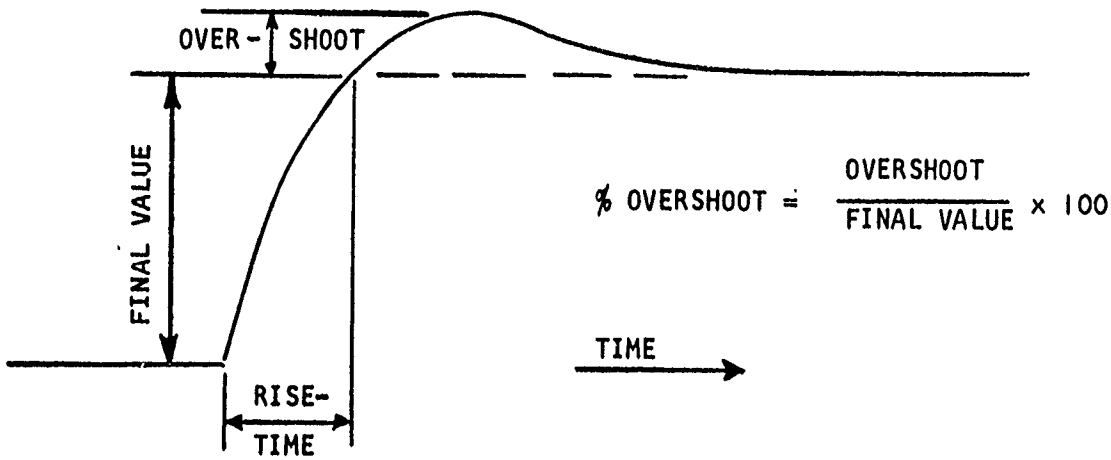

Fuel flow characteristics are highly nonlinear with respect to throttle area. System gain increases steadily with increased throttling, changing by a factor of 25 from 4 to 100 $\frac{lb}{sec}$/in.^{2} over the operating range. Rise-time and percent overshoot also increase with increased throttling. Rise-time increases from 1.0 to 7.5 sec. Percent overshoot increases from 15 percent to 65 percent but maintains a high degree of damping.

The dynamic characteristics discussed here indicate the response to small magnitude changes at discrete operating conditions. A large magnitude step change in throttle area covering the whole operating range between 14.5 and 1.9 lb/sec fuel flow would result in a rise-time somewhere between 1.0 and 7.5 sec. Probably a rise time of about 2 to 3 sec would be experienced as a result of the nonlinear relation between rise-time and fuel flow rate.

The increase in rise-time with increased throttling is primarily a result of the slope of the system operating torque-speed curve. This is demonstrated in Figure 56, which is a plot of torque vs speed for steady-state system operation. Two equal speed change requirements of 5000 rpm each are indicated at the low-speed and high-speed ranges, and are identified as ΔN_1 and ΔN_2, respectively. Assuming that a step change in throttle area were introduced to achieve

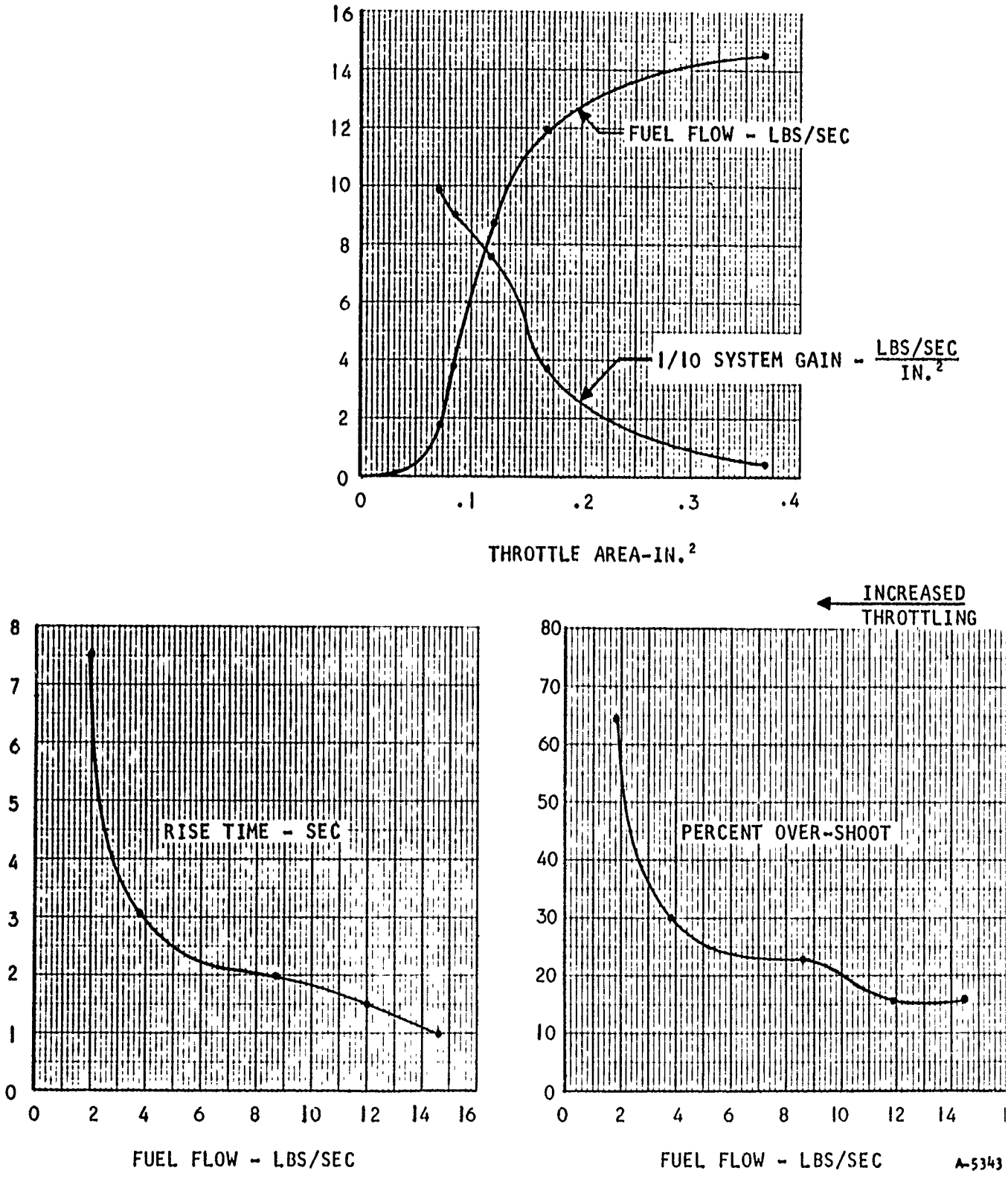

Figure 55. Open Loop Fuel Transfer System Characteristics

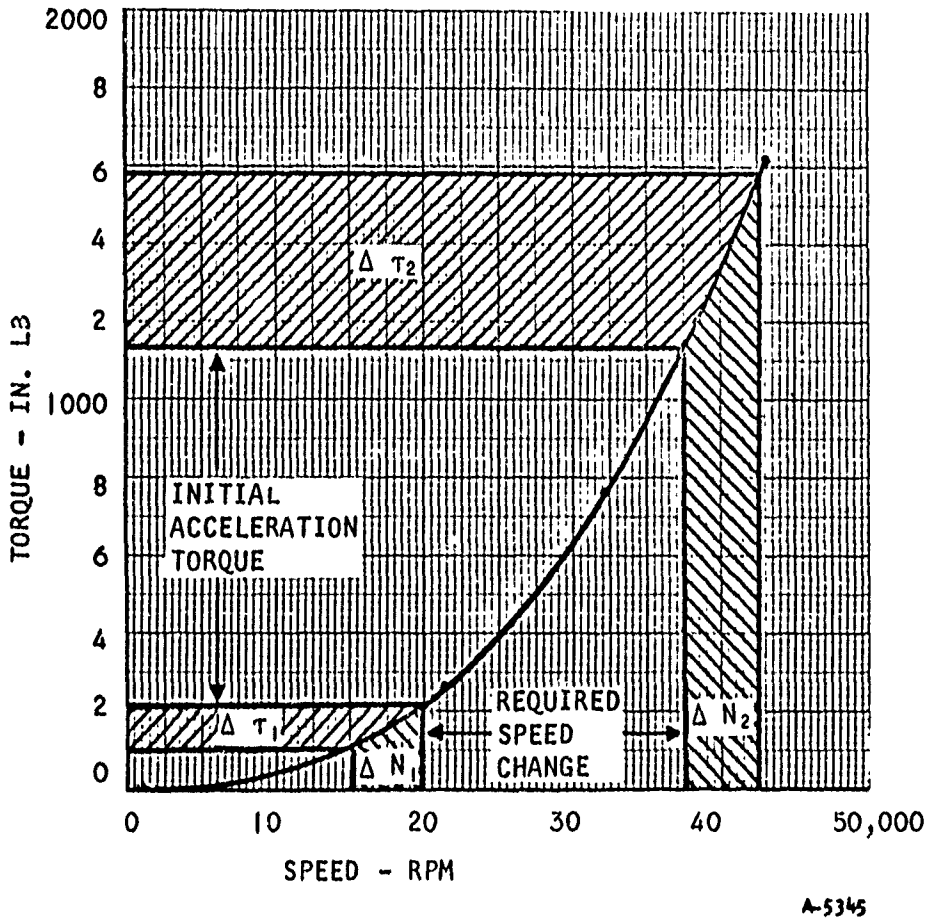

Figure 56. System Operating Torque - Speed Curve

these speed changes, the changes in steady-state system torque which would result are initially available for acceleration. It can be seen that the available acceleration torque for ΔN_1 (heavy throttling) is considerably less than that available for ΔN_2 (light throttling). The relative time required to achieve the speed changes can be seen by examining the impulse-momentum equation shown below in rotational terminology.

$$\Delta\tau . t = J \frac{2\pi}{60} \Delta N$$

The net torque available for acceleration times time (angular impulse) is equal to the mass moment of inertia times the change in rotational speed (change in angular momentum). The factor $2\pi/60$ converts rpm to radians per second. Since the mass moment of inertia and speed change are identical in the two cases and $\Delta\tau_1$ is less than $\Delta\tau_2$, it will take a longer time to obtain ΔN_1 than to obtain ΔN_2. This demonstrates the reason for increased rise time with increased throttling. It would not be so if the torque-speed relationship were linear. Assuming for simplicity that an average acceleration torque existed throughout the acceleration period, the time required to achieve a given speed change would be

$$t = J \frac{2\pi}{60} \frac{\Delta N}{\Delta \tau}$$

As ΔN approaches zero

$$t = J \frac{2\pi}{60} \frac{dN}{d\tau}$$

or $$t = J \frac{2\pi}{60} / \frac{d\tau}{dN}$$

which says that the time required would be inversely proportional to the slope of the torque-speed curve. If this is the predominant influence, then the ratio of rise-time should be approximately equal to the inverse ratio of torque-speed slope between conditions No. 1 and No. 5. A plot of the torque-speed slope vs speed is provided in Figure 57, which shows the following relations:

Rise Time

$$\frac{\text{Condition No. 5}}{\text{Condition No. 1}} = \frac{7.5 \text{ sec}}{1.0 \text{ sec}} = 7.5$$

Torque-Speed Slope

$$\frac{\text{Condition No. 1}}{\text{Condition No. 5}} = \frac{0.1075 \frac{\text{in.-lb}}{\text{rpm}}}{0.0156 \frac{\text{in.-lb}}{\text{rpm}}} = 6.9$$

or $$\frac{(tr)_5}{(tr)_1} \approx \frac{(d\tau/dN)_1}{(d\tau/dN)_5}$$

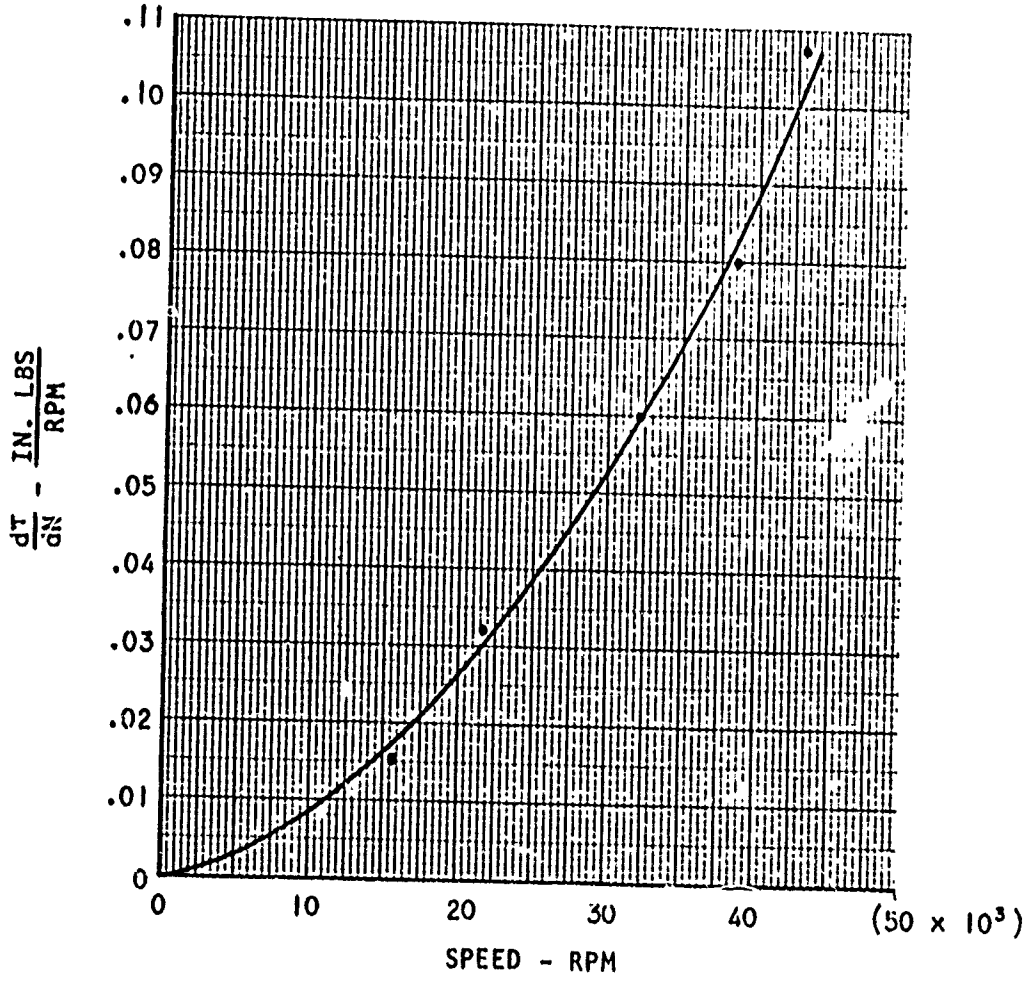

RISE TIME:

$$\frac{\text{COND NO.5}}{\text{COND NO.1}} = \frac{7.5}{1.0} = 7.5$$

TORQUE-SPEED SLOPE:

$$\frac{\text{COND NO.1}}{\text{COND NO.5}} = \frac{0.1075}{0.0156} = 6.9$$

Figure 57. Slope of System Operating Torque-Speed Curve

which supports the conclusion that the increase in rise time with increased throttling is predominantly a result of the decrease in slope of the steady-state torque-speed curve.

5. Closed-Loop Control

No detailed analysis of closed-loop control was made. However, it is mentioned here to point out that the relatively slow response displayed at the heavily throttled conditions can be significantly improved through proper closed-loop control. An open-loop response to a step change in the fuel flow demand sees a step change in throttle area as an input which was demonstrated in this study. A proper closed-loop control response to a step change in fuel flow demand would not see a step change in throttle area, but instead the throttle area would exceed its final value and would gradually return, thereby providing excess torque to increase system response. This is demonstrated in the sketch below.

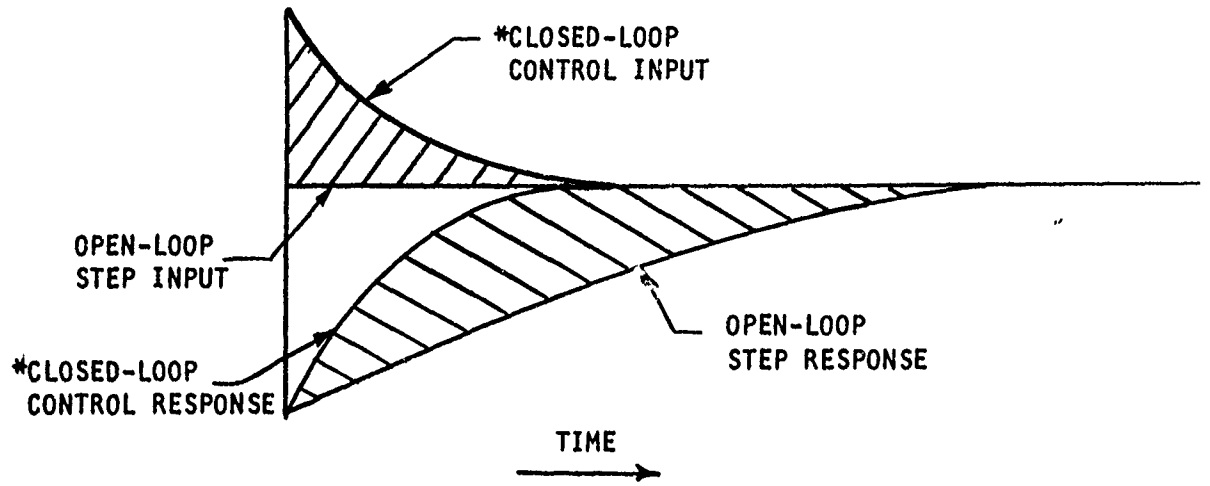

The shaded areas indicate the difference between open-loop and closed-loop throttle area inputs and fuel flow responses. The degree of excess throttle area desired at each operating condition would be different, requiring a nonlinear, variable gain control or a compromise providing the most satisfactory performance over the operating range.

DERIVATION OF SYSTEM EQUATIONS

The following is a discussion and derivation of the system equations making up a mathematical model of the fuel transfer system. This model consists of 33 simultaneous equations containing five time integrals and one time derivation resulting in a fourth-order dynamic system. The discussion will be separated into system component equations and the system fluid transport equations.

GH_2 Turbine

Torque is the output parameter of interest from the turbine with respect to system operation. Turbine torque is generated from the turbine power equations:

$$(\text{Shaft power}) = (\text{turbine isentropic power})\ (\text{efficiency})$$

$$\left(\tau_T\ N\ \frac{2\pi}{60}\right) = (W_T\ H_{ad})\ \eta_T$$

Torque times speed equals flow times adiabatic head times turbine efficiency. Speed in rpm is converted by $2\pi/60$ to radians per second. Solving the power equation for turbine torque provides the first system equation:

$$\tau_T = \frac{60}{2\pi} \cdot \frac{W_T\ H_{ad}\ \eta_T}{N} \qquad (18)$$

Turbine flow (W_T) and speed (N) will be generated in other sections of the mathematical model. Adiabatic head (H_{ad}) by definition is the available isentropic energy per pound of gas mathematically stated in terms of temperature as

$$H_{ad} = C_P\ (T_T - T_{ad})$$

where C_P is the gas specific heat, T_T is the inlet turbine temperature, and T_{ad} is the adiabatic discharge temperature. Using the temperature-pressure relation of the adiabatic process the adiabatic temperature in terms of pressure ratio is

$$T_{ad} = T_T\ P_{rT}^{\frac{k-1}{k}}$$

where P_{rT} is the turbine pressure ratio, and k is the adiabatic exponent. Substituting in the adiabatic equation and rearranging gives

$$H_{ad} = T_T C_P \left[1 - P_{rT}^{\frac{k-1}{k}} \right] \tag{19}$$

which becomes the second system equation.

Turbine pressure ratio is defined as

$$P_{rT} = \frac{P_N}{P_T} \tag{20}$$

where P_N is the discharge nozzle pressure and P_T is the turbine inlet pressure.

Turbine inlet flow is choked and turbine pressure is generated from the choked flow equation

$$P_T = K_T W_T \sqrt{T_T} \tag{21}$$

where K_T is the turbine inlet flow constant. Discharge nozzle flow is also choked and nozzle pressure is

$$P_N = K_N W_T \sqrt{T_N} \tag{22}$$

where K_N is the nozzle flow constant and T_N is the nozzle temperature.

Thermodynamic turbine efficiency is defined as the ratio of actual energy removed per pound of gas to available isentropic energy per pound of gas or mathematically expressed as

$$\eta_T = \frac{C_P (T_T - T_N)}{H_{ad}}$$

Solving for discharge nozzle temperature provides the sixth system equation

$$T_N = T_T - \frac{\eta_T H_{ad}}{C_P} \tag{23}$$

Thermodynamic efficiency is assumed to dominate the overall turbine efficiency, therefore mechanical deficiencies have been neglected.

Turbine efficiency is a function of turbine speed and adiabatic head. The equation generating turbine efficiency is a parabolic curve fit of the theoretical curve presented in the semi-annual Progress Report AAC-4574, and reproduced here in Figure 58. The resulting equation is

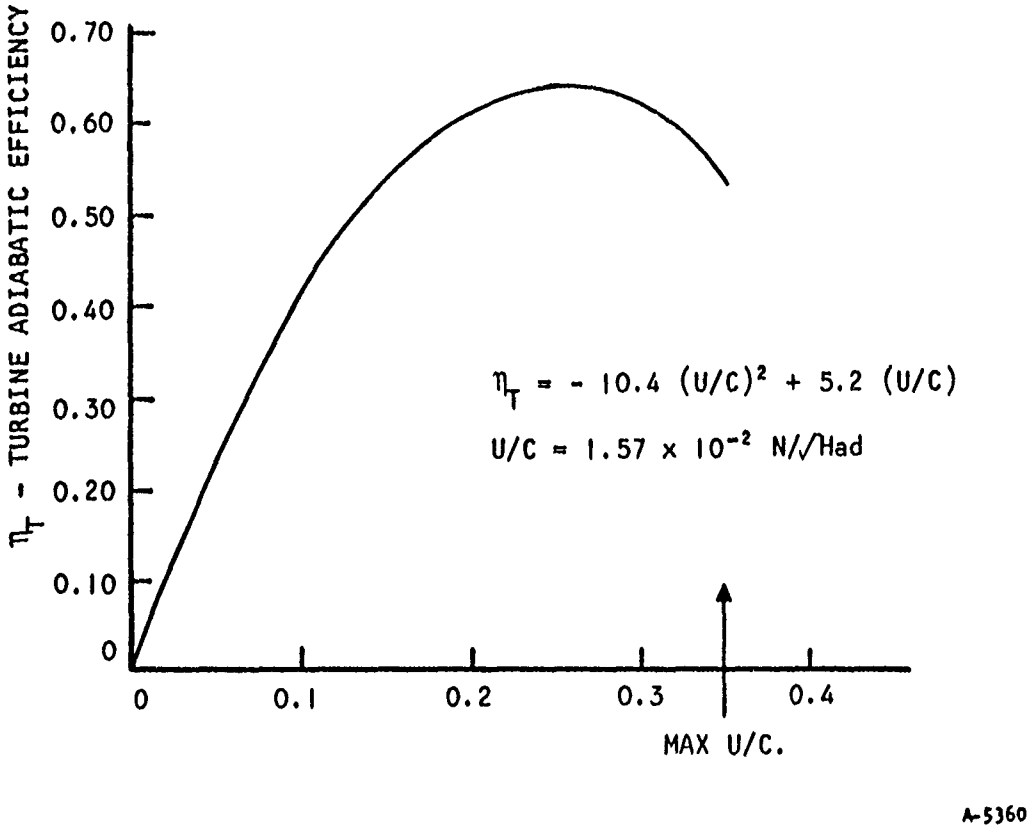

Figure 58. Theoretical Turbine Efficiency Curve

$$\eta_T = K_{\eta_1} \frac{N}{\sqrt{H_{ad}}} - K_{\eta_2} \frac{N^2}{H_{ad}} \qquad (24)$$

where K_{η_1} and K_{η_2} are coefficients of the curve fit.

An alternate expression for Equation (18) generating turbine torque can be obtained by substituting Equation (24) for turbine efficiency in Equation (18) which then becomes

$$\tau_T = W_T \left(\frac{60\ K_{\eta_1}}{2\pi} \sqrt{H_{ad}} - \frac{60\ K_{\eta_2}}{2\pi} N \right) \qquad (18)$$

This eliminates one of the variables (η_T) from Equation (18) and reduces it from two multiplications and one division of variables to one multiplication of variables for computer convenience.

LH_2 PUMP

Pump pressure is a function of pump flow and speed as represented in the estimated pump map of Figure 59. This map supersedes all previous estimates.

$$P_P = f_1 (W_P, N) \qquad (25)$$

Pump load torque is obtained from the pump power equation

(shaft power) (efficiency) = (flow power)

$$(\tau_P N \frac{2\pi}{60}) \eta_P = (P_P \frac{W_P}{\rho_P}) .$$

Solving for pump torque gives the ninth system equation

$$\tau_P = \frac{60}{2\pi\rho_P} \cdot \frac{P_P W_P}{N \eta_P} \qquad (26)$$

where ρ_P is LH_2 density at the pump and is assumed to be constant. Pump efficiency is also a function of pump flow and speed as represented by the estimated efficiency curves of Figure 60.

$$\eta_P = f_2 (W_P, N) \qquad (27)$$

Turbopump Speed

The turbine and pump are directly coupled with a 1:1 speed ratio, allowing the direct summation of turbine moment of inertia and pump moment of inertia into one overall turbopump moment of inertia. Turbopump speed is obtained from the basic F = ma relation in terms of angular motion,

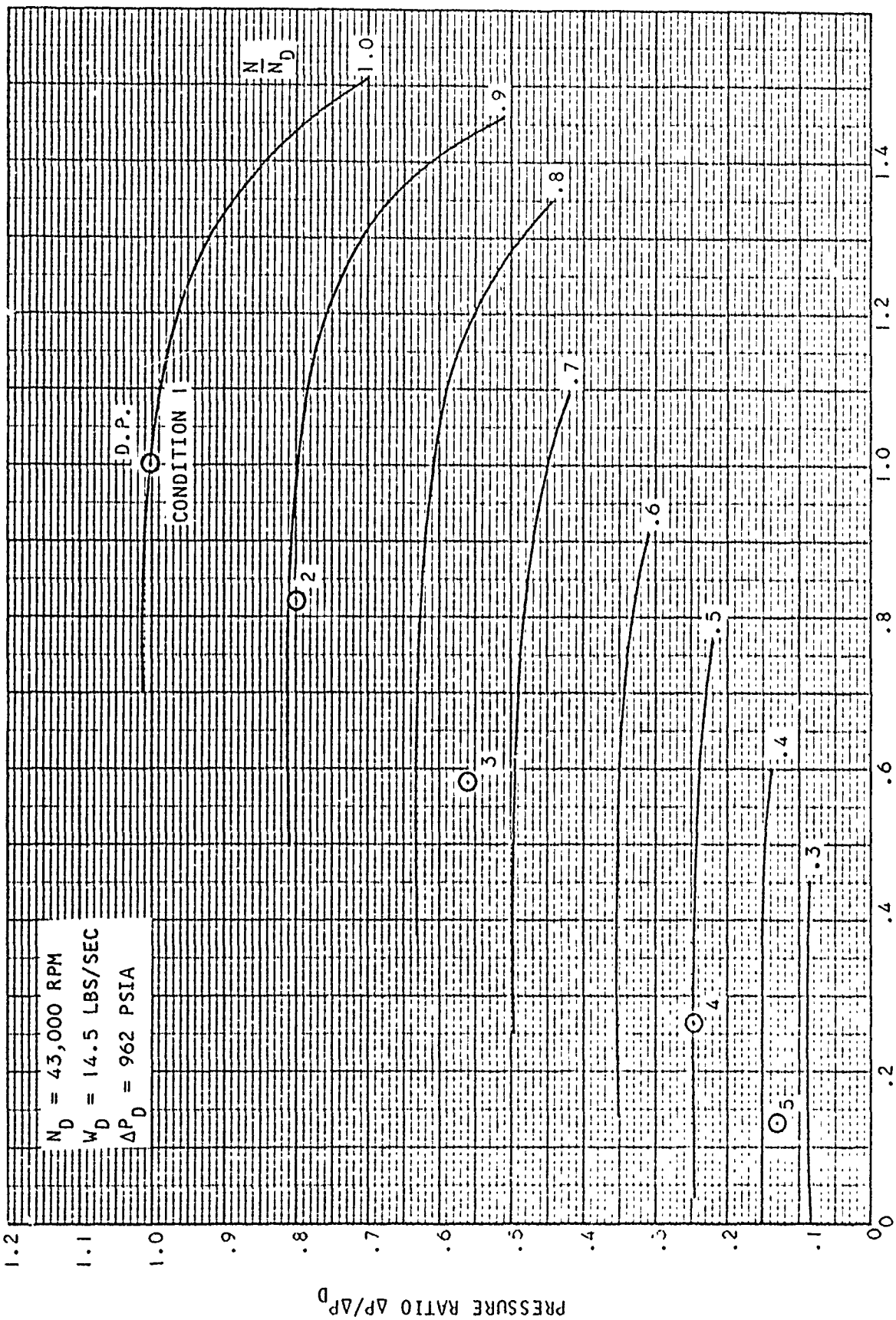

Figure 59. Estimated LH_2 Pump Map

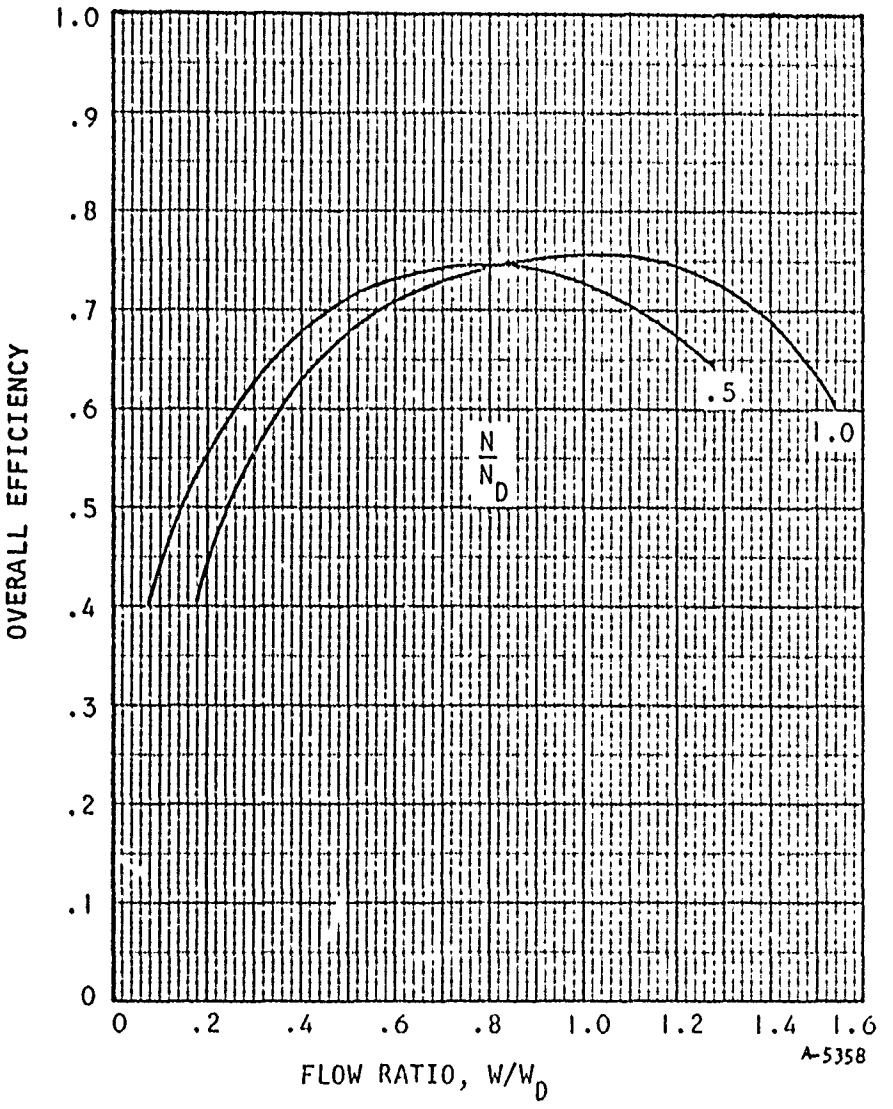

Figure 60. Estimated Pump Efficiency

$$\tau = J\left(\frac{2\pi}{60}\ \frac{dN}{dt}\right)$$

where τ is the excess or deficiency of torque available for speed change, J is the overall mass moment of inertia, $\frac{2\pi}{60}$ is a conversion constant between rpm and radian per second, and $\frac{dN}{dt}$ is the time rate of change of speed in rpm per second. Substituting for τ the difference between turbine developed torque and pump load torque $(\tau_T - \tau_P)$, and solving for turbopump speed gives

$$N = \frac{60}{2\pi J}\int (\tau_T - \tau_P)\, dt \qquad (28)$$

making turbopump speed a function of the time integral of the net torque difference between turbine and pump.

Heat Exchangers

One discussion is presented covering the mathematical description of both main and auxiliary heat exchangers, since their mathematical forms are identical. The subscripts used will be general and are applicable to both heat exchangers covering six pairs of equations ranging from 29 through 40.

Both the temperature drop and temperature level of the combustion products along the hot side of both heat exchangers are considered relatively constant. This is based on the heat exchanger design calculations, presented later on, which show a maximum upstream temperature of 4925°R and a minimum downstream temperature of 4590°R over five operating conditions covering the range of the engine. For a given operating condition, the small percent temperature drop along the heat exchangers is due to the large mass flow rate of the combustion products. A relatively small change in operating temperature level between conditions is due to an assumption of constant mixture ratio made in the design calculations of the heat exchangers.

The rate of heat transferred from the hot-side gases to the metal is

$$Q_H = h_H A (T_H - T_M) \qquad (29, 35)$$

where h_H is the hot-side heat transfer coefficient; A is the heat transfer surface area; T_H is the hot-side gas temperature; and T_M is the metal temperature. The coefficient h_H is a function of hot-side flow rate (W_H) and takes the form

$$h_H = \frac{dh_H}{dW_H}\ W_H \qquad (30, 36)$$

where $\frac{dh_H}{dW_H}$ is the rate of change of h_H with respect to W_H. Figures 61 and 62

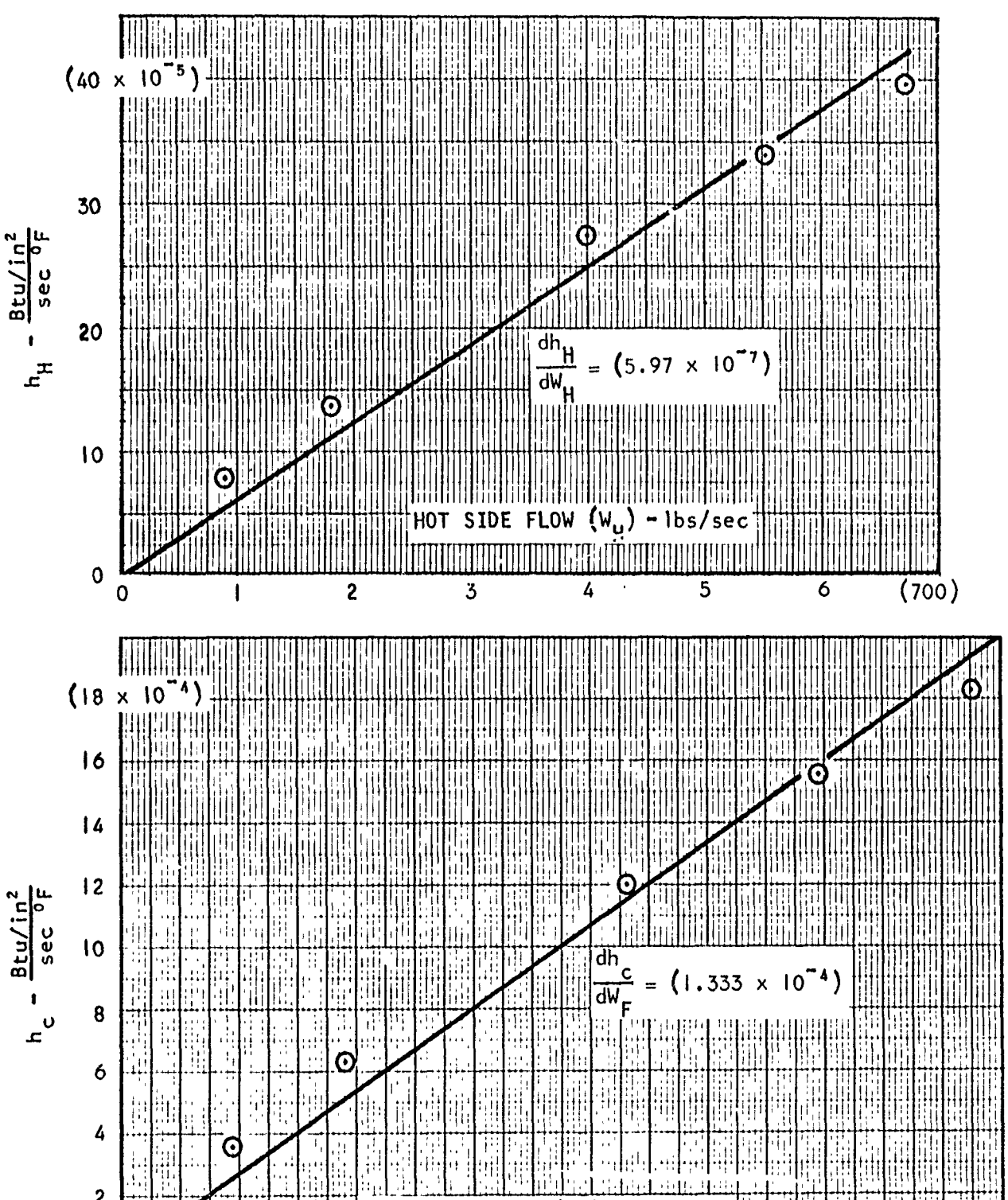

Figure 61. Heat Transfer Coefficients vs Flow for Main Heat Exchanger

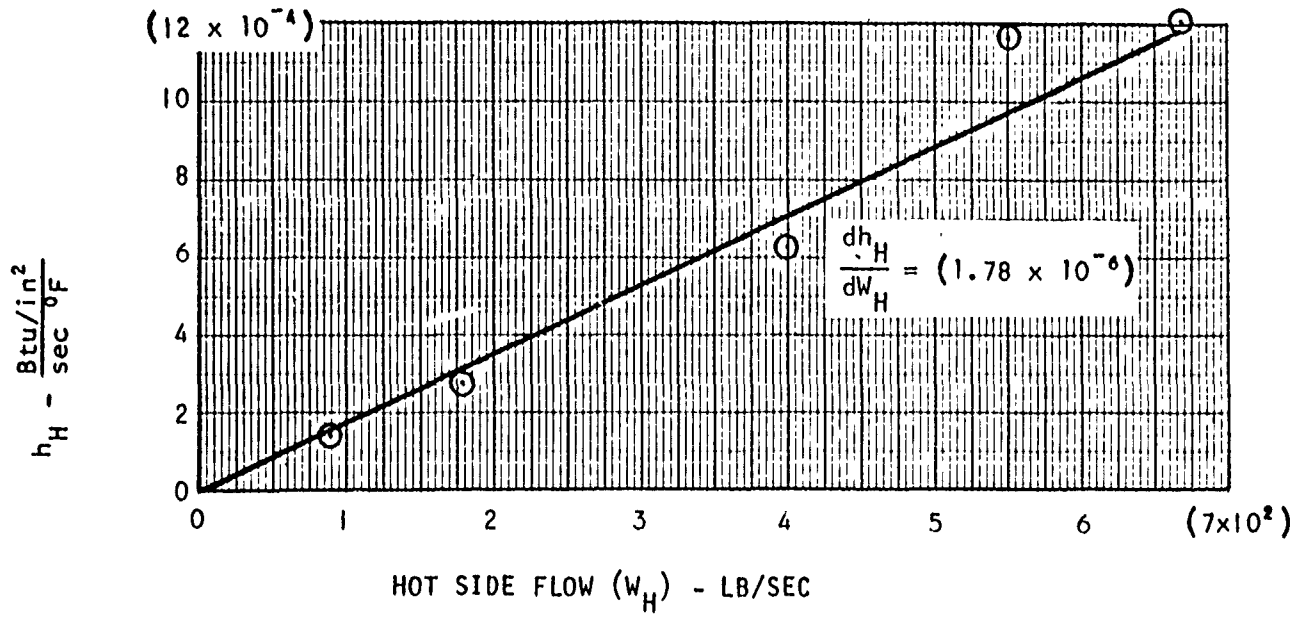

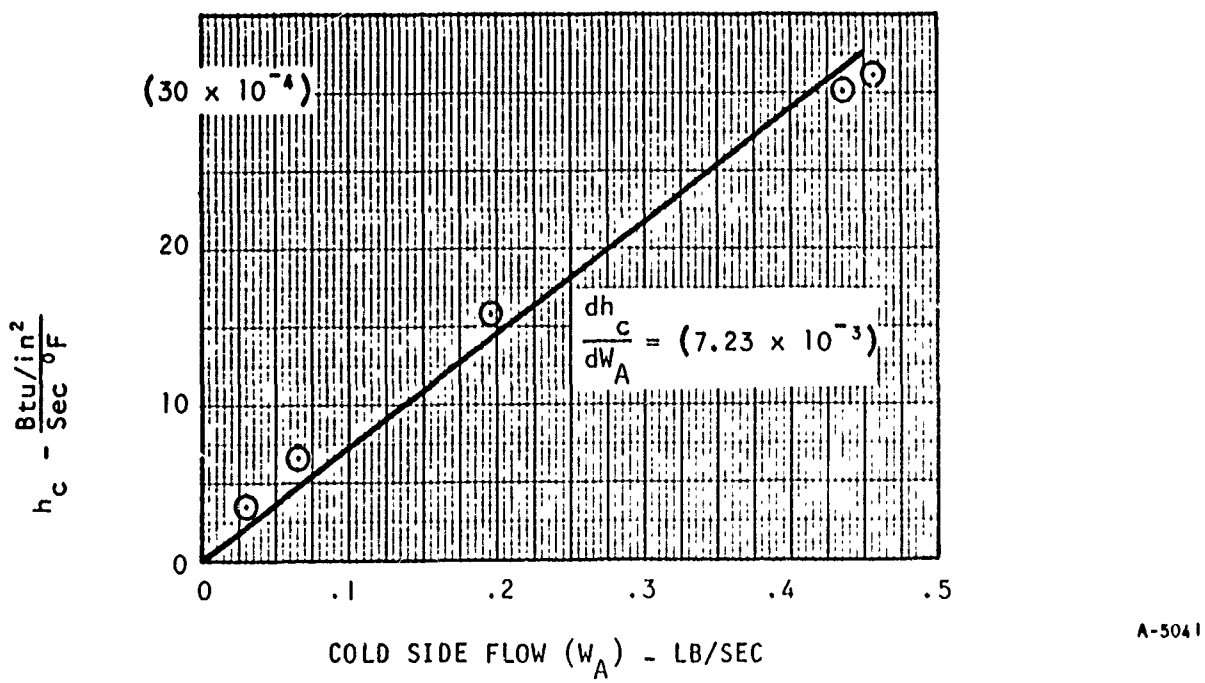

Figure 62. Heat Transfer Coefficients vs Flow for Auxiliary Heat Exchanger

are plots of heat transfer coefficients vs flow rate for both main and auxiliary heat exchangers; the plots have been made from the heat exchanger design calculations presented in Tables 3 through 7. The derivatives $\frac{dh}{dw}$ are considered constant and are evaluated from straight-line approximations of these plots.

The metal temperature is

$$T_M = \frac{1}{M\ C_{P_M}} \int (Q_H - Q_C)\ dt \qquad (31, 37)$$

where M is the metal mass, C_{P_M} is the metal specific heat, and $\int (Q_H - Q_C)\ dt$ is the time integral of the net rate of heat being stored in the metal.

The rate of heat being transferred from the metal to the cold side is

$$Q_c = h_c\ A \left(T_M - \frac{T_{C_1} + T_{C_2}}{2} \right) \qquad (32, 38)$$

where h_c is the cold-side heat transfer coefficient; A is again the heat transfer area; T_M is the metal temperature; and $\frac{T_{C_1} + T_{C_2}}{2}$ is the average cold-side temperature. Linear temperature distribution is assumed.

The cold-side heat transfer coefficient (h_c) is a function of cold-side flow (W_c) and also takes the form

$$h_c = \frac{dh_c}{dW_c}\ W_c \qquad (33, 39)$$

which was discussed in the description of Equations 30, 36.

Cold-side discharge temperature, which is of primary interest, is generated from:

$$T_{c_2} = T_{c_1} + \frac{Q_c}{W_c\ C_{P_c}} \quad \text{-----} \quad T_{c_2} < T_H \qquad (34, 40)$$

where T_{c_1} is the cold-side inlet temperature, and $\frac{Q_c}{W_c\ C_{P_c}}$ is the temperature rise due to heat added to the hydrogen flowing through the heat exchanger. Under no condition can T_{c_2} exceed T_H; in other words, the maximum cold-side discharge temperature is limited to the hot-side temperature as cold-side flow (W_c) approaches zero.

TABLE 3
HEAT EXCHANGER DESIGN CALCULATIONS

CONDITION NO. 1

Parameter	Main Heat Exchanger				Auxiliary Heat Exchanger			
	Hot Side		Cold Side		Hot Side		Cold Side	
	In	Out	In	Out	In	Out	In	Out
Weight flow, lb/sec	671		14.5		671		0.455	
Temperature, ^{0}R	4800	4760	46.2	400	4760	4745	46.2	2000
Heat transfer coefficient (h) Btu/in.^{2}-sec-^{0}F	4.01×10^{-4}		1.83×10^{-3}		1.22×10^{-3}		3.11×10^{-3}	
Heat flow, (Q), Btu/sec	19,800		19,800		3,220		3,220	
Core area, in.^{2}	13000		13000		1510		1510	
Specific heat, (C_p) Btu/lb-^{0}F	0.314		3.37		0.314		3.64	
Specific heat, (C_p) Btu/lb-^{0}F (Core)	0.070		0.070		0.070		0.070	
Core mass, lb	1210		1210		141		141	

TABLE 4
HEAT EXCHANGER DESIGN CALCULATIONS

CONDITION NO. 2

Parameter	Main Heat Exchanger				Auxiliary Heat Exchanger			
	Hot Side		Cold Side		Hot Side		Cold Side	
	In	Out	In	Out	In	Out	In	Out
Weight flow, lb/sec	550		11.9		550		0.435	
Temperature, ^{0}R	4756	4720	44.6	400	4720	4705	44.6	2000
Heat transfer coefficient (h) Btu/in.^{2}-sec-^{0}F	3.42×10^{-4}		1.56×10^{-3}		1.17×10^{-3}		3.0×10^{-3}	
Heat flow, (Q), Btu/sec	16,120		16,120		3060		3060	
Core area, in.^{2}	13000		13000		1510		1510	
Specific heat, (C_p) Btu/lb-^{0}F	0.314		3.37		0.314		3.64	
Specific heat, (C_p) Btu/lb-^{0}F (Core)	0.070		0.070		0.070		0.070	
Core mass, lb	1210		1210		141		141	

TABLE 5
HEAT EXCHANGER DESIGN CALCULATIONS

CONDITION NO. 3

Parameter	Main Heat Exchanger				Auxiliary Heat Exchanger			
	Hot Side		Cold Side		Hot Side		Cold Side	
	In	Out	In	Out	In	Out	In	Out
Weight flow, lb/sec	398		8.6		398		0.195	
Temperature, ^{0}R	4925	4880	42.8	400	4880	4870	42.8	2000
Heat transfer coefficient, (h) Btu/in.^{2}-sec-^{0}F	2.74×10^{-4}		1.20×10^{-3}		6.2×10^{-4}		1.58×10^{-3}	
Heat flow, (Q) Btu/sec	11770		11770		1370		1370	
Core area, in.^{2}	13000		13000		1510		1510	
Specific heat, (C_p) Btu/lb-^{0}F	0.315		3.37		0.315		3.64	
Specific heat, (C_p) Btu/lb-^{0}F (Core)	0.070		0.070		0.070		0.070	
Core mass, lb	1210		1210		141		141	

TABLE 6
HEAT EXCHANGER DESIGN CALCULATIONS

CONDITION NO. 4

Parameter	Main Heat Exchanger				Auxiliary Heat Exchanger			
	Hot Side		Cold Side		Hot Side		Cold Side	
	In	Out	In	Out	In	Out	In	Out
Weight flow, lb/sec	177		3.83		177		0.065	
Temperature, ^{o}R	4763	4720	40	400	4720	4710	40	2000
Heat transfer coefficient, (h) Btu/in.^{2}-sec-^{o}F	1.38×10^{-4}		6.32×10^{-4}		2.58×10^{-4}		6.56×10^{-4}	
Heat flow, (Q) Btu/sec	5300		5300		457		457	
Core area, in.^{2}	13000		13000		1510		1510	
Specific heat, (C_p) Btu/lb-^{o}F	0.314		3.37		0.314		3.64	
Specific heat, (C_p) Btu/lb-^{o}F (Core)	0.070		0.070		0.070		0.070	
Core mass, lb	1210		1210		141		141	

TABLE 7
HEAT EXCHANGER DESIGN CALCULATIONS

CONDITION NO. 5

Parameter	Main Heat Exchanger				Auxiliary Heat Exchanger			
	Hot Side		Cold Side		Hot Side		Cold Side	
	In	Out	In	Out	In	Out	In	Out
Weight flow, lb/sec	87		1.88		87		.029	
Temperature, ^{0}R	4641	4600	38.8	400	4600	4590	38.8	2000
Heat transfer coefficient, (h) Btu/in.^{2}-sec-^{0}F	7.82×10^{-5}		3.57×10^{-4}		1.34×10^{-4}		3.42×10^{-4}	
Heat flow, (Q) Btu/sec	2610		2610		204		204	
Core area, in.^{2}	13000		13000		1510		1510	
Specific heat, (C_p) Btu/lb-^{0}F	0.313		3.37		0.313		3.64	
Specific heat, (C_p) Btu/lb-^{0}F (Core)	0.070		0.070		0.070		0.070	
Core mass, lb	1210		1210		141		141	

Fluid Transport

Description of the fluid transport system is based on a series of lumped parameter concepts which are valid for the low frequency response range of the system.

The LH_2 transmission line creates an inertial lag between the pump and the engine heat exchangers. This manifests itself in the form of dynamic pressure drop across the transmission line as a result of acceleration of the liquid column. The line pressure (P_L) at the discharge end of the transmission line will be different from the pump discharge pressure (P_P) whenever flow is in the process of undergoing change (acceleration). The equation describing this phenomenon is:

$$P_L = P_P - \frac{\ell}{ag} \cdot \frac{dW_P}{dt} \tag{41}$$

where $\frac{\ell}{ag}$ is the inertial characteristics of the liquid column in terms of length, cross-sectional area and the gravitational constant; and $\frac{dW_P}{dt}$ is the liquid acceleration expressed as the time derivative of pump flow.

The pump flow is generated as the sum of flows going to the main heat exchanger (W_M) and to the auxiliary heat exchanger (W_A):

$$W_P = W_M + W_A \tag{42}$$

Fluid flow from the pump to the heat exchangers is assumed to be in the liquid state, changing to the gaseous state within the heat exchangers and being transported as a gas downstream.

Flow to the main heat exchanger is proportional to the square root of the pressure drop across the inlet portion of the heat exchanger:

$$W_M = K_M \sqrt{P_L - P_M} \tag{43}$$

where K_M is the constant of proportionality, P_L is the line pressure at the discharge end of the LH_2 transmission line and P_M is the gaseous pressure inside the heat exchanger. The total heat exchanger pressure drop has been lumped at the inlet to the heat exchanger.

Pressure inside the main heat exchanger is proportional to the quantity of gas stored which is the time integral of the difference between inlet and discharge heat exchanger flow. The effect of temperature variations on gas pressure in the heat exchanger is assumed small when compared to the effect of flow variations on gas pressure. The equation is:

$$P_M = K_{P_M} \int (W_M - W_F)\, dt \tag{44}$$

K_{P_M} is the proportionality constant and is evaluated from

$$K_{P_M} = \frac{R}{V_M} \cdot \frac{\bar{T}_F - T_L}{\text{Ln } \bar{T}_F/T_L}$$

where R is the gas constant, V_M is the heat exchanger volume, T_L is the inlet liquid hydrogen temperature and $\bar{T}_F$ is the design discharge fuel temperature. The expression $\frac{\bar{T}_F - T_L}{\text{Ln } \bar{T}_F/T_L}$ is the effective gas temperature in the heat exchanger assuming a linear temperature distribution with respect to volume; the derivation of this is presented in later on.

The fuel flow (W_F), which is the main heat exchanger discharge flow, is obtained from the sonic flow equation across the fuel injector, which is assumed to be choked:

$$W_F = K_{W_F} \frac{P_M}{\sqrt{T_F}} \tag{45}$$

where K_{W_F} is the injection nozzle sonic flow constant, P_M is the upstream pressure in the main heat exchanger, and T_F is the fuel injection temperature.

Flow to the auxiliary heat exchanger is generated in a similar manner as flow to the main heat exchanger discussed in Equation (43):

$$W_A = K_A \sqrt{P_L - P_A} \tag{46}$$

where P_A is the gas pressure inside the auxiliary heat exchanger. The volume of the GH_2 transmission line between auxiliary heat exchanger and throttle valve is lumped with the heat exchanger volume and one gaseous pressure is generated for both.

The auxiliary heat exchanger pressure is generated in a similar manner as the gaseous pressure inside the main heat exchanger, discussed in Equation (44), except that the GH_2 transmission line volume is lumped with the auxiliary heat exchanger volume:

$$P_A = K_{P_A} \int (W_A - W_T)\, dt \tag{47}$$

where K_{P_A} is the constant of proportionality W_A is the flow to the auxiliary heat exchanger, and W_T is turbine flow. K_{P_A} is evaluated from

$$K_{P_A} = R \frac{\bar{T}_T^{\,2} - T_L \bar{T}_T}{\bar{T}_T V_A \operatorname{Ln} \frac{\bar{T}_T}{T_L} + (\bar{T}_T - T_L) V_L}$$

where R is the gas constant, T_L is the liquid hydrogen inlet temperature, $\bar{T}_T$ is the design turbine inlet temperature, V_A is the volume associated with the auxiliary heat exchanger and V_L is the volume associated with the GH_2 transmission line. K_{P_A} is an expression of the effective temperature-volume relationship in a gas having a nonuniform temperature distribution which is partially linear and partially constant with respect to volume. K_{P_A} is also derived in later paragraphs.

Throttle Valve

Both choked and unchoked flow through the throttle valve is experienced in its operating range. Turbine flow is identical to throttle valve flow and is generated from the throttle valve flow equation. The equation is given the form of a choked flow equation modified by a pressure ratio function.

$$W_T = K_v \frac{A_v P_A}{\sqrt{T_T}} f(P_{rv}) \tag{48}$$

W_T is turbine flow, K_v is the subsonic flow constant, A_v is throttle area P_A is upstream (Aux Hx) pressure, T_T is turbine inlet temperature, and $f(P_{rv})$ is the valve pressure ratio function. The pressure ratio function takes the form

$$f(P_{rv}) = \sqrt{P_{rv}^{2/k} - P_{rv}^{\frac{k+1}{k}}} \tag{49}$$

$$0 < f(P_{rv}) < f(P_{rc})$$

$$P_{rc} = \left(\frac{2}{k+1}\right)^{\frac{k}{k-1}}$$

where k is the adiabatic exponent. The pressure ratio function is limited to its value of a function of the critical pressure ratio (P_{rc}). This means that

when the valve pressure ratio becomes supercritical the $f(P_{rv})$ becomes a constant equal to the $f(P_{rc})$. Equation (48) then becomes a choked flow equation where K_v times $f(P_{rc})$ equals the sonic flow constant. Throttle valve pressure ratio is defined as

$$P_{rv} = \frac{P_T}{P_A} \tag{50}$$

where turbine inlet pressure (P_T) is the downstream pressure, and auxiliary heat exchanger pressure (P_A) is the upstream pressure with respect to the throttle valve.

This completes the derivation and discussion of the system equations. A development of the linearized analog computer model from this system of nonlinear equations is presented following paragraphs.

Derivation of Gas Pressure Distributions

I. Gas With Linear Temperature Distribution With Respect to Volume

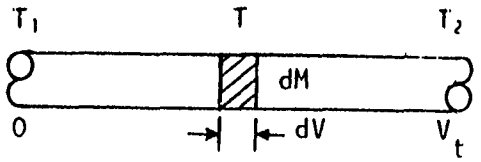

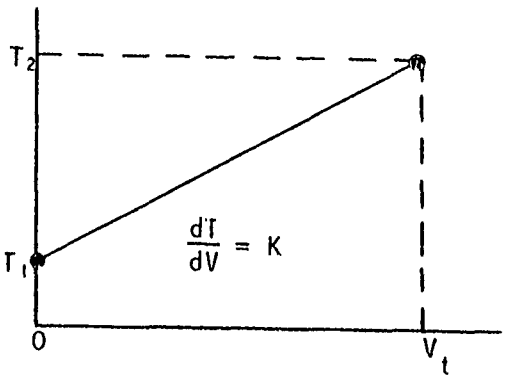

The equation of state is:

$$PV = MRT \tag{51}$$

for a uniformly distributed idea' gas.

The pressure in a nonuniformly distributed gas can be written as the differential form of the equation of state:

$$P = \frac{dMRT}{dV} \tag{52}$$

where dM is the differential mass contained in a differential volume (dV) at a temperature (T) along the container. The pressure is uniform throughout the container.

The equation relating temperature to volume is:

$$T = KV + T_1$$

$$dT = KdV \tag{53}$$

$$\frac{dT}{K} = dV$$

Substituting the differential volume (dV) of Equation (53) into the differential form of the equation of state Equation (52) gives:

$$P = \frac{dMRT}{dT/K}$$

and rearranging:

$$\frac{dT}{T} = \frac{KR}{P}\, dM \tag{54}$$

Equation (54) can be written in the form of a definite integral:

$$\int_{T_1}^{T_2} \frac{dT}{T} = \frac{KR}{P} \int_{o}^{M_t} dM$$

and performing the integration:

$$\left[\text{Ln } T_2 - \text{Ln } T_1\right] = \frac{KR}{P} \left[M_t - o\right]$$

and solving for pressure gives:

$$P = \frac{KRM_t}{\text{Ln } T_2/T_1} \tag{55}$$

where M_t is the total mass.

From Equation 53:

$$K = \frac{T_2 - T_1}{V_t} \tag{53}$$

where V_t is the total volume.

Substituting K of Equation (56) into Equation (55) gives:

$$\boxed{P = \frac{M_t R}{V_t} \cdot \frac{T_2 - T_1}{\text{Ln } T_2/T_1}} \tag{57}$$

where the expression $\frac{T_2 - T_1}{\text{Ln } T_2/T_1}$ is the effective temperature of the total gas in terms of Equation (51).

As a check, the effective temperature expression is evaluated as T_2 approaches T_1, resulting in a uniform temperature distribution.

$$\frac{T_2 - T_1}{\text{Ln } T_2/T_1} \quad \underset{T_2 \to T_1}{=} \quad \frac{0}{0}$$

which is indeterminate. Differentiating numerator and denominator:

$$\frac{dT_2}{\frac{T_1}{T_2} \cdot \frac{dT_2}{T_1}} = T_2 \underset{T_2 \to T_1}{=} T_1$$

which checks correctly for a uniform temperature distribution.

2. Gas With Discontinuous Temperature Distribution With Respect to Volume

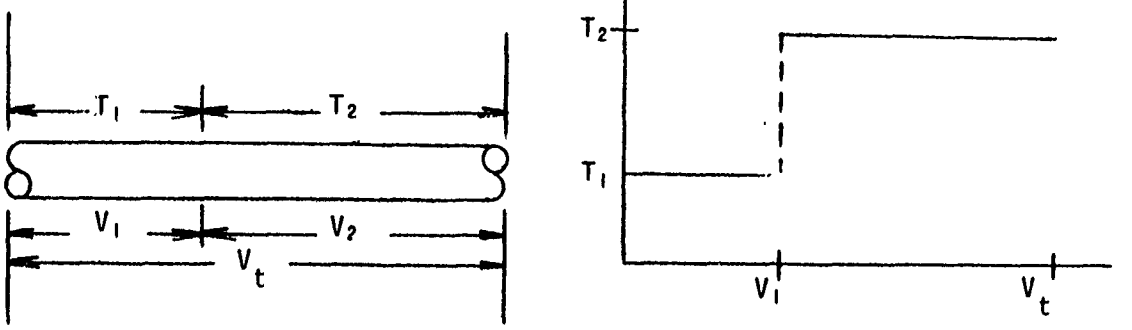

Using the equation of state for an ideal gas, the masses associated with volumes 1 and 2 are:

$$M_1 = \frac{PV_1}{RT_1} \tag{58}$$

$$M_2 = \frac{PV_2}{RT_2} \tag{59}$$

where the pressure is uniform throughout the total volume (V_t).

The equation can then be written:

$$M_t = M_1 + M_2 \tag{60}$$

where M_t is the total mass.

Substituting Equations (58) and (59) into Equation (60):

$$M_t = \frac{PV_1}{RT_1} + \frac{PV_2}{RT_2}$$

$$= \frac{P}{R}\left(\frac{T_2V_1 + T_1V_2}{T_1T_2}\right)$$

and solving for pressure:

$$\boxed{P = M_tR \quad \frac{T_1T_2}{T_2V_1 + T_1V_2}} \tag{61}$$

where the expression $\frac{T_1T_2}{T_2V_1 + T_1V_2}$ is the effective temperature-volume relationship.

Checking the expression as T_1 approaches T_2 for the case of uniform temperature distribution:

$$\frac{T_1T_2}{T_2V_1 + T_1V_2} \quad \underset{T_1 \to T_2}{=} \quad \frac{T_2^2}{T_2\,(V_1 + V_2)} = \frac{T_2}{V_t}$$

which checks correctly.

3. Gas With Discontinuous Temperature Distribution; Partially Linear and Partially Constant With Respect to Volume

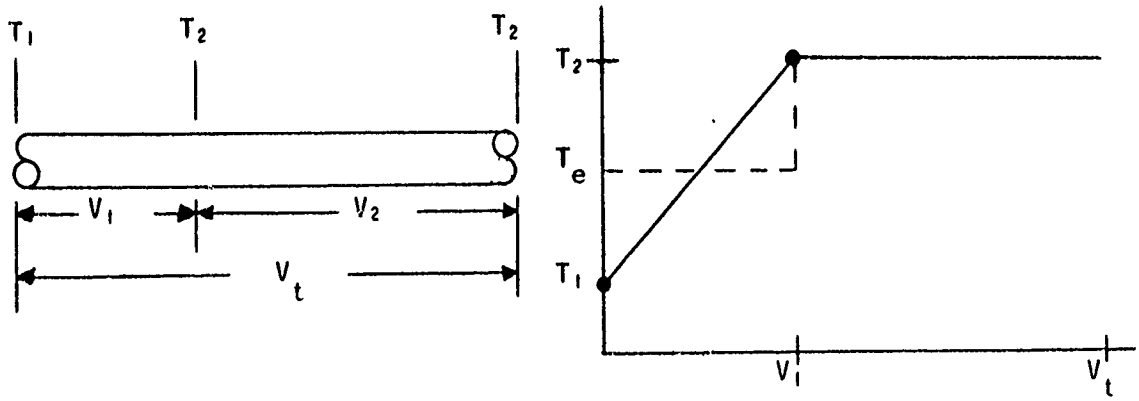

Assuming an effective temperature (T_e) for the linear distributed portion of the total volume and substituting it in place of T_1 in Equation (61) gives:

$$P = M_tR \quad \frac{T_eT_2}{T_2V_1 + T_eV_2} \tag{62}$$

The effective temperature of the linear distributed portion was developed in Equation 7 and is:

$$T_e = \frac{T_2 - T_1}{\ln T_2/T_1} \tag{63}$$

Substituting the effective temperature of Equation (63) into Equation (62) and reducing gives:

$$\boxed{P = M_t R \quad \frac{T_2^2 - T_1 T_2}{T_2 V_1 \ln T_2/T_1 + (T_2 - T_1) V_2}} \tag{64}$$

which defines the pressure of the gas in terms of the temperature-volume relations and the total mass or quantity of gas in the container. Again, the effective temperature-volume relationship is checked for the case of uniform temperature distribution as T_2 approaches T_1:

$$\frac{T_2^2 - T_1 T_2}{T_2 V_1 \ln T_2/T_1 + (T_2 - T_1) V_2} \quad \underset{T_2 \to T_1}{=} \quad \frac{0}{0}$$

which is indeterminate. Differentiation of numerator and denominator gives:

$$\frac{(2T_2 - T_1)\, dT_2}{V_1 (1 + \ln T_2/T_1)\, dT_2 + V_2\, dT_2} \quad \underset{T_2 \to T_1}{=} \quad \frac{T_1}{V_1 (1+0) + V_2} = \frac{T_1}{V_t}$$

which is correct for a uniform temperature distribution.

DEVELOPMENT OF ANALOG COMPUTER MODEL

This section deals with the development of an analog computer model from the basic set of system equations derived previously. The basic set of system equations is nonlinear in nature. The development will discuss linearization and normalization processes used on the system of equations, evaluation of system constants and linear coefficients, and construction of a computer circuit diagram from the final set of equations.

Nonlinear System of Equations

The basic set of nonlinear system equations given earlier is listed in summary here, followed by a list of assumptions used in their derivation. The system of equations is complete and capable of computer simulation when the number of equations equals the number of dependent variables, inputs being independent variables. Note that every dependent variable in the system has an independent equation generating that variable.

1. Turbine

$$(1)\quad \tau_T = \frac{W_T H_{ad} \eta_T}{\frac{2\pi}{60} N} = \frac{K_{\eta 1}}{2\pi/60} W_T \sqrt{H_{ad}} - \frac{K_{\eta 2}}{2\pi/60} W_T N$$

$$(2)\quad H_{ad} = T_T C_P \left[1 - P_{rT}^{\frac{k-1}{k}}\right]$$

$$(3)\quad P_{rT} = \frac{P_N}{P_T}$$

$$(4)\quad P_T = K_T W_T \sqrt{T_T}$$

$$(5)\quad P_N = K_N W_T \sqrt{T_N}$$

$$(6)\quad T_N = T_T - \frac{\eta_T H_{ad}}{C_P}$$

$$(7)\quad \eta_T = K_{\eta 1} \frac{N}{\sqrt{H_{ad}}} - K_{\eta 2} \frac{N^2}{H_{ad}}$$

2. Pump

$$(8)\quad P_P = f_1\,(W_P,\ N)$$

$$(9)\quad \tau_P = \frac{P_P W_P}{\frac{2\pi}{60} P_P N \eta_P}$$

$$(10)\quad \eta_P = f_2\,(W_P,\ N)$$

3. Turbopump Speed

$$(11)\quad N = \frac{60/2\pi}{J}\int (\tau_T - \tau_P)dt$$

4. Main Heat Exchanger

$$(12)\quad Q_H = h_H\, A\, (T_H - T_M)$$

$$(13)\quad h_H = \frac{dh_H}{dW_H} W_H$$

$$(14)\quad T_M = T_{Mo} + \frac{1}{MC_{P_M}}\int (Q_H - Q_c)\,dt$$

$$(15)\quad Q_c\ h_c A\ \left(T_M - \frac{T_L + T_F}{2}\right)$$

$$(16)\quad h_c = \frac{dh_c}{dW_F} W_F$$

$$(17)\quad T_F = T_L + \frac{Q_c}{W_F C_{P_c}} \text{ - - - - - - - - } T_F < T_H$$

5. Auxiliary Heat Exchanger

$$(18)\quad Q_H = h_H\, A\, (T_H - T_M)$$

$$(19)\quad h_H = \frac{dh_H}{dW_H}\ \dot{W}_H$$

$$(20)\quad T_M = \dot{T}_{Mo} + \frac{1}{MC_{P_M}}\int (Q_H - Q_c)dt$$

$$(21)\quad Q_c = h_c A \left(T_M - \frac{T_L + T_T}{2}\right)$$

$$(22)\quad h_c = \frac{dh_c}{dW_A} W_A$$

$$(23)\quad T_T = T_L + \frac{Q_c}{W_A C_{Pc}} \text{ - - - - - - - - } T_T < T_H$$

6. Fluid Transport

$$(24)\quad P_L = P_P - \frac{\ell}{ag} \frac{dW_P}{dt}$$

$$(25)\quad W_P = W_A + W_M$$

$$(26)\quad W_M = K_M \sqrt{P_L - P_M}$$

$$(27)\quad P_M = K_{P_M} \int (W_M - W_F)dt$$

$$K_{P_M} = \frac{R}{V_M} \cdot \frac{\overline{T}_F - T_L}{\ln \overline{T}_F/T_L}$$

$$(28)\quad W_F = K_{W_F} \frac{P_M}{\sqrt{T_F}}$$

$$(29)\quad W_A = K_A \sqrt{P_L - P_A}$$

$$(30)\quad P_A = K_{P_A} \int (W_A - W_T)dt$$

$$K_{P_A} = R \frac{\overline{T}_{T^2} - T_L \overline{T}_T}{\overline{T}_T V_A \ln \overline{T}_T/T_L + (\overline{T}_T - T_L)V_L}$$

7. Throttle Valve

$$(31)\quad W_T = K_V \frac{A_V P_A}{\sqrt{T_T}} f(P_{rv})$$

$$(32)\quad f(P_{rv}) = \sqrt{P_{rv}^{2/k} - P_{rv}^{\frac{k+1}{k}}} \quad ---- \quad 0 < f(P_{rv}) < f(P_{rc})$$

$$P_{rc} = \left(\frac{2}{k+1}\right)^{\frac{k}{k-1}}$$

$$(33)\quad P_{rv} = \frac{P_T}{P_A}$$

8. List of Assumptions

1) Flow in the turbine discharge nozzle is choked.

2) Properties and conditions of LH_2 at the pump inlet are constant.

3) Temperature of combustion products along the hot side of both heat exchangers is constant due to the high mass flow rate and there is a constant mixture ratio between operating levels.

4) Fluid flowing from the pump to the heat exchangers is in a liquid state, changing to a gaseous state within the heat exchangers and being transported as a gas downstream.

5) Temperature distribution is linear with respect to volume in heat exchangers.

6) There is no significant heat leak or steady-state pressure drop in fluid transport lines

7) Engine fuel injection flow is choked.

8) Flow at turbine inlet is choked.

9) L . d parameter fluid transport descriptions are valid for systems lo. frequency response range.

10) Turbine overall efficiency is dominated by its thermodynamic efficiency; mechanical deficiencies are negligible.

11) Heat exchanger pressure drops have been lumped at the inlet to the heat exchange-.

9. Mathematical Block Diagram

The system of nonlinear equations can be displayed in another form called a block diagram. The diagram shows the complex interrelation of parameter between equations and is effectively a schematic diagram of the system of equations. It also serves to demonstrate the completeness of the mathematical system if no loops are left open lacking required inputs. A block diagram of the nonlinear system equations was made, organizing the diagram into major component blocks to distinguish between inter- and intracomponent mathematical relations. It is presented as Figure 63.

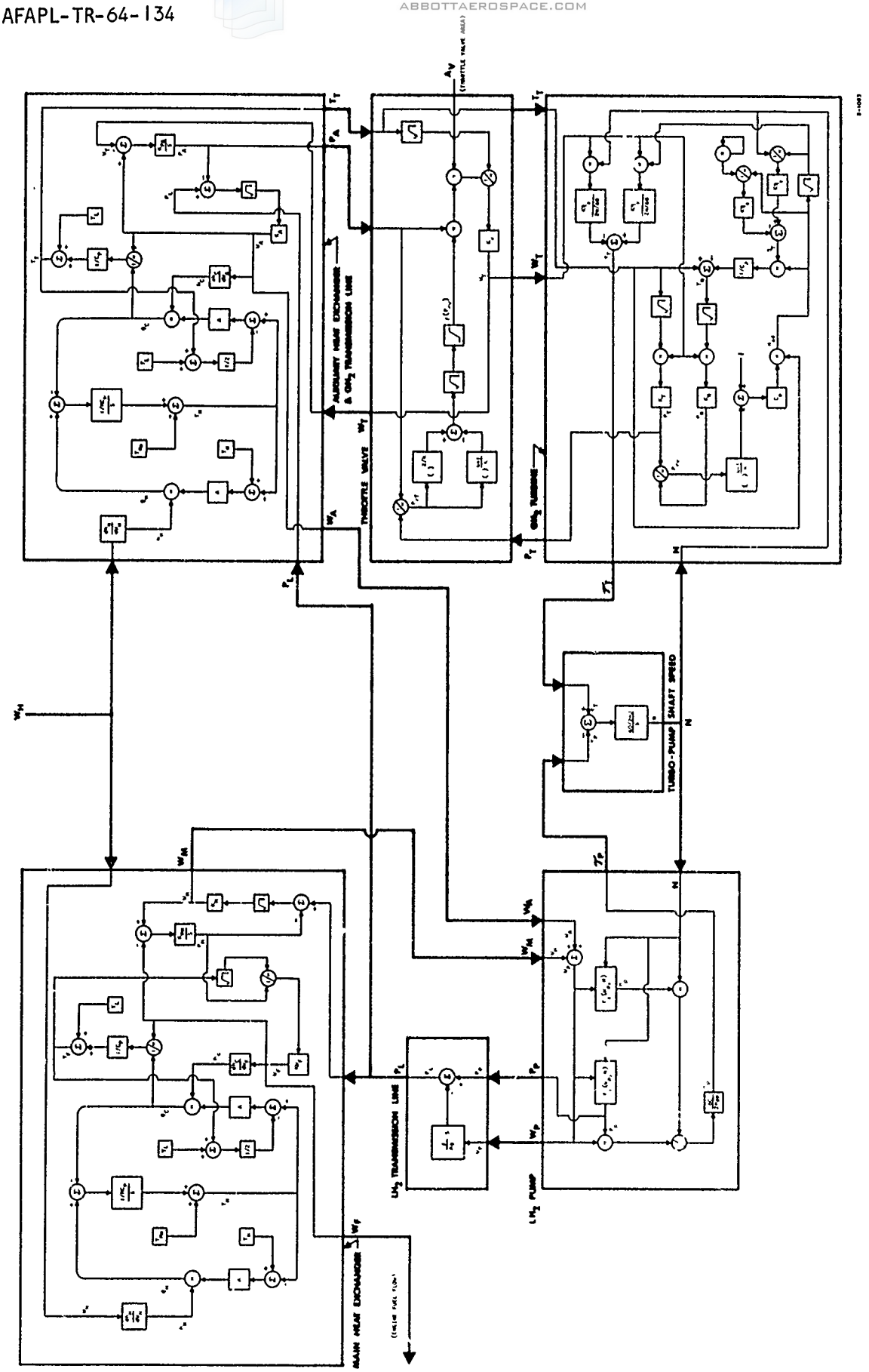

Figure 63. LH_2 Fuel Transfer System Mathematical Block Diagram

Linear Differential Equations

The system of nonlinear equations was linearized by differentiating each equation and writing it in its linear differential form. Each equation acquires a number of terms equal to the number of variables in the equation with relatively complex coefficients which are functions of nominal steady-state operating values. All variables are in terms of differentials or change from nominal values. While linearization simplifies computer operation and performance, the complexity goes into the system coefficients, and analysis is limited to points of operation within the system operating range. A list of the linear differential equations is presented with the coefficients expressed in literal symbolic terms.

1. Turbine

$$(1)\quad d\tau_T = \frac{K_{\eta 1}}{2\pi/60} \cdot \frac{W_T}{2\,H_{ad}^{1/2}}\, dH_{ad} + \frac{K_{\eta 1}}{2\pi/60}\, H_{ad}^{1/2} - \frac{K_{\eta 2}}{2\pi/60}\, N \quad dW_T - \frac{K_{\eta 2}}{2\pi/60}\, W_T dN$$

$$(2)\quad dH_{ad} = C_P \left[1 - P_{rT}^{0.286}\right] dT_T - C_P \frac{0.286\, T_T}{P_{rT}^{0.714}}\, dP_{rT}$$

$$(3)\quad dP_{rT} = \frac{dP_N}{P_T} - \frac{P_N}{P_T^2}\, dP_T$$

$$(4)\quad dP_T = K_T \frac{W_T}{2\,T_T^{1/2}}\, dT_T + K_T\, T_T^{1/2}\, dW_T$$

$$(5)\quad dP_N = K_N \frac{W_T}{2\,T_N^{1/2}}\, dT_N + K_N\, T_N^{1/2}\, dW_T$$

$$(6)\quad dT_N = dT_T - \frac{\eta_T}{C_P}\, dH_{ad} - \frac{H_{ad}}{C_P}\, d\eta_T$$

$$(7)\quad d\eta_T = \left(\frac{K_{\eta 1}}{H_{ad}^{1/2}} - K_{\eta 2}\, \frac{2N}{H_{ad}}\right) dN + \left[K_{\eta 2} \left(\frac{N}{H_{ad}}\right)^2 - K_{\eta 1}\, \frac{N}{2H_{ad}^{3/2}}\right] dH_{ad}$$

2. Pump

$$(8)\quad dP_P = \cancel{\frac{\partial P_P}{\partial W_P}}^{\,0}\, dW_P + \frac{\partial P_P}{\partial N}\, dN$$

In the vicinity of the system operating points, pump pressure is primarily a function of speed and is not significantly affected by flow change as indicated by the pump map of Figure 59.

$$(9)\quad d\tau_P = \frac{60}{2\pi\rho_P}\cdot\frac{P_P}{N\eta_P}\,dW_P + \frac{60}{2\pi\rho_P}\cdot\frac{W_P}{N\eta_P}\,dP_P - \frac{60}{2\pi\rho_P}\cdot\frac{P_P W_P}{N\eta_P^2}\,d\eta_P - \frac{60}{2\pi\rho_P}\cdot\frac{P_P W_P}{N^2\eta_P}\,dN$$

$$(10)\quad d\eta_P = \frac{\partial\eta_P}{\partial W_P}\,dW_P + \cancel{\frac{\partial\eta_P}{\partial N}}^{\,0}\,dN$$

Pump efficiency is primarily a function of pump flow as indicated by the efficiency curves of Figure 60. Pump partial derivative values were obtained through interpolation of curves and steady-state data.

3. Turbopump Speed

$$(11)\quad dN = \frac{60/2\pi}{J}\int (d\tau_T - d\tau_P)\,dt$$

4. Main Heat Exchanger

$$(12)\quad dQ_H = (AT_H - AT_M)\,dh_H - Ah_H\,dT_M$$

$$(13)\quad dh_H = \left(\frac{dh_H}{dW_H}\right)dW_H$$

$$(14)\quad dT_M = \frac{1}{MC_{PM}}\int (dQ_H - dQ_c)\,dt$$

$$(15)\quad dQ_c = \left(AT_M - \frac{AT_L}{2} - \frac{AT_F}{2}\right)dh_c + Ah_c\,dT_M - \frac{Ah_c}{2}\,dT_F$$

$$(16)\quad dh_c = \left(\frac{dh_c}{dW_F}\right)dW_F$$

$$(17)\quad dT_F = \frac{dQ_c}{C_{Pc}W_F} - \frac{Q_c}{C_{Pc}W_F^2}\,dW_F$$

5. Auxiliary Heat Exchanger

$$(18)\quad dQ_H = (AT_H - AT_M)\,dh_H - Ah_H\,dT_M$$

$$(19)\quad dh_H = \left(\frac{dh_H}{dW_H}\right)dW_H$$

$$(20)\quad dT_M = \frac{1}{MC_{PM}} \int (dQ_H - dQ_c)\, dt$$

$$(21)\quad dQ_c = \left(AT_M - \frac{AT_L}{2} - \frac{AT_T}{2}\right) dh_c + Ah_c\, dT_M - \frac{Ah_c}{2}\, dT_T$$

$$(22)\quad dh_c = \left(\frac{dh_c}{dW_A}\right) dW_A$$

$$(23)\quad dT_T = \frac{dQ_c}{C_{Pc}W_A} - \frac{Q_c}{C_{Pc}W_A^2}\, dW_A$$

6. Fluid Transport

$$(24)\quad dP_L = dP_P - \frac{\ell}{ag} \cdot \frac{dW_P}{dt}$$

$$(25)\quad dW_P = dW_M + dW_A$$

$$(26)\quad dW_M = \frac{K_M}{2(P_L - P_M)^{1/2}} (dP_L - dP_M)$$

$$(27)\quad dP_M = K_{PM} \int (dW_M - dW_F)\, dt$$

$$(28)\quad dW_F = \frac{K_{WF}}{T_F^{1/2}}\, dP_M - \frac{K_{WF}P_M}{2T_F^{3/2}}\, dT_F$$

$$(29)\quad dW_A = \frac{K_A}{2(P_L - P_A)^{1/2}} (dP_L - dP_A)$$

$$(30)\quad dP_A = K_{PA} \int (dW_A - dW_T)\, dt$$

7. Throttle Valve

$$(31)\quad dW_T = \frac{K_v A_v P_A}{T_T^{1/2}}\, f'(P_{rv}) + \frac{K_v A_v f(P_{rv})}{T_T^{1/2}}\, dP_A + \frac{K_v P_A f(P_{rv})}{T_T^{1/2}}\, dA_v - \frac{K_v A_v P_A f(P_{rv})}{2\, T_T^{3/2}}\, dT_T$$

$$(32)\quad f'(P_{rv}) = \frac{1.43\,P_{rv}^{0.43} - 1.715\,P_{rv}^{0.715}}{2\left(P_{rv}^{1.43} - P_{rv}^{1.715}\right)^{1/2}}\,dP_{rv}$$

$$(33)\quad dP_{rv} = \frac{dP_T}{P_A} - \frac{P_T}{P_A^2}\,dP_A$$

Normalized Linear Differential Equations

To normalize the linear differential equations, each differential variable is divided by its nominal operating value and represents a percent change from its nominal value. For example, take an arbitrary linear differential equation

$$dX = Ady + B\,dZ$$

and divide each differential variable by its nominal value without destroying the equality of the equation.

$$\frac{dX}{\bar{X}} = \frac{A\bar{Y}}{\bar{X}}\,\frac{dY}{\bar{Y}} + \frac{B\bar{Z}}{\bar{X}}\,\frac{dZ}{\bar{Z}}$$

Note that the coefficients A and B are now modified by the nominal values of the differential variables. By defining the ratio of the differential variable to its nominal value as a percent change, the equation is written in the form

$$\%X = \frac{A\bar{Y}}{\bar{X}}\,\%Y + \frac{B\bar{Z}}{\bar{X}}\,\%Z.$$

Normalization has the advantages of expressing all variables in terms of percent change, removing from their coefficients the effects of dimensions and virtually eliminating the computer scaling problem. It also tends to simplify the complexity of the coefficients which will be demonstrated shortly in evaluation of the coefficients.

A list of the normalized linear differential equations is presented with general symbolic coefficients (C_1, C_2, C_3, etc.). Some terms show no symbolic coefficient, which means that the coefficient is 1 and, in most cases, is due to simplification as a result of the normalization process mentioned above.

1. Turbine

(1) $\%\tau_T = C_1\,\%H_{ad} + \%W_T - C_3\%N$

(2) $\%H_{ad} = \%T_T - C_5\%P_{rT}$

(3) $\%P_{rT} = \%P_N - \%P_T$

(4) $\%P_T = C_8\%T_T + \%W_T$

(5) $\%P_N = C_{10}\%T_N + \%W_T$

(6) $\%T_N = C_{12}\%T_T - C_{13}(\%H_{ad} + \%\eta_T)$

(7) $\%\eta_T = C_{15}\%N - C_{16}\%H_{ad}$

2. Pump

(8) $\%P_P = C_{17}\%N$

(9) $\%\tau_P = \%W_P + \%P_P - \%\eta_P - \%N$

(10) $\%\eta_P = C_{22}\%W_P$

3. Turbopump Speed

(11) $\%N = C_{23}\int(\%\tau_T - \%\tau_P)\,dt$

4. Main Heat Exchanger

(12) $\%Q_H = \%h_H - C_{25}\%T_M$

(13) $\%h_H = \%W_H = 0$

(14) $\%T_M = C_{27}\int(\%Q_H - \%Q_c)\,dt$

(15) $\%Q_c = \%h_c + C_{29}\%T_M - C_{30}\%T_F$

(16) $\%h_c = \%W_F$

(17) $\%T_F = C_{32}(\%Q_c - \%W_F)$

5. Auxiliary Heat Exchanger

(18) $\%Q_H = \%h_H - C_{35}\%T_M$

(19) $\%h_H = \%W_H = 0$

(20) $\%T_M = C_{37}\int(\%Q_H - \%Q_c)dt$

(21) $\%Q_c = \%h_c + C_{39}\%T_M - C_{40}\%T_T$

(22) $\%h_c = \%W_A$

(23) $\%T_T = C_{42}(\%Q_c - \%W_A)$

6. Fluid Transport

(24) $\%P_L = \%P_P - C_{45}\frac{\%W_P}{dt}$

(25) $\%W_P = \%W_M + C_{47}\%W_A$

(26) $\%W_M = C_{48}\%P_L - K_{48a}\%P_M$

(27) $\%P_M = C_{49}\int(\%W_M - \%W_F)\,dt$

(28) $\%W_F = \%P_M - C_{51}\%T_F$

(29) $\%W_A = C_{52}\%P_L - C_{52}\%P_A$

(30) $\%P_A = C_{53}\int(\%W_A - \%W_T)\,dt$

7. Throttle Valve

(31) $\%W_T = \%f(P_{rv}) + \%P_A + \%A_v - C_{57}\%T_T$

(32) $\%f(P_{rv}) = -C_{58}\%P_{rv}$

(33) $\%P_{rv} = \%P_T - \%P_A$

Coefficient Evaluation

The general symbolic coefficient comprises three factors

C = (system constant)(differential coefficient) (normalizing coefficient)

The system constant appears in the original nonlinear equations; the differential coefficient is a result of the differential linearization process; and the normalizing coefficient is produced in the normalization process. Multiplied together, they form the total coefficient used in the analog computer model. For example, C_1 of Equation(1)would be evaluated as follows:

$$C_1 = \left(\frac{K\eta_1}{2\pi/60}\right)\left(\frac{\bar{W}_T}{2\bar{H}_{ad}^{1/2}}\right)\left(\frac{\bar{H}_{ad}}{\bar{\tau}_T}\right)$$

combining factors

$$C_1 = \frac{15K\eta_1 \bar{W}_T \bar{H}_{ad}^{1/2}}{\pi \bar{\tau}_T}$$

where $\bar{W}_T$, $\bar{H}_{ad}^{1/2}$, and $\bar{\tau}_T$ are nominal values. This is an example of a coefficient that does not significantly simplify in the normalization process and whose value will change with each operating condition.

Taking for the next example C_8 of Equation (4)

$$C_8 = (K_T)\left(\frac{\bar{W}_T}{2\bar{\tau}_T^{1/2}}\right)\left(\frac{\bar{T}_T}{\bar{P}_T}\right)$$

combining factors

$$C_8 = \frac{K_T \bar{W}_T \bar{T}_T^{1/2}}{2\bar{P}_T}$$

However, the nonlinear form of Equation (4) says that

$$\frac{W_T \sqrt{T_T}}{P_T} = \frac{1}{K_T}$$

therefore,

$$\frac{\bar{W}_T \bar{T}_T^{1/2}}{\bar{P}_T} = \frac{1}{K_T} \quad \text{and} \quad C_8 = \frac{K_T}{2K_T} = \frac{1}{2}$$

This is a sample of a coefficient that has been simplified by the normalization process to a value which is independent of operating codition.

The next example is C_2 of Equation (1)

$$C_2 = \left(\frac{K\eta_1}{2\pi/60}\right)\left(\bar{H}_{ad}^{1/2}\right)\left(\frac{\bar{W}_T}{\bar{\tau}_T}\right) - \left(\frac{K\eta_2}{2\pi/60}\right)(\bar{N})\left(\frac{\bar{W}_T}{\bar{\tau}_T}\right)$$

which acquired two terms in the differential linearization process. Combining factors gives

$$C_2 = \frac{\frac{K\eta_1}{2\pi/60} \bar{H}_{ad}^{1/2} \bar{W}_T - \frac{K\eta_2}{2\pi/60} \bar{N} \bar{W}_T}{\bar{\tau}_T}$$

but the nonlinear form of Equation (1) is

$$\tau_T = \frac{K'_{\eta 1}}{2\pi/60} W_T \sqrt{H_{ad}} - \frac{K_{\eta 2}}{2\pi/60} W_T N$$

therefore,

$$C_2 = \frac{\tau_T}{\tau_T} = 1$$

This is a sample of a coefficient that reduces to 1 and becomes independent of operating condition as a result of the normalization process.

A list of the system constants and their numerical values is presented next, followed by a table of the symbolic coefficients and their values for the five operating conditions studied.

LIST OF SYSTEM CONSTANTS

Component	Symbol	Numerical Value	Units
Turbine	$K_{\eta 1}$	8.15×10^{-2}	$in.^{1/2}/rpm$
	$K'_{\eta 2}$	2.56×10^{-3}	$in./rpm^2$
	C_P	3.22×10^{4}	$in.\cdot lb/lb\cdot {}^{0}F$
	k	1.4	-
	K_T	40.8	$sec/in.^2\ {}^{0}R^{1/2}$
	K_N	2.31	$sec/in.^2\ {}^{0}R^{1/2}$
Pump	ρ_P	2.63×10^{-3}	$lb/in.^3$
Speed	J	0.187	$in..lb\cdot sec^2$
Main heat exchanger	A	1.3×10^{4}	$in.^2$
	$(\frac{dh}{dW})_H$	5.97×10^{-7}	$\frac{Btu}{in.\cdot lb\cdot {}^{0}F}$
	M	1210	lb
	C_{PM}	0.070	$Btu/lb\cdot {}^{0}F$
	T_L	40	${}^{0}R$
	$(\frac{dh}{dW})_c$	1.333×10^{-4}	$\frac{Btu}{in.\cdot lb\cdot {}^{0}F}$

(Continued)

Component	Symbol	Numerical Value	Units
Main heat exchanger (Continued)	C_{Pc}	3.5	$\frac{Btu}{lb.^0F}$
Auxiliary Heat exchanger	A	1.51×10^3	$in.^2$
	$(\frac{dh}{dW})_H$	1.78×10^{-6}	$\frac{Btu}{in.\cdot lb\cdot^0F}$
	M	141	lbs
	C_{PM}	0.070	$Btu/lb\cdot^0F$
	T_L	40	^0R
	$(\frac{dh}{dW})_c$	7.23×10^{-3}	$\frac{Btu}{in.\cdot lb\cdot^0F}$
	C_{Pc}	3.5	$\frac{Btu}{lb.^0F}$
Fluid Transport	ℓ/ag	0.194	$sec^2/in.^2$
	K_M	1.45	$\frac{lb\cdot sec}{(Psi)^{1/2}}$
	K_{PM}	554	psi/lb
	R	9200	$\frac{in.\cdot lb}{lb\cdot^0R}$
	V_M	2600	$in.^3$
	$\overline{T}_F$	400	^0R
	K_{WF}	0.336	$\frac{in.^2.^0R^{1/2}}{Sec}$
	K_A	0.0685	$\frac{lb\cdot sec}{(Psi)^{1/2}}$
	K_{PA}	1.06×10^4	Psi/lb
	$\overline{T}_T$	2000	^0R
	V_A	302	$in.^3$

Component	Symbol	Numerical Value	Units
Fluid Transport (Continued)	V_L	530	$in.^3$
Throttle Valve	K_V	0.542	$^oR^{1/2}/sec$
	k	1.4	-
	P_{rc}	0.528	-

TABLE 8

TABLE OF SYMBOLIC COEFFICIENTS
AND THEIR NUMERICAL VALUES

Equation No.	Coefficient	Numerical Value Per Operating Condition				
		1	2	3	4	5
1	C_1	0.696	0.634	0.579	0.553	0.534
	C_3	0.308	0.250	0.193	0.122	0.085
2	C_5	0.212	→			
4	C_8	0.500	→			
5	C_{10}	0.500	→			
6	C_{12}	1.30	1.30	1.27	1.18	1.12
	C_{13}	0.314	0.310	0.276	0.179	0.128
7	C_{15}	0.759	0.746	0.760	0.845	0.880
	C_{16}	0.380	0.371	0.379	0.422	0.441
8	C_{17}	2.00	2.12	1.86	2.04	1.78
10	C_{22}	0.0614	0.0925	0.1075	0.200	0.381
11	C_{23}	1.92	1.60	1.20	0.612	0.365
12	C_{25}	0.343	→			
14	C_{27}	0.179	0.147	0.106	0.047	0.023
15	C_{29}	1.65	→			
	C_{30}	0.204	→			
17	C_{32}	0.900	→			
18	C_{35}	2.85	→			
20	C_{37}	0.0945	0.0636	0.0370	0.0119	0.0050
21	C_{39}	1.415	→			
23	C_{42}	0.980	→			
24	C_{45}	0.003	→			
25	C_{47}	0.0328	0.0269	0.0216	0.0157	0.0133
21	C_{40}	0.406	→			

TABLE 8 (continued)

TABLE OF SYMBOLIC COEFFICIENTS
AND THEIR NUMERICAL VALUES
(Cont)

Equation No.	Coefficient	Numerical Value Per Operating Condition				
		1	2	3	4	5
26	C_{48}	4.81	5.75	7.80	16.9	29.2
	C_{48a}	4.31	5.25	7.29	16.3	28.0
27	C_{49}	9.30	→			
28	C_{51}	0.500	→			
29	C_{52}	10	17.7	36.8	154	440
30	C_{53}	5.50	4.64	3.80	2.84	2.39
31	C_{57}	0.500	→			
32	C_{58}	9.10	1.45	0.430	0	0

Analog Computer Circuit

The analog computer circuits are obtained from the system of normalized linear differential equations. These equations serve as instructions for drawing the computer circuit diagram much as the nonlinear system of equations was used to draw the mathematical block diagram. The computer circuit diagram represents the electronic analogy of the system of equations from which it was constructed; each circuit represents a specific mathematical operation. For a linear system of equations with constant coefficients (no multiplying or dividing operations between variables) each equation can be represented by a single amplifier and each coefficient by a potentiometer; additional amplifiers are used for sign conversion. When the circuits are mechanized and put into operation, all equations perform simultaneously in real time as they would in the physical system being simulated.

The linear computer circuit diagram was drawn in a similar manner as the nonlinear block diagram. The circuits were arranged into major component blocks similar to the system schematic of Figure 43 so that inter- and intra-parameter relations of components could be clearly identified. A list of the potentiometer settings (pot sheet) was made up directly from the list of symbolic coefficients; each pot represents a single coefficient. The circuit diagram is presented in Figure 64, followed by the potentiometer settings (Table 9) and a list of symbols (Table 10).

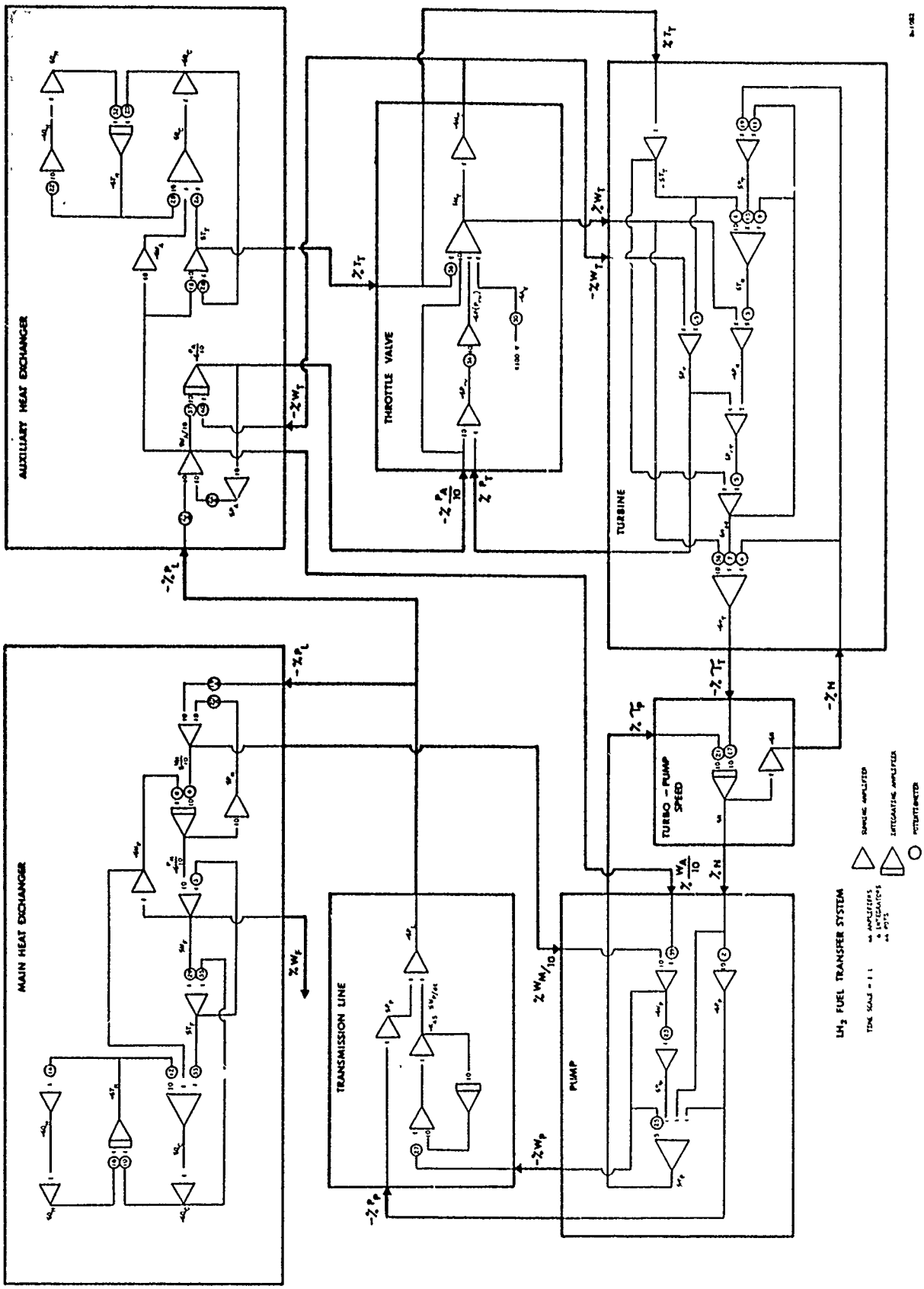

Figure 64. Analog Computer Circuit Diagram

TABLE 9

LIST OF POTENTIOMETER SETTINGS

Pot. No.	Coefficient	Settings				
		1	2	3	4	5
1	$C_{12/10}$	130	130	126	117	112
2	$C_{17/10}$	200	212	186	204	177
3	C_{10}	500	→			
4	C_3	308	250	193	122	085
5	C_5	212	→			
6	$C_{49/10}$	930	→			
7	C_1	696	634	579	553	534
8	$C_{49/10}$	930	→			
9	C_{13}	314	310	276	179	128
10	C_{27}	179	147	106	047	023
11	C_{16}	380	371	379	422	441
12	$C_{29/10}$	165	→			
13	C_{14}	314	310	276	179	128
14	C_{25}	343	→			
15	C_8	500	→			
16	C_{27}	179	147	106	047	023
17	$C_{23/10}$	192	159	120	061	036
18	C_{43}	980	→			
19	C_{15}	759	746	760	845	880
20	C_{37}	0945	0636	0370	0119	0050
21	$C_{23/10}$	192	159	120	061	036
22	$C_{35/10}$	285	→			
23	C_{22}	061	092	107	200	381

TABLE 9 (continued)

LIST OF POTENTIOMETER SETTINGS (Cont)

Pot. No.	Coefficient	Settings				
		1	2	3	4	5
24	K_{40}	406	→	→	→	→
25	1/5	200	→	→	→	→
26	C_{42}	980	→	→	→	→
27	$C_{45/T}$	292	300	306	315	312
28	$C_{39/10}$	141	→	→	→	→
29	C_{33}	900	→	→	→	→
30	%Av	INPUT				
31	C_{51}	500	→	→	→	→
32	C_{37}	0945	0636	0370	0119	0050
33	C_{30}	204	→	→	→	→
34	$C_{58/10}$	910	145	043	0	0
35	C_{32}	900	→	→	→	→
36	C_{57}	500	→	→	→	→
37	$C_{53/10}$	550	464	380	284	239
38	$C_{2/10}$	100	→	→	→	→
39	$10C_{47}$	328	269	216	157	133
40	$C_{53/10}$	550	464	380	284	239
Reac "A"						
19A	$C_{48/100}$	0481	0575	0780	169	292
20A	$C_{48a/100}$	0431	0525	0729	163	280
21A	$C_{52/100}$	100	177	368	999	999
22A	$C_{52/100}$	100	177	368	999	999

TABLE 10

LIST OF SYMBOLS

VARIABLES

τ	Torque (in.·lb)
W	Flow rate (lb/sec)
N	Speed (rpm)
H_{ad}	Adiabatic head (in.·lb/lb)
η	Efficiency
T	Temperature (^0R)
P	Pressure (psia)
Q	Heat transfer rate (Btu/sec)
h	Heat transfer coefficient (Btu/in.^{2}·sec ^0F)
A_V	Turbine throttle valve area (in.^{2})
t	Time (sec)

CONSTANTS

K	General
C_P	Specific heat (in.·lb/lb·^0R - or - Btu/lb·^0F)
ρ_P	LH_2 density at pump (lb/in.^{3})
π	3.14
J	Mass moment of inertia (in.·lb·sec^2)
A	Heat transfer surface areas (in.^{2})
T_H	Hot side combustion products temperature (^0R)
dh/dW	Rate of change of heat transfer coefficient with respect to flow change (Btu/in.^{2}·lb·^0F)
T_{Mo}	Initial heat exchanger metal temperatures (^0R)
M	Mass of heat exchanger (lb)
T_L	Liquid hydrogen temperature (^0R)

TABLE 10 (continued)

ℓ	Length of LH_2 transmission line (in.)
a	Cross-section area of LH_2 transmission line ($in.^2$)
g	Gravitational constant ($in./sec^2$)
R	Gas constant ($in.\cdot lb/lb\cdot {}^0R$)
V	Volume ($in.^3$)
$\bar{T}$	Design temperature (^0R)

SUBSCRIPTS

T	Turbine; upstream when applicable
η	Constants of turbine efficiency equation
N	Turbine discharge nozzle
P	Pump
X	Pump parametric speed relations
H	Hot side of heat exchanger
M	Metal of heat exchanger or main heat exchanger
C	Cold side of heat exchanger
L	Liquid hydrogen or LH_2 transmission line
F	Engine fuel injection nozzle
A	Auxiliary heat exchanger
P_M	Main heat exchanger pressure
W_F	Engine fuel injection flow
P_T	Upstream turbine pressure
W_T	Turbine Flow

OPERATORS

F	Function of
$\int$	Integral
d	Differential

SECTION 6

MECHANICAL DESIGN

PUMP COMPONENTS

Because Section 3 of this report reviews in detail hydrodynamic design of the hubless inducer and conventionally designed pump impellers and their diffusers, the design of these components will not be discussed in this section. Fabrication, mounting, and seal design activity, however, will be reviewed herein.

Pump Impeller

The "hubless" inducer pump impeller blade design was laid out initially on the basis of fabrication by a generating process, but as the design progressed, it became evident that this process was considerably more involved than originally contemplated. After reinvestigation of other methods of fabrication, a design was made to duplicate, rather than to generate, the blades. Five hubless inducer impellers were machined without difficulty utilizing this process (see Figure 65). An impeller shroud was fabricated separately from the same aluminum alloy material and brazed to the hub portion as shown in Figure 66. The five impellers were whirl tested to 44,000 rpm for one minute at room temperature. No measurable growth was observed. Zyglo inspection of the units after spinning showed no flaw in the brazing. The first impeller was fabricated with an inboard register which was drilled and tapped to accommodate five screws which fastened the impeller to a flange on the shaft. When a problem was encountered with the fit of the screws, it was decided to change to studs with self-locking nuts in lieu of the screws used on the first unit. Consequently, all impellers were reworked to incorporate studs.

Diffuser

The diffuser passages were also formed by duplicating. The completed diffuser prior to assembly is shown in Figure 67.

Impeller Seals

Labyrinth type seals were selected for both the impeller inlet seal and the seal at the thrust balance register on the inboard side of the impeller. These seals were fabricated from a material (A-286 stainless steel) harder than the impeller materials (6061-T6 aluminum alloy). The harder, sharp bevel teeth were designed to wear slight grooves in the softer impeller material resulting in minimum clearance and minimum seal leakage. Refer to Figure 68 for a view of the impeller after wear-in. Inlet seal clearances were selected to give interference at operating speed and liquid hydrogen operating temperature.

Shaft Seals

A welded bellows carbon face seal was used to seal the pump shaft at the drive end.

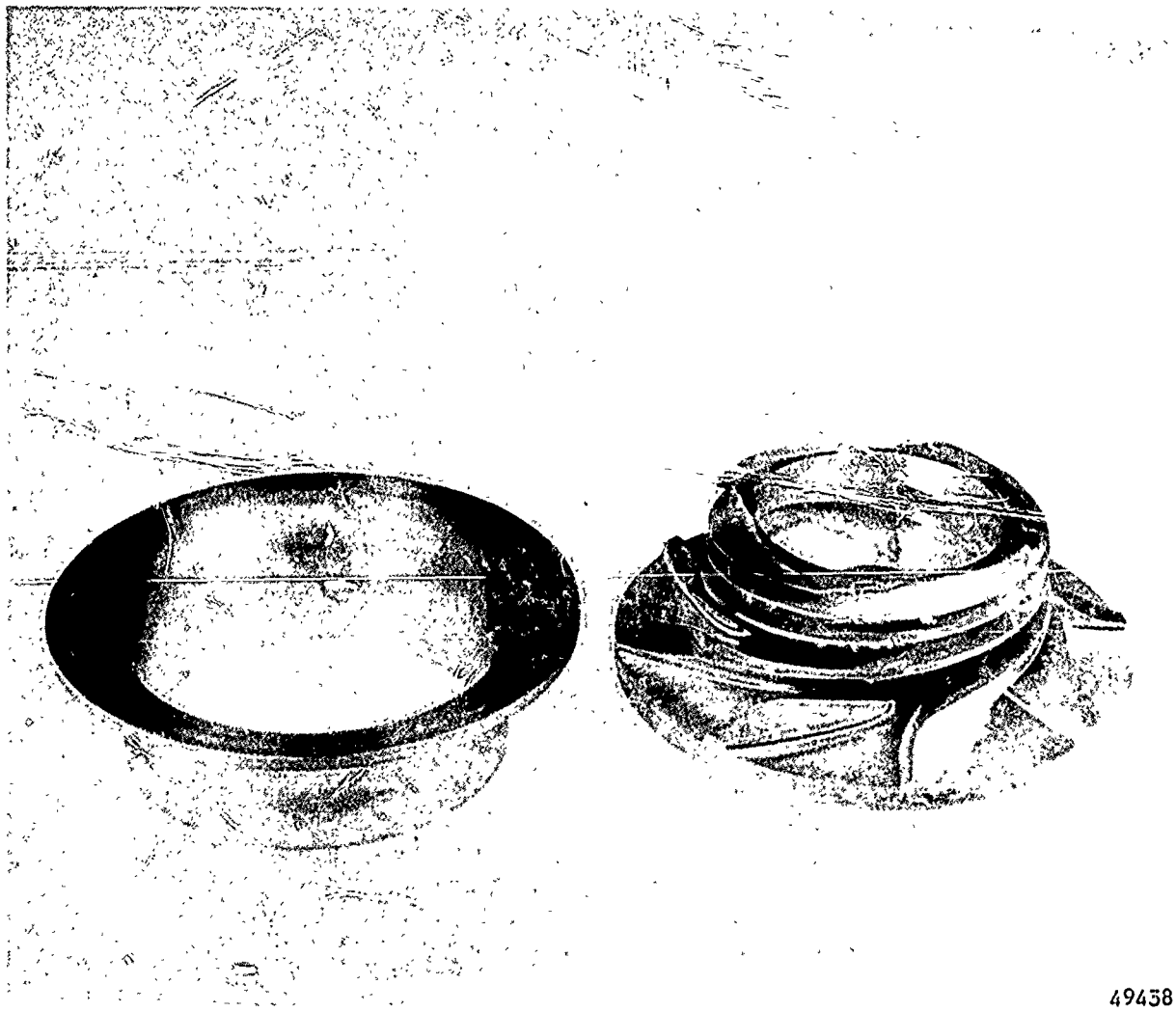

49438

Figure 65. Hubless Inducer Impeller and Shroud Prior to Brazing

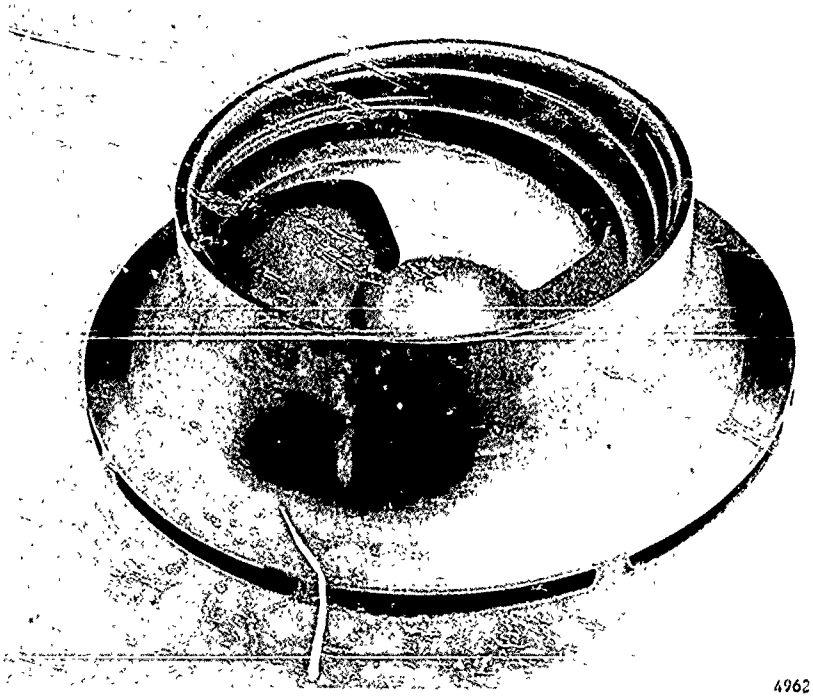

49621-9

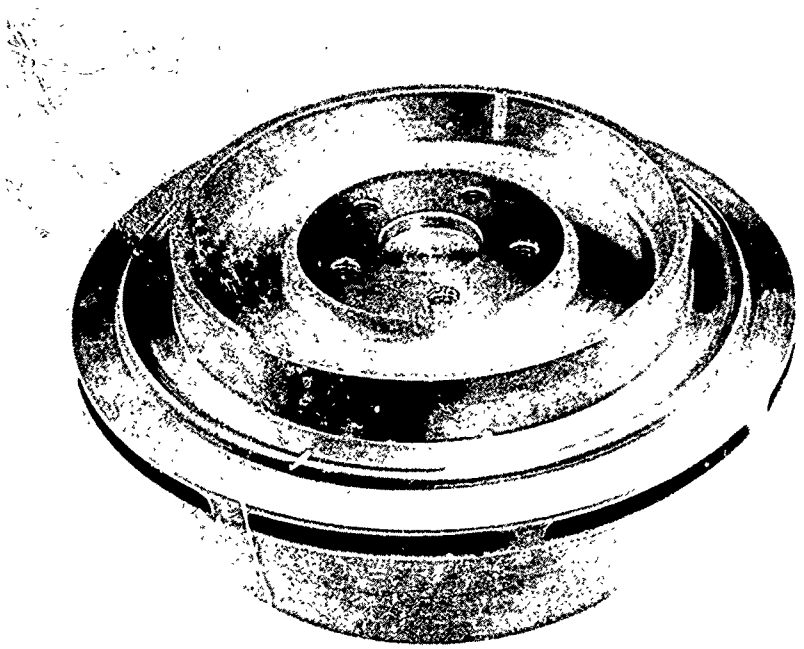

49621-7
F-500

Figure 66. Hubless Inducer Impeller Assembly After Brazing and Finish Machining

49436

Figure 67. Diffuser Halves Prior to Assembly

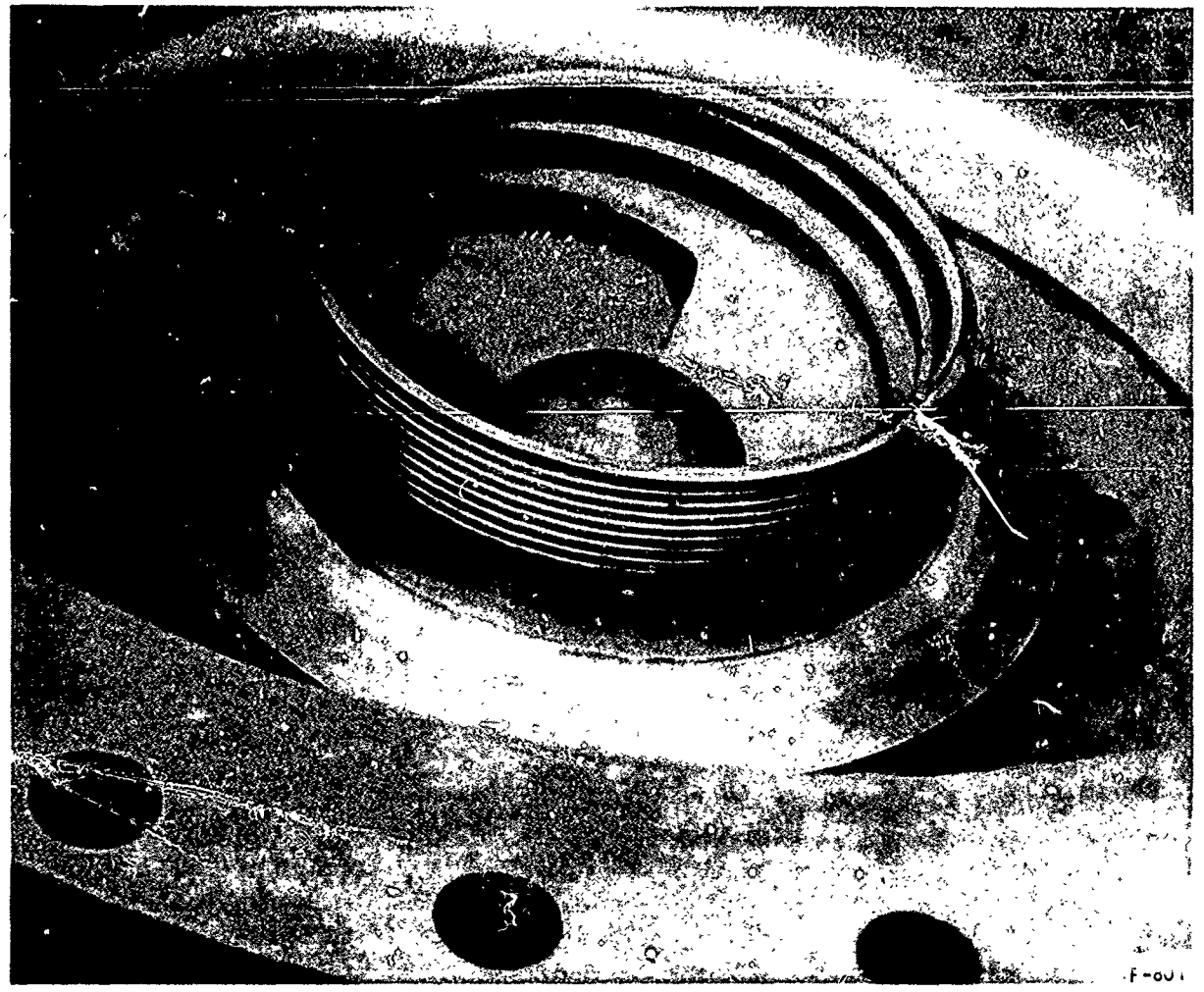

Figure 68. Impeller Showing Labyrinth Seal Wear-In

Bearings

Special ball bearing, embodying races and balls of 440-C stainless steel which has been stabilized -320°F, were procured for this pump. Separators were made from Armalon 405C-116 (refer to Figure 69). The bearings were accommodated in resilient amounts to reduce the effect of different thermal coefficients of expansion between the bearings and the housing. This mount method also allowed the pump rotor to rotate about its mass center, thus reducing bearing loads and increasing bearing life.

Bearing lubrication was effected by the leakage of liquid hydrogen past the thrust balance seals at the inboard register of the pump impeller. To maintain the pressure drop at a minimum value, each bearing was lubricant fed separately.

Pump Assembly

A cross-sectional view of the centrifugal pump tested is presented herein as Figure 70.

As a matter of general interest, a list of the materials to be utilized for the assembly has been prepared. The list is presented below:

Drawing No.	Part	Material
580044	Spacer, Bearing	Inconel, 718
580045	Sleeve, Preload	Inconel, 718
580046	Carrier, Bearing	Inconel, 718
580047	Nut, Shaft	Stainless Steel, A-286
580048	Spacer, Shaft	Inconel, 718
580049	Mount, Seal	Stainless Steel, 304
580053	Lock, Nut	Stainless Steel, 302
580055	Spring, Preload	Inconel, X
580056	Shaft	Inconel, 718
580058	Diffuser	Aluminum, 6061-T6
580059	Housing	Aluminum, 6061-T6
580062	Seal, Inlet	Stainless Steel, A-286
580063	Seal, Impeller	Stainless Steel, A-286
580064	Inlet, Pump	Aluminum, 6061-T6
580065	Tube Assembly, Vent	Stainless Steel, 321
580066	Ring, Mounting	Stainless Steel, A-286
580067	Mount, Resilient	Inconel, 718
580068	Impeller	Aluminum, 6061-T6
580085	Impeller Stud	Inconel, 718

To eliminate problems of hydrogen leakage at the shaft seal, insofar as possible, a sealed chamber between the pump and turbine was incorporated in the design. This chamber was pressurized with warm helium gas.

Thrust Balance

Hydraulic thrust on the pump impeller was balanced by an axially sealed balance drum. To prevent axial motion of the rotor in the event of thrust reversal, a double bearing preload was used.

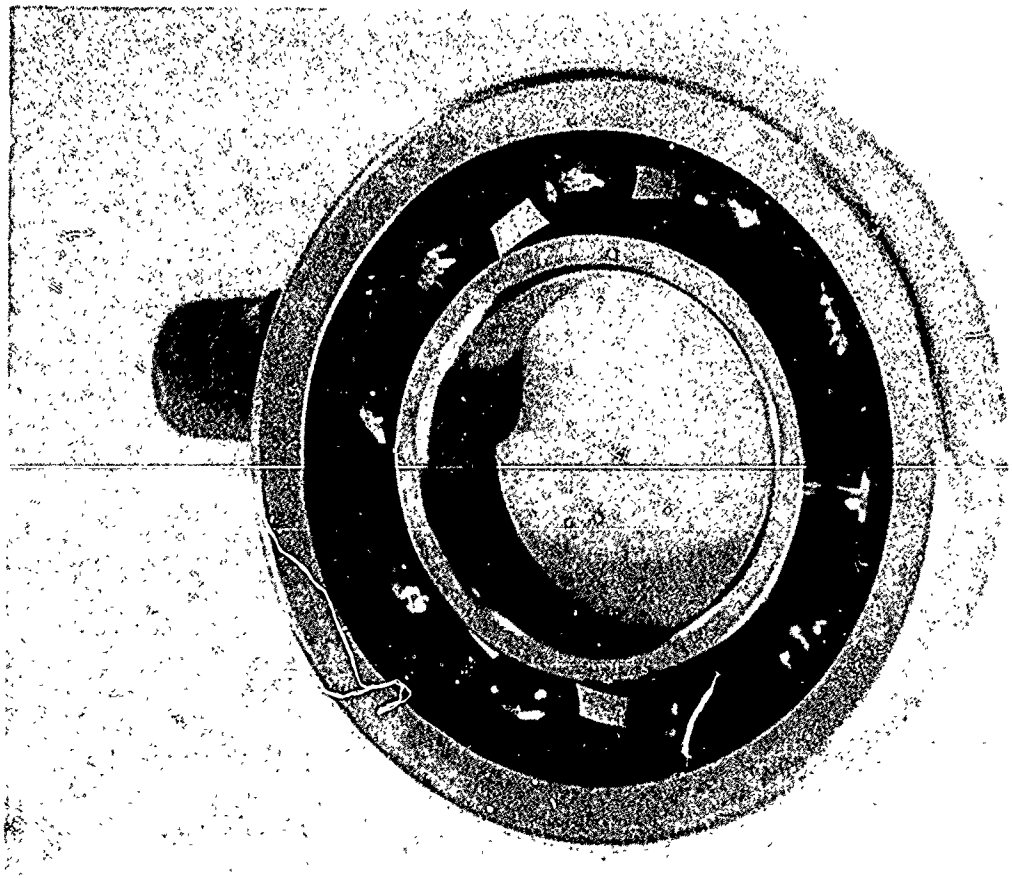

P23523-3

Figure 69. Cryogenic Ball Bearing with Armalon Separator

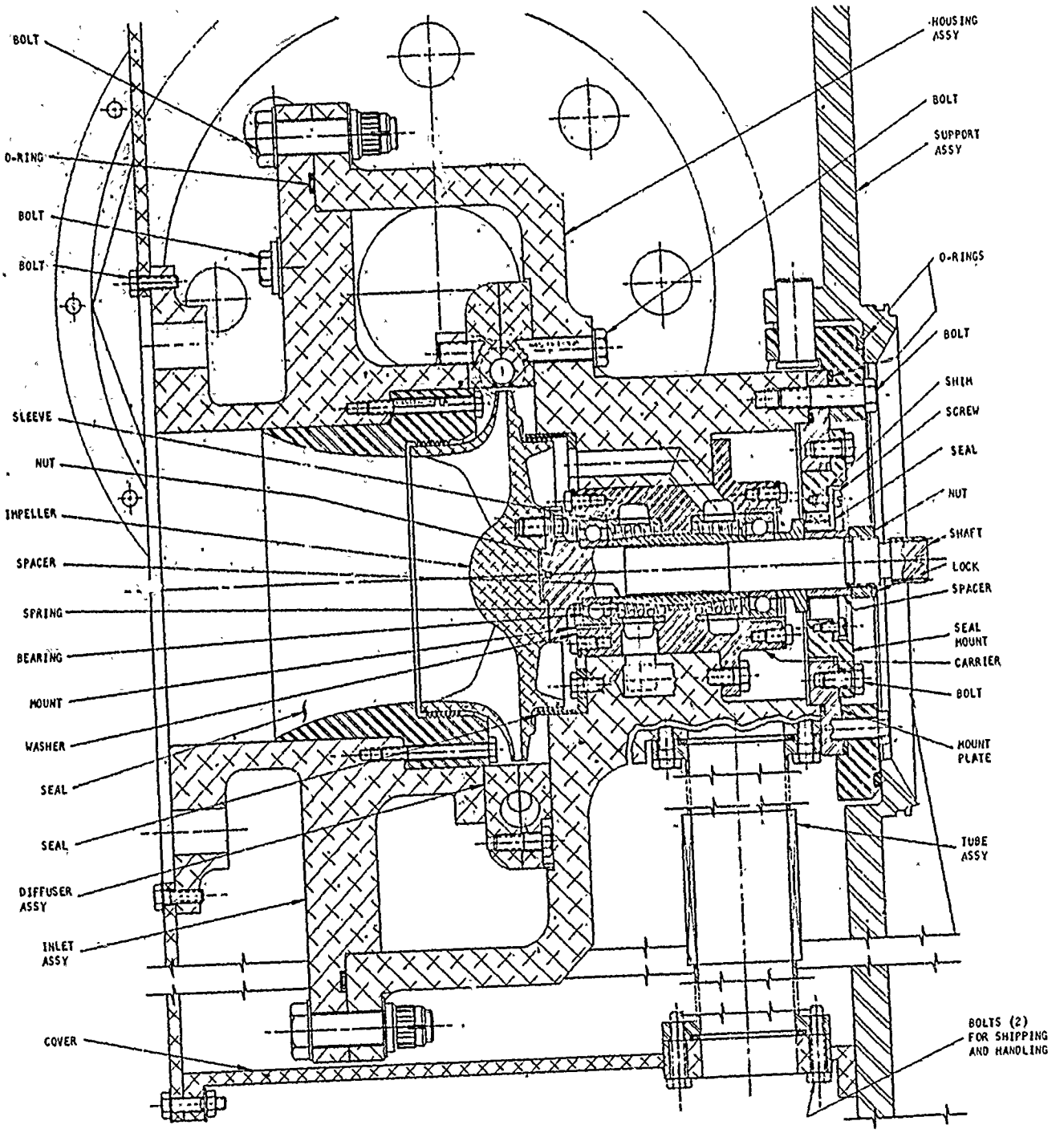

Figure 70 Cross-Section of Shrouded Hubless Inducer Pump

SECTION 7

TEST SETUP

TEST FACILITIES

The test facility used is located in San Tan Mountain Area of the Gila Indian Reservation, 38 miles southeast of Phoenix, Arizona. The nearest populated area is Chandler Heights, Arizona, which is located about five miles northeast of the test site. The remote test area is situated so as to limit public access and eliminate any possible interference with surrounding communities.

General Facility Description

The test facility is almost completely self-contained with ample storage tanks for water, liquid hydrogen, liquid and gaseous oxygen, liquid and gaseous nitrogen, helium, and other fuels such as JP-4 and gasoline. Electric power is supplied to the test area by a 300-kw transmission line. An overall view of the test facility is shown in Figure 71 and in Part (b) of Figure 72.

A 13,000 gallon liquid hydrogen tank was installed especially for this test. The test was monitored from the control room (Figure 73). The control room area, the jet engine area, and the liquid hydrogen tank and pump installation were placed in different locations on the test site, and were only interconnected by underground electrical control and power circuits. All equipment installed on the hydrogen pad was of explosion proof design.

In addition to the instrumentation in the control room, a trailer-housed data recording system was rented from Datacraft, Incorporated, Gardena, California. The trailer was located adjacent to the control room as shown in Figure 71.

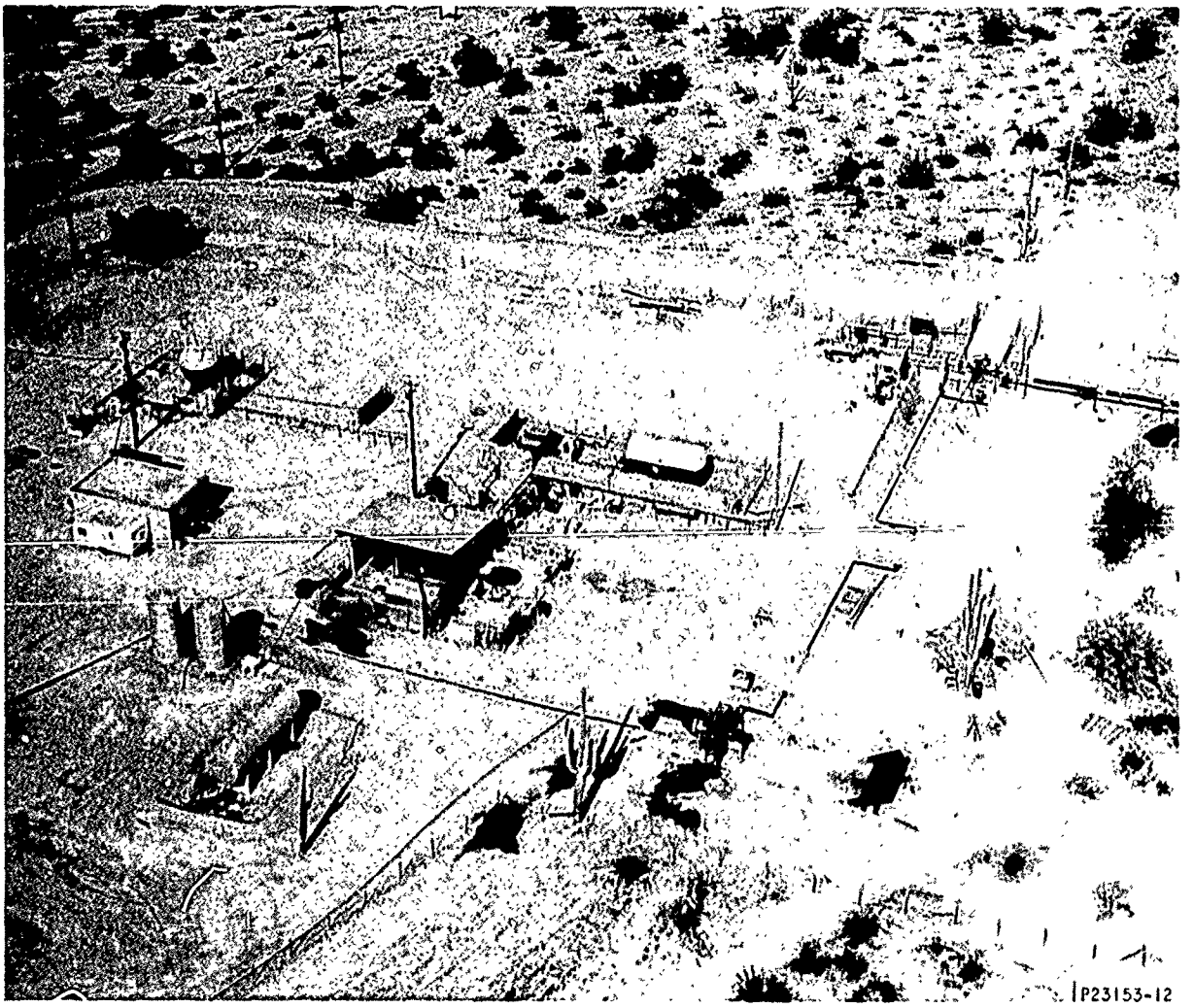

Figure 71. Liquid Hydrogen Pump Test Site, San Tan, Arizona

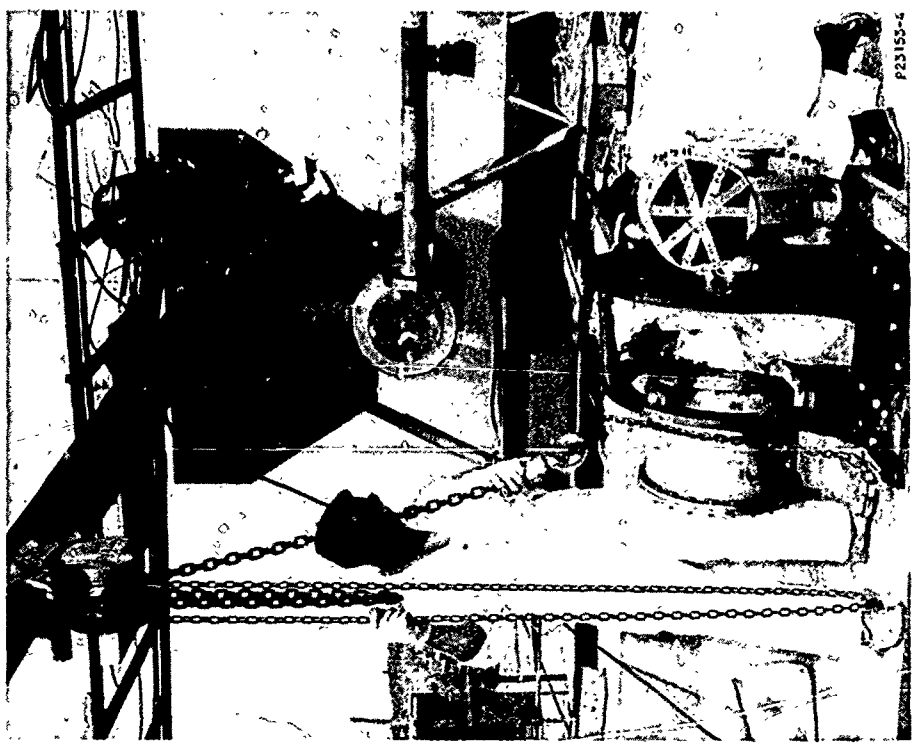

F-669

Figure 72. Installation of Pump and Overall Test Site

P19997-1

Figure 73. San Tan Test Site Instrument Control Room

TEST APPARATUS

Energy Source and Gas Turbine Pump Driver

A J-57 P43 engine (Figure 74) was purchased in order to furnish the bleed air necessary for driving the prime mover turbine. The prime mover is a combination of a GTCP85-291 turbine with a GTU turbine plenum and burner (Figure 75). The -291 unit was used because the bearing arrangement on this model allows reverse thrust. To obtain more power and overcome the temperature drop in the long engine bleed line, an inline combustor was incorporated in the turbine inlet line.

To assure maintenance of alignment of the pump and turbine shafts during temperature changes, each unit was supported on a pedestal through four radial pins.

Tankage and Plumbing

A 13,000 gallon liquid hydrogen tank, containing liquid level gauges and temperature and pressure instrumentation, was cradled in a load cell weighing system which was used as a backup flow measurement system. Figure 76 shows views of the fill end of the tank, with strain gauge load cells for the tank weight system under the tank supports, and pump supply end and test pump. The tank vent and ullage piping are also shown in these photographs.

Originally, a nitrogen purge system was contemplated for use with the liquid hydrogen system. However, a helium tank system was selected for test facility system purging in lieu of nitrogen plus hydrogen gas flushing. Cost estimates revealed that the additional cost of helium gas was more than offset by the cost of a more complex nitrogen tank system, piping, valves, and controls. In addition, the helium purge method is completely free of freeze-up problems.

Pump Inlet and Discharge Lines

A bellmouth intake section was hydrodynamically designed for high flow, minimum loss liquid hydrogen induction into the pump. This part was fabricated from laminated fiberglass. This specially designed inlet section was mounted within the tank and was connected to a remotely operated ball valve through a floating 8-inch diameter pipe. The valve and floating pipe are liquid hydrogen jacketed so that any vapor originating from heat leaks upstream of the pump inlet will not enter the inlet flow to the pump. Figure 77 presents a cross-sectional sketch of the pump inlet line and vacuum jacketed tank wall.

Polyurethane foam-in-place insulation was used to prevent excessive heat leaks into the system including the pump, from the pump inlet duct to the downstream flange of the discharge orifice section. The foam was removed and replaced as required prior to Runs 3 and 7.

Figures 78 and 79 show the insulated dump line and the hydrogen burner. At the lower right of Figure 78 is shown the pump discharge valve and the discharge section of the hydrogen flow orifice in the pump discharge line.

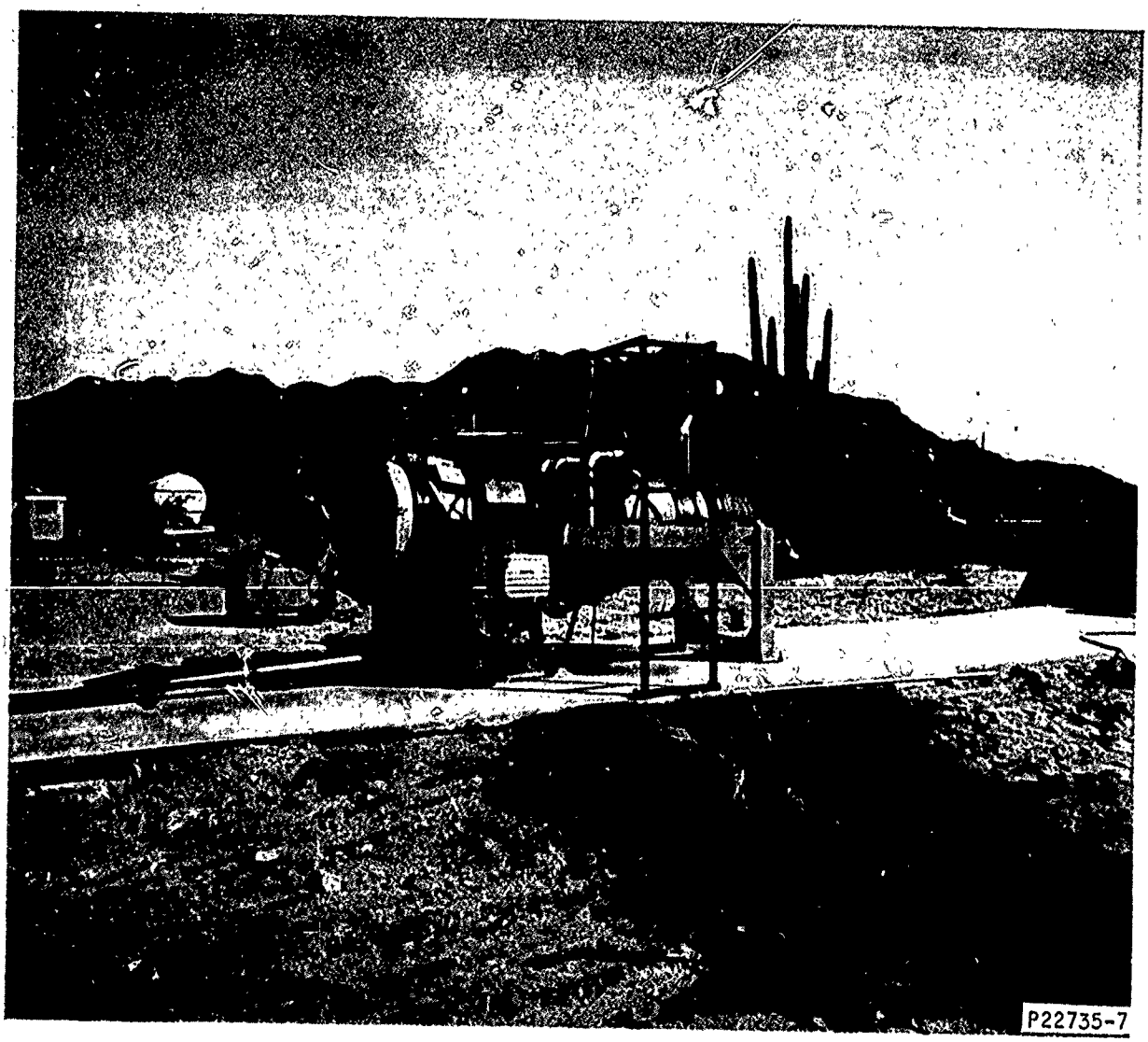

Figure 74. Bleed Air Supply J57 Jet Engine Installed on its Foundation

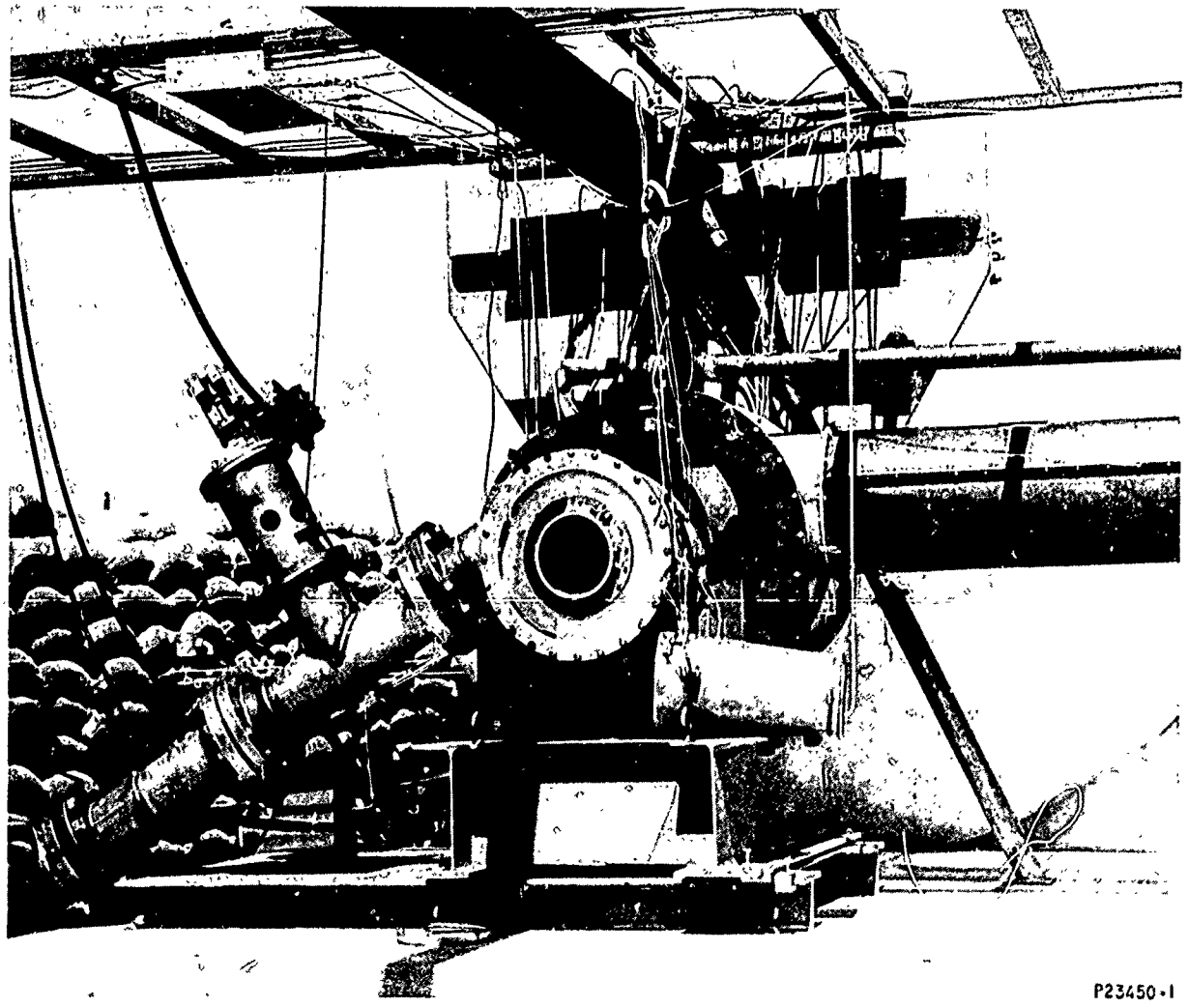

Figure 75. Modified GTCP-85-291 Gas Turbine Pump Drive Unit

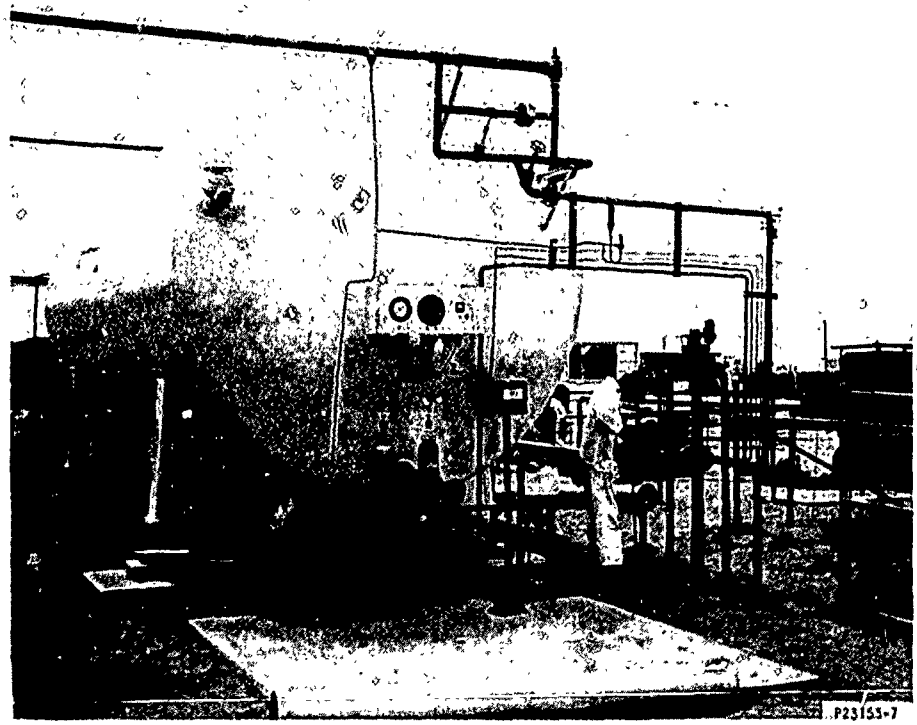

a. LIQUID HYDROGEN TANK-FILL END

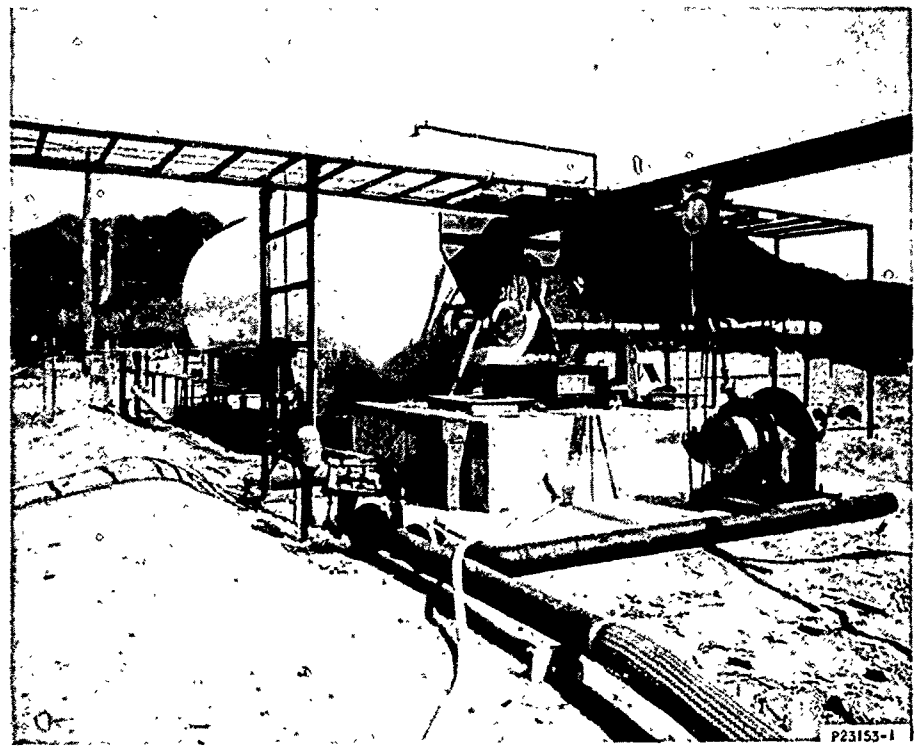

b. LIQUID HYDROGEN TANK - PUMP SUPPLY END F-667

Figure 76. 13,000-Gallon Liquid Hydrogen Supply Tank

B-904

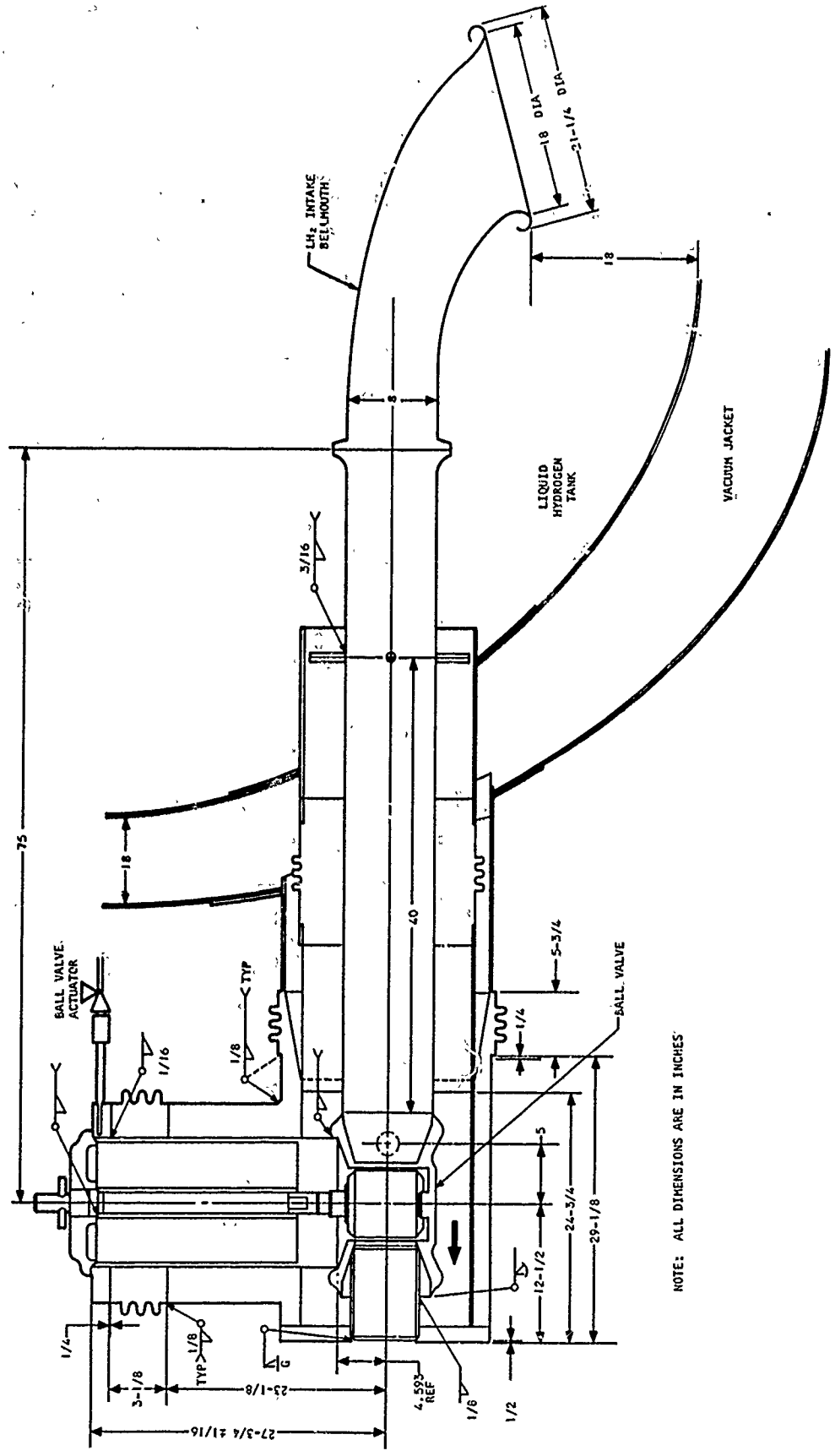

Figure 77. Pump-Tank Connection Line

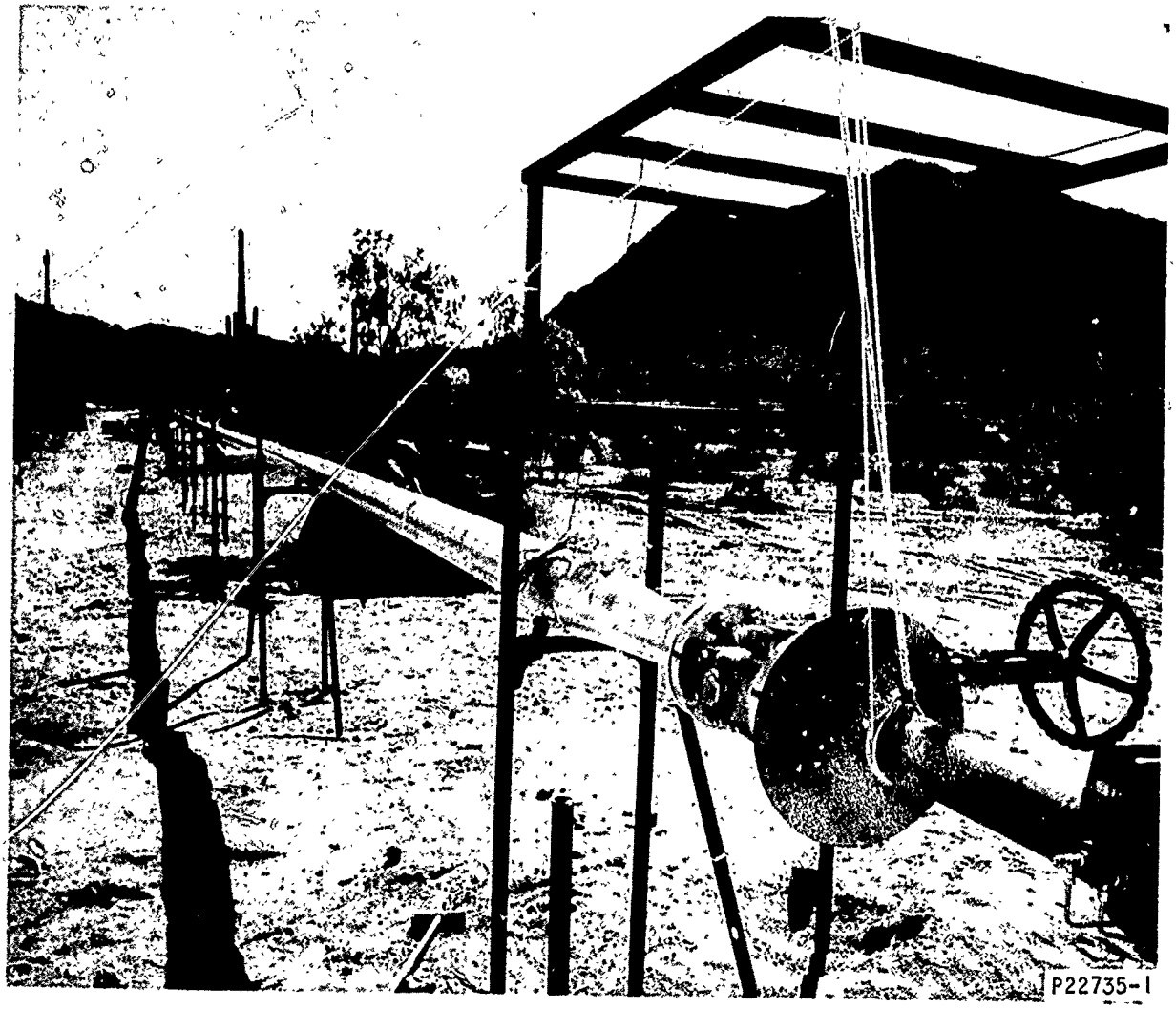

Figure 78. Pump Discharge Control Valve and Dump Line

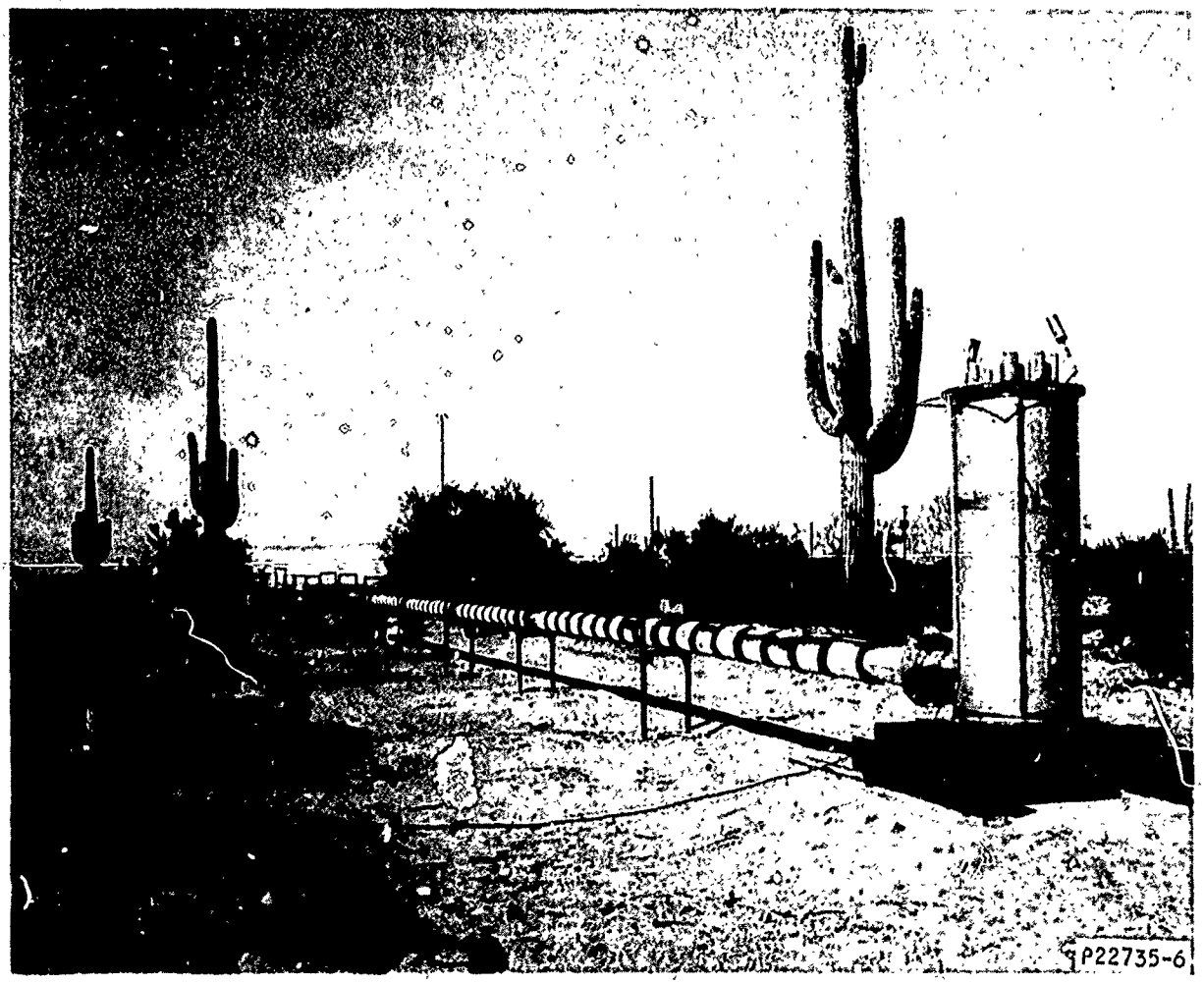

Figure 79. Insulated Dump Line and Hydrogen Burner

Figure 80 presents an overall view of the test pad, dump line, and hydrogen flare, and shows the hydrogen burning. This picture was taken by means of infra-red photography.

Schematic Diagram of Test Setup

Figure 81 is a sketch of the test setup and instrumentation. Withdrawal of fluid from the tank required introduction of gaseous hydrogen at constant pressure to avoid boiling and excessive agitation of the fluid. Cold gaseous hydrogen from auxiliary supply of liquid hydrogen was admitted through Valves V-109 and V-101. Valve V-101 was operated by a constant pressure controller. Pump discharge pressure was controlled by a manually operated throttle Valve V-104. As seen in the figure, two means of measuring pump flow are incorporated in the test setup. The primary means is a flow orifice in the pump discharge line downstream of temperature T3. In addition, the previously mentioned continuous tank weighing system was also available.

A differential pressure gauge LL_1 was used as an indication of liquid level in the tank. This pressure transducer was not set up for remote readout.

The tank vent system consisted of a manual valve, burst disk and relief valve all mounted in parallel and connected through a two-inch line to the tank vent flare. Except as noted during Run 5, Valve V_1 was closed at all times during the test runs.

Pump inlet ball valve position was noted by transducer X_3. This would indicate a light on the control panel when the ball valve was fully open or fully closed.

Transducers P_3, P_{11} and ΔP_1 form the NPSH measurement system which is discussed elsewhere.

Transducers X_1 and X_2 are variable reluctance coils mounted near the pump and turbine ends of the coupling. These coils measure the air gap between the coil and the coupling, and were phased to display this gap in the form of a Lissajous pattern on oscilloscopes.

INSTRUMENTATION

The test stand was instrumented with complete data recording instrumentation so that continuous recordings as well as visual monitoring of the more critical parameters was assured. Figure 82 presents the control console. Data fed into the trailer-hcused recording oscillograph was as follows:

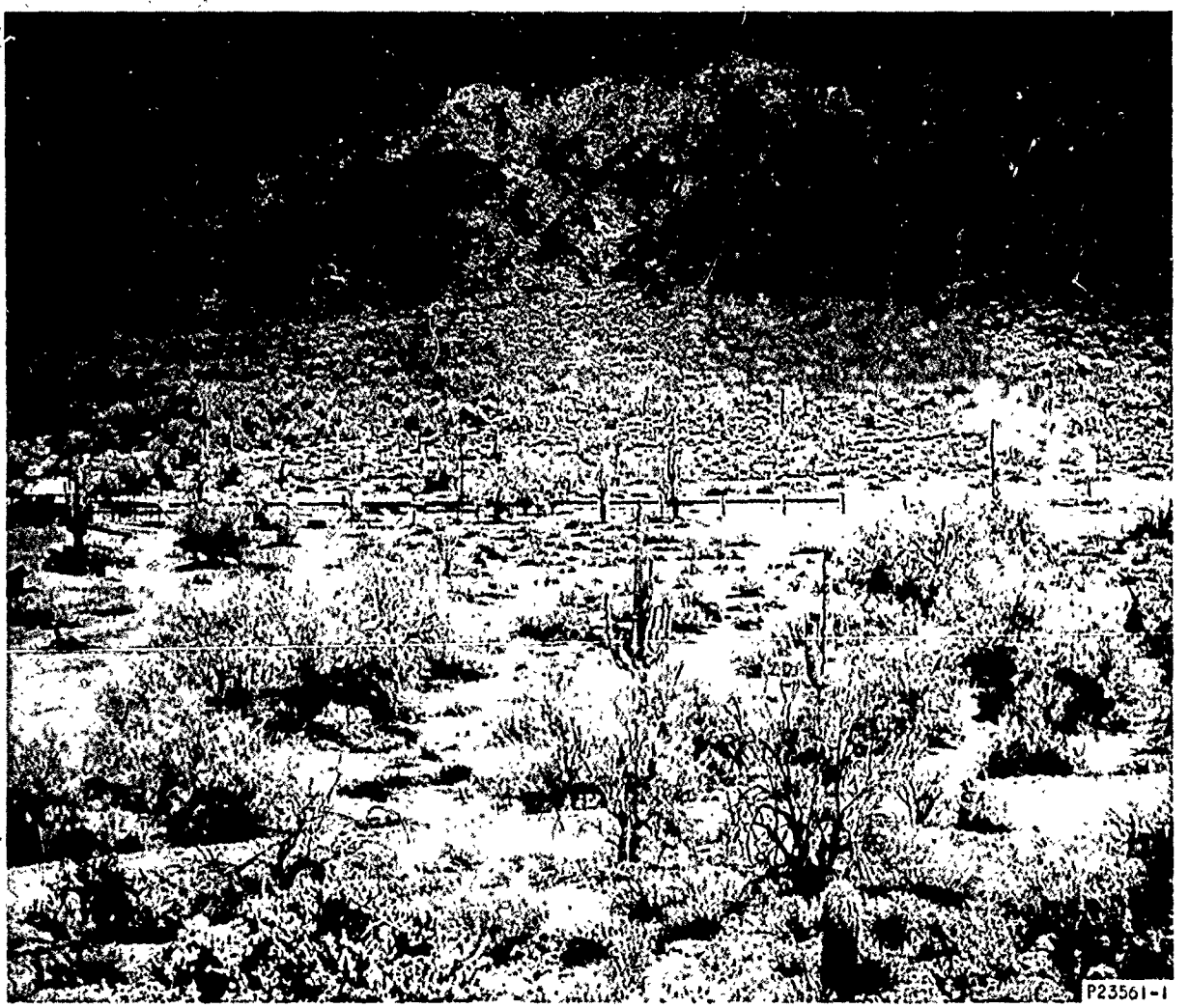

Figure 80. Liquid Hydrogen Pump Test Stand in Operation

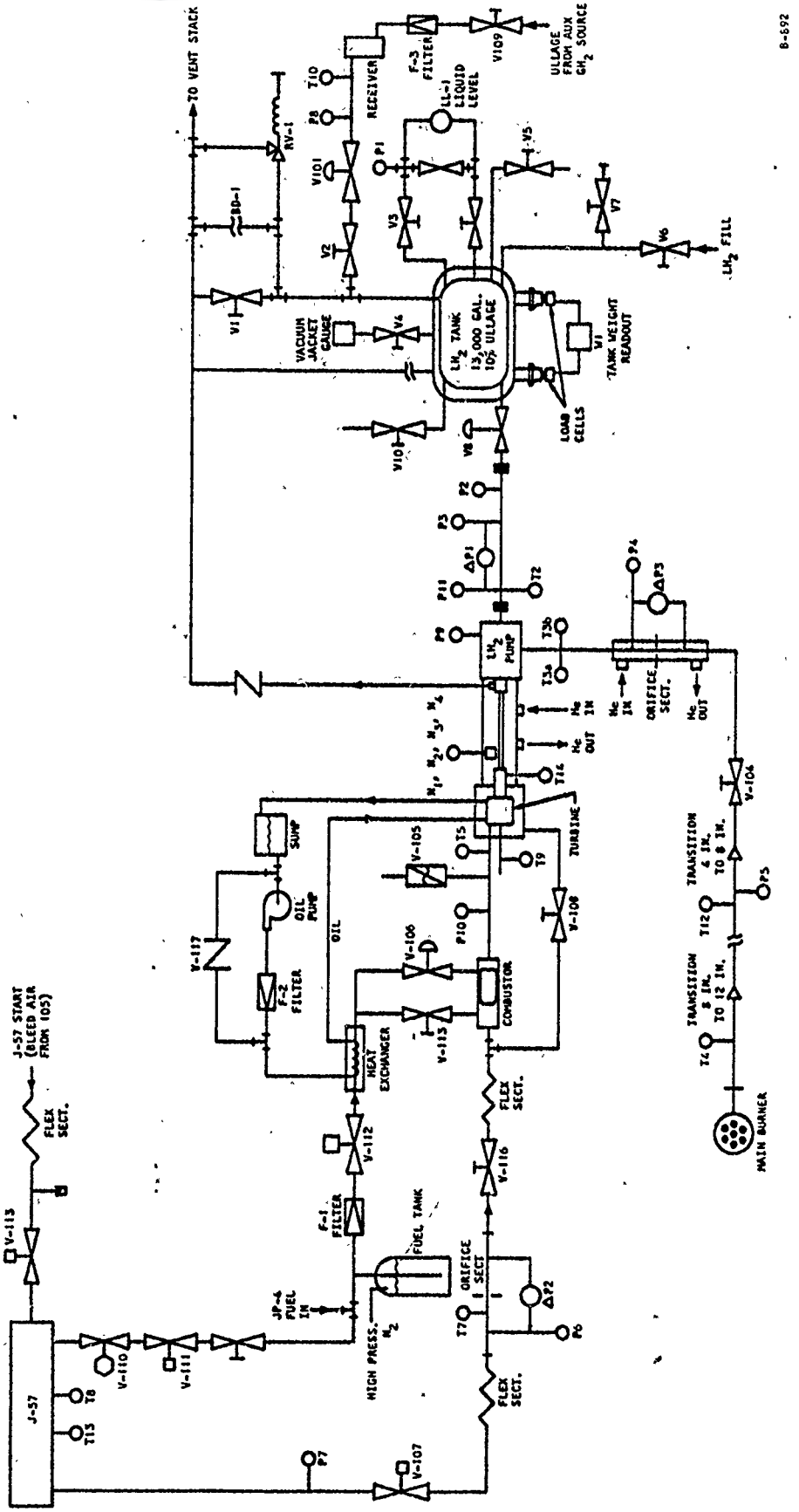

Figure 81. Schematic Diagram of Test Setup and Instrumentation

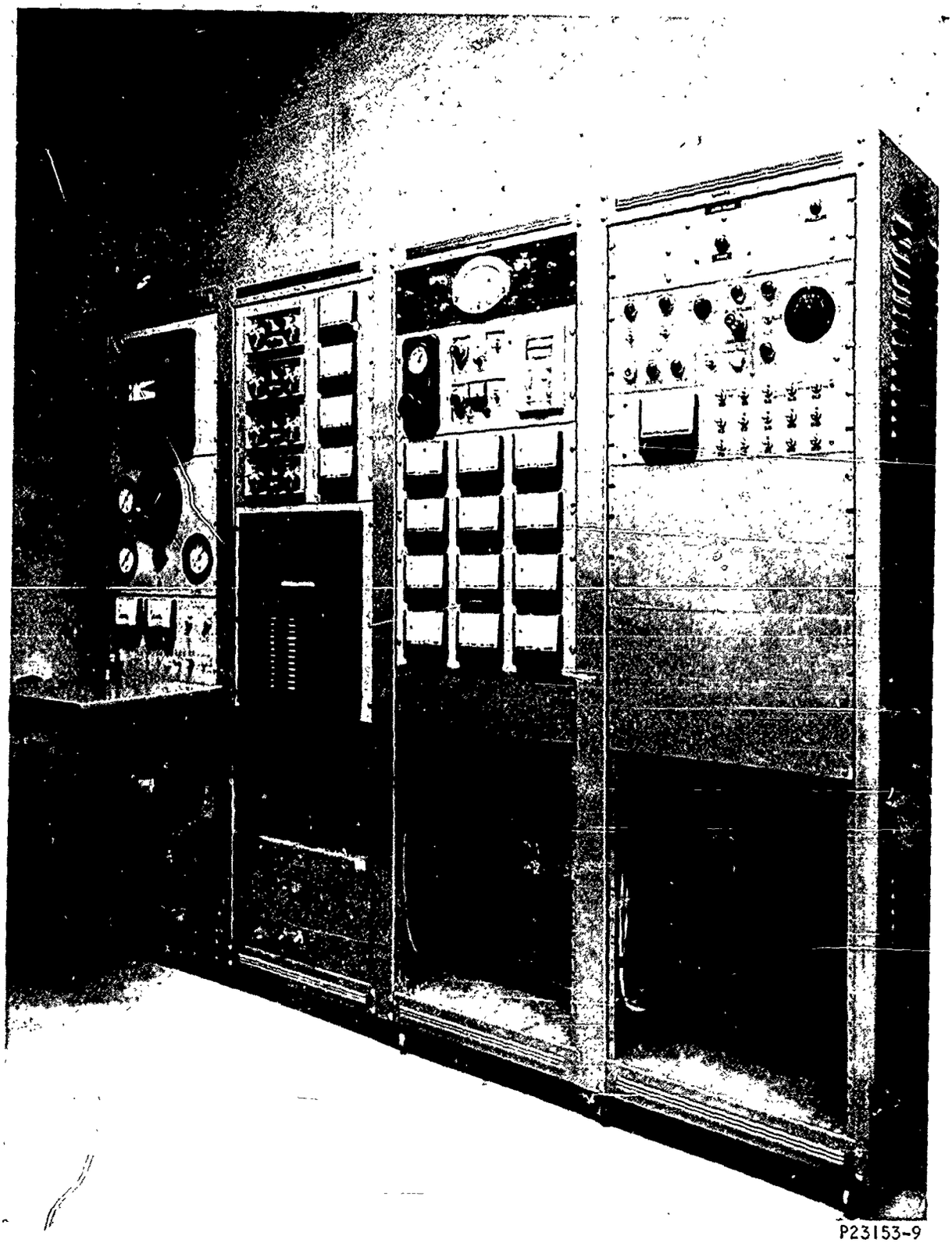

Figure 82. Control Room Instrument Console

Test Point	Location	Number of Channels
T_2	Pump Inlet Temperature	2
T_3	LH_2 Flow Orifice Temperature	1
T_5	Turbine Inlet Temperature	1
T_7	Turbine Flow Orifice Temperature	1
T_9	Turbine Exhaust Temperature	1
P_1	LH_2 Tank Pressure	1
P_2	Pump Inlet Static Pressure	1
P_3	Pump Inlet Total Pressure	1
P_4	Pump Discharge Static Pressure	2
P_6	Turbine Flow Orifice Pressure	1
P_9	Thrust Balance Pressure	1
P_{10}	Turbine Inlet Pressure	1
P_{11}	Pump Inlet Vapor Pressure	1
ΔP_1	Net Positive Suction Head	2
ΔP_2	Turbine Flow Orifice Differential Pressure	1
ΔP_3	LH_2 Flow Orifice Differential Pressure	1
W_1	Tank Weight	1
N_1	Shaft Speed	1

All other test points not listed above and shown in Figure 76 were for control panel monitoring purposes.

Specially Developed Instrumentation

Certain special instrumentation was developed for this particular test. Noteworthy achievements were reviewed below.

1. Net Positive Suction Head Measurement - In order to measure pump NPSH (Net Positive Suction Head) accurately, a special static test gauge was designed embodying an accuracy of 0.5 feet because of the low (4 to 10 feet) NPSH required for the test. This instrument consisted of a system which filled a vapor bulb

with a specific volume of liquid hydrogen, a capillary coil to condense gas to the liquid stage, and a pressure tube to measure pressure head at the level of the vapor bulb. Figures 83 and 84 show the vapor bulb filling system together with the vapor bulb coil, static pressure tube, and thermocouple.

This gauge was static tested with nitrogen and liquid hydrogen prior to actual pump performance testing to ascertain its accuracy. The desired accuracy plus or minus 0.5 feet was secured. For the actual pump installation, this system was expanded to include three separate vapor bulbs and pressure probes installed in the hydrogen jacketed pump inlet duct. NPSH instrument orientation is presented in Figures 85 and 86. A multiple filling system (Figure 87) utilizing remotely operated solenoid valves was constructed for use with this system.

2. Pump Power Measurement - In an effort to measure shaft power to the pump, a Bergen Laboratories magnetostrictive type torquemeter was incorporated in the design of the coupling between the turbine and the pump. This torquemeter consisted of three transducers, an external nulling system and combined power supply, and a readout gauge. This type of torquemeter measures strain in the coupling spaces without requiring slip rings or any other rubbing contact device. After undergoing static calibration tests in the Bergen Laboratories, the torquemeter nulling system was modified by the manufacturer to make mechanical nulling less critical. This was done by adding an external resistance capacitance balancing on each of the three transducers around the shaft. Figures 88 and 89 showed the magnetostrictive type torquemeter system components and liquid hydrogen pump drive shaft, respectively. With the revised nulling system, static calibration curves of the torquemeter using the torque shaft were successfully obtained.

During the static calibration test of the torquemeter using the torque shaft, it was found that the null balance was a function of torque shaft rotational position, which was undesirable. Three distinct peaks of output were obtained when the torque shaft was rotated 360^0 from the null position. After carefully eliminating all lost motion, and reducing the total indicated runout to less than 0.0001 in., the effect of rotation on output was still uncorrected. It was then found that the torque shaft was highly magnetized. After demagnetization, the effect mentioned above was reduced to less than 5 percent of full scale. After the first run of the pump without the impeller mounted, the torquemeter was assembled around the torque shaft. While accomplishing the nulling process, it was found that the rotational effect was still present although great care had been taken to demagnetize the torque shaft immediately prior to assembly. Consequently, the torque shaft was again removed and found to be highly magnetized. After demagnetization, it was again reassembled with the same result.

To determine if this effect could be neutralized by zeroing the instrument under no-load operation at speed conditions, the torquemeter was nulled at an arbitrary position and then operated at various speeds, the only load being pump bearing and slight windage losses. While it was possible to set the zero at any one speed, this setting would not be zero for any other speed. It was concluded that a magnetic field was present, created either by the base supporting the pump and turbine becoming magnetized, or an induction field

caused by stray current flow in the vicinity of the torque shaft. Since no facilities were available to demagnetize the base assembly, and time commitments were prohibitive, the torquemeter concept of torque measurement was then abandoned. Measurement of the mass flow through the turbine and the turbine inlet and discharge temperatures, being functions of the turbine output power, were used as a means of determining pump input power.

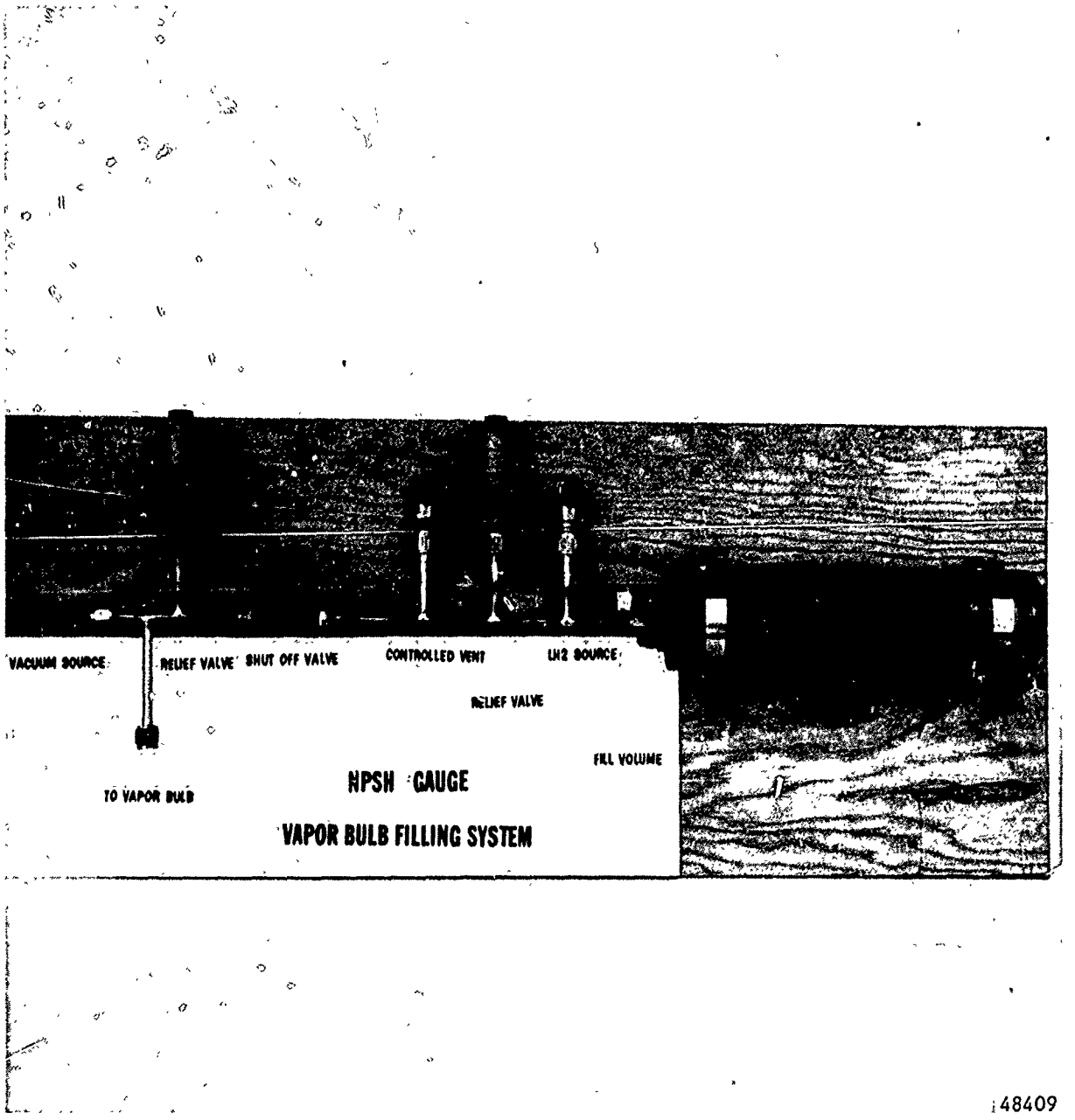

Figure 83. NPSH Gauge Vapor Bulb Filling System

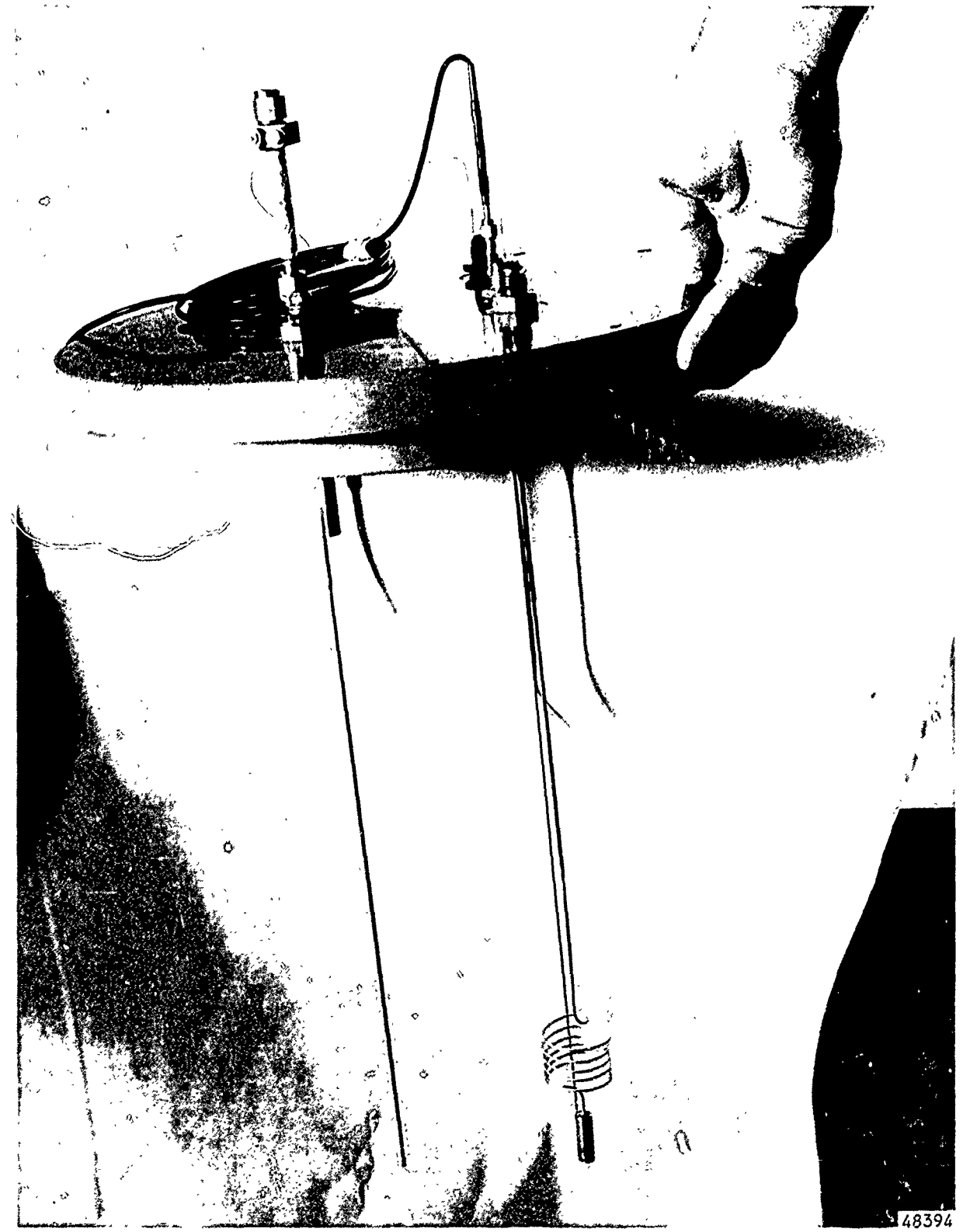

Figure 84. NPSH Gauge Static Test Rig

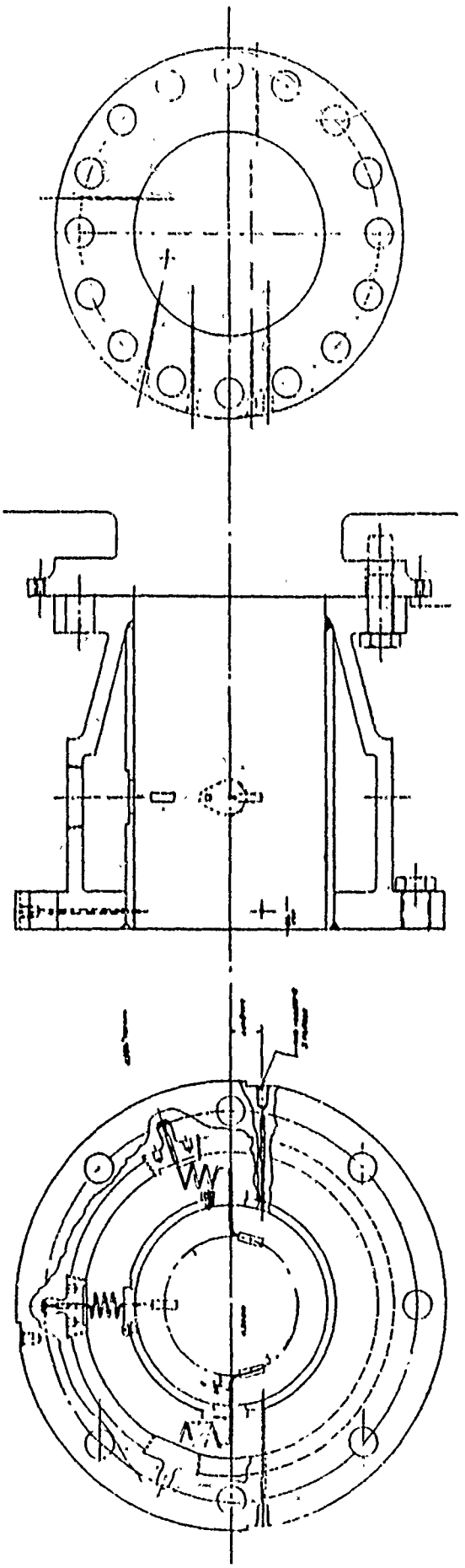

Figure 85. Sketch of Pump Inlet Duct Showing Instrumentation Locations

Figure 86. Internal View of Pump Inlet Duct and Instrumentation

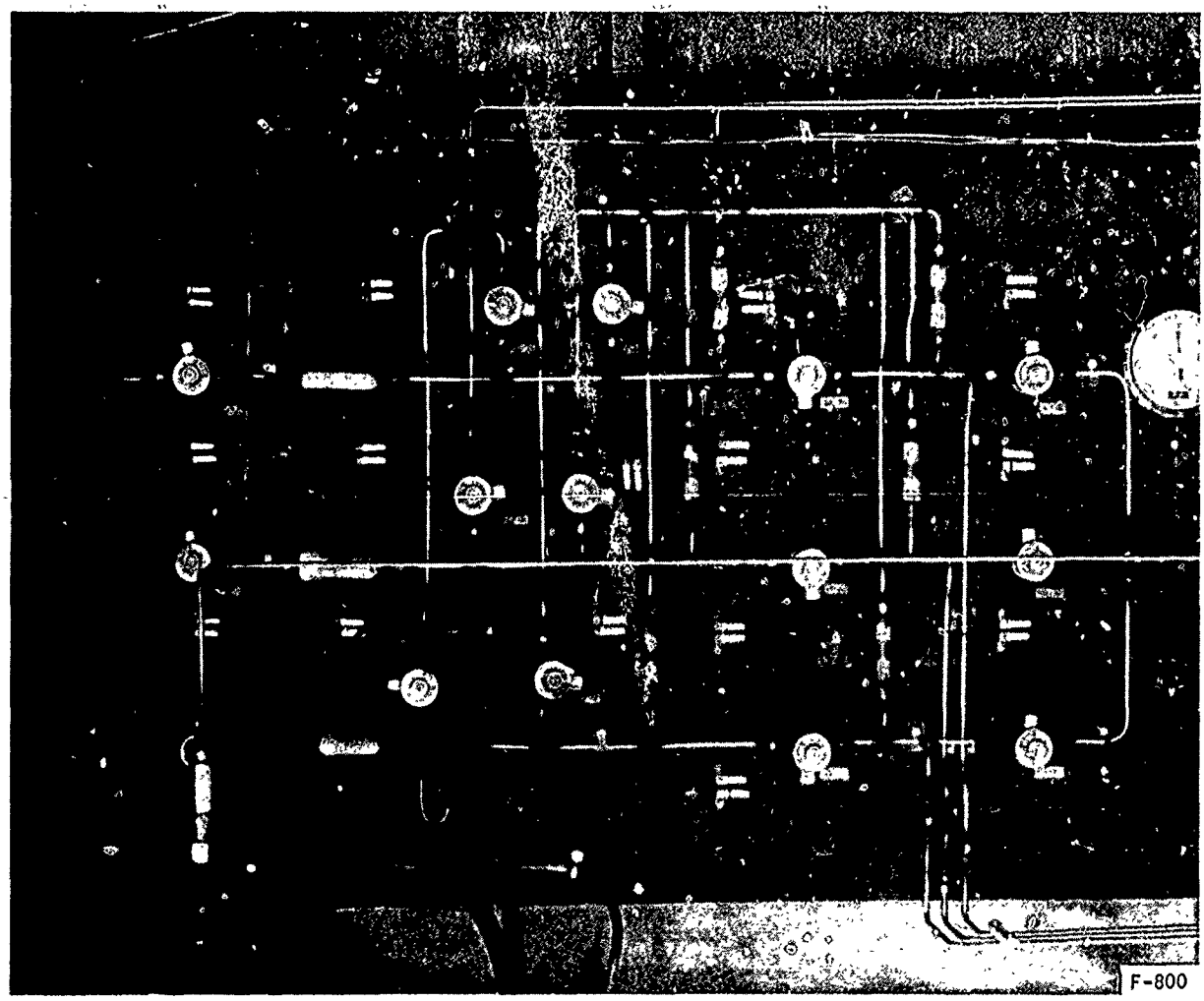

Figure 87. Multiple NPSH Gauge Vapor Bulb Filling System Used During Pump Test

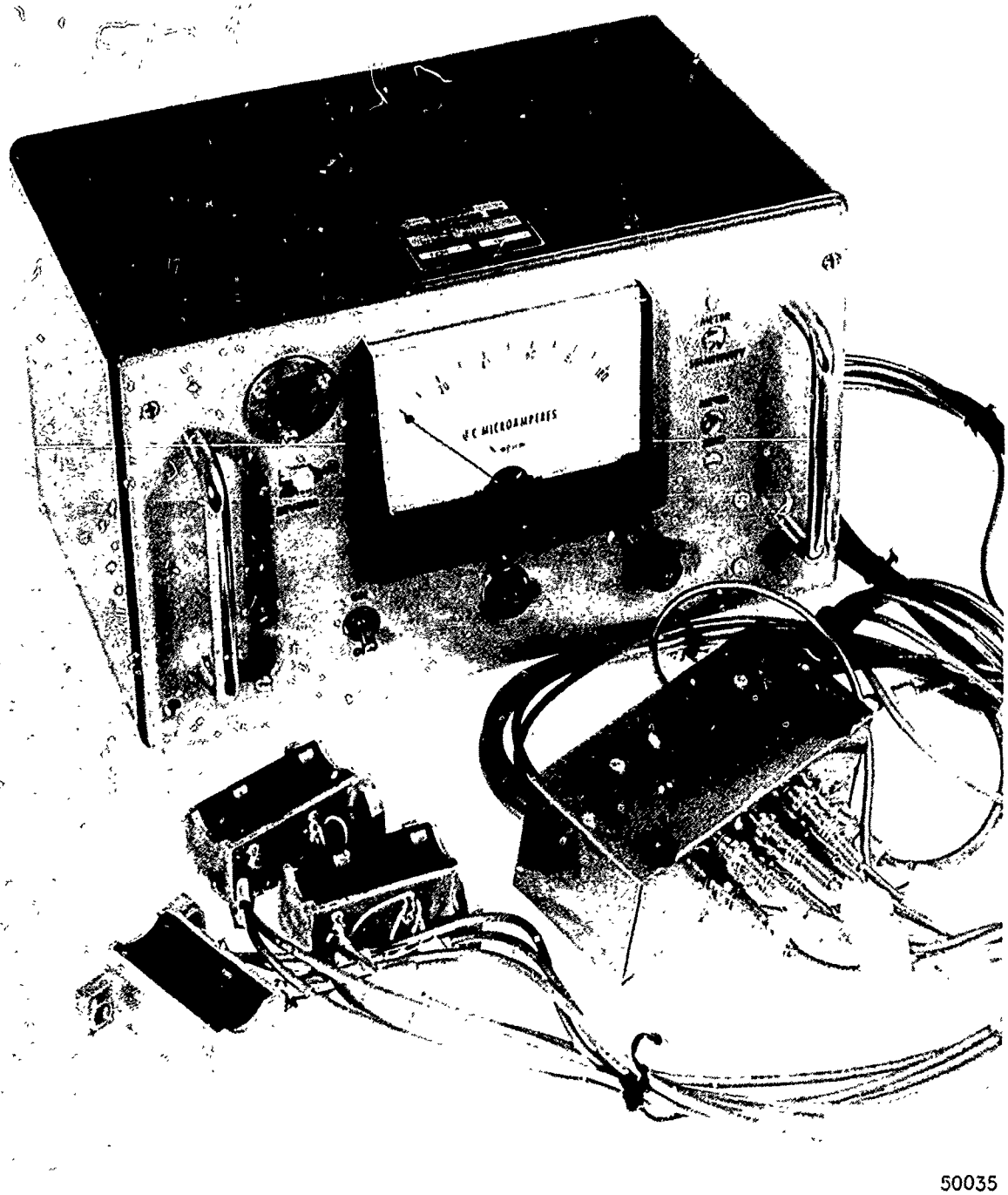

Figure 88. Magnetostrictive Type Torque Meter System Components

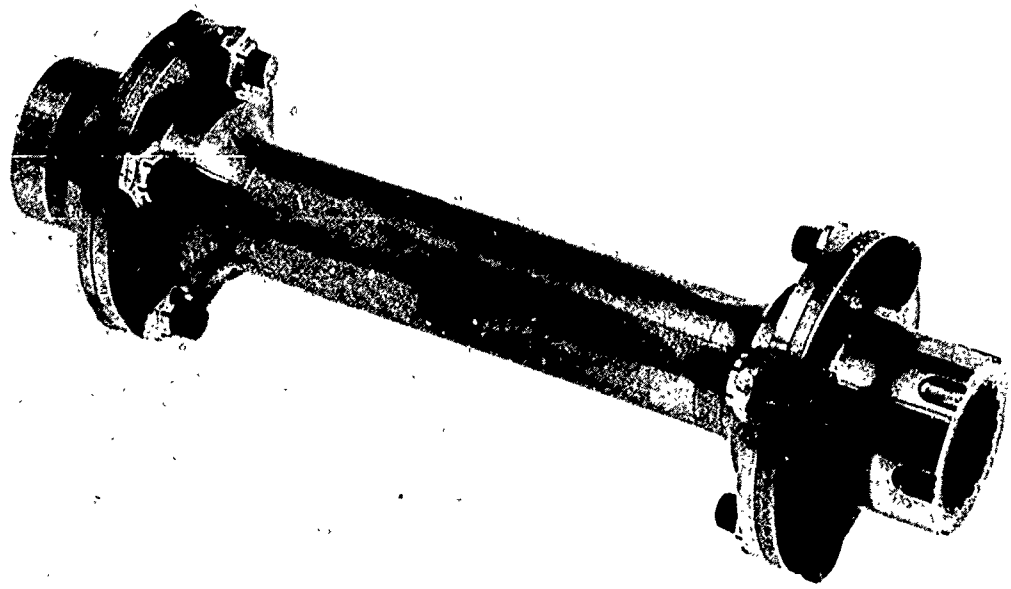

50034

Figure 89. Liquid Hydrogen Pump Drive Torque Shaft

SECTION 8

TEST PROCEDURE AND RESULTS

PRELIMINARY TESTING

The activities in the tests that follow are reviewed in chronological order.

The first pump assembly together with the drive turbine was run on March 23, 1964, in Los Angeles. This run was made to check unit critical speeds, torque shaft runout, and shaft displacement. The impeller was not assembled in the unit for the run and standard bearings were used. An external oil source was used to lubricate these bearings. Performance was satisfactory in all respects. The next runs were conducted with the torque meter pickups assembled around the torque shaft to observe the affects of the torque shaft runout, vibration, and speed on torquemeter performance. Results of this test have been previously reviewed under pump power measurement in Section 7. At this time, the shaft displacement measurement equipment, overspeed trip actuator and speed measuring equipment were also checked.

The next runs were conducted with impeller installed but with the impeller seals omitted. This was done to avoid seal rub while running dry. The unit was operated to a tripping speed of 42,000 rpm several times while the shaft runout was observed. Since performance was satisfactory, the unit was completely disassembled, cleaned and reassembled with seals and special ball bearings for cryogenic operation. This unit was then shipped to the test site for performance evaluation. In addition a spare pump, less rotating element, and two spare impellers were assembled to provide standby spares.

The pump was installed on the liquid hydrogen test stand in Arizona early in May. After alignment and connection to the tank duct was completed, the first check run was made to cold-check the alignment of the turbine and pump shafts. On May 18, 1964, 6000 gallons of liquid nitrogen were put into the tank and used to cool the pump to -320°F. Alignment checks before cooldown and after stabilization, with the pump and dump line full of liquid nitrogen showed a horizontal shift of 0.0065 inches. The ambient temperature alignment was corrected to 0.0090 inches to compensate for the shift expected when the pump is handling liquid hydrogen.

On May 25, the tank was filled with liquid hydrogen for the first time. On May 27, liquid hydrogen was first introduced into the pump and dump line preparatory to the first run. A leak in the pump discharge line became evident shortly after cooldown was initiated. Cooldown was discontinued to find and repair the leak. The leak occurred in the orifice section of the pump discharge line upstream of the pump discharge throttle valve. After the repair was completed, the orifice section was reinsulated with the polyurethane foam being used for thermal insulation of pump and other cold elements.

PUMP PERFORMANCE RUNS

Run 1

On June 3, the cooldown process was again started and since no serious leaks or other malfunctions were observed, cooldown was completed without mishap and the pump was operated with the discharge throttle valve in the full-open position for approximately 2 minutes. The following data was observed on the instrumentation console:

Total run time, min, sec	2:06
Hydrogen discharge pressure, psig	108
Hydrogen flow rate, gpm	1700
Shaft speed, rpm	21,000

The flow rate was based on a consensus of visual observations of the tank weight system. No permanent oscillograph trace was obtained during this run, due to a data acquisition system malfunction.

Run 2

On June 9, following instrument calibration, a second run was conducted. The discharge throttle valve was adjusted to a partially closed position, and the pump was operated at 25,000 rpm. Total run time was 7 minutes 11 seconds, and time at steady state speed was 1 minute 24 seconds. During this run, the tank pressure fluctuated from 0.35 to 0.60 psi. Data for this run is presented in Table II.

Prior to the run, both NPSH differential pressure transducers, the vapor bulb pressure transducer, and the pump inlet total pressure transducer were seriously overpressurized. Also, there was no pump inlet static pressure transducer. The overpressure possibly caused some inaccuracy in the recorded differential pressure, and because of the lack of redundant readings to corroborate the data, the values of NPSH and pump inlet total pressures are questionable.

The values of pump inlet temperature appeared to be inaccurate during this test run. Subsequent to this run, all three platinum resistance temperature sensors indicated open circuits, and the type of instrumentation selected for this parameter apparently was not adequate to provide the necessary information. No further attempt was made to record the pump inlet temperature, although a new platinum resistance sensor was installed after Run 7.

Following Run 2, the coupling between the pump and turbine was removed and manual rotation of the pump shaft indicated the pump bearings were rough. The bearings were replaced prior to Run 3.

Run 3

This run, made on 17 June 1964, was to operate the pump at design conditions (40,000 rpm and 800 psi differential pressure).

The discharge throttle valve was set 1/4 open.

The unit speed was maintained at 20,000 rpm for a period of 1-1/2 minutes and speed was then increased. At 30,000 rpm, the shaft displacement probes indicated violent shaft excursion and the pump was shut down. Several restarts confirmed the indication of this extreme shaft motion.

Total run time was 7 minutes 58 seconds.

Data for this run is presented in Table 12.

After the run, the pump was uncoupled from the turbine and the pump shaft manually rotated. (This inspection procedure was repeated after each subsequent run.) Pump bearings felt smooth, and therefore, were not removed. This pump was used for further testing.

The shaft displacement observed during test was believed to have been due to seal rub on the impeller during wear-in. Unit disassembly and inspection after Run 6 corroborated this assumption.

Run 4

This run, made on 19 June 1964, was to recheck system operation with respect to turbine inlet air combustion, supply tank pressure regulation, and shaft displacement instrumentation.

The discharge throttle valve was set to one turn less than 1/4 open. (Twenty turns are required to produce full travel of the valve gate.)

Trouble was experienced during this run in maintaining proper burning at the combustor; therefore, almost the entire run was made without use of this combustor. Data was obtained at speeds of 11,900, 12,900, 29,600 and 37,700 rpm. Total run time was 13 minutes 30 seconds.

While operating at 29,600 rpm, the hydrogen in the supply tank was depleted, and the pump subsequently shut down on an overspeed trip at 42,000 rpm, providing a check on the operation of that system.

Data for this run is presented in Table 13.

Run 5

This run, conducted on 22 June 1964, was to achieve design speed and discharge pressure.

The discharge throttle valve was set in a one-fourth open position, and in an attempt to maintain tank pressure at a more constant value than for previous runs, the tank vent line was opened. (For all previous runs, the tank pressure was controlled only by means of hydrogen entering the tank from the auxiliary tank.)

Run time was 2 minutes 53 seconds, with a steady state time of 11 seconds at a speed of 31,400 rpm.

Data for this run is presented in Table 14.

After the run was started, considerable difficulty was experienced in igniting the turbine inlet air combustor. Shortly after a combustor fire was achieved, the test was aborted because the combustor fuel pressurization system back pressured the J-57 engine fuel system causing a flame out.

It should also be noted that the attempt to control the hydrogen tank pressure was unsuccessful because back pressure from the pump bearing vent line caused an excessively high tank pressure.

The steady state speed attained was the maximum which could be attained with maximum J-57 engine bleed air and no subsequent heating (line combustor).

Run 6

This run was conducted on 24 June 1964 to check pump performance at a steady speed condition and to vary pump discharge flow and pressure by varying the position of the discharge throttle valve.

During this run, a steady state speed of approximately 33,000 rpm was maintained, and pump performance at three discharge valve positions was recorded. Two attempts to get data with the discharge valve in a more closed position were unsuccessful since a constant speed could not be maintained and overspeed trip resulted in each instance. Total run time was 10 minutes 27 seconds.

Data for this run is presented in Tables 15A and 15B.

Following Run 6, it was decided to obtain further data using a second pump unit.

Run 7

This run, conducted on 29 June 1964, was to achieve pump design conditions using the alternate pump configuration to obtain comparative data.

The tank pressure was regulated at 15 to 20 psig. The discharge throttle valve was set 1 turn less then 1/4 open. Pump steady state speed was approximately 34,000 rpm and was held for approximately 30 seconds. Total run time was 2 minutes 38 seconds.

Data for this run is presented in Table 16.

The operating speed was the maximum which could be held without heating the turbine inlet air. The combustor was operating, but as there was no indication of combustion in the test control room, the ignition and fuel were turned off.

The NPSH and pump inlet transducers were not reading during this run, however, vapor bulb pressure was visually observed during the run and was steady at 6.25 psig.

The run was terminated because of a pump bearing failure. This is reviewed in the Analysis of Test Results section.

Post-Run Activity

Immediately after Run 7, all faulty instrumentation was either repaired or replaced to insure complete data during intended future runs. Feedback from the completed runs was incorporated at this time to increase data accuracy and reliability.

In addition, it was decided to design and test a new seal configuration for the pump inlet and thrust balance seals at this time. (The seal design is discussed in the section that follows.) Unfortunately, the intended program was terminated due to lack of time and funds.

ANALYSIS OF TEST RESULTS

Design Changes and Improvements

As noted in the testing section, subsequent to Run 2, the coupling between the pump and turbine components of the unit was removed, and the pump shaft slowly rotated by hand. One rough spot could be felt periodically as the shaft was moved. The rotating group was removed and the bearings were carefully examined. A wide ball track and some evidence of excessive thrust were noted on the inboard bearing (bearing furthest from the pump impeller). Several slivers of aluminum from the seal lip were discovered in the lubrication passages; however, these were not considered harmful. The impeller showed a series of score marks on both the inlet seal and thrust seal register. The total run time in this set of bearings was 9 minutes 17 seconds. The inboard bearing and impeller are shown after test Figures 69 and 68 of Section 6. The bearing adjacent to impeller looked in excellent condition.

The pump was reassembled with a new set of bearings, a new impeller, and new seals. The seals were machined to provide an increase in seal diametral clearance of 0.004 in. at the pump inlet and 0.002 in. at the thrust seal register. In addition, a pressure tap was added behind the impeller to obtain an indication of thrust forces at this point. Runs 3 through 6 and conducted with this configuration. A total time of 34 minutes, 28 seconds was accumulated on this set of bearings.

Concurrent with the reassembly of the pump following Run 2, a second configuration was assembled as a standby. This pump incorporated large through-flow vents to prevent a buildup of thrust pressure forces. (These vents had the effect of bypassing the major amount of bearing lubrication hydrogen.) Seal dimensions were increased as noted above. Another major change was the replacement of the resilient bearing mounts with solid rings to reduce total shaft excursion. This configuration was installed for Run 7.

The bearing failure, which occurred during Run 7, was attributed primarily to the lack of lubrication to the bearings. However, seal labyrinth rub on the impeller which may have caused an unbalanced condition was also a possibility as the prime cause of failure. Because of the rigid bearing mounts, unbalance forces are less easily sustained by these bearings.

For the configuration for Run 8 (which was never accomplished), it was determined that the best possibility of successful operation would be a return to the lubrication configuration of Runs 1 through 6 and the reinclusion of the resilient bearing mounts. However, because of the cutting action of the labyrinth configuration, an effort was made to develop a seal that would not cut into the aluminum impeller.

An Armalon material was selected because (1) this was the basic material used in the bearing separator and hence was suitable for cryogenic application, (2) this material had been tested as a seal material at room temperatures with good results and (3) availability.

The selected material Armalon 414-141, is a TFE-impregnated fiberglass fabric (0.010-in. thick fiberglass sheet). The seals were designed and fabricated despite the absence of positive data relating to shrinkage and strength of this material at cryogenic temperatures. Inasmuch as the seals were never used, no information was obtained which would be helpful in future designs, but this would be a possible consideration.

The carbon-faced seal used as a shaft seal to prevent the escape of hydrogen into the area between the pump and turbine caused no problems.

For future tests, or designs, it is recommended that greater attention be given to the method of providing liquid hydrogen lubrication to the bearings. An auxiliary source of liquid hydrogen jetted directly at the bearing inner race is suggested as a possible method.

Instrumentation Problems

The Bergen Laboratories magnetostrictive type torquemeter was not used during the actual runs because of the calibration problems described elsewhere in this report. With proper selection of materials, a device of this sort might be developed to provide accurate torque measurement. In addition to the magnetostrictive torquemeter, an electronic device to measure angular displacement of a torque shaft was also designed, but fabrication of this device could not be completed within the time period allotted for this task. The method used to measure turbine input power consisted of a turbine flow measurement section and inlet and discharge thermocouples. This provided a measure of input power, but does not take into consideration certain power transfer losses, and as such, is inherently less effective and accurate than a direct measurement of pump input power. Furthermore, thermal heat lag became a definite problem during short duration steady state as well as all transient runs. The mass of the turbine wheel and housing was sufficiently large that data from the turbine discharge thermocouple lagged that from the inlet thermocouple to such an extent as to render the turbine output power meaningless for steady state runs of 45 seconds or less duration.

Liquid hydrogen temperature at the pump inlet was to be measured by means of three separate Microdot platinum resistance sensors. These proved to be too fragile for the test. Results of Run 2 indicated wide differences from two of the three probes and during the run, all failed. Due to inaccessibility, no attempt was made to replace these sensors until after Run 7 was complete, so no inlet temperature measurement was never obtained.

Some difficulty was encountered in measuring and recording liquid hydrogen pressures. In some instances, it appeared that the column of liquid hydrogen in the sense line, boiling violently, caused extreme fluctuations in pressure readouts of pressures which should have been relatively steady. It is recommended that, in future work, considerable additional attention be devoted to the design and placement of pressure sensing lines. Also, rapid fluctuations in pressures at the discharge flow orifice apparently led to several failures of the orifice differential pressure transducer. In an attempt to eliminate this problem, snubbing orifices were placed in the sense lines. However, data from the orifice was questionable as noted by the differences between the flows calculated from orifice data and from the strain gauge load cells.

The NPSH gauge designed for this test could not be used to accurately determine the NPSH value because of inaccuracies in the vapor pressure measurement. Time lag in the vapor pressure bulb was one major source of error. This could be prevented by using a smaller, thin-walled bulb. Although the bulbs in this test were only 0.010 in. thick, they were insulated with the Microdot temperature sensors. Also, a more steady tank pressure than was maintained would eliminate some of the necessity for extremely rapid time response. Mechanically, the NPSH fill system, as originally designed, was adequate. However, some problems were encountered with solenoid valve leakage. These valves could be set up for zero leakage for either pressure or vacuum, but would not seal tight in both directions. Following Run 6, the

solenoid valves were replaced with manual shutoff valves. This could be done since experience from the first six runs indicated no danger existed in the area of the NPSH fill system during the cooldown period.

Problems Encountered During Testing

1. Tank Pressure Regulation - The method used to maintain a constant pressure in the 13,000-gallon liquid hydrogen supply tank was to admit cold hydrogen gas from an auxiliary tank of liquid hydrogen. This hydrogen entered the tank in a gaseous state, and the amount was regulated by a differential pressure regulator. Because of the distance of the auxiliary tank from the primary supply tank, and the heat leak through the uninsulated connecting plumbing, the entering gaseous hydrogen was much warmer than liquid hydrogen temperature. It is believed that this warm hydrogen may have caused some boiling of the liquid hydrogen which led to an immediate increase in supply tank pressure over the regulation range. A more stable supply tank pressure could have been achieved by utilizing the differential pressure regulator to control a three-way valve with one outlet port connected to a separate vent stack to permit venting of excess hydrogen gas.

Runs 5 and 7 were at essentially constant pressure. In order to improve pressure regulation during Run 5, the supply tank vent line was opened. Back pressure from the pump bearing vents was, therefore, allowed to flow back into the tank and cause a relatively constant pressure. However, the supply tank resultant pressure level was much higher than desired.

For Run 7, it was desired to maintain a very high tank pressure. The supply tank was pressurized directly from the auxiliary tank without using the differential regulator. The large volume of the auxiliary tank coupled with the short duration of Run 7, produced a stable pressure, but did not permit the degree of regulation desired.

Turbine Combustor

All runs, commencing with the second, included efforts to burn fuel in the turbine inlet duct in order to increase turbine power and to also provide a more stable means of speed control. The operation of the line combustor was not successful probably due to improper fuel-air mixtures and therefore all runs were made with direct engine bleed air.

Prior to Run 7, the combustor ignition and fuel systems were revamped and a revised technique for light-off was established.

At the beginning of Run 7 the combustor was again tried and although test stand instrumentation indicated no light-off subsequent investigation of the oscillograph trace indicated that a light-off had been achieved.

Pump Pressure Rise Performance

The measured pressure rises were plotted against the delivered flow in Figure 90. Each point is identified by its designation according to Tables II through 16.

The results were insufficient to give a complete head-capacity curve. To be able to make a comparison between the measured and the predicted performance, the points were plotted on the pressure-flow diagram printed by the IBM computer when performing the design calculations. This plot is presented as Figure 91. Many of the measured points form groups, designating only one point. In this case, only one point was shown on the IBM diagram. As can be seen, the data points fall closely on the predicted performance for all speed values between 40 percent and 85 percent of the design speed. At a speed of 33.600 rpm, pressure rise was 560 psi (Run 7G). This result, at 85 percent design speed, is close to the design point, and permits a projected estimate that indicates on the basis of the similarity laws of turbomachinery, the design objective at full speed would be met.

Cavitation Performance

The pump was tested through a very wide range of cavitation. The number of test points are not large enough to give the exact numerical relationship between the performance parameters and the state of cavitation. It can be seen, however, that promising cavitation performance has been demonstrated.

In test Runs 2 and 6 (Tables II and 15A), the pump operated at 24,000 to 25,000 rpm while the NPSH was allowed to change. Negative values of NPSH have been recorded while the pump pressure rise remained practically unchanged. Here, suction specific speeds ranged from 93,000 to infinity, and also to negative values.

For the purpose of analyzing the cavitation performance, it is generally desired to make use of the head coefficients

$$\psi = \frac{gH_o}{u_2^2}$$

and the cavitation parameter

$$\tau = \frac{2gNPSH}{W_1^2}$$

The experimental results are presented in Figure 92. They show that the head coefficient ψ still holds up where the pump operates with small or negative values of τ(negative NPSH). No pounding or oscillation has been reported in this range of operation.

Despite the scarcity in data points, the slope of the ψ, τ curves are practically the same for each run showing just a straight reduction of the pressure output without the usual cavitation breakdown.

Pump Efficiency

Due to the lack of torque measurements, precise efficiency of the pump is not available. However, the test data can be evaluated using the work input coefficient ($q_{input} = H_{input}/\frac{u_2^2}{g}$) as obtained from performance prediction studies. In the present design, this coefficient has been established from experimental data on the slip factor and blade angles of a large number of pumps. Thus, it can be reasonably assumed that the values of q_{input} used to arrive at the predicted performance in Figures 38 and 39 are actually that of the test pump.

For a given pump, the work input coefficient is controlled by the flow and speed parameters. The test pump coefficient can be obtained by:

$$(q_{input})_{test\ pump} = q_{calculated}$$

with

$$(w/w_D)_{test} = (w/w_D)_{calculated}$$

where subscript D denotes design conditions

and

$$(N/N_D)_{test} = (N/N_D)_{calculated}$$

The test pump efficiency can be calculated as:

$$\eta_{test\ pump} = \frac{\left(\frac{H_{output}}{u_2^2/g}\right)}{q_{calculated}}$$

or

$$\frac{\eta_{test\ pump}}{\eta_{calculated}} = \frac{\Delta P_{test\ pump}}{\Delta P_{calculated}}$$

(at the same flow and speed parameters)

Thus, the efficiency of the test pump can be tabulated for various reliable data points based on predicted performance obtained from Figures 38 and 39 in conjunction with the ratio of pump pressure rises as shown in the table on the following page.

	Speed, rpm	Speed Ratio(N/N_D)	Flow, gmp	Flow Ratio(W/W_D)	Pressure Rise, psi	Pump Efficiency
Test Data (Run 7E)	33,600	0.84	1340	0.79	560	0.738
Predicted Performance	-	0.84	-	0.79	565	0.731
Test Data (Run 3E)	28,400	0.71	1500	0.883	364	0.740
Predicted Performance	-	0.71	-	0.883	385	0.710
Test Data (Run 3B)	19,600	0.49	890	0.524	200	0.750
Predicted Performance	-	0.49	-	0.524	190	0.712

Since the pressure rises of the test data and the predicted performance in Figure 38 are remarkably close, the efficiencies are also similar. In the range of high speed (N/N_D = 0.84), a test point gives an efficiency of 0.731, a value less than 1 percent lower than the predicted value of 0.738. Since this test point is close to design speed (N/N_D = 1.0), it can be reasonably anticipated that, at design speed, the predicted pump efficiency of 0.75 can be achieved. Hydrodynamic laws governing pump behavior, within a small range of speed variation also contribute to the support of this conclusion.

Thus, the test data indicates reasonably good pump performance, with a design point efficiency of 75 percent as predicted.

Determination of Pump Inlet Temperatures

Malfunction of the pump inlet thermocouples, first observed during Run 2, rendered this instrumentation useless. Consequently, the pump inlet temperature was computed by trial and error means until an enthalpy balance was achieved as follows:

1. Pump efficiency was computed based on the ratio of actual differential pressure to predicted differential pressure using the method reviewed in the previous section.

2. Pump inlet temperature was first assumed to be equal to saturation temperature at the pump inlet pressure or tank pressure, whichever was available.

3. Pump inlet and discharge enthalpies were determined based on pressures and temperatures at these points. The enthalpy differential (ΔH) was calculated from these values.

4. Theoretical enthalpy change (ΔH_{THI}) was computed as the product of ΔH and pump efficiency determined in Step 1.

5. A pump discharge enthalpy was calculated based on an isentropic pressure rise from the assumed inlet point to the actual pump discharge pressure.

6. The theoretical enthalpy change (ΔH_{TH2}) was calculated based on the Step 5 isentropic condition and compared with the ΔH_{TH1} value from Step 4.

7. If the disparity between ΔH_{TH1} and ΔH_{TH2} is greater than 5 percent, a new pump inlet temperature is assumed and the ΔH determination is repeated.

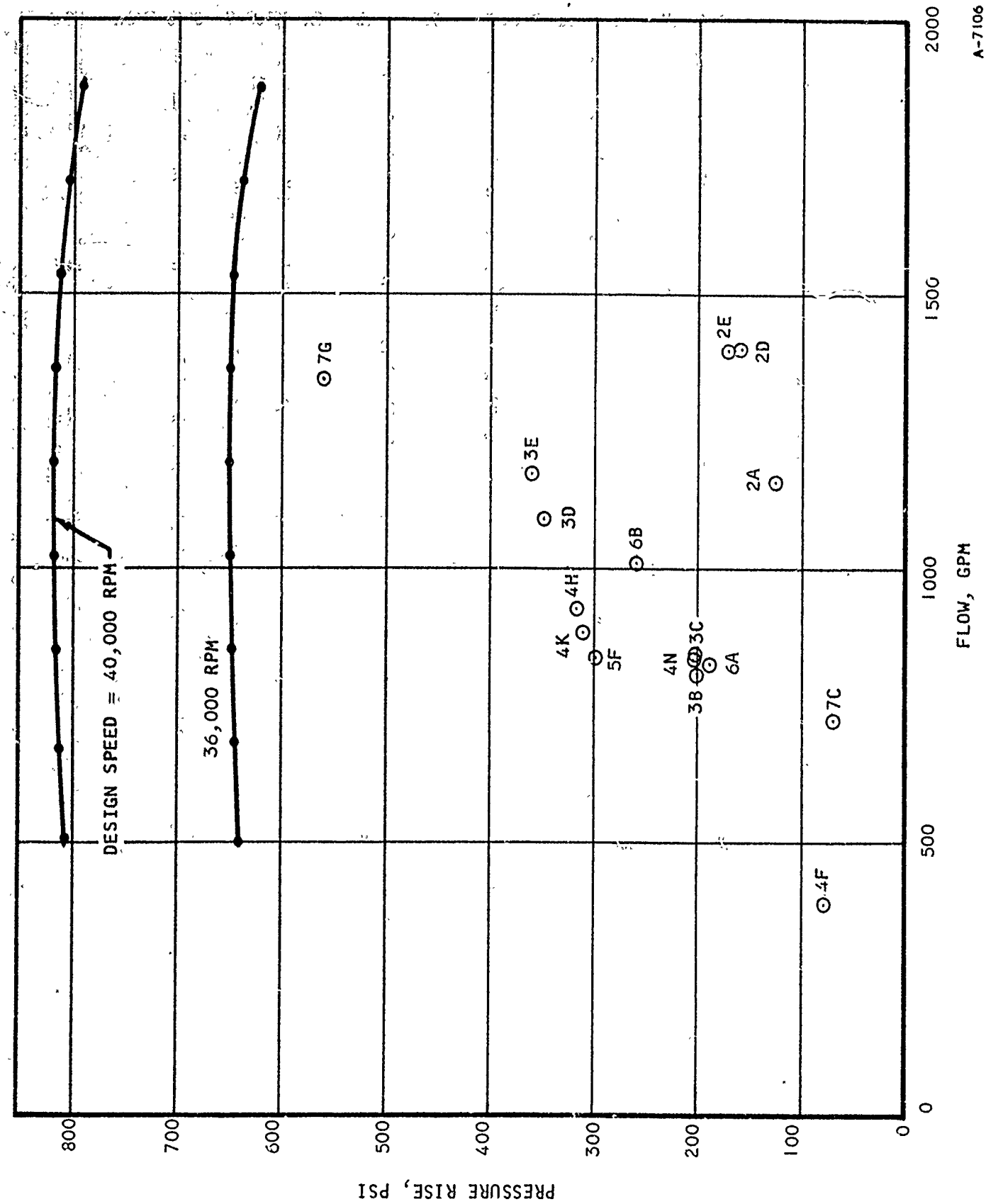

Figure 90. Pressure - Flow Curve Showing Test Data Points

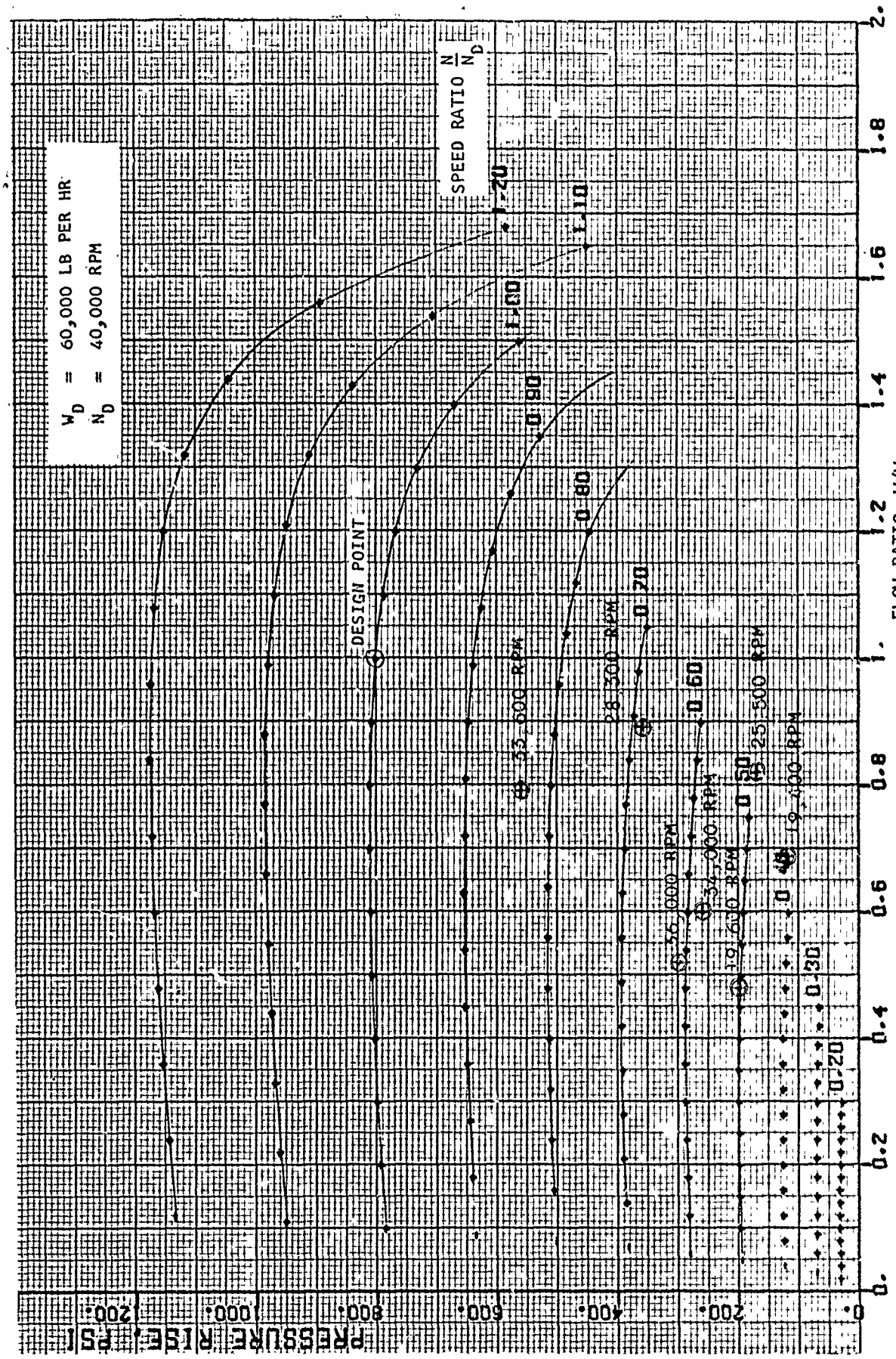

Figure 91 Comparison of Liquid Hydrogen Pump Predicted and Actual Performance

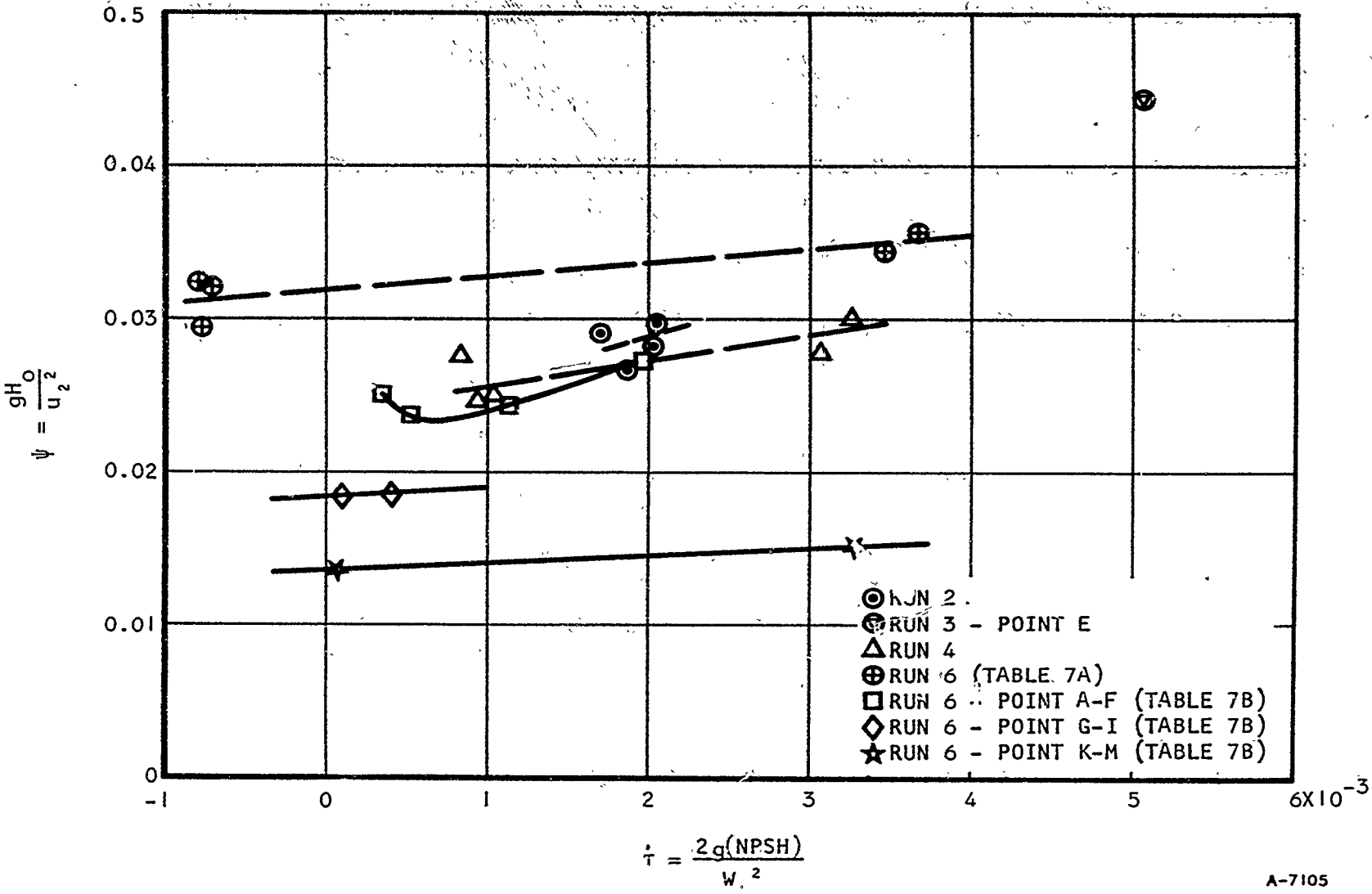

Figure 92. Pressure Factor versus Cavitation Number

TABLE II

RESULTS OF TEST RUN 2

	A (1)	B	C	D	E
Run time interval, min: sec	3:23	4:50	5:21	5:43	6:14
Tank pressure, psig (2)	0.35	0.49	0.48	0.49	0.52
Pump inlet vapor pressure, psig	No record (3)				
Pump inlet static pressure, psig	No record				
Pump inlet total pressure, psig (4)	0.18	0.28	0.22	0.24	0.25
Pump inlet temperature, °R (5)	37.4	31.2	31.0	31.0	30.5
Pump inlet temperature, °R (estimated) (6)	37.4				
Pump outlet static pressures, psig	122	160	163	159.5	178.5
	112	154	162.5	159.5	173.5
Pump outlet temperature, °R	40.7	41.6	43.0	43.3	43.3
Pump speed, rpm	19,400	24,500	25,000	25,600	25,500
Hydrogen flow (from ΔP), gpm	1172	1310	1300	1300	1313
Hydrogen flow (from tank wt loss), gpm	1155	1400			
Pump hydraulic power, horsepower	80	120	124	121	135
Turbine air power, horsepower	144	160	152	164	149
Turbine inlet static pressure, psig	15.0	29.5	30.5	31.0	35.0
Turbine inlet air temperature, °F	200	186	187.5	199	194
Turbine outlet static pressure, psia	14.0				
Turbine outlet air temperature, °F	95	96	101	103	110
Turbine air flow rate, lb per m	243	315	316	316	309
Measured NPSH, ft LH^2	7.4	6.7	11.5	13.9	11.3
Suction specific speed	147000 (3)	211,000	145,000	128,000	149,000

(1) Condition A taken during pump acceleration. Conditions B, C, D, and E are steady state, 25,000 rpm conditions.

(2) Pressure fluctuations were ±0.15 psi throughout the run.

(3) Vapor pressure values read were approximately zero.

(4) Pressure fluctuations were ±0.07 psi throughout the run.

(5) Instrumentation calibration believed to be faulty.

(6) Refer to text for method of computation

TABLE 12

RESULTS OF TEST RUN 3

	A	B	C	D	E
Run time interval, min. sec	1:06	1:51	2:36	3:02	3:25
Tank Pressure psig	4.71	4.76	3.63	3.46	3.69
Pump inlet vapor pressure psig	1.22	0.92	0.81	.66	1.05
Pump inlet static pressure, psig	(1)	(1)	3.17	2.63	2.80
Pump inlet total pressure, psig	2.14	2.21	1.74	2.17	2.25
Pump inlet temperature, °R (Estimated)	39.5	39.5	39.0	38.0	38.0
Pump outlet static pressures, psig	187	200	203	349	364
	187	191	196	344	354
Pump outlet temperature, °R	41.8	42.0	42.2	43.9	44.4
Pump speed, rpm	19,400	19,600	20,600	28,100	28,400
Pump outlet flow orifice ΔP, psi	3.3	3.3	3.6	6.2	6.9
Hydrogen flow (from ΔP), gpm	802	802	847	1090	1170
Hydrogen flow (from tank wt loss), gpm	←	890	→	← 1500	→
Pump hydraulic power, horsepower	←	103	→	← 1315	→
Turbine air power, horsepower	104	124	139	336	333
Turbine inlet static pressure, psig	24	19	23	44	44
Turbine inlet air temperature, °F	153	171	193	225	229
Turbine outlet static pressure, psia	14.0	14.0	14.0	14.0	14.0
Turbine outlet air temperature °F	63	58	67	55	63
Turbine air flow rate, lb per min	205	194	195	350	355
Measured NPSH, ft LH_2	(1)	(1)	65.2	(1)	(1)
Suction specific speed	-	-	25,700	-	-

(1) Value off oscillograph tape.

TABLE 13

RESULTS OF TEST RUN 4

	A ①	B	C	D	E	F	G	H	I	J	K	L	M	N
Run time interval, min: sec	2:54	3:26	:58	1:56	2:34	3:00	3:58	4:21	5:21	6:21	7:21	8:19	9:17	10:05
Tank pressure, psig	.49	.68	.76	.88	.62	1.65	.94	1.15	1.06	.45	.45	.39	.47	.38
Pump inlet vapor pressure, psig	.49	.42	.29	.11	.08	.38	.30	.28	.17	.14	.10	.04	.02	.08
Pump inlet static pressure, psig	N.R.	N.R.	N.R.	N.R.	N.R.	N.R.	N.R.	N.R.	N.R.	N.R.	N.R.	N.R.	N.R.	N.R.
Pump inlet total pressure, psig	.48	1.00	1.25	1.36	1.08	2.52	1.60	1.20	1.10	.39	.40	.32	.39	.33
Pump inlet temperature, °F (estimated)	37.5					38.5		42.0					36.5	
Pump outlet static pressures, psig	24.0	32.0	52.0	51.0	49.0	85.0	88.0	318	316	316	316	313	227	206
	14.0	17.0	38.0	39.0	38.0	72.0	71.0	310	307	307	313	302	211	188
Pump outlet temperature, °R	40.5	40.1	40.4	40.8	40.8	41.6	41.7	48.3	48.8	49.2	49.6	50.5	45.0	44.7
Pump speed, rpm	11,700	12,100	12,900	12,900	12,900	15,800	16,400	34,400	35,700	35,800	37,700	37,700	28,600	29,600
Pump outlet flow orifice ΔP, psi	0.6	0.6	0.6	0.7	0.6	Instrumentation malfunction								
Hydrogen flow (from ΔP), gpm	Negligible					Instrumentation malfunction								
Hydrogen flow (from tank wt loss), gpm	272		170			383		932		882			850	
Pump hydraulic power, horsepower	Negligible					19.0	19.7	173	172	163	163	161	112	102
Turbine air power, horsepower	Negligible					143	82	250	376	384	425	425	198	188
Turbine inlet static pressure, psig	NR	NR	NR	NR	NR	NR	NR	NR	NR	NR	NR	NR	NR	NR
Turbine inlet air temperature, °F	130	129	1,239	1285	1292	684	736	212	248	291	333	392	399	362
Turbine outlet static pressure, psia	14.0	14.0	14.0	14.0	14.0	14.0	14.0	14.0	14.0	14.0	14.0	14.0	14.0	14.0
Turbine outlet air temperature, °F	117	121	761	970	1,018	452	575	123	80	97	118	168	225	202
Turbine air flow rate, lb per min	Negligible					108	86	495	395	350	350	335	202	208
Measured NPSH, ft LH² ②	Negative		2.6	6.6	13.2	Negative		25.6	25.9	7.2	9.8	8.8	10.8	9.2
Suction Specific Speed	-	-	8000	4070	2430	-	-	93500	96900	241000	202000	219000	139000	164000

Start 1 | Start 2 | Start 3

① All conditions tabulated were steady state points.

② Valves of measured NPSH are not consistent with corroborating instrumentation.

TABLE 14

RESULTS OF TEST RUN 5

	A①	B	C	D	E	F	G	H	I	J	K	L	M
Run time interval, min: sec	2:02	3:15	2:08	2:11	2:14	2:17	2:20	2:23	2:26	2:29	2:32	2:35	2:37
Tank pressure, psig ②	6.08	5.88	5.88	5.92	5.92	5.92	5.90	5.96	5.88	5.90	5.98	5.94	5.88
Pump inlet vapor pressure, psig ②	No record												
Pump inlet static pressure, psig ②	6.70	6.54	6.61	6.59	6.62	6.60	6.55	6.59	6.60	6.57	6.60	6.61	6.56
Pump inlet total pressure, psig ②	(>5.15)③												
Pump inlet temperature, °F (estimated)	36.5								37.0				
Pump outlet static pressures, psig	89.0	81.0	247	245	293	299	247	268	300	301	319	312	301
	83.0	77.0	242	240	282	292	243	261	300	299	313	313	298
Pump outlet temperature, °R	40.2	40.5	44.3	44.8	45.7	44.9	44.9	45.6	46.3	46.5	47.0	46.7	46.8
Pump speed, rpm	12400	12900	28300	30400	31200	31800	33300	34200	35100	35100	35500	36000	36000
Pump outlet flow orifice ΔP, psi	No record												
Hydrogen flow (from ΔP), gpm	No ΔP record												
Hydrogen flow (from tank wt loss), gpm	722		838 (Average)										
Pump hydraulic power, horsepower	34.9	31.5	118	112	140	143	118	128	144	144	153	150	144
Turbine air power, horsepower	Negligible		157	189	222	217	278	311	322	346	379	381	298
Turbine inlet static pressure, psig	6	6	31	34	38	37	41	44	47	49	51	52	49
Turbine inlet air temperature, °F	154	121	215	223	217	217	228	234	232	240	236	236	240
Turbine outlet static pressure, psia	14.0												
Turbine outlet air temperature, °F	101	113	148	130	119	113	102	93	96	94	76	83	80
Turbine air flow rate, lb per min	Negligible		320	360	360	370	390	390	420	420	420	440	330
Measured NPSH, ft LH²	No record												
Suction specified speed	No data available												

Start 1 — Start 2

① Conditions A and B are steady state at low speed. Conditions C through H represent gradual pump acceleration. Conditions I through L are high speed steady state points, while Condition M was taken immediately after bleed air engine flame-out.

② Inlet instrumentation questionable because overpressure may have damaged transducer and no calibration is available in range of test run. See text for explanation of high tank pressure during this run.

③ Value off oscillograph tape.

TABLE 15

RESULTS OF TEST RUN 6

	A ①②	B	C	D	E	F	③ G	H	I	J
Run time interval, min: sec	1:12	1:17	1:30	1:35	1:48	1:53	2:07	2:12	2:41	2:40
Tank Pressure, psig	0.16	2.86	0.06	2.88	0.09	2.94	0.18	2.26	0.10	2.20
Pump inlet vapor pressure, psig	1.00	1.01	1.00	0.94	0.90	0.93	0.87	0.87	0.81	0.83
Pump inlet static pressure, psig	0.00	1.30	0.01	1.26	0.00	1.26	0.10	1.17	0.05	1.06
Pump inlet total pressure, psig	0.06	1.45	0.00	1.39	0.09	1.38	0.00	1.35	0.14	1.09
Pump inlet temperature, °F (estimated)	36.6						36.6			
Pump outlet static pressures, psig	172	199	167	199	164	192	207	226	205	233
	158	183	152	185	156	181	191	217	203	222
Pump outlet temperature, °R	40.8	41.0	41.4	41.0	41.0	41.4	41.3	41.4	41.1	41.2
Pump speed, rpm	24,000	25,000	24,800	24,600	23,600	24,000	25,200	24,900	25,700	25,100
Pump outlet flow orifice ΔP, psi	Not recorded									
Hydrogen flow (from ΔP), gpm	LH_2 orifice ΔP trace too faint to be legible									
Hydrogen flow (from tank wt loss), gpm	825									
Pump hydraulic power, horsepower	83.6	95.5	80.0	95.5	78.6	92.3	99.5	109	985	112
Turbine air power, horsepower	Turbine air flow not obtainable									
Turbine inlet static pressure, psig	29.0	29.0	30.0	28.0	34.0	30.1	28.0	31.0	27.0	28.0
Turbine inlet air temperature, °F	184	188	199	196	198	210	215	225	237	241
Turbine outlet static pressure, psia	14.0									
Turbine outlet air temperature, °F	48	56	63	62	57	54	61	62	75	85
Turbine air flow rate, lb per min	Turbine air orifice ΔP trace too faint to be legible									
Measured NPSH, ft LH_2	Negative	14.4	-32.4	14.8	-26.6	14.8	-28.6	15.8	-22.0	8.2
Suction Specific Speed	-	93,000	-	95,200	-	93,000	-	89,900	-	149,500

① All runs are steady state 25,000 rpm operation at varying pump discharge pressures.

② Time intervals selected to show effect of tank pressure variations.

③ Discharge valve setting changed to increase pump pressure rise.

TABLE 15 (Continued)

RESULTS OF TEST RUN 6

	A ①③	B	C	D	E	F	④ G	H	I	J	④ K	L	M	N	O
Run time interval, min. sec	1:04	1:37	1:41	1:59	2:04	2:25	2:38	2:41	3:18	3:26	3:48	4:22	4:28	5:14	5:19
Tank pressure, psig	.46	.89	.51	1.00	.41	.99	.49	1.02	.29	1.02	.26	.27	2.02	.24	1.76
Pump inlet vapor pressure, psig	.17	.10	.18	.16	.14	.11	.14	.08	.14	.10	.17	.12	.16	.12	.10
Pump inlet static pressure, psig	.37	.52	.22	.51	.28	.56	.15	.46	.09	.52	.08	.05	.88	.06	.70
Pump inlet total pressure, psig	.31	.52	.26	.58	.27	.60	.23	.54	.16	.60	.18	.13	.97	.06	.83
Pump inlet temperature °F	← 40.0 →						← 39.0 →				← 40.5 →				
Pump outlet static pressures, psig	255	260	261	268	260	265	207	209	205	205	155	148	165	149	162
	247	254	250	258	255	260	199	200	191	201	152	138	157	138	151
Pump outlet temperature, °R	49.0	49.1	49.6	49.4	49.3	49.5	48.2	48.4	48.6	48.4	47.7	47.8	47.2	47.8	47.6
Pump speed rpm	33,800	33,400	33,900	33,700	34,700	34,300	34,700	33,200	34,800	33,700	35,200	34,600	34,300	35,400	34,700
Pump outlet flow orifice ΔP, psi	← ΔP record too faint to be legible →														
Hydrogen flow (from ΔP), gpm	← No LH_2 orifice ΔP record →														
Hydrogen flow (from tank wt loss), gpm	← 1010 →						← 1270 →				← 1330 →				
Pump hydraulic power, horsepower	150	153	154	158	153	156	153	155	152	152	120	115	128	116	126
Turbine air power, horsepower	← Turbine air flow not obtainable →										238 ②	214	213	222	231
Turbine inlet static pressure, psig	48	43	45	47	47	48	46	46	46	48	50	40	42	42	42
Turbine inlet air temperature, °F	257	272	282	289	291	308	312	310	326	322	351	349	368	372	381
Turbine outlet static pressure, psia	← 14.0 →														
Turbine outlet air temperature, °F	78	92	102	96	100	110	112	111	127	126	137	144	165	164	164
Turbine air flow rate, lb per min	← Turbine air orifice ΔP trace too faint to be legible →										370 ②	360	365	363	362
Measured NPSH, ft LH^2	8.5	13.4	2.6	13.8	4.3	16.1	2.9	15.1	.7	16.4	.33	.33	25.6	.20	23.8
Suction Specific Speed	217,000	152,000	517,000	151,000	370,000	146,000	533,000	155,000	1,620,000	148,000	-	-	110,000	-	118,000

① All runs are steady state 34,000 rpm operation at varying pump discharge pressures.
② Based on visual observation of differential pressure gauge as recorded on taped run comments.
③ Time intervals selected to show effect of tank pressure variations.
④ Discharge valve setting changed to decrease pump pressure rise.

TABLE 16

RESULTS OF TEST RUN 7

	A (1)	B	C	D	E	F	G
Run time interval, min: sec	0:37	0:52	1:09	1:45	1:54	2:03	2:13
Tank pressure, psig	18.5	18.4	18.2	16.7	16.1	16.0	15.5
Pump inlet vapor pressure, psig (5)	No record						
Pump inlet static pressure, psig (2)	21.7	20.6	20.9	23.9	23.4	22.7	20.3
Pump inlet total pressure, psig	No record						
Pump inlet temperature, °F (estimated)	39.5			41.0			
Pump outlet static pressures, psig	29	33	71	557	560	560	555
	28	31	69	554	557	556	548
Pump outlet temperature, °R	39.7	39.6	40.1	47.6	47.8	48.0	47.9
Pump speed, rpm	200	5000	10,500	33,600	33,600	33,700	33,700
Pump outlet flow orifice ΔP, psi	-0.7 (3)	-0.7	-0.5	2.7	2.65	2.7	2.55
Hydrogen flow (from ΔP), gpm	Negligible			750	746	749	728
Hydrogen flow (from tank wt loss), gpm	165	611	720	1340			
Pump hydraulic power, horsepower	0.96	4.06	20.4	422	424	424	419
Turbine air power, horsepower	Negligible		409 (4)	268	357	470	498
Turbine inlet static pressure, psig	0	0	3	69	69	69	68
Turbine inlet air temperature, °F	1944	1993	2324 (4)	185	192	211	219
Turbine outlet static pressure, psia	14.0	14.0	14.0	14.0	14.0	14.0	14.0
Turbine outlet air temperature, °F	618	815	1053	119	103	93	93
Turbine air flow rate, lb per min	Negligible		57	720	710	705	700
Measured NPSH, ft LH^2	No record						
Suction specific speed	No data available						

(1) Conditions A, B and C taken during pump acceleration with combustor ignited. Conditions D through G are steady state at 33,700 rpm with combustor de-energized.

(2) Instrumentation fluctuations were ±7.5 psi throughout test run.

(3) Instrumentation calibration questionable.

(4) Temperatures were excessive and damaged the thermocouple casings.

(5) Vapor pressure during run was 6.25 psig during test based on visual observation of the pressure gauge. Valve was steady throughout the test run.

SECTION 9

MATERIALS SECTION (TABLE LXXV)

No work was accomplished involving the development, improvement, and/or application of materials and processes to end item and equipment designs.

REFERENCES

1. "Advanced Inducer Study," Thompson Ramo Wooldrige Inc., Report ER 5288 NASA Contract NA5 84006.

2. W. W. Wilcox, P. R. Meing, R. L. Davis, "Performance of an Inducer - Impeller Combination at or Near Boiling Conditions For Liquid Hydrogen". Cryogenic Engineering Conference, August 14-16, 1962.

3. J. K. Jakobsen, "On the Mechanism of Thread Breakdown in Cavitating Inducers,"

4. W. Jetat, "The Worthington Inducer," Report prepared by Worthington Corporation under NASA Contract NA5 8-2680.

5. A. Shaffer and J. Rousseau, "Thermodynamic Properties of 20.4 Equilibrium Hydrogen," ASD TR 61-360.

6. J. E. Coppage et al., "Study of Supersonic Radial Compressors For Refrigeration and Pressurization Systems," WADC Report TR 55-257.

7. B. A. Wartman, L. R. Rendau, and S. J. Kline, "Effect of Inlet Conditions on Performance of Two-Dimensional Subsonic Diffusers," ASME, 1961.

8. Bragg, S. L., and Hawthorne, W. R., "Some Exact Solutions of the Flow Through Annular Cascade Actuator Discs," JAS Vol 17, No. 4, April 1950.

9. Horlock, J. H., "Some Actuator-Disc Theories for the Flow of Air Through an Axial Turbomachine," ARC R and M No. 3030, December 1952.

10. Jahnke and Emde, "Tables of Functions."

11. T. E. Coppage, F. Dallenbach, H. P. Eichenberger, G. E. Hlavka, E. M. Knoernschild, N. Van Le, "Study of Supersonic Radial Compressor," AiResearch - WADC-TR-55-257, 1956.

12. G. F. Wislicenus, "Fluid Mechanics of Turbomachinery" McGraw Hill, 1947.

13. O. E. Balje, "A Contribution to the Problem of Designing Radial Turbomachines," ASME, 1952.

14. B. Eckert, "Axialkompressoren und Radialkompressoren," Springer, 1933.

15. R. C. Dean, Y. Senoo, "Rotating Wakes in Vaneless Diffusers," ASME, 1960.

16. B. A. Wartman, L. R. Reneau, S. T. Kline, "Effect of Inlet Conditions on Performance of Two Dimensional Subsonic Diffusers," ASME, 1961.

17. K. E. Nichols, D. G. McPherson, O. E. Balje, "Study of Turbine and Turbopump Design Parameters," Volume IV, "Low-Specific-Speed Turbopump Study" Sunstrand Turbo Division Report No. 1735, 1960.

REFERENCES (Continued)

18. R. Spies, "Energy Conversion Systems Reference Handbook," Volume VIII, "Other Devices," WADS-TR-60-699, 1960.

19. A. T. Stepanoff, "Centrifugal and Axial Flow Pumps," 1957.

20. L. F. Florant, H. F. Snider, "Centrifugal Pumping of Liquid Hydrogen," Ohio State Research Foundation Technical Report 333-4, 1950.

21. B. Sternlicht, W. Zabriskie, "Labyrinth Seal Leakage Analysis," ASME, 1959.

22. R. Rotzoll, "Untersuchungen an einer Langsamlaufigen Kreiselpumpe bei Verschiedenen Reynolds-Zahlen," Dissertation, 1957.